LIÈGE université Sciences

Mechanisms of element exchange and genesis of stratiform chromitite in the Stillwater Complex

A dissertation submitted for the degree of

Doctor of Science

by

Bai Yang

Supervisor: Prof. Bernard Charlier, University of Liege, Belgium

Co-supervisor: Prof. Ben-Xun Su, Chinese Academy of Sciences, Beijing, Chine

Soutenue publiquement le 13 octobre 2023, devant le jury de thèse composé de

Prof. Valentin Fischer	Président	Université de Liège, Belgique
Prof. Jacqueline Vander Auwera		Université de Liège, Belgique
Prof. Max Collinet		UNamur, Belgique
Prof. Olivier Namur		KU Leuven, Belgique
Prof. Ben-Xun Su	Co- Promoteur	Chinese Academy of Sciences, Beijing, Chine
Prof. Bernard Charlier	Promoteur	Université de Liège, Belgique

Acknowledgements

I would like to thank my supervisors Prof. Bernard Charlier and Prof. Ben-Xun Su for discussions and reviews that improved the thesis considerably. For help during field work I sincerely thank Prof. Yan Xiao, Prof. Chen Chen, Dr. Yang Sun, and Dr. Yan Hu. Dr. Xiao Yan Gu, Dr. Meng-Meng Cui, Dr. Xia Liu and Dr. Jie-Jun Jing helped with carrying out FTIR and H_2O calculation in Zhejiang University (Zhejiang) and Prof. Ding-Shuai Xue, Dr. Bing-Yu Gao, Prof. Wen-Jun Li are sincerely thanked for carrying out XRF and LA-ICP-MS analyses in the Institute of Geology and Geophysics, Chinese Academy of Sciences (Beijing). Xiao-Qing He and Prof. Li-Ping Qin helped with separates dissolved and Cr isotopic analysis in Chinese Academy of Sciences University (Hefei). Column chemistry and mass spectrometry for Fe-Mg isotopes were performed at the Isotope Geochemistry Lab, China University of Geosciences (Beijing). We also thank Prof. Paul T. Robinson, Prof. Patrick Asamoah Sakyi and Dr. Wang Jing for comments on the original revision. Robert Dennen is acknowledged for extensive editing of the thesis. The **chapter 3** has also benefited from careful reviews by four anonymous referees and Editor Shi-Chun Huang. We thank Stefan Weyer and three anonymous reviewers who provided many useful suggestions for the **chapter 4**. We appreciate the constructive reviews from Daniela Rubatto, Alan E. Boudreau and an anonymous reviewer, who markedly improved the **chapter 5**. Two anonymous reviewers for providing insightful and constructive reviewer comments that significantly improved the **chapter 6**, and the associate editor from GSA Bulletin for handling it and providing very helpful additional comments. This thesis was supported by the National Natural Science Foundation of China (41973012, 91755205 and 41772055) and the Second Tibetan Plateau Scientific Expedition and Research Program (STEP) (2019QZKK0801), the State Key Laboratory of Lithospheric Evolution (201701), and the Youth Innovation Promotion Association, Chinese Academy of Sciences (2016067). Bernard Charlier is a Research Associate of the Belgian Fund for Scientific Research-FNRS.

Abstract

The interpretation of the chemical evolution of layered intrusions and stratiform chromitite formation involves inversion of mineral composition trends to infer compositions of parent magmas. Three principal elemental re-equilibrated processes must be taken into account when interpreting mineral compositions in cumulate rocks: 1) changes in the composition of the parent magma due to different magma mixing proportions, fractional crystallization, contamination etc, proportions, consequently leading to chemical disequilibrium between the magmas and crystallizing minerals; 2) superimposed modification of mineral compositions as a result of crystallization of trapped interstitial or extraneous evolved melt/liquid; 3) redistribution of elements due to sub-solidus re-equilibration between silicate and oxide minerals. This thesis is an attempt to distinguish these effects, through a series of zoning information and stable isotopic systems.

To better understand and distinguish the role of inter-mineral diffusion during subsolidus processes and compositional shifts during melt/fluid infiltrating, we investigated the Fe and Mg isotopic compositions of olivine, orthopyroxene, and chromite separates from the Peridotite Zone of the Stillwater Complex. Olivine and orthopyroxene show limited Mg isotopic variations, with δ^{26}Mg values ranging from -0.40 to -0.26‰ and from -0.29 to -0.22‰, respectively, similar to mantle peridotite values. In contrast, chromite displays extremely large Mg isotopic variations, with δ^{26}Mg ranging from -0.05 to +0.84‰. The δ^{56}Fe values in olivine and orthopyroxene range from 0.00 to +0.17‰ and -0.04 to +0.06‰, whereas chromites have δ^{56}Fe values ranging from -0.09 to +0.13‰. Most olivine-orthopyroxene pairs in our samples show no clear Fe-Mg isotopic differences, whereas those between silicates and chromite display disequilibrium inter-mineral fractionation, as they fall off the theoretically predicted equilibrium fractionation lines. Higher δ^{56}Fe values in silicates than chromite and higher δ^{26}Mg values in chromite than silicates indicate that subsolidus re-equilibration between silicates and chromite is responsible for the observed

disequilibrium Fe-Mg isotope fractionation.

The Cr isotopes are also analyzed in same samples, which olivine and orthopyroxene have δ^{53}Cr values ranging from -0.09 to 0.25‰ and from -0.11 to 0.07‰, respectively, higher than the values of coexisting chromite with δ^{53}Cr from -0.23 to -0.07‰. Evolving chromite Cr isotopic compositions may be a geochemical indicator of magmatic differentiation. Chromite-olivine pairs in silicate cumulates tend to have larger fractionation factors than those in chromitites, which is interpreted as the result of re-equilibration between interstitial melt/liquids.

Stable isotopes of Li-O in major minerals of chromitite, dunite, poikilitic harzburgite and bronzitite were also examined and measured in our thesis. The Li isotopes in olivine range from 4 to 26‰ in δ^{7}Li with uniform Li contents of 1 to 3 ppm, whereas orthopyroxene and clinopyroxene have Li contents of 0.5 to 5 ppm and 4 to 8 ppm, and δ^{7}Li ranges of -13 to 7‰ and -14 to -6‰, respectively. The δ^{18}O values vary from 4.91 to 5.72‰ in olivine, from 5.11 to 5.87‰ in orthopyroxene, and from 4.64 to 5.86‰ in clinopyroxene. For a given sample, olivine displays more variable and higher δ^{7}Li but lower δ^{18}O values than orthopyroxene, indicating that olivine experienced more extensive compositional modification after crystallization relative to orthopyroxene. The general Li and O isotopic compositions are interpreted as the result of re-equilibration between interstitial liquids, from which pyroxenes crystallized, and cumulus minerals. The inter-mineral and inter-sample isotopic variations correlate with mineral assemblages, crystal sizes and major and trace element compositions, revealing that the interstitial liquids varied compositionally mainly due to mixing between fractionated magma and newly injected primitive magma. Abrupt mineralogical and geochemical changes from silicate rocks to chromitites imply that hydrous fluids, which collected on chromite surfaces and were later released from chromite seams, played an additional, critical medium of chemical exchange between minerals in the chromitites.

Our research results provided different results between Fe-Mg isotopes and Cr-Li isotopes. The inter-mineral element diffusion has been demonstrated by conjugated Fe-Mg isotopic variations in chromite and silicates. On the contrary, the Cr-Li isotopic

elevations in silicates are interpreted as the result of re-equilibration between interstitial melt/liquids. For these distinctions, we hold the opinion that the elemental contents in minerals relative to the mineral/fluid should be the dominant factor. The Li and Cr content differences between in silicates and liquids are similar, nevertheless, the Fe-Mg elemental contents in cumulus minerals are obviously higher than those in interstitial melt/liquid. Therefore, we can also speculate that the major elemental and isotopic variations in cumulus minerals are controlled by inter-mineral diffusion, whereas the trace elements, fluid mobility elements and their isotopic variations are more likely to be changed by melt/liquid shifts.

Both the inter-mineral diffusion and diffusion between mineral and interstitial can be restricted by separates, which has significant in explain the disequilibrium isotopic composition in disseminated samples. However, the migration of fluids between different layers, especially for the chromitite and silicate cumulates, have still no limited. A FTIR study of H_2O in silicates shows reverse H_2O contents in olivine and poikilitic orthopyroxene in chromitite whereas co-increasing H_2O contents in oikocrysts in silicate cumulates. Massive hydrated mineral inclusions in chromite and high fluid-mobile elements in included silicates support that the chromitite crystallized from a fluid-enriched parental magma, and the early crystallizated chromite microlites collecte fluids leading to their re-distribution between olivine and poikilitic orthopyroxene. On the other hand, chromite grains could be efficiently floated by these fluids, causing them to migrate away from the silicate minerals, leading eventually to formation of nearly monomineralic chromitite seams. This process demonstrates that the chromitite seams in layered intrusions could be the result of mechanical sorting.

Key words: Elemental diffusion, Layered intrusions, Fe-Mg isotopes, Cr-Li isotopes, Inclusion, Liquid, Stratiform chromitite

Table of contents

1. Introduction

This thesis studies different types of elemental diffusion mechanisms in the Ultramafic Series of the Stillwater Complex, a large layered intrusion typical of intrusions worldwide, by analyzing the isotopic compositions of major elements (Fe-Mg) and trace elements (Cr-Li) in cumulus separates. Inclusions in chromite and H_2O contents of co-existing silicate minerals are also analyzed to reveal the elemental migration effects between different layers, and eventually, to explain the origin of stratiform chromitite.

1.1 Layered intrusions and stratiform chromitite

1.1.1 Fundamentals of layered intrusions

Layered intrusions are typically stratiform, usually sill-like bodies of cumulate rocks, at least a few hundred meters and as much as 10 km thick, characterized by the presence of a variety of different types of layering over a range of length scales (Wager and Brown, 1968; Parsons, 1987; Cawthorn, 1996; Charlier et al., 2015; O'Driscoll and VanTongeren, 2017; Brooks, 2019; Boudreau, 2019; Latypov et al., 2020; Cawthorn, 2021). They are the solid record of differentiation processes of mainly basaltic magmas. They contain a significant majority of the world's known reserves and resources of important industrial metals, particularly the platinum-group elements (PGE), chromium (Cr) and vanadium (V), and are important sources of nickel (Ni), copper (Cu) and cobalt (Co) (e.g., Naldrett, 2004; Mungall and Naldrett, 2008; Hughes et al., 2021; Smith and Maier, 2021). Currently, layered intrusions are not common, with the most famous examples including the Bushveld Complex in South Africa, the Great Dyke in Zimbabwe, the Stillwater Complex in the United States, and the Muskox intrusion in Canada (see Figure 1.1 and Table 1.1).

Compared to other types of mafic-ultramafic rocks, layered intrusions exhibit the following typically characteristics: (1) Layered intrusions have a wide age span and can be found in various geological settings, ranging from Precambrian cratons to Paleozoic Mountain belts. The radiometric isotopic ages of these intrusions have been well-documented (see Table 1.1; Cameron, 1980; Alapiti et al., 1990; Cawthorn et al., 2005); (2) Layered intrusions commonly have tabular and sheet-like shapes, but they can also exhibit basin-like or funnel-like structures. Tectonic events or erosional processes following their emplacement can expose these intrusions in tilted or inclined orientations relative to the Earth's surface (Ferreira Filho et al., 1995; Eales et al., 1996; Emeleus et al., 1996); (3) Layered intrusions are often of immense size. For example, the Bushveld Complex, as an illustration, has an elliptical shape on the Earth's surface with east-west dimensions of up to 450 km and north-south dimensions of around 250 km. It covers an approximate area of 40,000 km² and can reach a total thickness of up

to 5 km (Hatton and Von Gtuenewaldt, 1990; Girardi et al., 2006; Garuti et al., 2007); (4) Layered intrusions typically intrude at shallow to mid-crustal depths, ranging from a few kilometers to around one kilometer deep. The depth of emplacement is influenced by various factors, including the density, temperature, and viscosity of the magma (Irvine, 1975; Lee, 1996; Hillier et al., 2003). As magma ascends and cools, its temperature and viscosity increase, and the formation of a small number of crystalline nuclei may further increase the dynamic conditions required for magma ascent (Lipin et al., 1993; Marques and Ferreira-Filho, 2003; Lord et al., 2004).

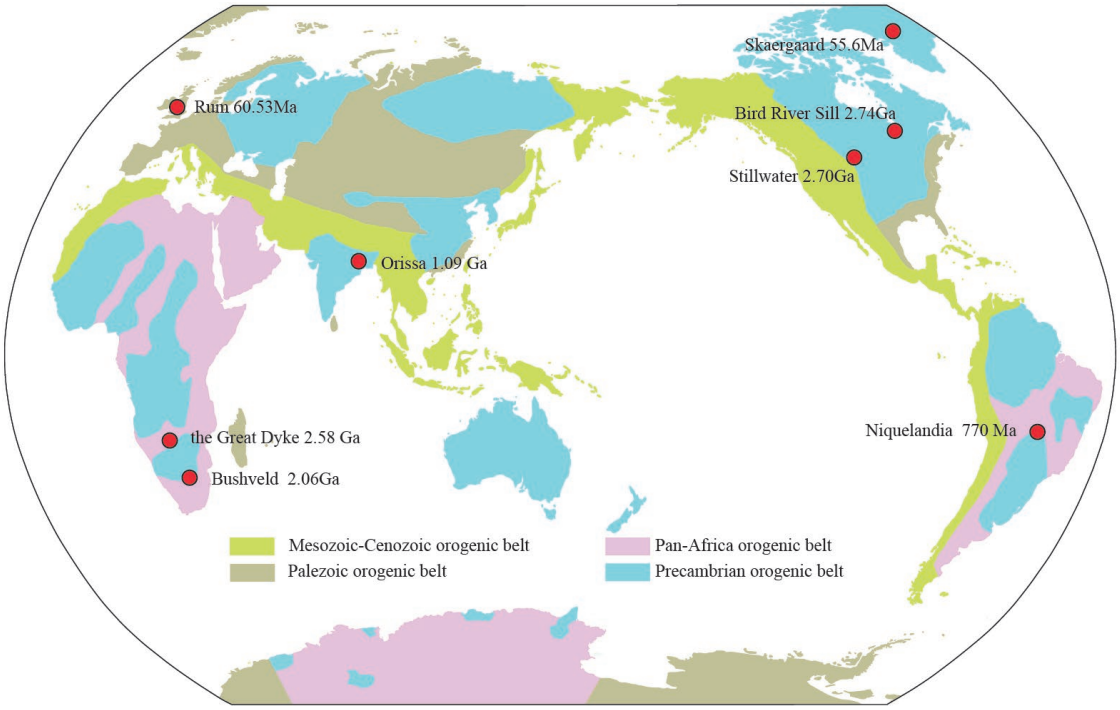

Figure 1.1 Distribution and age of the largely layered intrusions worldwide (for data sources of layered intrusions see Table 1.1)

Compared to other types of mafic-ultramafic intrusions, layered intrusion typically undergoes more extensive magmatic differentiation, including ultramafic and mafic rock types within a single layered intrusion (Naslund and McBirney, 1996; O'Driscoll et al., 2009). Among these, ultramafic rocks may include dunite, harzburgite and pyroxenite, while mafic rocks can comprise norite, gabbro, diorite, olivine-norite, olivine gabbro, and olivine diorite, among others. Some intrusions can even feature more acidic rocks like syenite and granite facies (Sharkov et al., 1995; Tepley and

Davidson, 2003). The layering structure within these rock bodies is typically categorized into four levels (the terminology used in this paper follows this convention): (1) Series: layered intrusions are usually subdivided into upper series, lower series, and sometimes basal series (Jackson, 1968; Ulmer, 1969; Theyer, 1991). The upper and uppermost series are often composed of mafic rock types, while the lower series comprises ultramafic rocks. The basal zone represents the cooled edge of the intrusion. While the upper series may not always be present, the other three series are commonly observed; (2) Zones: series are divisions into zones, such as the peridotite zone within the ultramafic series. Zone typically consists of multiple layering rock facies, with their characteristic rock assemblage, locations, and continuity in the whole intrusion; (3) Units: Within a single zone, different rock assemblages may exhibit repeated sequences of one to three specific rock facies. For example, in the peridotite zone of the Stillwater Complex, 21 lithological cycles units may be observed, each composed of dunite, harzburgite and pyroxenite. Hence, each lithological cycle units often consists of multiple rock facies. (4) Layer: layers are the fundamental units that make up the complex. Each of rock layer is composed of a specific rock type, but its internal characteristics may vary significantly, including mineral composition evolution, fluctuation in mineral pattern proportions, changes in grain size, and even variations in mineral orientation.

Due to their enormous scale and slow cooling, layered intrusions, which are typically emplaced in highly stable cratons, provide magma with prolonged time and conditions for differentiation, leading to the formation of various distinct rocks (Emeleus et al., 1996; Garuti et al., 2005, 2007). The occurrence of multiple layers within these intrusions results in pronounced diffusion processes. Layered intrusions, with their complex and long-lasting formation history, serve as exceptional natural laboratories for studying the effects of diffusion on mineral composition changes. Furthermore, the presence of various layering structures, combined with processes such as mineral crystallization differentiation, assimilation of surrounding rocks, and magma replenishment, makes it challenging to precisely determine the chemical composition

of their parental magma. Currently, the compositional analysis of the chilled margins at the bottom and top contacts of the intrusion with the surrounding rocks may provide the closest approximation to the parental magma composition. These margins often consist of magmatic bodies that have undergone differentiation and are enriched in Al_2O_3, falling into the category of felsic and basaltic rocks (Theyer, 1991; Naslund and McBirney, 1996; Tepley and Davidson, 2003).

1.1.2 Chromitite

Chromitite are rocks composed predominantly of chromite. They may occur as nodules or pods, as in the case of obducted and uplifted mantle material (Arai, 1997), or as layers, seams, and lenses in layered mafic-ultramafic intrusions. These stratiform layers are most often located in the lower ultramafic-mafic portions of intrusions (e.g., Bushveld, Stillwater), yet may occur in the central to upper, often gabbroic, portions (e.g., Koitelainen and Akanvaara; Hanski et al., 2001; Figure 8). Typically, stratiform chromitite range from a few millimeters to 10s of centimeters in thickness and may persist laterally for several 10s to 100s of kilometers (Jackson, 1961; Cameron, 1964; Cawthorn et al., 2005). However, layered intrusions may also host thick (up to ~ 100 m) discontinuous chromitite bodies that are often hosted by ultramafic rock types (e.g., Inyala and Railway Block, Black Thor, Ipueira-Medrado sill of the Jacurici Complex, Nuasahi-Sukinda; Mondal et al., 2006; Prendergast, 2008; Marques et al., 2017; Lesher et al., 2019). This has led to the subdivision of stratiform-type and conduit-type chromitite (Prendergast, 2008; Lesher et al., 2019). It has been hypothesized that podiform and stratiform chromitite are connected. Arai (2021) proposed that chromite crystals in stratiform chromitite formed in the mantle during the reaction between mantle peridotite and magma and were subsequently entrained and deposited.

Stratiform chromitite are commonly rich in PGE relative to their bracketing units and rarely associated with magmatic Ni-Cu-(PGE) mineralization (e.g., Uitkomst). Chromitite of the Great Dyke, Bushveld, and Stillwater complexes host the majority of the world's Cr reserves, and significant PGE mineralization in the case of

the Bushveld's UG-2 chromitite. While chromitite ores at these localities typically host 40-45 wt.% Cr_2O_3, (Stowe, 1994; Naldrett, 2004), elsewhere, chromitite ores range from 21 wt.% (Rum intrusion) to 57 wt.% Cr_2O_3 (Schulte et al., 2010). These chromitite may bifurcate, undulate, and persist despite irregular footwall topologies (Latypov et al., 2015). They often share sharp to weakly diffuse, planar to cm-scale undulatory contacts with their bracketing rocks units, which typically are anorthosite, gabbronorite, and pyroxenite (Lenaz et al., 2011; Scoon and Costin, 2018; Maghdour-Mashhour et al., 2020; Smith et al., 2021b). In contrast, conduit-type chromitite occur in relatively ultramafic sill-like intrusions (e.g., Black Thor, Ipueira-Medrado, Uitkomst), and as such, are thought to be the product of komatiitic magmas (Yudovskaya et al., 2015; Marques et al., 2017; Lesher et al., 2019). Their Cr_2O_3 grades are comparable to that of stratiform-type chromitite (35-40 wt.% at Ipueira, Marques et al., 2017; ~33.5 wt.% at Uitkomst, Maier et al., 2018a). Many layered intrusions with chromitites are Archean to Proterozoic in age, with few Phanerozoic examples (e.g., Rum; Smith and Maier, 2021).

1.2 Diffusion mechanisms in Ultramafic Zone of layered intrusions

The magma differentiation process of mafic-ultramafic intrusive rocks has been extensively studied in various geological settings, apart from the initial composition of the magma, other physicochemical conditions including temperature (Jackson, 1961; Irvine, 1965, 1967; Evans and Moore, 1968; Wager and Brown, 1968), pressure (Cameron, 1969, 1975; Irvine and Smith, 1969; Haggerty, 1976), and oxygen fugacity during magma cooling and crystallization (Parsons, 1987; Agata, 1988; Jan and Windley, 1990) all have significant influences on the composition of minerals. These factors are all part of equilibrium processes and have a wide range of geochemical indicators for calculation (Hamlyn and Keays, 1979; Fisk and Bence, 1980; Dick and Bullen, 1984). For example, the distribution of cations between oxides and coexisting silicate minerals can be used to indicate changes in equilibrium temperature, while the content of valence-changing ions in oxides can serve as an effective indicator of magma

oxygen fugacity (Roeder et al., 1979; Fabrics, 1979).

On the other hand, due to the relatively high initial temperature, magma viscosity, and the fact that mafic-ultramafic magmas are in a more evolved stage of magma evolution, minerals that crystallize early in the process often undergo prolonged and continuous magmatic processes. Taking layered intrusions as an example, minerals rich in Mg-Fe elements such as chromite, coexisting silicate minerals like olivine and pyroxenes, which are among the earliest crystallizing minerals (Leblanc and Nicolas, 1992; Zhou et al., 1996; Melcher et al., 1997; Teng et al., 2011; Collinet et al., 2017), may exhibit significant chemical concentration differences due to varying proportions of magma supply or rapid crystallization of single-phase minerals like chromite, leading to noticeable changes in melt composition and disequilibrium with minerals. Additionally, the continuous modification of minerals by interstitial residual melt/fluid can result in significant changes in mineral composition. As the temperature decreases, interstitial minerals that reach equilibrium co-crystallization at magma temperatures, especially between silicate minerals and oxides, can develop chemical concentration differences due to changes in partition coefficients between elements in these phases, leading to diffusion (e.g., Chopra et al., 2012; Sio et al., 2013; Oeser et al., 2015; Pogge von Strandmann et al., 2015; Chen et al., 2018). Currently, the common behaviors of minerals in terms of element diffusion from their surroundings can be broadly categorized into three types:

1) During the magmatic process, disequilibrium can form between the melt and minerals. Apart from element diffusion resulting from different sources between the melt and minerals (such as diffusion occurring between basaltic magma and olivine cumulates, this paper only discusses element diffusion under the same source conditions), magmatic mixing is one of the most common occurrences during magma evolution. Even in closed magma chamber systems formed by a single magmatic intrusion (e.g., the Skaergaard intrusion; Wager and Brown, 1968), melt composition can change to some extent due to mingling and convective layering within the magma (Cawthorn et al., 2015). Existing literature has shown that continuous replenishment of

the primary magma is a critical mechanism for the formation of sufficient oxide cumulates in mafic-ultramafic intrusions, and it can also trigger the crystallization of more silicate minerals (e.g., Irvine, 1977; Cawthorn et al., 2005; O'Driscoll et al., 2009; Su et al., 2020). When a higher proportion of primary melt is injected into partially crystallized magma chambers, it can lead to concentration differences with minerals already in equilibrium with early melt, thus inducing mineral diffusion growth (Figure 1.2; McCallum, 1996, 2002; Mondal and Mathez, 2007; Oeser et al., 2015), and even the formation of distinct mineral zoning structures (Weidendorfer et al., 2014). In such cases, even if the minerals that crystallized early and those that recrystallized after mixing with the magma may not differ in composition (both are in equilibrium with the melt in terms of elemental composition), they may exhibit differences in mineral crystal shapes, grain sizes, and isotopic compositions (Watson and Baker, 1991; Tepper and Kuehner, 1999; Chamberlain et al., 2014).

Conversely, there is the phenomenon of melt composition undergoing abrupt changes towards more evolved compositions, leading to element diffusion between the melt and minerals. In contrast to the high-temperature and more primitive initial melt, the sources of melts that have undergone crystallization differentiation may be more diverse, and reports related to this are more common. For example, the common phenomenon of wall-rock assimilation during chromite crystallization (Spandler et al., 2005), the injection of magmas carrying deep-seated crystalline minerals into magma chambers, and their subsequent mixing with already evolved magma, are processes that can lead to such diffusion (Cawthorn et al., 2015; Figure 1.3). In these cases, the diffusion of elements between minerals and the melt can be considered as a record of changes in magma composition during the growth of crystals, involving two or more distinct stages (Kahl et al., 2011; Longpre et al., 2014).

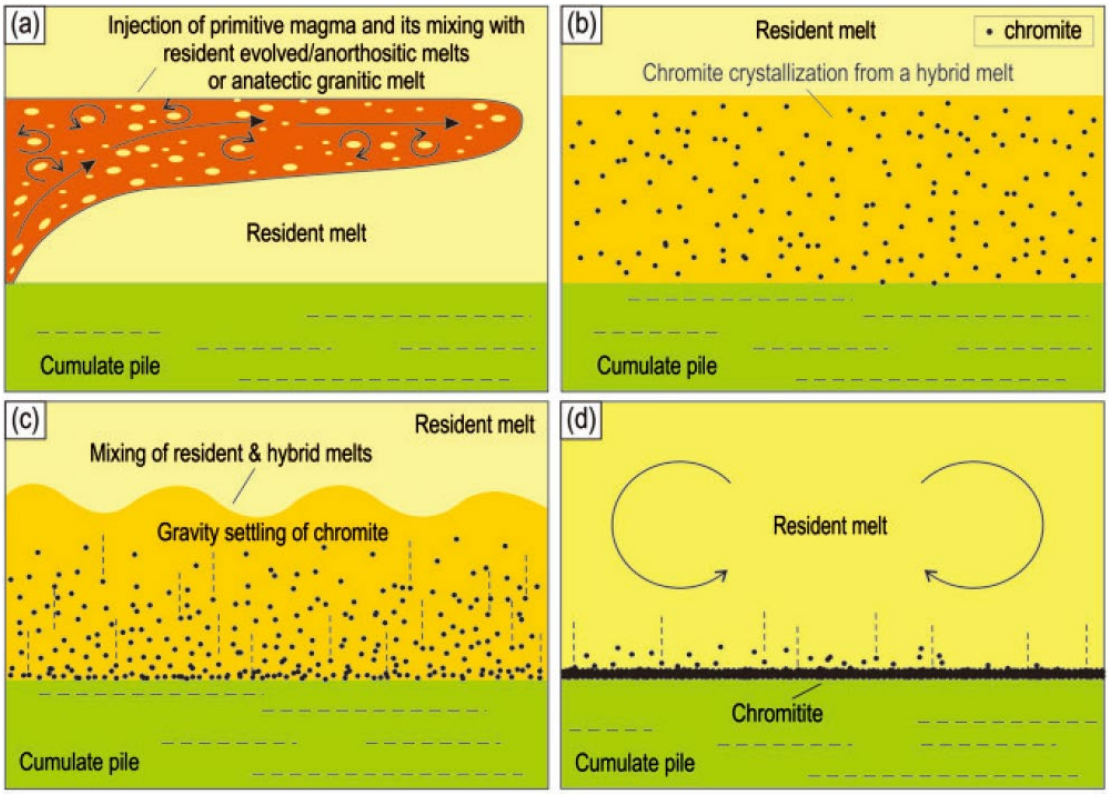

Figure 1.2 Sketch of the different mixing proportions leading to the chemical disequilibrium between the magmas and crystallizing minerals (modified from Irvine, 1975, 1977; Jenkins and Mungall, 2018). The key idea is that mixing of primitive magma with resident evolved melt or anatectic granitic melt will result in a hybrid melt saturated in chromite and olivine that subsequently settles to the base of the chamber.

Furthermore, compositional differences between crystals and the melts can lead to changes in crystal grain size, which may further promote the occurrence of diffusion (Donaldson, 1975; Brearley and Scarfe, 1986; Donaldson, 1990; Armienti et al., 1991; Jambon et al., 1992; Figure 1.4). In general, slow cooling of magma can ensure that the melt surrounding crystalline minerals exchanges sufficiently with the melt farther away from the minerals as the temperature decreases, thus maintaining or approaching homogeneity in the entire magma system. However, rapid mineral crystallization processes or quenching of the melt may not produce mineral phases in equilibrium with the melt composition (e.g., Watson and Muller, 2009; Goel et al., 2012). In such cases, the crystallized minerals are often more depleted compared to the melt, especially for high-valence and high-atomic-number elements with slow diffusion rates. This

depletion can lead to the formation of zoning within minerals, resulting in element diffusion between minerals and the melt.

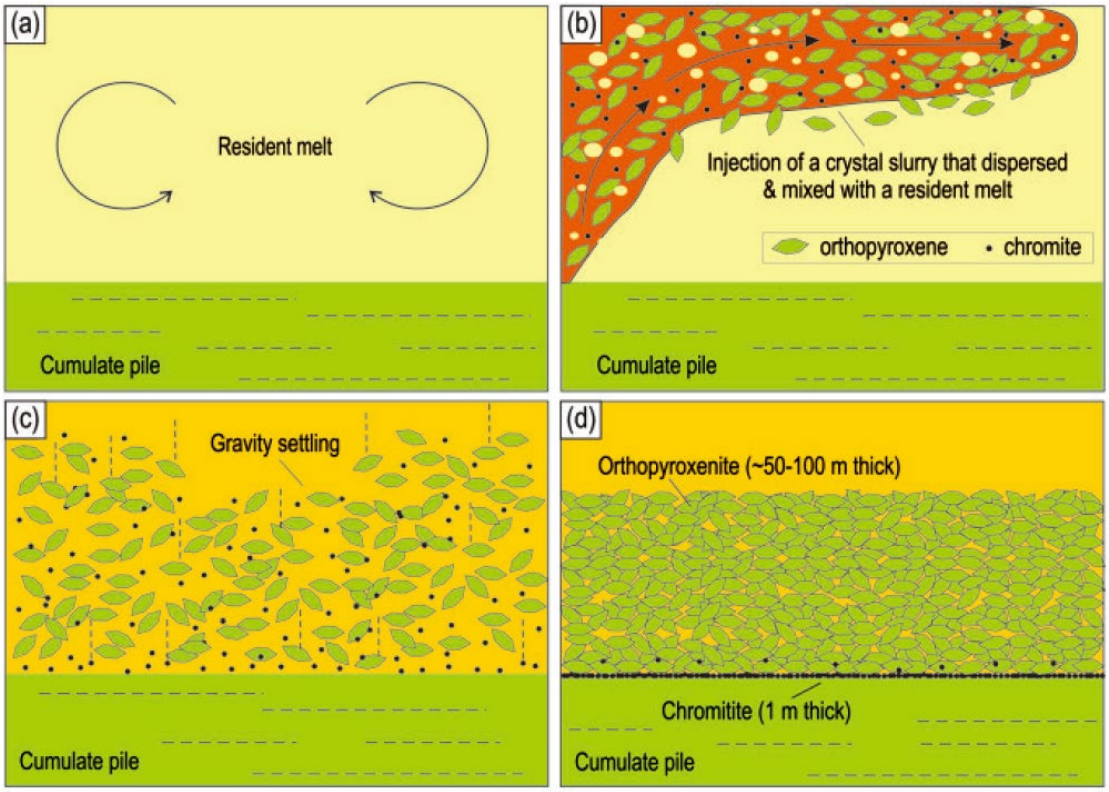

Figure 1.3 The model formulated by Eales and Costin (2012) for the formation of massive chromitites, which appeals to the emplacement of a crystal-rich slurry from a deep-seated magma chamber. The slurry is disaggregated in response to forceful mixing with a resident melt and then upon settling chromite separates from olivine and pyroxenes to form a basal layer of massive chromitite overlain by about a 50~100 m thick column of orthopyroxenite.

2) The enrichment and migration process of interstitial melt/fluid can also modify the composition of minerals. Irvine (1980) first proposed that interstitial melt/fluid, gradually enriched during magma crystallization differentiation, could be trapped by minerals and exchange elements with them. Another possible mechanism is that melt/fluid may aggregate in the interstices of cumulus minerals and migrate extensively upwards, leading to significant metasomatic alteration of minerals they pass through (Figure 1.5; Naldrett et al., 1982). This model has also been used to explain the diversity

in cumulate mineral compositions between different cycles in layered mafic-ultramafic intrusions.

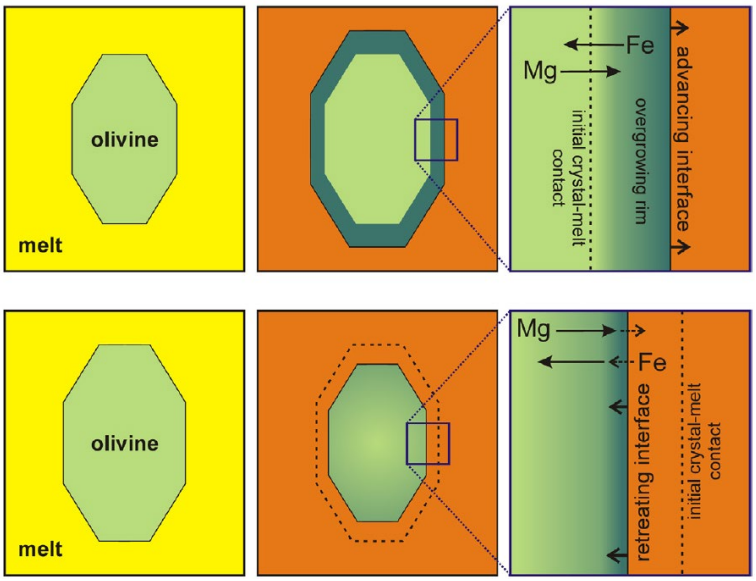

Figure 1.4 Illustration of the three scenarios in order to theoretically investigate the effects of diffusion between mineral and melts, along with crystal growth (a), dissolution (b) producing a diffusive boundary layer around the growing crystal. Cartoons are modified after Oeser et al. (2015).

Campbell et al. (1986) extensively discussed this model and proposed that the compaction resulting from large-scale cumulate formation provides a dynamic basis for the upward migration of large-scale melt/fluid through mineral interstices. The migration of interstitial melt/fluid can have other effects as well. For example, during the cumulation process of olivine and orthopyroxene, fluids released from chromitite layers may react with olivine, resulting in the formation of orthopyroxene at the margins of olivine grains, displaying an obvious olivine-encapsulating texture. This structure is common in large layered intrusions such as the Stillwater (Jackson, 1961), Skaergaard (Wager and Brown, 1968), and Jimberlana (Campbell, 1987) complexes. It is the most common structure in the silicate cumulate rocks within the olivine zone and is a crucial indicator for the presence of chromitite layers. Kaufmann et al. (2018) found in their studies on chromitite cycles in the critical zone of the Bushveld complex that upward fluid migration could also result in minor element variations and differences in crystal

growth orientations.

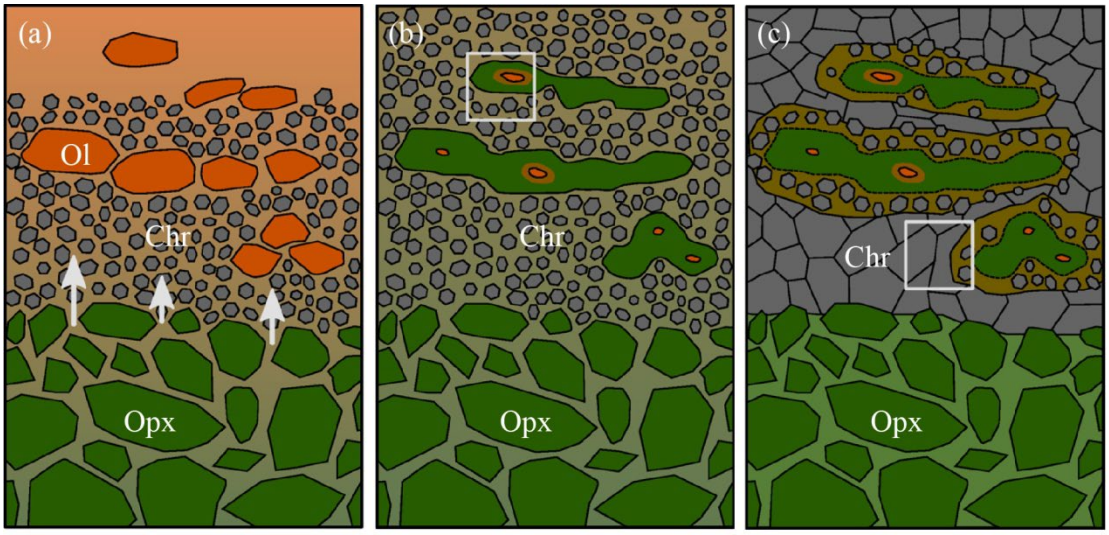

Figure 1.5 Proposed model for the reaction between silicates and liquids as well as the formation of orthopyroxene oikocrystal in the chromite seams: (a) crystal setting of olivine grains; (b) replacement of olivine by orthopyroxene by an upwards percolating melt in a liquid solid reaction; (c) re-equilibration and accumulation of chromite.

3) Element exchange behavior between minerals during the subsolidus process is also a crucial factor contributing to changes in mineral composition. The prolonged cooling history of mafic-ultramafic intrusions has long been a major focus of research on these types of rocks, including exchanges of elements between silicate minerals, oxides, and even elemental metals and sulfides (e.g., Boyd, 1973; Wood and Banno, 1973). Inter-mineral element re-equilibration, which occurs at grain boundaries but has diffusion rates similar to volume diffusion, was once thought to have negligible effects on crystal compositions. However, with the development of in-situ techniques, extensive work on elemental and isotopic studies has repeatedly demonstrated that the decrease in temperature can result in significant redistribution of predominantly low-valence elements such as Fe-Mg between silicate minerals and oxides (Wilson, 1982). This exchange-induced element heterogeneity is particularly pronounced at grain boundaries of these two mineral types (Irvine, 1967; Medaris, 1975; Clark, 1978; Arai,

1980; Wilson, 1982). Currently, the extent of such inter-mineral re-equilibration has become an important geological parameter for estimating whether a rock body has reached chemical equilibrium and the time required for this process (Ozawa, 1983, 1984). As research has advanced, the close relationship between inter-mineral subsolidus exchanges and mineral proportions, as well as the elemental contents of minerals themselves, has gained significance in economic geology (Figure 1.6; Xiao et al., 2016). This area of study has gradually become a hot topic in recent years, with the use of various new techniques, methods, and models further refining our understanding of element behavior in this process (e.g., Xiao et al., 2016; Zhang et al., 2019; Tian et al., 2020).

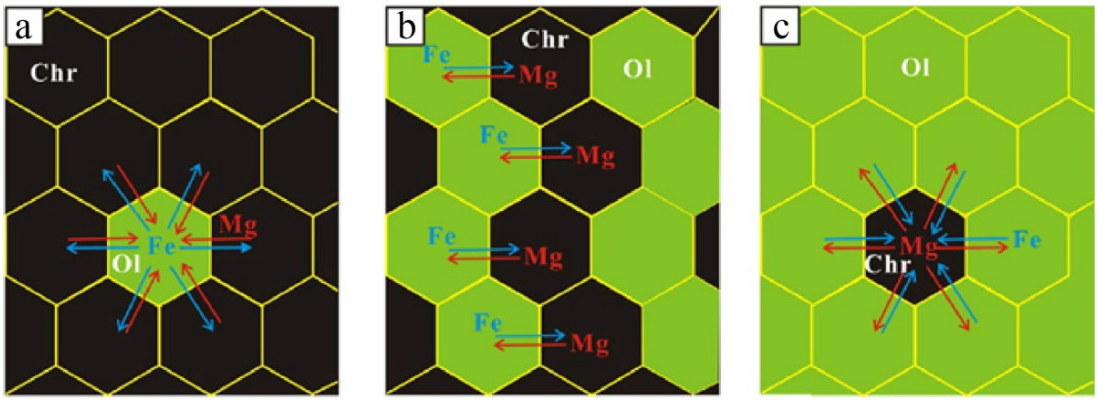

Figure 1.6 The change in chromite composition during re-equilibration with olivine is a function of their relative proportions in the rock. When the proportion of chromite is more than 90%, the change in chromite composition is little, but olivine Fo increase largely (a). With the proportion of chromite decreasing, the variation of chromite composition (Mg#) becomes much more obvious (b, c). Figures modified from Xiao et al., (2016).

1.3 Complex diffusion mechanisms in Ultramafic Zone of layered intrusions

Layered intrusions are important tools for understanding the composition of the mantle and the evolution of mantle-derived magmas. In comparison to mantle xenoliths, layered intrusions offer a more diverse range of formation environments, larger sample sizes, and more comprehensive evolutionary sequences. However, due to the diffusion

processes mentioned above that alter their mineral compositions, this also leads to the complexity of tracing the source of mafic-ultramafic magmas through mineral components (Dick and Bullen, 1984; Barnes and Roeder, 2001; Kamenetsky et al., 2001; Pagé and Barnes, 2009). Therefore, research into element exchange mechanisms during the formation and mineralization processes of such rocks becomes particularly important. Overall, there are currently several issues, including the following.

1.3.1 Whether the exchange of elements is widespread and its scale?

We continue to examine the early crystallized chromite and coexisting silicate minerals in the layered intrusions. The Mg# of ultramafic minerals is not only used as a parameter for crystallization differentiation but is also commonly employed as a geochemical indicator of elemental diffusion processes. This is because major elements can help us qualitatively analyze trends in element exchange and compare the scales of element exchange between different types of rocks. On the other hand, it is also noted that Fe-Mg, as divalent elements, have relatively high diffusion rates and are thus more easily identifiable.

Cumulus gabbros, orthopyroxenites, and clinopyroxenites in the layered intrusions, have Mg# values of silicate minerals with generally concentrated in the range of 78 to 86 (Figure 1.7a). In disseminated and massive chromitites, their Mg# values are more widely distributed, typically falling within the range of 82 to 90. It has even been reported that olivine in chromite inclusions can have Fo values exceeding 96 (Jackson, 1961; McCallum, 1996). The Mg# variation in chromite is similar to that of silicate minerals, typically ranging from 40 to 60 in chromtites and decreasing to between 10 and 40 in silicates layers. Such processes can indeed be explained by intergranular element exchange between silicate minerals and oxides (Figure 1.6; Xiao et al., 2016). Silicates layers have a higher proportion of olivine and pyroxene, leading to more extensive alteration of chromite. Conversely, chromite-rich layers equally alter the Fo and Mg# of silicate minerals, resulting in a noticeable increase in these values (Leblanc and Nicolas, 1992; Melcher et al., 1997; Chopra et al., 2012; Chen et al., 2018).

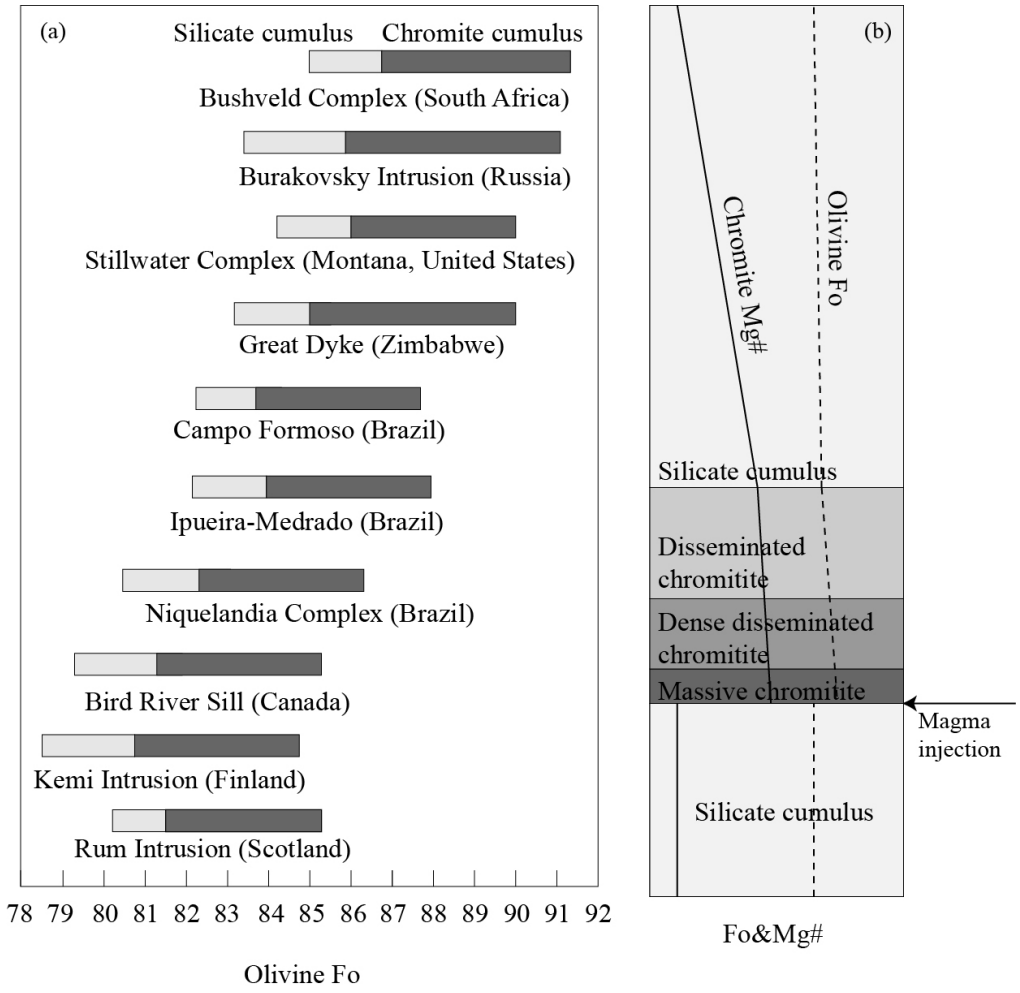

Figure 1.7 The distribution range of the Fo value of the olivine in typical layered mafic-ultramafic intrusions in the world (a) and the change trends in the of Fo or Mg# of culumus mienrals in silicate cumulates and chromitite (b). Date derived from Eales et al. (1993); Eales and Cawthorn (1996); Cawthorn et al. (2005); McCallum (1996); Higgins et al. (1997); Alapieti (1990); Tepley and Davidson (2003); Emeleus et al. (1996); Ferreira Filho et al. (1995); Garuti et al. (2005); Wilson (1996); Ohnenstetter et al. (1986); Marques and Ferreira Filho (2003); Power et al. (2000); Girardi et al. (2006); Theyer (1991); Jackson (1968); Stowe (1994); Lee (1996); Garuti et al. (2007); Alapieti et al. (1989); Lord et al. (2004); Naldrett (2004); O'Driscoll et al. (2009); Sharkov et al. (1995).

However, from the perspective of crystallization differentiation, if we acknowledge that Fo values and Mg# of cumulus minerals can also serve as effective parameters indicating magma crystallization differentiation processes (Irvine, 1965,

1967; Sobolev et al., 2005, 2007; Ammannati et al., 2016), then the appearance of chromite-rich layers represents the initial products of magma crystallization. The gradual decrease in Fo and Mg# of silicate minerals can be considered as a balanced magma differentiation process, without the occurrence of elemental diffusion (Figure 1.7b). When looking at the idealized profile of a layered intrusion presented by Jackson (1961), such a process seems to align with a crystallization differentiation sequence from disseminated chromitite to olivine-rich rocks, and finally to clinopyroxenite, as the chromite content gradually decreases in the magma. Therefore, it is challenging to distinguish whether the observed changes in mineral composition are indicative of an equilibrium melt process or a re-equilibrium diffusion process solely based on variations in mineral composition between samples. This also raises an important issue with using the Fo and Mg# of cumulus minerals in layered intrusions as the indicators of magma processes.

More paradoxically, we always emphasized the influence of diffusion processes on the Fe-Mg elemental compositions of minerals, and on the other hand, we still use other elements or elemental ratios in these cumulus minerals to indicate changes in the physical and chemical conditions of magmas. For example, the content of Ca, Zn, Ni, and Mn in olivine indicates the mantle source and partial melting degree (Thompson and Gibson, 2000; Sobolev et al., 2005, 2007; Li et al., 2007, 2013), while elements like Al and Cr in chromite indicate the depth and pressure of the magma source region, and Ti indicates the water content in mantle and their oxygen fugacity (Deer et al., 1966; Paster et al., 1974; Sigurdsson and Schilling, 1976; Ballhaus et al., 1991; Nielsen et al., 1994). Moreover, some of these elements exhibit similar geochemical behavior and diffusion rates to Fe and Mg elements (Figure 1.8). The distribution coefficients of elements between minerals and melts are fundamental parameters in our geochemical research, and many of the partition coefficients commonly used today are derived from layered intrusions or other mafic-ultramafic rocks. If we consider the elemental exchange behavior in minerals, then all distribution coefficients should correspond to the closure temperature at which elements diffuse within the minerals, rather than the

magma temperature.

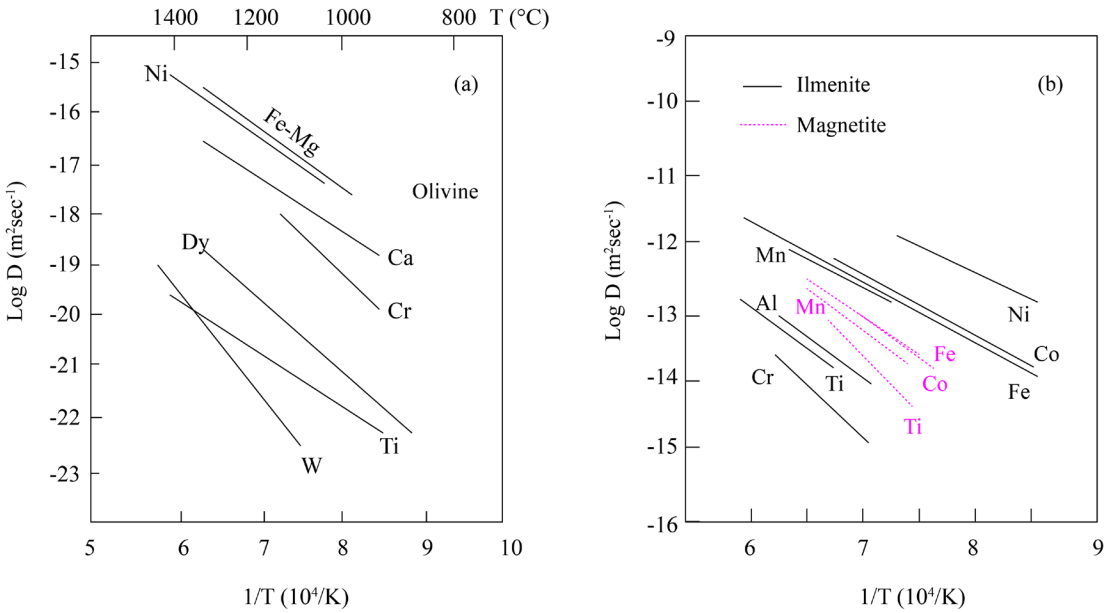

Figure 1.8 Diffusion of different elements in olivine and oxides. Data sources are from Cherniak and Liang (2014) and Van Orman and Crispin (2010).

In addition, we often mention that the diffusion of elements between mineral grains is mostly concentrated between silicate minerals and oxides, while research on whether diffusion occurs between different silicate minerals remains insufficient. Scak (1980) once indicated that the partition coefficient Kd of Fe-Mg elements between olivine and pyroxene is almost independent of temperature in the range of 1200 to 800 °C. Measurement values of the Fe-Mg element inter-mineral distribution coefficient Kd between coexisting olivine, pyroxene, and clinopyroxene in the Stillwater complex are similarly indistinguishable from experimental values obtained at magmatic temperatures (Barnes and Naldrett, 1988). It is currently widely accepted in the academic community that isotopic fractionation usually occurs only between minerals with significantly different crystal structures during high-temperature processes, such as between silicate minerals and oxides, sulfides, etc. Therefore, from a theoretical perspective, there is indeed no possibility of intergranular diffusion between the two. However, for the same sample, apart from the covariant Mg# values,

pyroxenes typically have slightly higher Mg# values than olivine, and clinopyroxene generally has slightly higher Mg# values than orthopyroxene. This is often explained as evidence for re-equilibration among silicate minerals (Wilson, 1982). Therefore, whether there is chemical equilibrium between silicate minerals should also be considered, which is of great significance for crystalline rocks mainly composed of silicate minerals, such as peridotite and pyroxenite.

1.3.2 How to distinguish different diffusion behaviors through geochemical methods?

The changes in geochemical indicators such as Mg# of minerals caused by magmatic crystallization differentiation processes and inter-mineral subsolidus exchange processes may appear similar. For example, the Mg# of cumulate minerals shows a positive correlation with oxide proportions and a negative correlation with mineral ratios of silicate minerals. This process aligns with the mineral compositional changes caused by crystallization differentiation processes. In fact, when explaining chemical compositions such as high Mg# in silicate minerals and low Mg# in chromite within cumulate layers of rocks like chromitite, apart from the inter-mineral subsolidus exchange, other diffusion factors may similarly contribute to causing similar variations.

In the previous reported, we have mentioned several different mechanisms of reactions between melts and minerals. For instance, the injection of a higher proportion of primitive magma can lead to diffusion of elements between silicate minerals near the chromitite layers and the Mg-enriched melt, resulting in these minerals becoming richer in Mg (Figure 1.2; Campbell and Murck, 1993; Cawthorn et al., 2005). This also causes the silicate minerals in the chromitite layers to have a higher Mg# compared to the silicate mineral layers when compared to chromite. Simultaneously, with the injection of the primitive magma, solo crystallization of chromite can further increase the relative MgO content in the melt (Murck and Campbell, 1986). Therefore, the high Mg# content of cumulate minerals in chromitites can also be explained as a result of diffusion between minerals and the more Mg-rich melt (Figure 1.9). If this process controls the

elemental composition of cumulate minerals, then minerals in the silicate cumulate layers are closer to equilibrium because they undergo fewer processes like magma mixing or rapid crystallization in unbalanced crystallization domains. Therefore, we should also analyze the minerals in the silicate cumulate layers when seeking the initial crystalline composition of minerals.

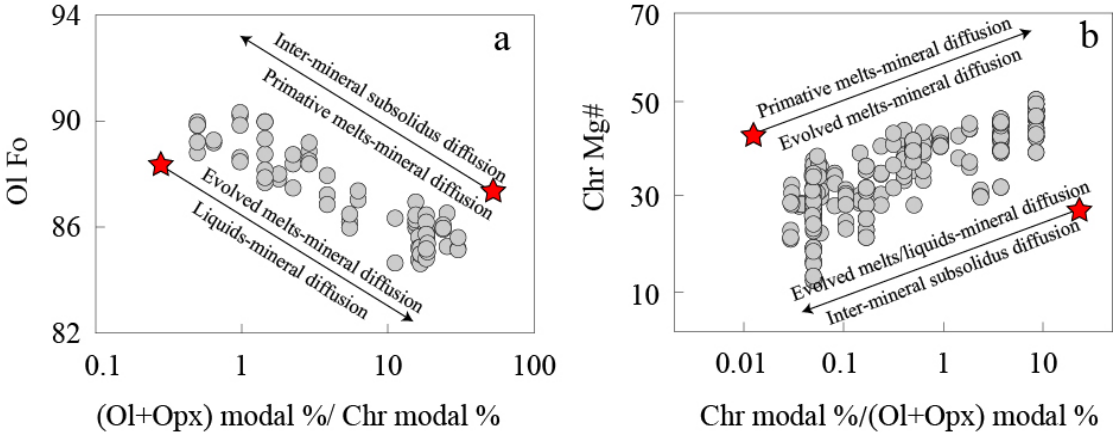

Figure 1.9 Fo and Mg# of olivine and chromite versus their mineral proportions in our samples. The lines represent the patterns of elemental variations induced by several scenarios. The arrows represent their shifty directions, and these stars correspond to the initial compositions (originally magmatic crystallization).

Evolved melts and inter-mineral melts/fluids affecting minerals is more prominent in silicate cumulate rocks (Figure 1.9). This is due to the upward migration of inter-mineral melts/fluids caused by compaction or changes in confining pressure (which also involves the convergence and release of melts/fluids during the crystallization of chromite will emphasize later). This alteration impacts the chemical composition of silicate minerals in the cumulate layer (e.g., Matveev and Ballhaus, 2002; Edmonds et al., 2015; Knipping et al., 2019). Therefore, the gradual decrease in the Mg# of cumulate minerals from chromitites to silicate cumulates can also be attributed to the accumulation of fluids or evolved melts gradually from bottom to top (Figure 1.9; Scowen et al., 1991; Bell and Claydon, 1992; Cawthorn et al., 1992). As the modal ratios of chromite minerals decreases, the rate of crystal accumulation gradually

stabilizes. Crystals can maintain sufficient elemental diffusion with fluids, resulting in the Mg# of silicates being maintained within a smaller range compared to that in chromitites (Figure 1.7). In this scenario, the mineral composition within chromitite layers is relatively closer to the initial crystalline state, and our search for the parent magma composition should also focus on the minerals within the chromitite layers.

By comparison, we can even draw the following conclusion: based solely on the observed changes in mineral elements, the diffusion processes between minerals and the original melt, inter-mineral melts/fluids, and minerals can all lead to a gradual decrease in the Mg# of minerals as cumulation progresses. In other words, the compositional changes in cumulate minerals resulting from these three element exchange mechanisms are similar, and therefore, it is not possible to distinguish between these three mechanisms based solely on compositional changes.

On the other hand, we also observe that while different mechanisms result in consistent trends in mineral composition changes, the direction of these changes is different (Figure 1.9). Mineral-melt exchange typically leads to higher initial cumulate minerals having a higher Mg#, whereas fluid and intergranular diffusion processes result in later crystallizing minerals collectively increasing their Fe#. In the case of inter-mineral exchange, silicate minerals and chromite exhibit conjugate element changes, but variations in mineral proportions lead to distinct differences in diffusion effects among different samples. This difference causes both minerals to exhibit a trend of decreasing Mg# as the proportion of chromite decreases. However, the direction of element changes is different for chromite and silicate minerals. Therefore, to distinguish between different element diffusion mechanisms, the direction of element migration should be the primary focus of the research, rather than relying solely on the correlations exhibited by the results of compositional changes (Figure 1.9).

Mineral zoning is considered one of the most definitive pieces of evidence for changes in element diffusion direction. Studies on spinel and olivine compositions in magma by Scowen et al. (1991) and Teng et al. (2011), respectively, have provided important evidence regarding the direction of element migration through mineral

zoning (Figure 1.10; Sio et al., 2013; Oeser et al., 2015; Pogge von Strandmann et al., 2015; Collinet et al., 2017). However, for mafic-ultramafic intrusions, especially for layered bodies where magmatic processes are prolonged and gradual, volume diffusion within mineral grains is often sufficient to eliminate compositional zoning caused by grain boundary diffusion. In such cases, alternative methods are urgently needed to trace the direction of element migration.

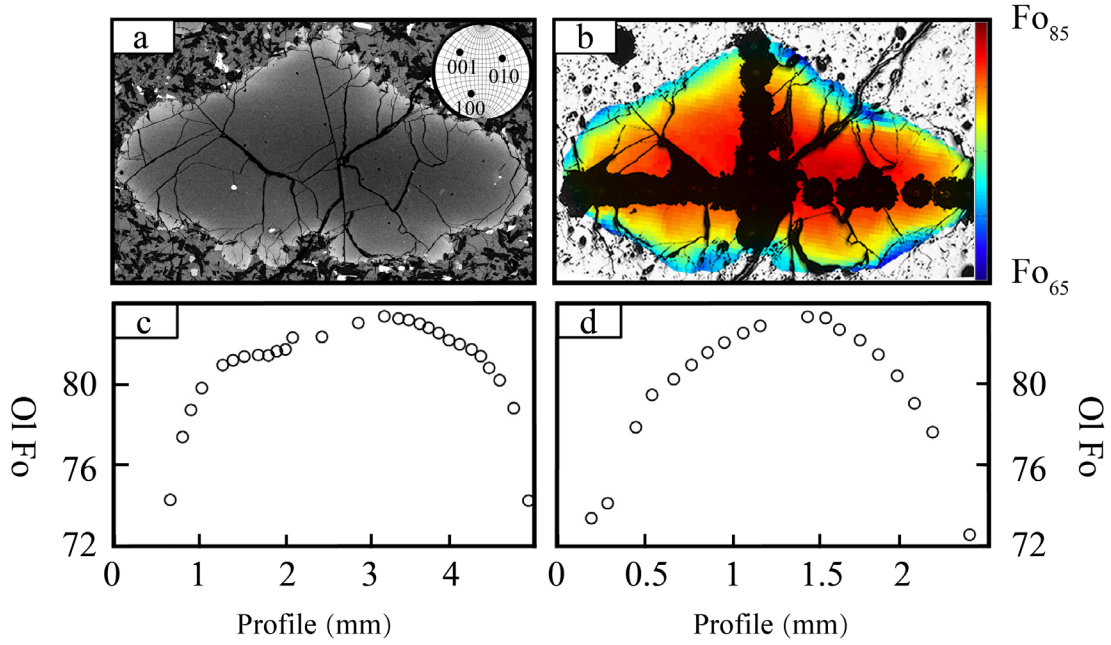

Figure 1.10 (a) BSE image of the Kilauea Iki olivine phenocryst. The top corner shows stereographic projections of the olivine's crystallographic orientation; (b) False-color chemical map superimposed on microdrilling casts; (c) and (d) shows the Fo of the olivine traverses in (b). These figures are modified from Sio et al. (2013).

1.3.3 When multiple diffusion processes overlap, which process may become the dominant factor?

The study of various diffusion types within layered rock formations in the geological community has a history spanning half a century (e.g., Irvine, 1965, 1967; Wilson, 1982; Scowen et al., 1991; Bell and Claydon, 1992; Cawthorn et al., 1992). These concepts have been widely applied to the study of a variety of geological settings, including medium-acidic intrusive rocks, volcanic and subvolcanic rocks with various

enrichment phases, among others. They have provided satisfactory explanations for some anomalous phenomena (e.g., Medaris, 1976; Clark, 1978; Jaques, 1981). There is a wealth of corresponding mineralogical and geochemical evidence for the alteration of mineral compositions by intergranular melts/fluids and the intergranular re-equilibration processes of elements during subsolidus phases. This not only underscores the geological community's attention to element diffusion processes but also reflects that current research in this field has largely been conducted independently on these different diffusion processes.

In fact, for mafic-ultramafic rock bodies, especially layered complexes, the final composition of minerals is more likely the result of a combination of various diffusion processes during the evolution. During the high-temperature, multi-stage magma injection phase, diffusion between minerals and melt may play a more prominent role. As minerals settle at the bottom of the magma chamber, inter-mineral melts/fluids may have a greater influence on mineral compositions. As the temperature further decreases, intergranular diffusion during the subsolidus phase appears to become the primary control factor for mineral compositions. In the case of these overlapping multi-processes, the urgent task is to compare and identify the most dominant controlling factors (or, for a specific set of samples, their primary controlling factors). It is also crucial to seek geochemical indicators corresponding to each process in order to better understand these complex interactions.

1.4 The origin of chromitite

Stratiform chromitites are the most distinctive and enigmatic geological features in layered intrusions. Interpretation of the origin of massive chromitites lead to two puzzles of chromite extraordinary enrichment (Campbell and Murck, 1993; Roeder et al., 2006) and melt volume unbalance (Eales, 2000; Maier and Barnes, 2008; Carson et al., 2013). Models in term of the former traditionally focused on providing mechanisms for magmas that were saturated solely in chromite via: (1) magma mixing by primitive magma and differentiated magma (Irvine, 1977; Huppert and Sparks, 1981; Eales, 1987;

Alapieti et al., 1989; Campbell and Murck, 1993) or different sources (Irvine et al., 1983; Irvine and Sharpe, 1986; Nex, 2004; Kottke-Levin et al., 2009), (2) country-rock assimilation (Irvine, 1975; Kinnaird et al., 2002; Marques et al., 2003; Spandler et al., 2005; Woods et al., 2019), (3) pressure increase (Liu and Presnall, 1990) induced by magma-chamber deformation (Cameron, 1977, 1980, 1982), bubble expansions (Lipin, 1993) or magma replenishment and expulsion (Cawthorn, 2005, 2011), (4) fluctuations in oxygen fugacity facilitated by gas release (Cameron and Desborough, 1964; Ulmer, 1969; Cameron, 1975; Murck and Campbell 1986; Roeder and Reynolds 1991) or diffusion (Ferreira Filho and Araujo, 2009), (5) absorption of water by the magma (Prendergast, 2008; Schannor et al., 2018; Veksler and Hou, 2020), (6) incongruent partial melts of pre-existing cumulates (Mathez and Mey, 2005; O'Driscoll et al., 2009; Mathez and Kinzler, 2017; Hepworth et al., 2018; Scoon and Costin, 2018, Yudovskaya et al., 2019, 2022), volatile-induced hydration melting of Cr-bearing pyroxene (Nicholson and Mathez, 1991; Boudreau, 2002, 2004, 2016, 2019; Marsh et al., 2021), or infiltration metasomatism of Fe-Ti oxide-rich rocks (Rollison, 1997; Lesher et al., 2014, 2016, 2019). These assumptions were supposed to crystallize "on-stage" throughout the entirely melt-dominated magma chamber, with subsequent gravity-induced settling (Nex, 2004; Naldrett et al., 2012; Cawthorn, 2018) or in situ nucleation and growth at liquid-cumulate interface (Boorman et al., 2004; Kruger, 2005; Holess et al., 2017; Latypov et al., 2018; Schannor et al., 2018). A large, long-lived, and molten magma chamber facilitates the operation of these mechanisms throughout various locations within the gaint magma chamber, ensuring the formation of laterally extensive layers of monomineralic chromitites (Latypov et al., 2022), however, the total volume of basaltic magma far exceed the volume of magma chamber in addressing this mass-balance requirement (Cawthorn and Walraven, 1998; Naldrett et al., 2012).

Over several decades, the "off-stage" models have been proposed to circumvent such melts volume problems, whereby predominantly silicate phases with minor chromite are crystallized to form a slurry either in some shallow-level chambers (Maier and Barnes, 2008; Maier et al., 2013; Jenkins and Mungall, 2018; Mitchell et al., 2019a,

2019b; Robb and Mungall, 2020; Scoon et al., 2020) or from deep-seated vast staging chambers (Eales, 2000; Mondal and Mathez, 2007; Voordouw et al., 2010; Eales and Costin, 2012; Mungall et al., 2016). The slurry is then injected into the magma chamber (Eales, 2000; Mondal and Mathez, 2007; Voordouw et al., 2010; Jenkins and Mungall 2018; Latypov et al., 2018) and slumped from the margins of intrusion into the final repository (Wilson and Prendergast 1989; Naldrett et al. 2012; Maier et al. 2013, 2018; Forien et al. 2015). This model essentially denies the necessity of chromite-only saturated interval, and the crystal-dominated magmatic plumbing system extending from the base to top of the lithosphere could provide enough chromite grains (Cashman et al., 2017; Jackson et al., 2018; Sparks et al., 2019). The monomineralic chromitite layers can be sorted either by separation of heavy chromite from lighter silicate minerals during crystal settling in flowing magmas (Eales, 2000; Eales and Costin, 2012), earthquakes with associated shock waves (Cawthorn, 2015), kinetic sieving induced by crystal slurry slumping (Maier et al., 2013; Mungall et al., 2016) or by downwards percolation of small and dense chromite grains through interstitial spaces between large crystals of silicate phases (Mondal and Mathez, 2007; Manochehri and Schmidt, 2014). The crystal slurry ideas have become increasingly more popular and appear to derive support from recent volcanological studies (Cashman et al., 2017; Sparks and Cashman, 2017), which portray crustal magma chambers as being almost entirely composed of crystal-rich mushes with a small amount of interstitial liquid (Yang et al., 2019; Hepworth et al., 2020; Yao et al., 2021; Xing et al., 2022; Annen et al., 2022).

Over the past decade, the debate between the “on-stage” and “off-stage” models has emerged as a highly contentious topic, garnering significant attention for the studies of layered intrusions. Proponents of respective model have presented respective evidences from various angles and methodologies, such as: (1) Morphological studies of chromite and chromite clusters/chains by high-resolution X-ray computed tomography (Godel et al., 2012; Vukmanovic et al., 2013; Barnes et al., 2021; Latypov et al., 2022), spatial distribution pattern analyses (Godel et al., 2013; Prichard et al., 2015; Hunt and O’Driscoll, 2021; Holness et al., 2022) and crystal size distribution

analyses (Magee et al., 2010; Vukmanovic et al., 2013; Kaufmann et al., 2019; Barnes et al., 2021), as well as the texture (Nex, 2004; Marques et al., 2017; Scoon and Cosin, 2018) and field relationships of chromitite layers (Alapieti et al., 1989; Voordouw et al., 2009; Junge et al., 2014; Mukherjee et al., 2017; Pebane and Latypov, 2017; Hasch and Latypov, 2021; Laudadio et al., 2022); (2) Analogous experiments including the flume-tank (Forien et al., 2015), centrifuge (Manoochehri and Schmidt, 2014) and internally heated pressure vessel (Veksler and Hou, 2020); (3) Physics analyses including infrared spectroscopy (Tang et al., 2023; Bai et al., 2024), electron back-scatter diffraction (Vukmanovic et al., 2013; Kaufmann et al., 2018), and Laser Induced Breakdown Spectroscopy (Meima and Rammlmair, 2020; Meima et al., 2022); (4) Numerical simulations including fluid mechanics (Robb and Mungall, 2020; Hepworth et al., 2020; Maghdour-Mashhour and Hayes, 2021), thermodynamic modelling (Latypov et al., 2017; Woods and Stock, 2019; Yao et al., 2021; Annen et al., 2022) and Markov Chain statistical calculation (Jenkins and Mungall, 2018); (5) Geochronological evidences (Mungall et al., 2016; Wall et al., 2018; Hayes et al., 2018).

Compared to these interdisciplinary approaches, the geochemical and compositional studies appear to be gradually restricted and overlooked. The abundant trapped melts (Sparks et al., 1985; Barnes, 1986; Barnes et al., 1998; Kamenetsky et al. 2001) and prolonged postcumulus processes (Roeder and Campbell, 1985; Hunter, 1987; Scowen et al., 1991; Barnes and Roeder, 2001; Voigt and von der Handt 2011) could vastly modify the initial compositons of bulk-rock and cumulus minerals, respectively. Elements with higher backgrounds and valences (Page and Barnes, 2011; Junge et al., 2014; Langa et al., 2021, 2023; Barnes et al., 2023) as well as the high mineral mode ratios (Yudovskaya and Kinnaird, 2010; Xiao et al., 2016) are supposed to be less influenced by these two processes, whereas the compositional shifts have also been proven to exist (Spandler et al., 2007; Watkins and Antonelli, 2021), and might be further promoted by abundant of interstitial fluids (Mookherjee et al., 2008; Karki et al., 2009). Such re-equilibration even contributes to the entirely distinct elemental distributions across the massive chromitite, with the uniform increasing trends

indicating an in-situ process of magmatic settling (Scoon and Teigler 1994; Naldrett et al. 2012) and the regular zonal pattern arguing for an intrusive emplacement of a sill-like body (Maier and Barnes 2008; Voordouw et al. 2009). In addition, the over-saturated chromite crystallization should contribute to significantly chromium depleted in melts whilst also not present in following cumulates (Campbell and Murck, 1993; Cawthorn and Walraven, 1998). Isotope studies have also been employed during the formation of chromitite seams. Multiple sulphur (Penniston-Dorland et al., 2012; Ripley et al., 2017; Yudoskaya et al., 2017; Keir-Sage et al., 2020), osmium (Horan et al. 2001; Marquies et al., 2003; Reisberg et al., 2011), oxygen and hydrogen isotopes (Harris et al., 2005; Zhou et al., 2021) from the chromitite seams constriaints on the crustal contamination, homogeneity strontium (Kruger et al., 1987; Kinnaird et al., 2002; Naldrett et al., 2012; Karykowski et al., 2017; Schannor et al., 2018; Scoon et al., 2020; Maghdour-Mashhour et al., 2021) and iron isotopes (Bilenker et al., 2019; Nebel et al., 2020) indicated interaction between pre-existing crystal-melt mush and infiltrated fluids without notable isotope fractionation. Nevertheless, due to isotopic variations are typically influenced by multiple factors, in many cases, the results have also faced considerable scrutiny and questioning.

2. The Stillwater layered intrusion

2.1 Regional geological background

North America's Wyoming Craton extends across the states of Montana, Wyoming, and Idaho. As the sole Archean craton in the northwestern United States, it covers an area of over 500,000 square kilometers, representing the initial continental nucleus of North America. The Late Cretaceous to Paleogene Laramide uplift resulted in partial exposure of the Archean basement of the craton at the surface (Houston et al., 1993), accounting for approximately 10% of the overall Archean basement (indicated as the dark portion in Figure 2.1). The extensive exposure of the Archean basement makes the Wyoming Craton one of the most extensively studied cratons globally. The Wyoming Craton is bordered by Precambrian collisional orogens on its south, north, and east sides. The southern boundary is well-exposed, delineated by the Archean rocks of the Cheyenne Belt, which formed by the collision of Archean rocks from the Medicine Bow and Sierra Madre Mountains in the southeastern part of the craton with Paleoproterozoic volcanic rocks to the south (Karlstrom and Houston, 1984; Duebendorfer and Houston, 1987; Chamberlain, 1998; Duebendorfer et al., 2006). Additionally, to the west of the Cheyenne Belt, the Uinta Mountains have exposures of the early Cambrian Owiyukuts Complex and Red Creek intrusive rocks (e.g., Sears et al., 1982; Mueller et al., 2004). The Great Falls Tectonic Zone is considered the northern boundary of the Wyoming Craton (O'Neill and Lopez, 1985). Within this tectonic zone, prominent east-dipping high-angle faults, and linear structures, along with evidence of Paleoproterozoic mineral ages in the Archean basement, are interpreted as products of collision and subsequent closure of an ocean basin between the Wyoming Craton and the Medicine Hat Block between 1.86 to 1.77 Ga (Mueller et al., 2002, 2004). In the eastern part of the Wyoming Craton, the Dakota segment of the Hudson Orogen crosses, and the craton's margin features numerous exposures of Archean rocks in the Black Hills (McCombs et al., 2004; Dahl and McCombs, 2005; Dahl, 2006) and the Hartville Uplift (Krugh, 1997). These rocks are believed to represent the collision between the Wyoming Craton and the Superior Block around 1.83 to 1.72 Ga (Dahl et al., 1999, 2005). The exact western extent of the Wyoming Craton remains less well-defined.

Archean rocks have been found in the Belt Basin and the Raft River-Albion-Grouse Creek Mountains (Compton et al., 1977; Lush et al., 1988). U-Pb zircon ages from the crustal source captured in the Snake River Plain's Cenozoic volcanic rocks also suggest the presence of Archean basement material (Wolf et al., 2005). However, due to the scarcity of Precambrian outcrops in this region and a lack of comprehensive geophysical data, the precise western boundary of the craton remains to be firmly established.

The Wyoming Craton is commonly divided into three research areas from old to new: The Montana Sedimentary Metamorphic Belt (MMP), the Beartooth-Bighorn Magmatic Zone (BBMZ), and the Southern Accretionary Zone, as shown in Figure 2.1. The oldest part is in the northern region of the craton, including the Montana Metamorphic Belt (MMP) and the Beartooth-Bighorn Magmatic Zone (BBMZ) (Mogk and Mueller, 1990). The MMP is composed mainly of relatively younger quartzites, shales, and carbonates, interspersed with older (3.30-3.50 Ga) Archean quartz-feldspar gneisses (Mueller et al., 1993, 2004). The BBMZ consists primarily of 2.80-3.00 Ga TTG (Tonalite-Trondhjemite-Granodiorite) rocks, including amphibolite, granulite, and migmatite (Wood et al., 1988; Frost and Fanning, 2006). It also contains small amounts of high-potassium granitoids and granites. Evidence from detrital zircon ages in the range of 2.80-3.00 Ga and inherited zircons in the range of 3.30-4.00 Ga in quartzites and gneisses, as well as Nd model ages from metamorphic igneous rocks and sedimentary rocks of the Middle and Early Archean, reveals the early crustal formation history (Wood and Mueller, 1988; Frost, 1993; Mueller et al., 2004; Frost et al., 2006; Grace et al., 2006). The Beartooth-Bighorn Magmatic Zone contains rocks with significantly enriched $^{207}Pb/^{204}Pb$ isotope signatures, particularly in tonalite and evolved granitoids. This isotope signature distinguishes the Wyoming Craton from other Archean cratons in the surrounding region (Mueller and Wood, 1988; Woodn and Mueller, 1988, Frost et al., 1998). Furthermore, in the BBMZ region, there is a crust that is nearly 50 km thick, with a 15-20 km thick high-density layer in the upper crust interpreted to be composed of mafic to ultramafic rocks (Snelson et al., 1998; Gorman

et al., 2002). Although the age of this mafic layer is not clear, numerous mafic to ultramafic dikes and the well-known Stillwater Complex have ages distributed around 2.71 to 2.68 Ga, which align with the age of the oldest rocks (2.80 to 3.00 Ga). This coincidence suggests a potential association between the formation of these mafic to ultramafic rocks and the mafic layer.

The Beartooth Range is one of the largest exposed blocks of the Wyoming Craton and preserves evidence of major crustal formation events in the craton from 3.0 to 2.74 Ga (Wooden and Mueller, 1989). This series of events ultimately resulted in the formation of a significant number of granodiorites and the Long Lake Suite granite sequence during the period of 2.78 to 2.74 Ga. The formation of mafic to ultramafic rocks, including those represented by the Stillwater Complex, in this region may also be related to these events. During the Proterozoic, a substantial intrusion of mafic rocks occurred within previously formed gneissic and host rocks, leading to low-grade metamorphism in the region. In the late Proterozoic, the Beartooth Range experienced uplift and tilted northward, undergoing erosion processes. Since the Paleozoic era, sedimentary deposits from the Cambrian to the Cretaceous have partially covered the Beartooth Range, with some areas accumulating sedimentary rocks up to 3 km thick. However, during the late Cretaceous to the early Cenozoic Laramide orogeny, further uplift, tilting, and erosion occurred in this region, revealing the Late Proterozoic erosional surface once again.

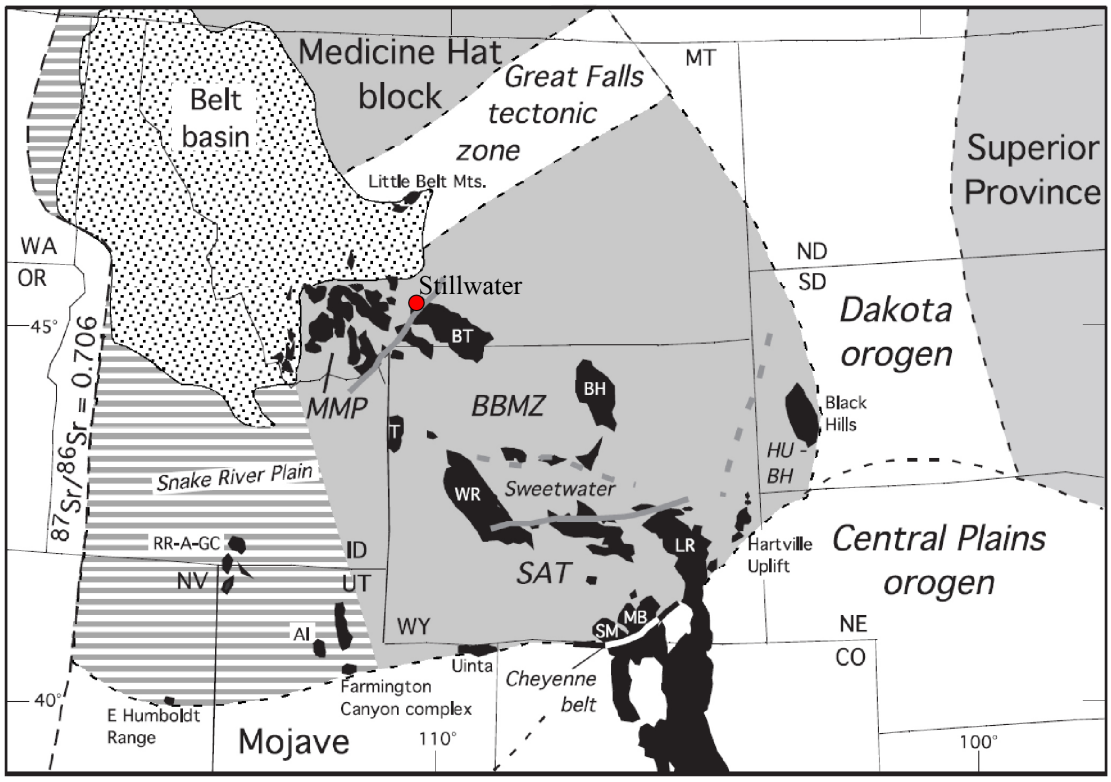

Figure 2.1 Location map of the Wyoming Province, showing its relationship to surrounding orogens and Precambrian provinces from Foster et al. (2006) and Chamberlain et al. (2003). The only boundary of the province that is exposed lies in the Sierra Madre and Medicine Bow Mountains, where Proterozoic rocks are juxtaposed against the Wyoming Province along the Cheyenne belt. The Montana metasedimentary province (MMP) and Beartooth–Bighorn magmatic zone (BBMZ) represent the portions of the province that were cratonized earliest (ca. 2.80 Ga). To the south lie the Southern accreted terranes (SAT), a collage of terranes that were joined to the southern margin of the Wyoming Province by ca. 2.63 Ga and cratonized by 2.50 Ga. The Sweetwater subprovince is that portion of the BBMZ that was metamorphosed and deformed in the late Archean, and the Hartville uplift-Black Hills block (HU-BH) was affected by Proterozoic west-vergent thrusting (Chamberlain et al., 2003). The area of Precambrian crust between the Wyoming craton and the $^{87}Sr/^{86}Sr = 0.706$ line includes both Archean and Proterozoic rocks. Areas shown in black are Precambrian exposures. AI, Antelope Island; BH, Bighorn Mountains; BT, Beartooth Mountains; LR, Laramie Range; MB, Medicine Bow Mountains; RR-A-GC, Raft River-Albion-Grouse Creek Mountains; SM, Sierra Madre; T, Teton Range; WR, Wind River Mountains.

2.2 Geological background of the Stillwater Complex

The Stillwater Complex is located on the northern margin of the Beartooth Range (Figure 2.2a). The complex is primarily controlled by the Mill Creek-Stillwater fault zone and the West Boulder fault zone, with the Beartooth Range main body and the North Snowy block to the east and west, respectively. The contact between the southern margin of the complex and the underlying sedimentary rocks is visible in the Boulder River, Chrome Mountain, and Mountain View areas. Particularly between Chrome Mountain and the West Fork of the Stillwater River, there is a faulted contact between the complex and the underlying metamorphic rocks. In the area between the main stem of the Stillwater River and its tributary, the West Fork, the complex is in faulted contact with a later quartz-chlorite zone along the Bluebird Thrust. However, in the eastern region to the east of the Stillwater River, this quartz-chlorite zone is in intrusive contact with the complex. Along the northern edge of the complex, a significant amount of Paleozoic and Mesozoic sedimentary rocks covers the complex. Except for the area controlled by the Stillwater River and its West Fork, most contact zones exhibit clear angular unconformities controlled by the Horseman Thrust.

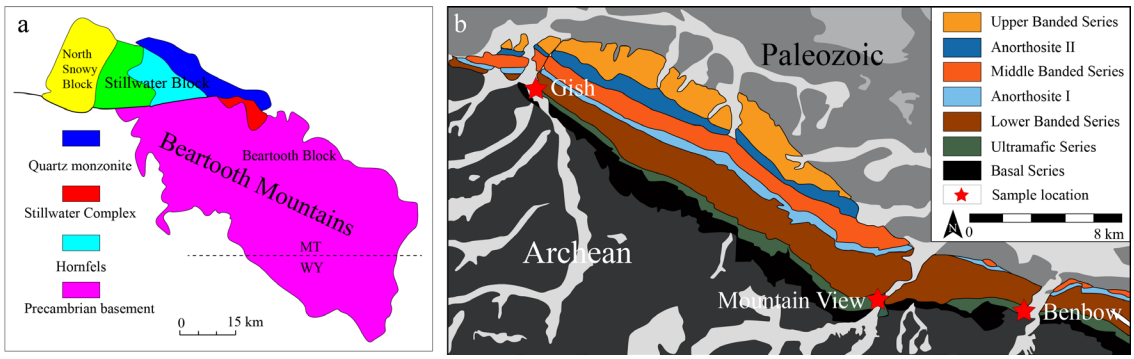

Figure 2.2 (a) Location map of the Stillwater Complex in the northwestern part of the Beartooth Mountains, and the major blocks that make up the Beartooth Mountains; (b) Generalized geologic map of the Stillwater Complex, with major subdivisions and adjacent rocks (after McCallum, 1996). Red stars show sampling locations within the Peridotite Zone discussed in this study.

The exposed area of the complex on the Earth's surface is approximately 180

square kilometers, with an east-west extension of up to 47 kilometers and a maximum north-south width of 8 kilometers (Figure 2.2b). Geophysical data for this region indicates that the Stillwater Complex extends to depths of up to 25 kilometers beneath the northern front of the Beartooth Range (Blakely and Simpson, 1984; Kleinkopf, 1985). Recent 3D gravity models suggest that the maximum burial depth of the Stillwater Complex to the north could be up to 30 kilometers and up to 40 kilometers to the east (Finn et al., 2013, 2016).

Due to the widespread Laramide uplift in the Beartooth region, the area where the complex is located has been uplifted by nearly 6 kilometers. According to studies by Jone (1960) and People et al. (1960), the elevation in this region was already close to 3 kilometers during the Middle Cambrian. The Laramide uplift also resulted in the formation of five high-angle normal faults within the complex (Figure 2.3). The faults that appear in the Banded Series sequences typically dip steeply northward, such as the South Prairie Fault, which is nearly parallel to the bedding planes in the complex. Additionally, the uplift caused by these normal faults has exacerbated the erosion of the upper rock sequences in the Banded Series. Steeply dipping normal faults that trend southward is usually found within the Ultramafic and Basal Series of the complex (Page and Nokleberg, 1974). In the West Fork area, the presence of a normal fault known as the Bluebird Thrust has even uplifted the Basal Series to the same elevation as the Ultramafic Series, resulting in the uplift of the Mountain View block and faulted contact with the overlying rock sequences (Lake-Nye Fault). As a result of the uplift of the lower block, the chromite layers have also undergone significant erosion, with the depth of erosion reaching up to 1 kilometer in the Nye Creek area. Additionally, these high-angle faults have generated numerous secondary faults within the Basal and Ultramafic Series, with spacing ranging from less than one meter to several hundred meters. The frequent occurrence of faults within the Stillwater Complex may reflect the formation of many faults at the margins of the active basin during the complex's formation process.

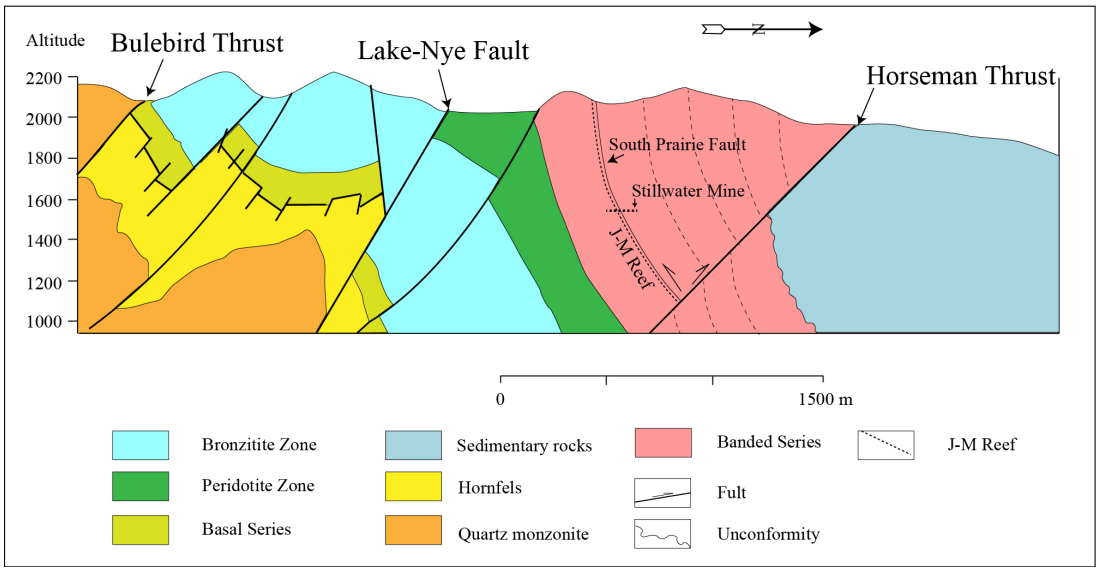

Figure 2.3 Structural section through the complex at Mountain View (after Turner et al., 1985).

It is currently believed that the Stillwater Complex was emplaced at a shallow depth within the Earth's crust, typically within a range of 6 to 7 kilometers. Therefore, the Stillwater Complex is often considered to have intruded into Middle Archean mudstone, banded iron formations, and quartzites as part of a subvolcanic system at around 3.3 billion years ago (Page, 1977; Mogk and Mueller, 1990; Helz, 1995; Labotka and Kath, 2001). Contact metamorphism is commonly developed in the contact zones of the complex. For example, in the East Boulder Plateau area, mudstones underwent thermal metamorphism, resulting in the formation of hornfels near the contact zone between the complex and the surrounding rocks. Hornfels formed by metamorphism typically appear in two forms: quartz-bearing hornfels and non-quartz-bearing hornfels (Page, 1977). The former is more commonly found near the contact zone (within 500 to 1000 meters) and is typically composed of quartz, pyroxene, feldspar, and garnet. In areas farther from the contact zone (within 500 to 1500 meters), pyroxene replaces pyroxenite (Labotka, 1985). Non-quartz-bearing hornfels is relatively less abundant and is typically only found in the contact zone and within the complex's cumulate bodies. Common mineral assemblages include pyroxene, garnet, and occasionally feldspar, along with localized occurrences of abundant sulfides.

Additionally, characteristic blue quartzite layers have formed within the hornfels, and this type of quartzite is widely distributed in the banded iron formations of Iron Mountain and the southern parts of Chrome Mountain. The mineral assemblages in the banded iron formations are consistent with metamorphic temperatures of 825°C and pressures of 3 to 4 kilobars. Furthermore, the complex has been intruded by numerous mafic dikes (~1.7 billion years ago), leading to local greenschist facies metamorphism and associated mineral assemblages. Isochron dating of minerals in the West Fork gabbro by Depaolo and Wasserburg (1979) yielded an age of 2701±8 million years. Zircon U-Pb age dating by Nunes (1981) and Premo et al. (1990) on samples from the Basal Series and related dikes provided ages of 2713±3 million years and 2705±4 million years, respectively. More recently, Wall et al. (2018) reanalyzed the high-precision U-Pb ages of zircon grains from rock samples at different locations within the Stillwater Complex. Their results indicated a crystallization age range from 2712 million years (Basal Series) to 2709 million years (Banded Series), spanning a period of 3 million years.

The Stillwater Complex is one of North America's most significant repositories of base metal sulfides, chromite, and platinum group elements (PGEs). Since the 19th century, sulfide minerals occurring within the Ultramafic Series, Basal Series, and adjacent hornfels zones have been extensively mined and serve as important sources of Cu and Ni in the North American region. Chromite seam associated with the Ultramafic Series have also been extensively studied and exploited. The chromite resources within the Stillwater Complex account for approximately 80% of the reserves in the United States. The development of chromite resources, particularly in the Benbow, Mountain View, and Giah areas (as shown in Figure 2.2b), played a crucial role during periods of high demand for chromium, such as during wartime. The development of platinum group elements (PGEs) in the Stillwater Complex initially focused on Pt-Pb minerals occurring within the chromite seams of the Ultramafic Series. It wasn't until 1973 that the PGE layers within the J-M Reef of the Banded Series were discovered and subsequently exploited. As of the author's fieldwork period, efforts to extract PGE

resources from the PGE layers within the J-M Reef in the Stillwater Valley and East Boulder Plateau regions were ongoing.

The Stillwater Complex is divided into five main rock series from bottom to top, namely the Basal series, Ultramafic series, Lower Banded Series, Middle Banded series, and Upper Banded series. Each series can typically be further subdivided into a series of zones or subzones (see Figure 2.4). Page (1979) referred to the combination of all igneous rock sequences below the widespread cumulus olivine as the Basal Series of the Stillwater Complex. The Basal Series generally has a thickness ranging from about 60 to 400 meters and appears as irregular sheet-like rock walls, often dissected by faults into multiple segments (see Figure 2.2). Furthermore, there are distinct sedimentary units that crosscut the Basal Series, indicating an unconformity contact with the country rocks. The Basal Series can be roughly divided into two subzones: the Upper subzone is composed of homogeneous bronzitite, with interstitial mineral content decreasing noticeably with increasing elevation (Page, 1979). The Lower subzone consists of similarly cumulus-textured norite, gabbro, anorthosite, and small amounts of peridotite and massive sulfides, often accompanied by xenoliths of pyroxene-hornfels from the country rocks (McCallum, 1996). Although these rock types are also found in the overlying rock sequence units of the intrusion, their occurrence within the Basal Series lacks continuity and exhibits no discernible lithological pattern. The enrichment of Fe-Ni-Cu sulfides is one of the most significant features of this unit, displaying massive and sponge-textured structures, indicating direct sulfide precipitation from the melt. The Basal Series is intruded by two distinct types of dikes: one with a pronounced diabasic texture and rock compositions ranging from augite gabbro to norite, typically devoid of sulfides, and genetically related to anorthosite; the other type consists of more Mg-rich norite, with sulfide content ranging from 2% to 40%. This type is likely associated with the Mg-rich magmas responsible for forming the Stillwater Complex and shares similarities in U-Pb age (Premo et al., 1990). Samples lacking cumulus texture are considered the chilled margins of the intrusion and are significant for analyzing the composition of the parental magma of the intrusion.

Figure 2.4 Composite stratigraphic column showing the lithologic series of the Stillwater Complex and field photos of representative rocks: (a, b) chromitite occur as layers in Peridotite Zone; (c, d) Peridotite and bronzitite in Ultramafic Series; (e-h) Banded Zone is composed of norite, gabbronorite and gabbro, with inch-scale layers.

The defining characteristic of the Ultramafic Series is the extensive crystallization of olivine, with the upper boundary marked by the appearance of plagioclase feldspar as a major cumulus phase (see Figure 2.4). Currently, the rock sequence of the Ultramafic Series is well-preserved in the western section of the intrusion, particularly in the Mountain View and Benbow areas. This series can be divided into a lower Peridotite Zone and an Upper Bronzitite Zone (see Figure 2.4 a-d; Jackson, 1961; Raedeke and McCallum, 1984; McCallum, 1996). Within the Peridotite Zone, cumulus minerals include olivine, orthopyroxene, and chromite, while in the Bronzitite Zone,

Bronzite predominates as the cumulus mineral, with only minor occurrences of olivine and thin layers of chromite. The thickness of the Ultramafic Series varies from 840 meters to 2000 meters, reflecting uneven basement topography that resulted in variations in magma accumulation depths.

Raedeke and McCallum (1984) described 21 cyclic units in the Peridotite Zone, of which 15 had ideal lithological cyclic units (the other 5 lacked peridotite, and 1 lacked bronzitite), by pridotite-harzburgite-bronzitite , and the composition of chromite seams with variable thickness: pridotite usually serves as the first cumulate phases in each ideal cyclic unit, and is in contact with the bronzitite of the previous cyclic unit, in which olivine and chromite are used as cumulus minerals and are wrapped by pyroxene oikocrysts. The total content of plagioclase, phlogopite and other inter-mineral cumulate minerals does not exceed 15% at most; chromite seams are defined as A zone to K chromitite layers from the bottom to the top, and their thickness distribution is heterogeneous, and can be seen at the scale of hand specimens (Figure 2.5 a–d).

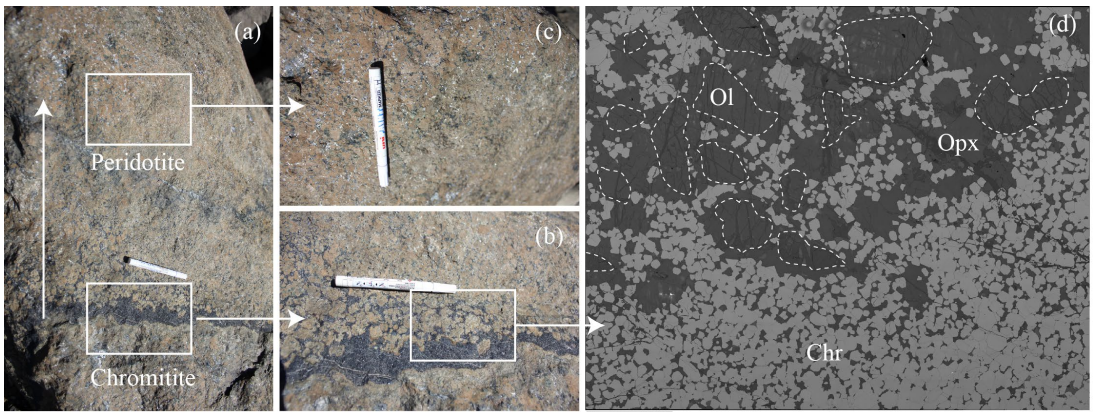

Figure 2.5 Field outcrops showing contacts between chromitite seams and silicate rocks (a-c) and the BSE images (d); Massive chromitite shows sharp contacts with anti-nodular chromitite (b) and then gradually grades into poikilitic harzburgite (c); Average chromite crystal size increases uniformly upward (d).

The rock boundary between the Peridotite Zone and Bronzitite is typically characterized by the transition from orthopyroxene as oikocrysts and poikilitic minerals

to appearance as cumulate minerals. Within the Bronzitite zone, alternating layers of centimeter-scale thickness rich in olivine and orthopyroxene are observed, with olivine content gradually decreasing with height, averaging around 35%. Generally, the grain size of minerals within Bronzitite zones is larger compared to the peridotite zones, exhibiting distinct signs of secondary enlargement, possibly implying reactions between minerals and melt/fluids (Figure 2.6). In Peridotite Zone olivine shows absorption edge features indicative of olivine reacting with interstitial melt/fluids, suggesting that minerals in this zone have undergone significant melt/fluid modification. Bronzitite Zone primarily consist of clinopyroxene, orthopyroxene, and plagioclase as the main mineral phrases. Clinopyroxene surrounds orthopyroxene as primary crystals, likely resulting from reactions between orthopyroxene and fluids (Figure 2.5d). Small amounts of chromite and quartz can appear, while the biotite and apatite show reduced interstitial content. Generally, Bronzitite Zone and bronzitite in the peridotite zone share similar mineral compositions. However, the Bronzitite Zone exhibits a more uniform mineral pattern and larger crystal sizes. Additionally, the plagioclase components within cumulate minerals in this zone is more variable, with more pronounced banding characteristics, indicating stronger reactions between minerals and interstitial melt/fluids.

The abundant presence of plagioclase as a cumulate mineral signifies the base of the Banded Series, which can be further divided from bottom to top into three Series: Lower Banded Series, Middle Banded Series, and Upper Banded Series (Figure 2.5e-h). The thickness of the Banded Series varies from 4,468 meters (in the Contact area) to 1,935 meters (in the Picket Pin area) and is most well-preserved in the Contact Mountain and Picket Pin areas. The Lower Banded Series primarily consists of norite, gabbroic norite, and minor olivine-bearing cumulate rocks. The Pt-group element-rich J-M Reef is also found in this zone. Additionally, numerous inch-scale rhythmic layers are observed within the rock sequence of this zone (Figure 2.4e, f), possibly indicating magma chamber fluctuations and melt convection processes.

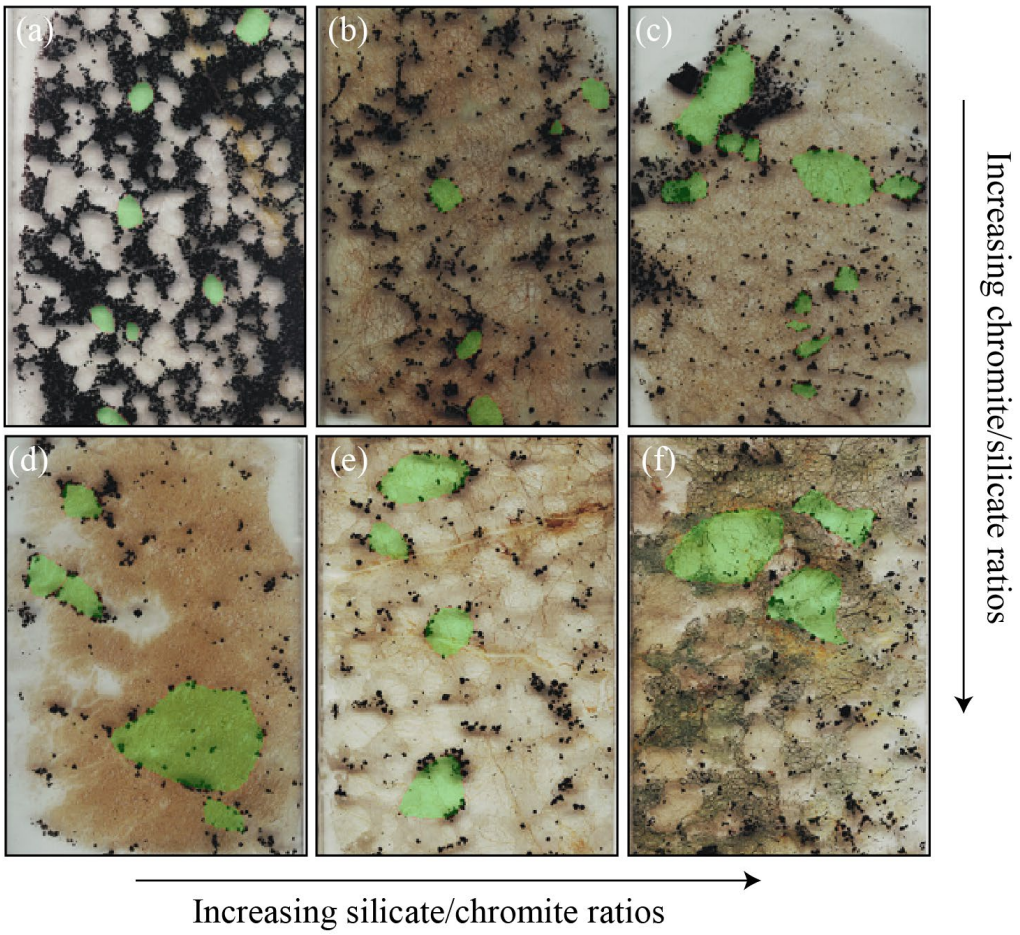

Figure 2.6 Scanned images of thin-sections of the Stillwater Complex samples showing distribution and relation of minerals and general variations of crystal size from chromitite (a-b), peridotite (c-d) to harzburgite (e-f).

The Middle Banded Series is mainly composed of gabbro, olivine-bearing gabbro, and gabbronorite. Plagioclase minerals dominate, with contents reaching over 80%, while Mg-rich minerals such as olivine and clinopyroxene are more enriched compared to other series. Orthopyroxene content in this zone is lower, possibly due to later crystallization compared to clinopyroxene, likely caused by increased fluid presence. Furthermore, the grain size of feldspar is typically 2-3 times larger in the Middle Banded Series than in the Lower Banded Series and Upper Banded Series, showing complex banding patterns that are distinct from the plagioclase of magmatic origin found in the Ultramafic Series and Lower Banded Series. Platinum-group element mineralization with sulfides is also found in the Picket Pin within this zone, likely

related to residual melt/fluid migration into the gabbroic layer (Boudreau and McCallum, 1992). The Upper Banded Series mainly consists of norite, gabbro, and gabbroic norite (Figure 2.5 g-h). Its mineral composition and petrological sequence are similar to the Lower Banded Series.

2.3 Sample description, petrography and mineral chemistry

The rock-forming minerals in the Stillwater Complex are olivine, orthopyroxene, clinopyroxene, plagioclase, amphibole, and chromite. Minor minerals such as quartz, biotite, hornblende, apatite, magnetite, ilmenite, and minor sulfides are also present. Additionally, there are numerous secondary minerals, including serpentine and talc formed from olivine and orthopyroxene, zeolite and prehnite formed from plagioclase , and chlorite and epidote formed from amphibole. The mineral compositions in different rock types are summarized in Table 2.1.

Table 2.1 Major rock names and containing minerals of Stillwater Complex

Rock type	Cumulate minerals	Interstitial minerals
Pridotite	Ol (±Chr)	Opx, Cpx, Plag, Phl, (Amph, Ap)
Harzburgite	Ol, Opx (± Chr)	Cpx, Plag, (Phl, Amph, Ap)
Chromitite	Chr (±Ol)	Opx, Cpx, Plag, (Phl, Amph, Ap)
Bronzitite	Opx	Plag, Cpx, (Qtz, Phl, Ap)
Norite	Plag, Opx/Pig	Cpx, (Ap, Qtz)
Ol-Gabbro	Plag, Cpx, Ol	Opx (Ap)
Ol-Norite	Plag, Opx/Pig, Cpx	(Qtz, Ap, Mt)
Troctolite	Plag, Ol	Opx, Cpx (Ap)
Ol-Gabbronorite	Plag, Opx, Cpx, Ol	(Ap)
Anorthosite	Plag	Opx/Pig, Cpx, Qtz, (Mt)

Note: The table includes peridotite, which encompasses dunite and poikilitic harzburgite, with granular harzburgite especifically referring to "granular harzburgite." Mineral abbreviations: Ol, olivine; Opx, orthopyroxene; Cpx, clinopyroxene; Plag, feldspar; Chr, chromite; Ap, apatite; Qtz, quartz; Mt, magnetite; Amph, amphibole; Phl, biotite.

Olivine: Olivine is the primary cumulate mineral in dunite, harzburgite, olivine

gabbronorite, and olivine pyroxenite (Figure 2.7). In the Ultramafic Series, the Fo values of olivine typically range from 79 to 90 (Boudreau and McCallum, 1986). In samples from the Ultramafic Series, olivine composition is usually confined to a Fo value variation between 84 and 86. Olivine with a higher Fe component typically comes from the Lowermost part of the Peridotite Zone, while olivine with a higher Mg component is often associated with chromite. In olivine gabbronorite and olivine pyroxenite, the Fo range of olivine can vary from 79 to 64 (Boudreau and McCallum, 1989). There is a lack of overlapping olivine composition ranges between the Ultramafic Series and the Banded Series, which is consistent with the absence of olivine in the lithological sequence between the Peridotite Zone and the Lower Banded Series observed in field stratigraphy and rock profiles (Raedeke, 1982; Todd et al., 1982; McCallum, 1996). Olivine can be partially serpentinized to fully altered, forming combinations of serpentine + magnetite + talc + calcite mineral assemblages. In olivine gabbronorite, olivine typically alters to light brown amphibole, surrounded by light green chlorite without direct contact with plagioclase (Raedeke and McCallum, 1984; Campbell and Murck, 1993; McCallum, 2002).

Pyroxenes: Orthopyroxene appears as a cumulate mineral in bronzitite, norite, and gabbronorite, while in granular harzburgite, it occurs as interstitial mineral phases (Figure 2.7b, c; Wager et al., 1960; Wager and Brown, 1968). Clinopyroxene is present in all rock sequences and, like orthopyroxene, can occur as cumulate or interstitial minerals. However, its overall abundance is much lower compared to orthopyroxene (Jackson, 1961, 1967; Irvine, 1982; Raedeke, 1982; Todd et al., 1982). In all rock sequences where both olivine and pyroxenes coexist, pyroxenes are typically slightly more Mg-rich than olivine, suggesting possible equilibrium between the two minerals (Campbell, 1978; McBirney and Noyes, 1979; Boudreau, 2016). Furthermore, orthopyroxene often lacks prominent compositional zoning, but in its (100) lattice direction, clinopyroxene blades commonly occur. Therefore, in terms of composition, the rim of orthopyroxene is typically depleted in Ca and REE elements compared to the core (Boudreau, 1987; Meurer and Boudreau, 1996; Cooper, 1997).

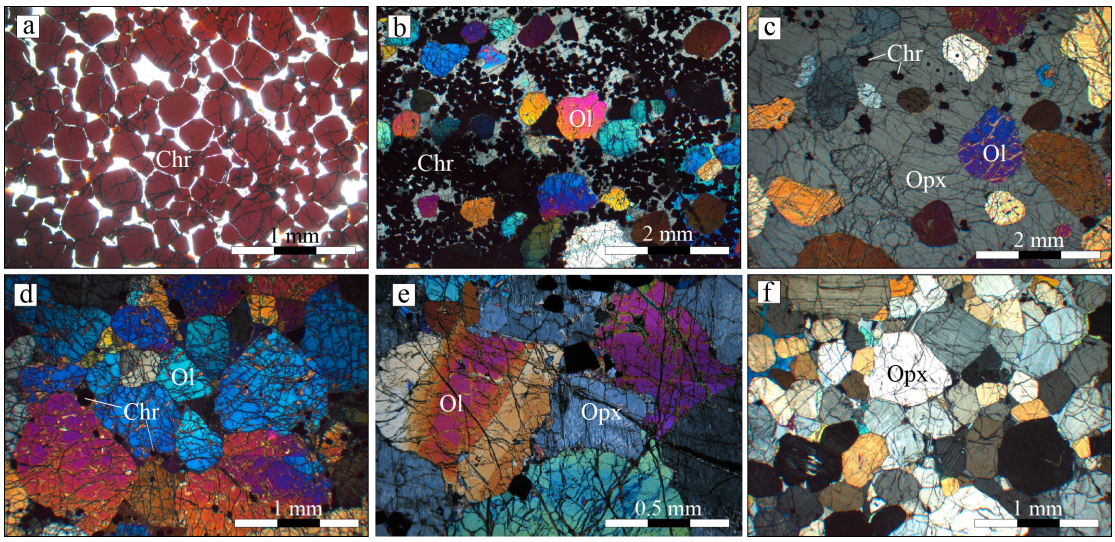

Figure 2.7 Plane- (a) and cross-polarized optical images (b-f) of sample thin sections: (a) massive chromitite, (b) anti-nodular chromitite, (c) disseminated chromitite, and silicate cumulates consisit of peridotite (d), harzburgite (e), bronzitite (f). Abbreviations: olivine (Ol), orthopyroxene (Opx), chromite (Chr).

Plagioclase: Plagioclase is the most common cumulate mineral in the entire Banded Series and serves as one of the main interstitial cumulate minerals in the Ultramafic Series, often occurring alongside clinopyroxene. Plagioclase crystals at hand-sample scales can range from less than 0.1 to 1 cm, and in vertical zonation, upper plagioclase generally possesses larger crystal radii (McCallum et al., 1980, 1996; Boudreau, 1987; Barnes et al., 2015; Prichard et al., 2017). Such variations in scale can even be observed within a range of several meters (Salpas et al., 1983; Boudreau and McCallum, 1986). Plagioclase compositions span from An90 to An60 and exhibit vertical compositional zoning from bottom to top in the vertical zonation (Raedeke and McCallum, 1984; Murck, 1986; Loferski et al., 1990; Reichl, 1992; Cooper, 1997). Additionally, in norite, gabbronorite, gabbronorite, and norite pyroxenite, plagioclase often displays distinct igneous features in the form of stripes and has relatively uniform compositions. However, in olivine gabbronorite and pyroxenite, there are no apparent igneous features, and only a small amount of plagioclase exhibits banding. Throughout the entire rock sequence, plagioclase alteration is usually not pronounced, limited to kaolinization or epidotization only at the edges.

Chromite: In the Ultramafic Series, abundant chromite cumulate typically appears in the olivine component of each cyclic unit, not directly associated with bronzitite, and forms single phase mineral layers that are several centimeters to several meters thick. Chromite crystals often have well-defined forms and exhibit distinct magmatic features (Irvine, 1975, 1977; Campbell and Murck, 1993; Cameron and Desborough, 1993; Maier et al., 2012; Forien et al., 2015; Mungall et al., 2016). In granular harzburgite and bronzitite, chromite is distributed as star-shaped or sparse interstitial occurrences. It's worth noting that chromite exhibits more pronounced compositional variations than silicate minerals, and according to previous research, it has undergone extensive subsolidus compositional exchange with surrounding silicate minerals (Jones et al., 1960; Jackson, 1961; Campbell and Murck, 1993; Cooper, 2002). We will focus on this aspect in later chapters.

Accessory minerals: Apatite, hornblende, and biotite occur as accessory minerals or as mineral inclusions (Zientek et al., 1984; Cooper, 1997; Cooper, 2002). In the rock sequences below the J-M Reef, apatite is typically characterized as Cl-rich apatite (>6.0% Cl), distinctly different from the F-rich apatite (>1.4% F) above this layer. The occurrence of such high-Cl apatite in igneous rocks suggests a high-temperature hydrothermal origin (Boudreau and McCallum, 1989). Biotite usually appears in association with chromite in peridotite. Page et al. (1987) noted that biotite in the Stillwater Complex is enriched in Cl (up to 0.5%) and F (up to 0.5%), a phenomenon not reported in other layered intrusions apart from the Bushveld Complex. Compared to biotite, hornblende is rarer and has only been reported in the Lowermost layer of the peridotite zone, and microscopic examination shows that biotite and hornblende cannot coexist in the same sample (Boudreau, 1984). It is currently believed that hornblende surrounding chromite is a secondary mineral of pyroxene, representing reaction relationships between melt and minerals. Sulfides in the Basal Series are primarily composed of pyrite, chalcopyrite, and pentlandite, and they can locally accumulate to industrial grades. In the Ultramafic Series, the abundance of sulfides decreases significantly, and its concentration is positively correlated with chromite content.

3. Magnesium and iron isotopic evidence of inter-mineral diffusion in ultramafic cumulates of the Peridotite Zone, Stillwater Complex[1]

[1] This chapter is published in Geochimica and Cosmochimia Acta - Bai, Y., Su, B.X., Xiao, Y., Cui, M.M., Charlier, B., 2021. Magnesium and iron isotopic evidence of inter-mineral diffusion in ultramafic cumulates of the Peridotite Zone, Stillwater Complex. Geochimica et Cosmochimica Acta 292, 152-169. doi: https://doi.org/10.1016/j.gca.2020.09.023

Elemental iron and magnesium diffusion profiles are commonly observed in ferromagnesian and oxide minerals in volcanic rocks (e.g., Scowen et al., 1991; Costa and Dungan, 2005; Costa et al., 2008), meteorites (e.g., Peslier et al., 2010; Gross et al., 2013), and metasomatized mantle peridotites (e.g., Smith and Ehrenberg, 1984; Peslier et al., 2008; Jollands et al., 2018). Diffusive chemical exchange between crystals and an evolved melt is usually considered the most plausible process to produce such chemical zonations (Kahl et al., 2011; Druitt et al., 2012). Such re-equilibrations commonly produce silicates with Fe-rich rims (e.g., Sio et al., 2013; Oeser et al., 2015; Sio and Dauphas, 2018) and oxides with Mg-rich rims (e.g., Gervilla et al., 2012; Ahmed and Surour, 2016). Recently, diffusive isotope fractionations have also been observed in minerals. Indeed, negatively correlated Fe and Mg isotopic ratios are well documented for elemental chemical diffusion between crystals and evolved melts (e.g., Teng et al., 2011; Sio et al., 2013; Collinet et al., 2017; Zhao et al., 2015, 2017), in which heavy Fe and light Mg isotopes are preferentially fractionated into silicates, and their respective light and heavy counterparts into oxides (e.g., Dauphas et al., 2010; Teng et al., 2011; Sio and Dauphas, 2018).

Chemical zonations also result from continuous subsolidus diffusion between silicates and oxides (Roeder et al., 1979; Lehmann, 1983; Ozawa, 1983; Dohmen and Chakraborty, 2007) due to the variable elemental exchange coefficients of minerals in cooling magmatic bodies (e.g., Fujii, 1978). Irvine (1965, 1967) first illustrated that inter-mineral Mg^{2+} diffusion from chromite to olivine could produce chemical profiles opposite to those expected during crystal-melt diffusion. Furthermore, chromite grains with Fe^{2+}-enriched cores within enstatites of the Alpine-type Red Mountain complex (New Zealand) record co-occurring changes in oxides during inter-mineral re-equilibration (Sinton, 1977). Numerous studies have subsequently reported such diffusive features in various mafic-ultramafic complexes, including ophiolite complexes (Jaques, 1981) and Alaskan-type (Clark, 1978) and layered intrusions (Wilson, 1982). Subsolidus inter-mineral diffusion is now known to significantly affect mineral compositions (e.g., Medaris, 1976; Ozawa, 1983; Dohmen and Chakraborty,

2007; Thakurta et al., 2008; Bai et al., 2017), although higher mixing proportions with primitive magmas and subsequently superimposed modifications by interstitial liquids or evolved melts can also produce similar mineral compositional patterns (e.g., Barnes, 1986; Bell and Claydon, 1992). In-situ elemental diffusive profiles in crystals should distinguish these trends, but are often obscured by prolonged subsolidus intra-mineral diffusion in large layered intrusions (e.g., Yang and Seccombe, 1993). Nonetheless, isotopic variations induced by elemental migration are expected to reveal possible inter-mineral re-equilibration processes (Chen et al., 2014, 2018; Xiao et al., 2016; Albert et al., 2019; Tian et al., 2020).

Layered mafic-ultramafic intrusions are key illustrations of the compositional diversity of magmas at crustal depths (e.g., Parsons, 1987; Cawthorn, 1996). They represent critical links in the differentiation of basaltic magmas derived from partial melting of the mantle, stored in crustal reservoirs, and eventually erupted (Helz, 1995; Charlier et al., 2015; Wall et al., 2018). The Neoarchean Stillwater Complex, one of the world's largest known layered intrusions and host to a rich chromite deposit known as the Peridotite Zone, represents the initial evolution of igneous processes and the mineralization of mantle-derived melts in crustal magma chambers (e.g., Campbell and Murck, 1993; Eales and Costin, 2012). Here, we present combined Fe and Mg isotopic data for olivine, orthopyroxene, and chromite mineral separates from well-characterized chromitite, dunite, harzburgite, and bronzitite units of the Peridotite Zone. Mineral compositional variations in the Peridotite Zone are predominantly controlled by fractional crystallization and were modified by re-equilibration during subsolidus inter-mineral diffusion (Hess and Smith, 1960; Jackson, 1961; McCallum, 1996). The world-class chromite deposits preserve well-defined lithological layers that constrain the roles of oxide/silicate crystallization and accumulation (Jackson, 1961; Raedeke and McCallum, 1984). We use our results, combined with those of studies on the Fe-Mg isotopic compositions of mineral separates from mantle peridotites (Macris et al., 2015; Zhao et al., 2015, 2017), other layered intrusions (Chen et al., 2014, 2018), and other types of mafic-ultramafic massifs such as the podiform chromitite from the

Luobusa ophiolite (Chen et al., 2015; Xiao et al., 2016), to reveal Fe-Mg isotopic variations during subsolidus inter-mineral diffusion.

3.1 Sample and analytical methods

3.1.1 Sample selected

Twenty-one samples were selected for Fe-Mg isotopic analyses (Table 3.1). Chromitite and poikilitic harzburgite samples used in this study were collected from the B and G chromitite layers in the Benbow Area and Mountain View, respectively, the most representative chromium mining sites in the Stillwater Complex (Hess and Smith, 1960; Jackson, 1961). Samples of dunite, granular harzburgite, bronzitite, and one plagioclase-bearing harzburgite were collected from an un-mineralized cyclic unit of the Lowermost layer in the Gish Area. These samples span the lithological range of the Peridotite Zone, and the chemical compositions of the major cumulus minerals are representative of chemical variations throughout the series (Figure 3.1).

Chemical variations of forsterite content (Fo) in olivine and Mg# (100 × Mg/[Mg + Fe]) in orthopyroxene and chromite in the Peridotite Zone are illustrated in Figure 3.1. In the Lowermost layer and silicate cumulates of the G chromitite layer, olivine Fo values are ~84–86 and orthopyroxene Mg# values are ~85–87, but both distinctly decrease (to Fo ≈ 83 and Mg# ≈ 84) in the lowermost sample 16SW-3-11 collected near the chilled margin of the Basal Series. Olivine Fo and orthopyroxene Mg# values in the chromitites range from 86 to 90 and 87 to 90, respectively. These trends are similar to the observations of Irvine (1967), Roeder et al. (1979), and Raedeke and McCallum (1984). Chromite grains in massive and anti-nodular chromitites have Mg# ≈ 50–60, a range higher and more restricted than chromite in disseminated chromitites and silicate cumulates (Mg# ≈ 20–50).

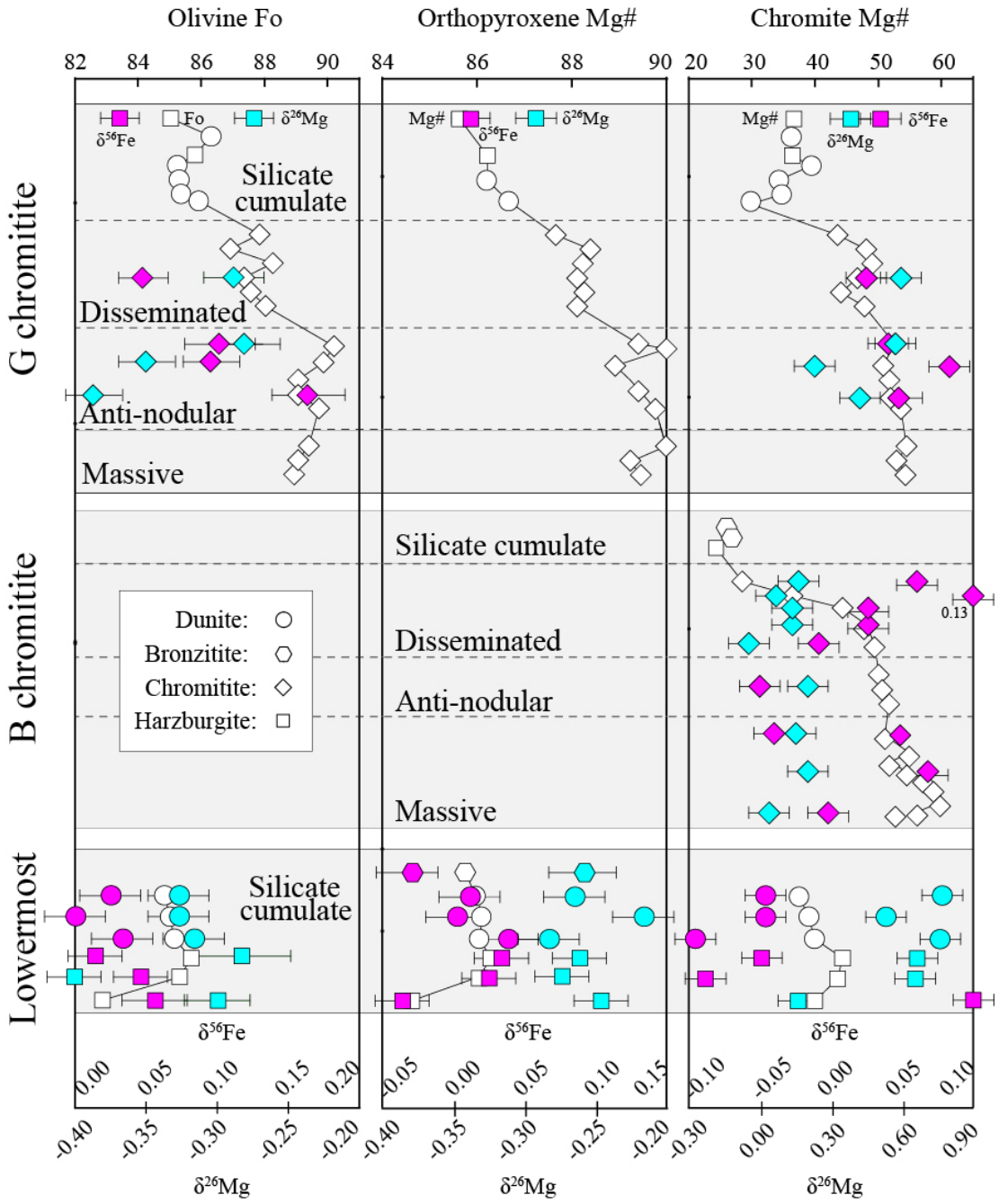

Figure 3.1 Stratigraphic variations of olivine Fo and orthopyroxene and chromite Mg# (= 100 × $Mg^{2+}/[Mg^{2+} + Fe^{2+}]$) compared to Fe and Mg isotopic variations in a selected subset of mineral separates from the Peridotite Zone of the Stillwater Complex. White symbols with solid lines represent average olivine Fo composition and orthopyroxene and chromite Mg# (data from Bai et al., 2019; all major elemental compositions are reported in Appendix 10.1). Magenta and cyan symbols represent the corresponding Fe and Mg isotopic compositions, respectively (see Table 3.1).

Table 3.1 Fe and Mg isotopic compositions of mineral separates in rocks from the Stillwater Complex

Location	Sample	lithology	olivine				orthopyroxene				chromite			
			δ^{56}Fe	2se	δ^{26}Mg	2sd	δ^{56}Fe	2se	δ^{26}Mg	2sd	δ^{56}Fe	2se	δ^{26}Mg	2sd
Lowermost layer	16SW-3-4	Dunite	0.02	0.03	-0.32	0.06	0.01	0.03	-0.27	0.01	-0.04	0.03	0.84	0.04
Lowermost layer	16SW-3-3	Dunite	0.04	0.03	-0.30	0.03	0.04	0.03	-0.28	0.06	-0.09	0.03	0.82	0.05
Lowermost layer	16SW-3-2	Dunite	0.00	0.03	-0.32	0.06	0.00	0.03	-0.22	0.05	-0.04	0.03	0.51	0.04
Lowermost layer	16SW-3-9	Granular harzburgite	0.02	0.03	-0.40	0.02	0.02	0.03	-0.27	0.05	-0.08	0.03	0.65	0.04
Lowermost layer	16SW-3-5	Granular harzburgite	0.05	0.03	-0.26	0.10	0.03	0.03	-0.26	0.06	-0.05	0.03	0.66	0.04
Lowermost layer	16SW-3-11	Granular harzburgite	0.06	0.03	-0.28	0.08	-0.04	0.03	-0.25	0.03	0.10	0.03	0.25	0.03
Lowermost layer	16SW-3-6	Bronzitite					-0.02	0.03	-0.26	0.03				
G chromitite	16SW-1-15	Poikilitic harzburgite	0.03	0.03	-0.27	0.10	0.06	0.03	-0.29	0.03	0.03	0.03	0.37	0.04
G chromitite	16SW-1-9	Disseminated chromitite	0.05	0.03	-0.29	0.04					0.01	0.03	0.59	0.03
G chromitite	16SW-1-27	Disseminated chromitite	0.11	0.03	-0.27	0.06					0.04	0.03	0.57	0.08
G chromitite	16SW-1-8	Anti-nodular chromitite	0.17	0.03	-0.39	0.07					0.08	0.03	0.25	0.05
G chromitite	16SW-1-26	Anti-nodular chromitite	0.10	0.03	-0.35	0.08					0.04	0.03	0.29	0.04
B chromitite	16SW-2-21	Disseminated chromitite									0.06	0.03	0.13	0.01
B chromitite	16SW-2-12	Disseminated chromitite									0.02	0.03	0.11	0.03
B chromitite	16SW-2-4	Disseminated chromitite									0.13	0.03	0.05	0.04
B chromitite	16SW-2-17	Disseminated chromitite									0.02	0.03	0.11	0.03
B chromitite	16SW-2-8	Disseminated chromitite									-0.01	0.03	-0.05	0.06
B chromitite	16SW-2-14	Anti-nodular chromitite									-0.05	0.03	0.20	0.08
B chromitite	16SW-2-13	Massive chromitite									-0.04	0.03	0.12	0.04
B chromitite	16SW-2-15	Massive chromitite									0.00	0.03	0.03	0.04
B chromitite	16SW-2-6	Massive chromitite									0.07	0.03	0.19	0.03

3.1.2 Mineral digestion and chemical separation

Rocks were crushed to <30 mesh and fresh mineral separates (olivine, orthopyroxene, and chromite in the G chromitite and Lowermost layers; chromite in B chromitite layer) were handpicked under a binocular microscope. Notably, due to the overall serpentinization of silicates in the B chromitite (Figure S9.1 in Appendix 9.1), we were unable to separate olivine and orthopyroxene from the layer. Picked minerals were cleaned with Milli-Q water in an ultrasonic bath to remove residues from their surfaces and cracks. Procedures for sample dissolution, column chemistry, and instrumental analysis are similar to those reported in previous studies (e.g., Teng et al., 2011; He et al., 2015), and are briefly summarized here. Olivine and orthopyroxene separates were dissolved overnight in a mixture of HF, HCl, and HNO_3 at 130 °C in capped Savillex beakers. Chromite separates were ground to a very fine powder and dissolved in concentrated 3:1 HF-HNO_3 in a microwave oven at increasing temperatures of 180, 210, 220, and 225 °C for half-hour intervals. All mineral solutions were dried on a hot plate and re-dissolved in 6 N HCl in preparation for chromatographic separation. Column chemistry was performed at the Isotope Geochemistry Lab, China University of Geosciences, Beijing, following the procedure reported in previous studies (e.g., Dauphas et al., 2010; Teng et al., 2011; Xiao et al., 2016). After complete acid digestion, Fe was chemically separated with a polypropylene column using an anion exchange resin (Bio-Rad AG1X-8, 200–400 mesh) in an HCl medium. The matrix elements during Fe column chemistry were collected for Mg purification, and Mg separation was achieved by cation exchange chromatography with Bio-Rad AG50W-X8 resin (200–400 mesh). Both purifications were performed twice to obtain pure solutions for mass spectrometry, and the overall procedural blank is less than 5 ng for both Mg and Fe.

3.1.3 Mass spectrometry

Fe and Mg isotopic measurements were performed on Thermo Scientific Neptune Plus and Thermo Finnigan Neptune Plus multi-collector inductively coupled plasma

mass spectrometers, respectively, using the sample-standard bracketing method. Each measurement consisted of a 3-s idle time and 30 cycles of 4.19-s (Fe) or 8.39-s (Mg) integration times. Runs of samples and standards were separated by washes using 3% HNO_3 for 2 min to avoid cross-contamination. Isotopic data are expressed in standard δ notation as per-mil deviations relative to the IRMM-014 and DSM-3 standards as $\delta^{56}Fe$ [‰] = $[(^{56}Fe/^{54}Fe)_{sample}/(^{56}Fe/^{54}Fe)_{IRMM\text{-}014} - 1] \times 1{,}000$ and $\delta^{26}Mg$ [‰] = $[(^{26}Mg/^{24}Mg)_{sample}/(^{26}Mg/^{24}Mg)_{DSM\text{-}3} - 1] \times 1{,}000$, respectively. The isotopic compositions reported herein are the average values from four analyses, and uncertainties are reported as two standard errors (2SE) and two standard deviations (2SD) for $\delta^{56}Fe$ and $\delta^{26}Mg$, respectively. In addition, the international basaltic standard BCR-2 was analyzed to monitor accuracy and yielded $\delta^{56}Fe = +0.11 \pm 0.01$‰ ($n = 4$, 2SE), identical to the recommended value (Craddock and Dauphas, 2011). Two international geostandards (BHVO-2 and GSP-2) were also measured to monitor accuracy during the course of column chemistry. We obtained their isotopic compositions to be $\delta^{26}Mg = -0.25 \pm 0.05$‰ and $\delta^{56}Fe = +0.09 \pm 0.03$‰ for BHVO-2 and $\delta^{26}Mg = +0.06 \pm 0.05$‰ and $\delta^{56}Fe = +0.15 \pm 0.03$‰ for GSP-2, consistent with their recommended values (BHVO-2: $\delta^{26}Mg = -0.20 \pm 0.07$‰, $\delta^{56}Fe = +0.11 \pm 0.01$‰; GSP-2: $\delta^{26}Mg = +0.04 \pm 0.02$‰, $\delta^{56}Fe = +0.16 \pm 0.01$‰; He et al., 2015; Teng et al., 2015).

3.2. Results

3.2.1 Stratigraphic Fe and Mg isotopic variations

The Fe and Mg isotopic compositions of olivine, orthopyroxene, and chromite are presented in stratigraphic profiles in Figure 3.1. Both olivine and orthopyroxene Fe and Mg isotopic compositions covary with stratigraphic height (excepting the lowermost sample of the Lowermost layer, 16SW-3-11). In detail, the Fe isotopic compositions of olivine in the G chromitite ($\delta^{56}Fe$ = 0.03–0.14‰) are slightly heavier than those of olivine in the Lowermost layer ($\delta^{56}Fe$ = 0.00–0.06‰), whereas their Mg isotopic compositions are similar ($\delta^{26}Mg$ = –0.39 to –0.27‰ in the G chromitite and –0.40 to –

0.26‰ in the Lowermost layer). The $\delta^{56}Fe$ and $\delta^{26}Mg$ values of the sole orthopyroxene sample collected from the G chromitite ($\delta^{56}Fe$ = 0.06‰ and $\delta^{26}Mg$ = –0.29‰) are slightly higher and lower, respectively, than those of orthopyroxene in the Lowermost layer ($\delta^{56}Fe$ = –0.04 to +0.04‰, $\delta^{26}Mg$ = –0.28 to –0.22‰). In addition, silicate $\delta^{56}Fe$ values decrease regularly from the base to the top of each cyclic unit (except for the lowermost sample analyzed), consistent with Fo and Mg# variations, whereas silicate $\delta^{26}Mg$ values increase upward (Figure 3.1).

The stratigraphic trends of chromite Fe and Mg isotopic compositions differ from those of coexisting silicates. The Fe isotopic compositions of chromite in the G chromitite ($\delta^{56}Fe$ = 0.01–0.08‰) are distinctly heavier than those of chromite in the Lowermost layer ($\delta^{56}Fe$ = –0.09 to –0.04‰, apart from 16SW-3-11 with a high $\delta^{56}Fe$ value of 0.10‰). The Mg isotopic compositions of chromite in the G chromitite ($\delta^{26}Mg$ = 0.25–0.59‰) are lighter than those of chromite in the Lowermost layer ($\delta^{26}Mg$ = 0.51–0.84‰, except for 16SW-3-11, which has a very low $\delta^{26}Mg$ value of 0.25‰). The isotopic compositions of chromite in the B chromitite are distinct from chromite in the other two layers, showing a wider range of $\delta^{56}Fe$ values (–0.05 to +0.13‰) and lighter $\delta^{26}Mg$ values of –0.05 to +0.20‰. Although chromite Fe and Mg isotopic compositions vary more broadly than those of coexisting silicates, they do not covary with stratigraphic height (Figure 3.1).

3.2.2 Inter-mineral Fe and Mg isotope fractionations

Peridotite Zone chromite $\delta^{56}Fe$ values (–0.09 to +0.13‰, averaging 0.01 ± 0.03‰) are, on average, lighter than those of spinel from mantle xenoliths (Figure 3.2; average spinel $\delta^{56}Fe$ = 0.15‰; Macris et al., 2015; Zhao et al., 2015, 2017), whereas Peridotite Zone olivine ($\delta^{56}Fe$ = 0.00–0.17‰, averaging 0.06 ± 0.03‰) and orthopyroxene ($\delta^{56}Fe$ = –0.04 to +0.06‰, averaging 0.01 ± 0.03‰) are isotopically heavier than most data reported for olivine and orthopyroxene in mantle xenoliths (Figure 3.2; average $\delta^{56}Fe$ = –0.04‰; Liu et al., 2011; Macris et al., 2015; Zhao et al., 2015, 2017). Interestingly, the Fe isotopic compositions of coexisting chromite and silicates in the Peridotite Zone display a distinct inter-mineral fractionation compared to those of minerals in mantle

xenoliths (Figure 3.2): silicates in mantle xenoliths commonly have lighter Fe isotopic compositions than coexisting spinel, whereas the Peridotite Zone cumulus minerals have compositions generally following the order $\delta^{56}Fe_{Ol} \geq \delta^{56}Fe_{Opx} = \delta^{56}Fe_{Chr}$ (Xiao et al., 2016; Zhang et al., 2019).

Olivine and orthopyroxene in the Peridotite Zone have Mg isotopic compositions ($\delta^{26}Mg$ = –0.40 to –0.22‰) generally within the range of the mean mafic Earth ($\delta^{26}Mg$ = –0.25 ± 0.07‰; Figure 3.2; Teng et al., 2010), but with a slightly lower average value ($\delta^{26}Mg$ = –0.29 ± 0.07‰). These silicate averages and ranges are in agreement with those observed in some mafic-ultramafic complexes (Su et al., 2017; Tian et al., 2019), but contrast the slightly elevated silicate $\delta^{26}Mg$ values observed in other mafic-ultramafic complexes (Xiao et al., 2016; Chen et al., 2018), lavas (Dauphas et al., 2010; Teng et al., 2011), and mantle xenoliths (Liu et al., 2011; Zhao et al., 2015, 2017). In contrast, Peridotite Zone chromites display a broad range of $\delta^{26}Mg$ values, from –0.05 to +0.84‰ (Figure 3.2), and the cumulus minerals in our samples generally follow the order $\delta^{26}Mg_{Chr} \geq \delta^{26}Mg_{Opx} = \delta^{26}Mg_{Ol}$, similar to inter-mineral Mg isotope fractionations observed in mantle xenoliths (Teng et al., 2007; Huang et al., 2011; Hu et al., 2016).

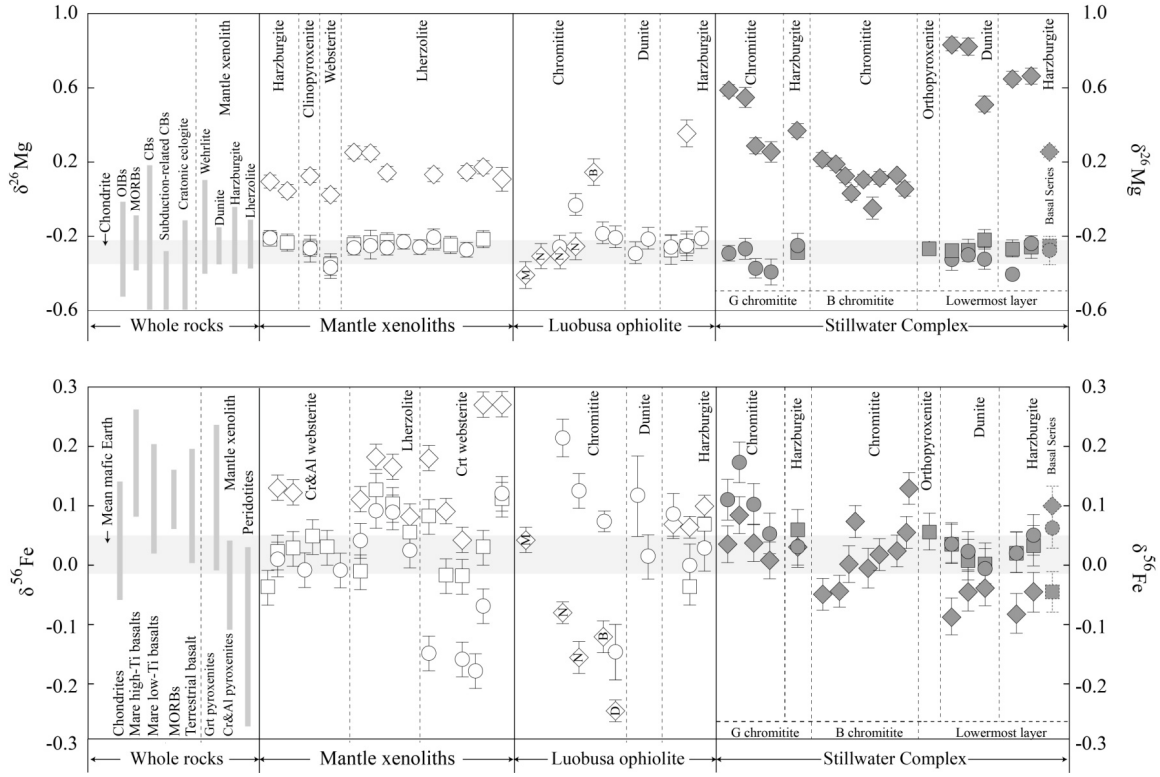

Figure 3.2 Fe and Mg isotopic compositions of olivine, orthopyroxene, and chromite in the Stillwater Complex compared to published mineral-specific data in ophiolites (Xiao et al., 2016) and mantle peridotites (Hu et al., 2016; Zhao et al., 2015, 2017), as well as various whole-rock data (Teng et al., 2010; Huang et al., 2011). Circles represent olivine, squares represent orthopyroxene, and diamonds represent chromite in intrusions or spinel in mantle xenoliths. The chondritic Mg isotopic compositional range and the Fe isotopic compositional range of the mean mafic Earth (gray shaded areas in the top and bottom plots, respectively) are from Weyer et al. (2005), Weyer and Ionov (2007), and Teng et al. (2009). OIBs, ocean island basalts; MORBs, mid-ocean ridge basalts; CBs, continental basalts; M, Massive chromitite; N, Anti-nodular chromitite; B, Banded chromitite; D, Disseminated chromitite.

3.3 Disequilibrium Fe-Mg isotope fractionation between silicates and chromite

Equilibrium isotope fractionations commonly depend on elemental bonding environments, with heavier isotopes preferring stronger bonds and lower-coordination polyhedra (e.g., Schauble, 2011; Huang et al., 2013). Since Fe and Mg have similar bonding environments and ion occupancies in olivine and orthopyroxene, Fe and Mg isotopic discrepancies between them are expected to be limited (≤0.1‰) at magmatic temperatures. Indeed, except for the harzburgite sample 16SW-3-11 collected from the contact between the Basal Series and Peridotite Zone (i.e., the bottom of the Lowermost layer), most olivine-orthopyroxene pairs in our samples show small isotope fractionations ($\Delta^{26}Mg_{Opx\text{-}Ol} = \delta^{26}Mg_{Opx} - \delta^{26}Mg_{Ol}$ and $\Delta^{56}Fe_{Opx\text{-}Ol} = \delta^{56}Fe_{Opx} - \delta^{56}Fe_{Ol}$) within ±0.10‰ (Figure 3.3). These inter-mineral Fe and Mg isotope fractionations are also consistent with theoretical considerations (Schauble, 2011) and measurements from mantle xenoliths (e.g., Young et al., 2009, 2015; Huang et al., 2011; Liu et al., 2011; Zhao et al., 2015, 2017; Hu et al., 2016) indicating that inter-mineral compositional shifts and isotope fractionations between olivine and orthopyroxene can be negligible.

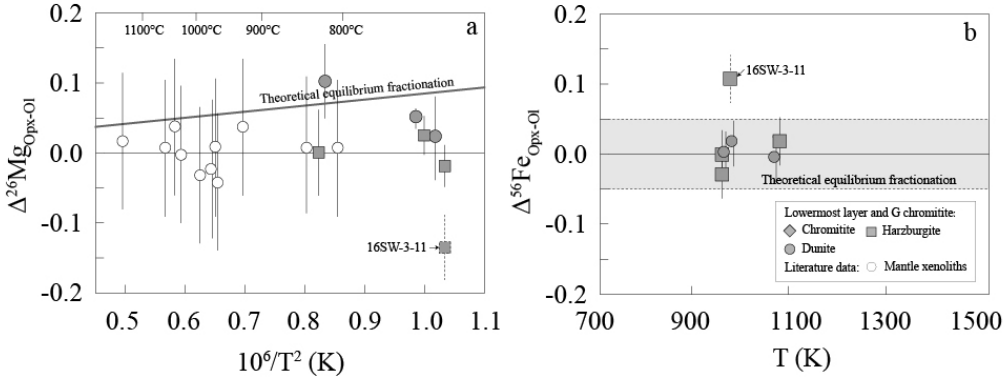

Figure 3.3 Calculated orthopyroxene-olivine inter-mineral equilibrium (a) Mg and (b) Fe isotope fractionation factors as a function of temperature in the Stillwater Complex. The equilibrium temperature for these samples was calculated based on the olivine-spinel re-equilibration thermometer of Balluhaus (1993), and the calculation parameters reported in Appendix 10.1. The mantle peridotite samples are cited from Liu et al. (2011) and Macris et al. (2015). The gray line in (a) and the gray field in (b) denote theoretical equilibrium inter-

mineral isotope fractionation factors.

The disequilibrium inter-mineral isotope fractionation is most distinct between silicates and chromite. Apart from sample 16SW-3-11, $\Delta^{56}Fe_{Chr\text{-}Ol}$ (= $\delta^{56}Fe_{Chr} - \delta^{56}Fe_{Ol}$) values in our samples vary from –0.12 to 0.00‰ (Figure 3.4a) and $\Delta^{56}Fe_{Chr\text{-}Opx}$ (= $\delta^{56}Fe_{Chr} - \delta^{56}Fe_{Opx}$) from –0.12 to –0.03‰ (Figure 3.4b). In the spinel structure, Fe^{2+} and Fe^{3+} are in tetrahedrally and octahedrally coordinated cation sites, respectively, whereas olivine incorporates only Fe^{2+} into its structure and always in octahedral coordination (Polyakov and Mineev, 2000; Williams et al., 2005; Polyakov et al., 2007). Thus, spinel-group minerals usually have heavier Fe isotopic compositions than coexisting olivine, as observed in equilibrium mantle peridotites (e.g., Weyer and Ionov, 2007; Zhao et al., 2010; Macris et al., 2015). On the other hand, oxygen fugacity exerts an important control on Fe isotope fractionations during magmatic processes (Weyer et al., 2005; Weyer and Ionov, 2007; Teng et al., 2008; Poitrasson et al., 2013; Liu et al., 2014; Cao et al., 2019), and the incorporation of heavy Fe isotopes into phases with higher $Fe^{3+}/\sum Fe$ ratios may further increase $\Delta^{56}Fe_{Chr\text{-}Ol}$ and $\Delta^{56}Fe_{Chr\text{-}Opx}$ values. Therefore, the reversed sequence of $\delta^{56}Fe_{Chr} \geq \delta^{56}Fe_{Ol} = \delta^{56}Fe_{Opx}$ observed in our samples cannot have been produced by equilibrium magmatic processes, but only by diffusion-related kinetic processes (e.g., Huang et al., 2011; Chen et al., 2014, 2018; Xiao et al., 2016; Tian et al., 2019).

As Mg commonly has only one valence state (Mg^{2+}) in minerals and melts, equilibrium inter-mineral Mg isotope fractionations during magmatic processes are expected to be limited (Teng et al., 2007, 2010, 2016; Dauphas et al., 2010; Liu et al., 2010; Hu et al., 2019). Theoretical calculations suggest that the extent of inter-mineral Mg isotope fractionations between spinel-group minerals ($A^{2+}B_2^{3+}O_4^{2-}$, where A and B are the tetrahedral and octahedral ions, respectively) and silicates depends only on the octahedral ion composition (B_2^{3+}) of the spinel mineral (Young et al., 2009, 2015; Schauble, 2011). For example, at 1000 K, inter-mineral Mg isotope fractionations are 0.6‰ for spinel ($MgAl_2O_4$), 0.2‰ for magnesiochromite ($MgCr_2O_4$), and 0.1‰ for magnesioferrite ($MgFe_2O_4$) (Figure 3.4c; Schauble, 2011; Liu et al., 2011). Chromite

phases in layered intrusions commonly contain Al, Fe, and Cr as octahedral ions, and chromites in our samples have the general formula $(Mg_{0.45}Fe^{2+}_{0.56})^{IV}(Al_{0.74}Cr_{1.10}Fe^{3+}_{0.13})^{VI}O_4$ (Table 3.2).

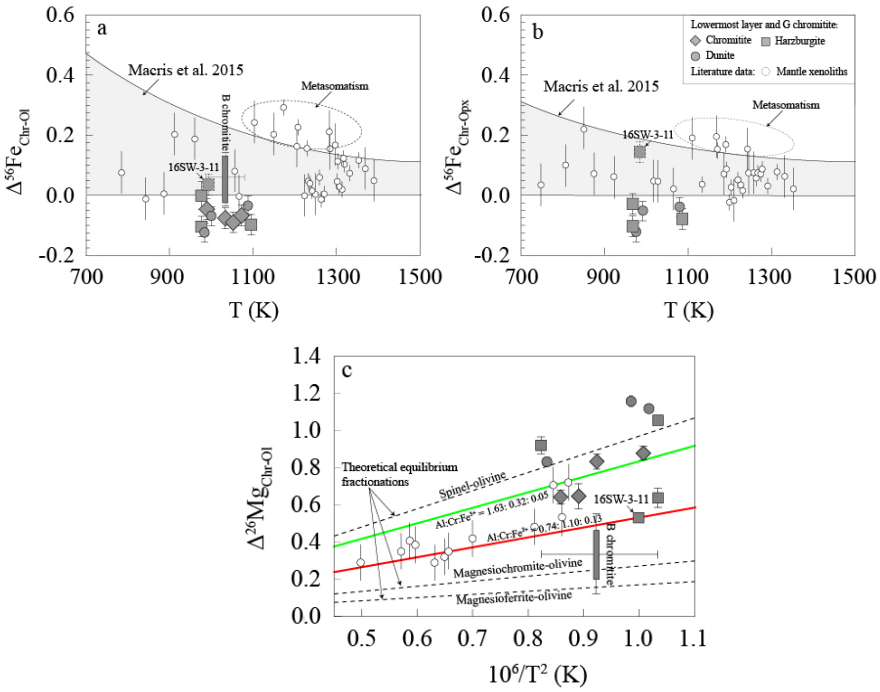

Figure 3.4 Calculated (a) chromite-olivine and (b) chromite-orthopyroxene equilibrium Fe isotope fractionation factors and (c) chromite-olivine equilibrium Mg isotope fractionation factors as a function of temperature in the Stillwater Complex, compared with samples from mantle peridotites (Young et al., 2009; Liu et al., 2011; Zhao et al., 2015, 2017). The gray fields in (a) and (b) and the dashed lines in (c) denote theoretical equilibrium isotope fractionations (Liu et al., 2011; Macris et al., 2015). The equilibrium temperature for these samples was calculated based on the olivine-spinel re-equilibration thermometer of Ballhaus (1993), and the calculation parameters reported in Appendix 10.1. Because fractionation factors for samples in the B chromitite cannot be directly calculated without silicate data, we used the average temperatures of other samples, and the lowest and highest temperatures are reported as estimated errors. The green line in panel (c) denotes the equilibrium fractionation factor for mantle peridotite samples (Liu et al., 2011), and the red line is that for the Peridotite Zone calculated based on the average chemistries of chromite in

selected samples (Table 3.2).

Table 3.2 Dominating metallic ions of chromite from the Peridotite Zone of the Stillwater Complex.

Sample	16SW-3-4	16SW-3-3	16SW-3-2	16SW-3-9	16SW-3-5	16SW-3-11	16SW-1-15	16SW-1-9	16SW-1-27	16SW-1-8
Ti^{4+}	0.017	0.017	0.015	0.016	0.014	0.016	0.017	0.012	0.012	0.011
Al^{3+}	0.823	0.807	0.842	0.788	0.841	0.713	0.788	0.78	0.765	0.718
Cr^{3+}	1.116	1.127	1.097	1.159	1.101	1.112	1.007	1.066	1.076	1.108
Fe^{3+}	0.026	0.028	0.030	0.021	0.029	0.140	0.169	0.131	0.134	0.153
Fe^{2+}	0.629	0.610	0.622	0.589	0.567	0.602	0.635	0.563	0.519	0.481
Mg^{2+}	0.377	0.396	0.381	0.415	0.435	0.402	0.370	0.436	0.481	0.519

Sample	16SW-1-26	16SW-2-21	16SW-2-12	16SW-2-4	16SW-2-17	16SW-2-8	16SW-2-14	16SW-2-13	16SW-2-15	16SW-2-6
Ti^{4+}	0.009	0.050	0.008	0.021	0.016	0.009	0.008	0.018	0.01	0.011
Al^{3+}	0.748	0.569	0.653	0.683	0.754	0.700	0.696	0.746	0.646	0.739
Cr^{3+}	1.107	0.968	1.149	1.036	1.083	1.154	1.170	1.062	1.183	1.040
Fe^{3+}	0.123	0.363	0.179	0.236	0.131	0.126	0.116	0.156	0.149	0.199
Fe^{2+}	0.463	0.750	0.545	0.670	0.516	0.506	0.483	0.487	0.429	0.463
Mg^{2+}	0.536	0.281	0.451	0.338	0.488	0.491	0.515	0.520	0.569	0.537

Based on the relative proportions of these three octahedral ions in our samples, a theoretical equilibrium $\Delta^{26}Mg_{Chr\text{-}Ol}$ value of about 0.56‰ at 1000 K is presented in Figure 3.4c, and the equilibrium $\Delta^{26}Mg_{Chr\text{-}Ol}$ line drawn. The $\Delta^{26}Mg_{Chr\text{-}Ol}$ values of olivine-chromite pairs in the G chromitite and Lowermost layer vary from 0.64 to 1.16‰ (Table 3.1; except for sample 16SW-3-11 with $\Delta^{26}Mg_{Chr\text{-}Ol} = 0.53 \pm 0.04$‰), deviating from the expected equilibrium inter-mineral fractionation value and thus indicating a disequilibrium kinetic fractionation (Teng et al., 2011; Sio et al., 2013; Oeser et al., 2015).

3.4 Diffusion-driven kinetic isotope fractionation

The systematic Fe-Mg isotopic variations in our samples reveal disequilibrium kinetic diffusion between silicates and chromite. Both thermal (Soret) and chemical diffusion are known to produce such large isotope fractionations. However, Soret diffusion preferentially enriches heavy isotopes down the thermal gradient (Richter et al., 2008, 2009; Huang et al., 2011), which would yield a positive correlation between $\delta^{56}Fe$ and $\delta^{26}Mg$. Furthermore, Soret diffusion is not a viable process at the mineral scale in large plutonic bodies (Chen et al., 2014, 2018). Therefore, the negative correlations of Mg and Fe isotopic compositions observed in olivine (Figure 3.5a), orthopyroxene (Figure 3.5b), and chromite (Figure 3.5c) requires disequilibrium Fe-Mg isotope fractionation and Fe-Mg substitution induced by chemical diffusion. In the following subsections, we investigate chemical diffusion scenarios capable of producing the observed disequilibrium kinetic fractionations.

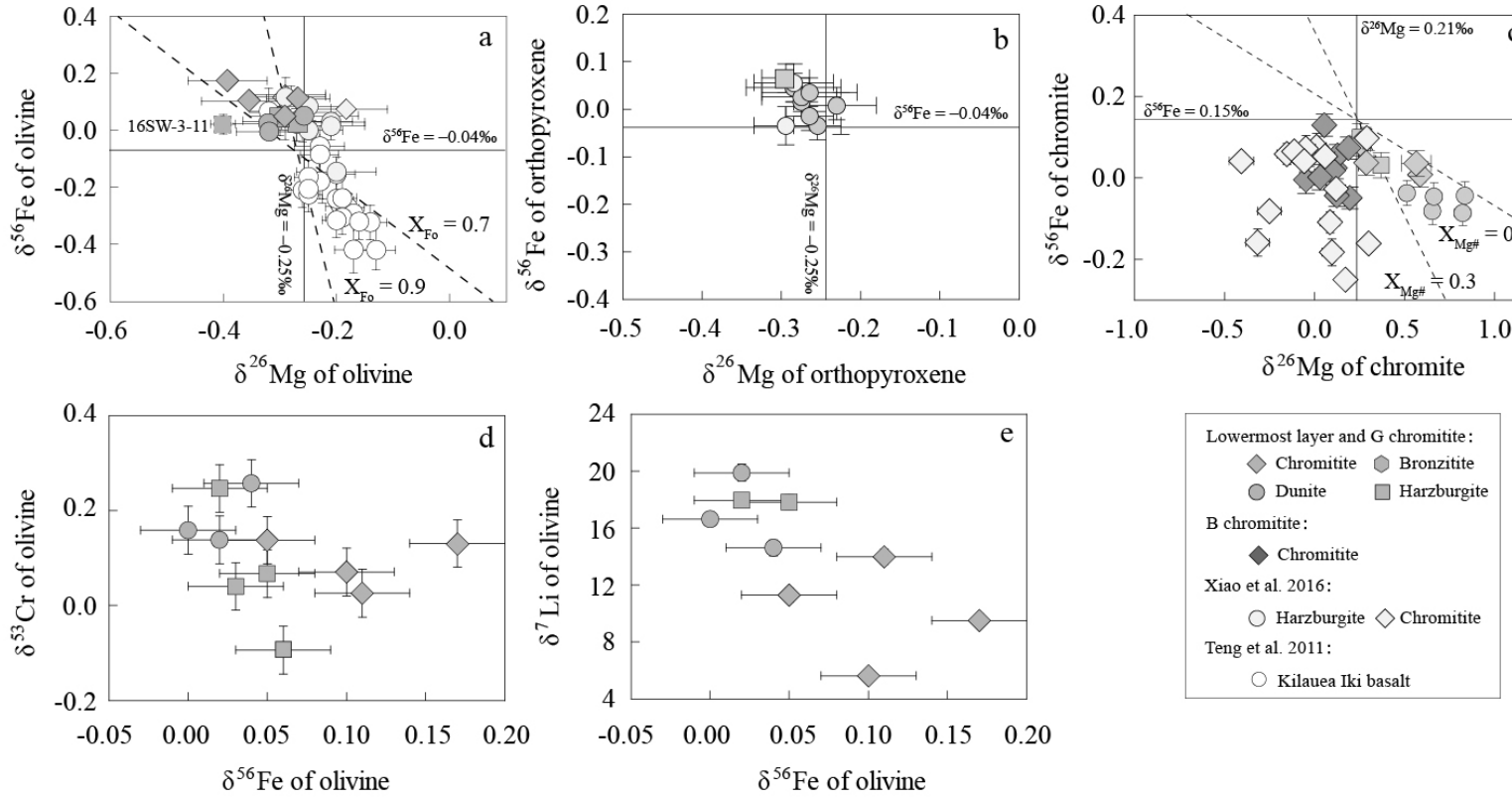

Figure 3.5 Fe-Mg isotope fractionations in (a) olivine, (b) orthopyroxene, and (c) chromite from the Peridotite Zone of the Stillwater Complex and from other literature data (Teng et al., 2011; Xiao et al., 2016). The data define linear relationships with slopes depending on the chemical compositions of the minerals. The straight lines in (a) and (b) represent $\delta^{26}Mg = –0.25‰$ and $\delta^{56}Fe = –0.04‰$ of olivine and orthopyroxene from mantle xenoliths (e.g., Liu et al., 2011; Macris et al., 2015; Zhao et al., 2015, 2017). The straight lines of $\delta^{56}Fe = 0.15‰$ in (c) represent spinel from mantle xenoliths, and $\delta^{26}Mg = 0.21‰$was calculated using the equilibrium inter-mineral fractionation factor $\Delta^{26}Mg_{Chr\text{-}Ol} = 0.46‰$ at 750 °C based the observed chromite compositions. Correlation diagrams of $\delta^{56}Fe$ versus (d) $\delta^{53}Cr$ (Bai et al., 2019) and (e) average $\delta^{7}Li$ (Su et al., 2020a) in olivine of the Peridotite Zone are also shown.

3.4.1 Diffusion between minerals and fluids/melts

Superimposed modifications of early-precipitated minerals by trapped interstitial liquids are known to generate diffusion-controlled re-equilibration (e.g., Barnes, 1986; Bell and Claydon, 1992; Bodreau, 2016; Baker and Boudreau, 2019) and isotopic kinetic fractionations (Bai et al., 2019; Su et al., 2020a). Trace elemental variations and elevated Li-Cr isotopic compositions of olivine in Peridotite Zone silicate cumulates have been demonstrated to be related to trapped liquid shifts (Bai et al., 2019; Su et al., 2020a). Taking into account that olivine and orthopyroxene in these silicate cumulates have Mg# values of 84–86, lower than those in chromitite samples (Figure 3.1; olivine Fo = 86–90; orthopyroxene Mg# = 87–91), upward-increasing liquids inherited from the overlying cumulate pile (Li et al., 2005) or wall rocks (Spandler et al., 2005) could have produced their decreased Mg# values. It may be argued that the observed Fe-rich chromite trends from chromitite (Mg# = 40–60) to silicate cumulates (Mg# = 30–40) also result from re-equilibration by trapped fluid shifts (Barnes, 1986; Scowen et al., 1991). However, the simultaneous inward replacement of Mg by Fe should produce cumulus minerals enriched in light Fe and heavy Mg isotopes, rather than the conjugate Fe-Mg isotopic variations shown in the stratigraphic profiles of Figure 3.1. The heavier Fe and lighter Mg isotopic compositions of silicates in our samples relative to equilibrated minerals in mantle xenoliths also suggest reverse Fe-Mg substitution trends (Figure 3.2; Liu et al., 2011; Macris et al., 2015; Zhao et al., 2015, 2017). In addition, negative correlations observed between Li and Fe isotopes and between Cr and Fe isotopes in olivine further confirm that the elevated olivine δ^{56}Fe values are controlled by different factors than those controlling Li and Cr isotopes (Figure 3.5d, e).

Cumulus phases may contact hotter, more primitive melts during magma replenishment (Oeser et al., 2015). This process is recognized in layered intrusions with rhythmic sequences that result from repeated injections of primitive magma (e.g., Raedeke and McCallum, 1984; Campbell and Murck, 1993; Yang and Seccombe, 1993). The basically within normal mantle ranging O isotopic compositions of olivine in silicate cumulates and chromitites (Su et al., 2020a; $\delta^{18}O_{Ol}$ = 4.91–5.72‰) also indicate

that frequent primitive magma injections could have modified the mineral isotopic compositions. The higher Mg and lower Fe contents of primitive melts (relative to evolved melts that equilibrated with cumulus minerals) could cause the inward replacement of Fe by Mg, with minerals becoming enriched in light Mg and heavy Fe isotopes (Oeser et al., 2015). Increased mixing proportions with primitive magmas than during preceding magmatic cycles may also generate similar elemental migrated trend, and higher Mg# of silicates in chromitite samples, in this case, might reflect more frequent injections and turbulence during their initial deposition. Nevertheless, the simultaneous inward replacement of Fe by Mg in all cumulus minerals contradicts the conjugate Fe-Mg isotopic variations observed in our stratigraphic profiles (Figure 3.1) and higher $\delta^{26}Mg$ in chromite than spinels in equilibrated mantle xenoliths (Figure 3.2). Because chromite contains less Mg than silicates, Mg isotopic decreases may be more pronounced in the former. Elevated $\Delta^{26}Mg_{Chr\text{-}Ol}$ values relative to the calculated inter-mineral Mg isotopic equilibrium line (Figure 3.4c) are also inconsistent with expected isotopic changes for this scenario.

Metasomatic and metamorphic processes may produce opposing elemental trends in silicates and chromite, leading to conjugate Fe-Mg isotopic variations. The most common mantle metasomatic processes could enrich ^{26}Mg and deplete ^{56}Fe in silicates (termed “normal zoning” by Oeser et al., 2015; Figure 3.5a, b) and deplete ^{26}Mg and enrich ^{56}Fe in spinel-group minerals (Figure 3.5c; e.g., Young et al., 2009, 2015; Dauphas et al., 2010; Teng et al., 2011; Pogge von Strandmann et al., 2011; Xiao et al., 2013; Sio and Dauphas, 2018). Such cation exchange reactions have been recently verified in mafic-ultramafic intrusions (Ceuleneer, 2004; Bai et al., 2018; Guotana et al., 2018; Ei Dien et al., 2019). Stillwater Complex was also subjected to a greenschist facies metamorphic event at 1.7 Ga, and heating associated with the metamorphic event would induce Fe and Mg inter-mineral diffusion in pyroxenes (McCallum et al., 2006). However, the isotopic variations in metasomatic mantle peridotites are opposite to those observed in our samples, with silicates depleted in ^{26}Mg and enriched in ^{56}Fe (Figure 3.5a, b) and chromites enriched in ^{26}Mg and depleted in ^{56}Fe (Figure 3.5c). Importantly,

such a diffusive process would produce increasing chromite-silicate Fe fractionation factors ($\Delta^{56}Fe_{Chr\text{-}Ol}$ and $\Delta^{56}Fe_{Chr\text{-}Opx}$) and decreasing Mg fractionation factors ($\Delta^{26}Mg_{Chr\text{-}Ol}$ and $\Delta^{26}Mg_{Chr\text{-}Opx}$). For example, Al-websterites in mantle xenoliths have relatively high $\Delta^{56}Fe_{Chr\text{-}Ol}$ and $\Delta^{56}Fe_{Chr\text{-}Opx}$ values (Figure 3.4a, b) and relatively low $\Delta^{26}Mg_{Chr\text{-}Ol}$ values (Figure 3.4c) reflecting metasomatism and mineral-melt diffusion. These trends are opposite to the low $\Delta^{56}Fe_{Chr\text{-}Ol}$ and $\Delta^{56}Fe_{Chr\text{-}Opx}$ values (Figure 3.4a, b) and high $\Delta^{26}Mg_{Chr\text{-}Ol}$ values (Figure 3.4c) observed in our samples.

3.4.2 Inter-mineral diffusion between silicates and oxides

After crystallization and subsequent modification by mineral-melt/fluid reactions, subsolidus inter-mineral diffusion is the most likely mechanism to have produced the observed mineral compositional changes (e.g., Chen et al., 2014, 2018; Xiao et al., 2016; Bai et al., 2019; Albert et al., 2019; Tian et al., 2019). Such elemental redistributions are known to produce kinetic isotope fractionations, and negative correlations between the Fe and Mg isotopic compositions of silicates and oxides have been reported in ophiolites (Xiao et al., 2016; Zhang et al., 2019) and other layered intrusions (Chen et al., 2014, 2018; Tian et al., 2019). Here, we explore the characteristics of ^{56}Fe enrichment and ^{26}Mg depletion in silicates (Figure 3.5a, b) and ^{56}Fe depletion and ^{26}Mg enrichment in chromite (Figure 3.5c), and demonstrate that inter-mineral diffusion might be the most important factor to consider when interpreting the major elemental evolution of minerals in layered intrusions.

Experimental studies have demonstrated that Fe^{2+}-Mg distribution coefficients between oxides and silicates ($K_d^{Ox\text{-}Sil} = [Fe/Mg]_{Ox}/[Fe/Mg]_{Sil}$) are temperature-dependent. For example, Ono (1983) empirically obtained $\ln(K_d^{Chr\text{-}Ol}) = 0.397/(T \times 10^4) - 0.832$, and Sato et al. (2008) empirically obtained $\ln(K_d^{Chr\text{-}Opx}) = 2.341/(T \times 10^4) - 1.134$. Therefore, if chromite that crystallized at high magmatic temperatures re-equilibrates at relatively low subsolidus temperatures, it tends to lose Mg to and extract Fe^{2+} from coexisting silicates (Ozawa, 1983, 1984; Dohmen and Chakraborty, 2007; Thakurta et al., 2008; Bai et al., 2017). Although intra-mineral re-equilibration can

obscure core-to-rim chemical zonings (Figure S9.2 in Appendix 9.1), higher average silicate and lower average chromite Mg# values induced by inter-mineral diffusion may be preserved (e.g., Jackson, 1961; Roeder et al., 1979; Wilson, 1982; Ozawa, 1983). Indeed, in our samples, olivine and orthopyroxene Mg# increase from 84–86 in silicate cumulates to 90 in chromite-rich cumulates, and chromite Mg# decrease from 60–40 in chromitites to 40–30 in silicate cumulates (Figure 3.1; Raedeke and McCallum, 1984; Campbell and Murck, 1993). The trends of cumulus mineral Mg# as a function of relative modal abundance (Figure 3.6) further indicate that Fe-Mg inter-mineral exchange plays an important role in controlling mineral compositions in cumulates of layered intrusions.

Isotopically, the negative correlations between δ^{26}Mg and δ^{56}Fe in cumulus minerals of the Stillwater Complex differ from the trends expected for mineral-melt/fluids reaction. Specifically, olivine Fe isotopic variations in chromitite (Figure 3.5a) and chromite Mg isotopic variations in silicate cumulates (Figure 3.5c) are more pronounced, in accordance with the dependence of Fe-Mg exchange on relative modal abundance (e.g., Ozawa, 1983, 1984; Bai et al., 2017), suggesting that inter-mineral diffusion produced the Fe and Mg disequilibrium kinetic fractionation observed in our samples. Otherwise, minerals present in higher modal percentages undergo less-extensive elemental re-equilibration, preserving relatively primary compositional and isotopic signatures (e.g., Xiao et al., 2016; Zhang et al., 2019).

In addition, although a 1:1 Fe-Mg substitution is typically assumed in crystal lattices, our samples show that inter-mineral diffusion significantly enriches ^{56}Fe in silicates and ^{26}Mg in chromite, and slightly depletes them in ^{26}Mg and ^{56}Fe, respectively (Figure 3.5a, c). These results imply that mineral Fe-Mg contents can also influence isotopic variations during diffusion (e.g., Roeder et al., 1979; Wilson, 1982; Ozawa, 1983). According to Dauphas et al. (2010), the δ^{56}Fe/δ^{26}Mg ratio roughly depends on the Mg# of chromite ($X_{Mg\#}$) or the Fo content in olivine (X_{Fo}) as (presented in the case of olivine):

$$\frac{\delta^{56}Fe}{\delta^{26}Mg} = -2 \times \left(\frac{M_{^{56}Fe} / M_{^{54}Fe} - 1}{M_{^{26}Mg} / M_{^{24}Mg} - 1} \right) \times \left(\frac{X_{Fo}}{1 - X_{Fo}} \right),$$

where M is the mass of the subscripted isotope. The slope of the correlation between δ^{56}Fe and δ^{26}Mg varies between –2.1 for X_{Fo} = 0.7 and –8.0 for X_{Fo} = 0.9 for olivine (Figure 3.5a), and between –0.89 for $X_{Mg\#}$ = 0.5 and –0.38 for $X_{Mg\#}$ = 0.3 for chromite (Figure 3.5c), further emphasizing the effect of mass balance on diffusion-driven isotope fractionations.

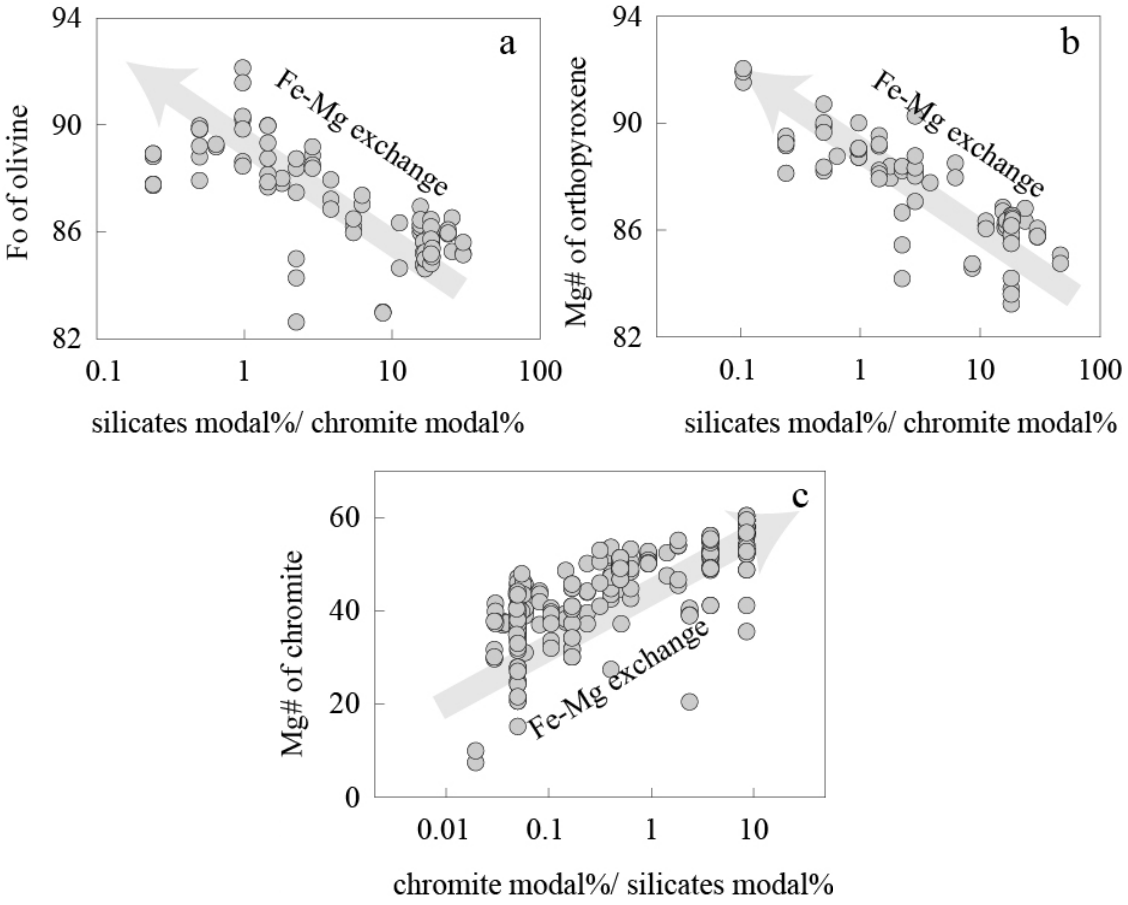

Figure 3.6 (a) Olivine Fo and (b) orthopyroxene and (c) chromite Mg# versus mineral modal percentage in all rock types of the Peridotite Zone of the Stillwater Complex. Arrows represent the expected Fe-Mg exchange trends between silicates and chromite, and the mineral modal ratios are cited from Bai et al. (2019).

3.5 Isotopic diffusion models

In the case of disequilibrium Fe and Mg isotope fractionation between silicates

and chromite generated by inter-mineral diffusion, Fe-Mg isotopic variations should covary with mineral-specific Fo or Mg# values, and can be quantitatively modeled (e.g., Oeser et al., 2015; Collinet et al., 2017; Tian et al., 2019). In this section, we use our olivine and chromite data to develop an isotopic diffusion model to reproduce the observed isotopic variations. In addition, the empirical fractionation factor β of each element depends on the diffusion medium (Richter et al., 2009). Although they were first determined to be about $\beta_{Fe} = \beta_{Mg} = 0.05$ in Fe and Mg diffusion experiments in silicate melts (Richter et al., 2008, 2009), the values remain debated for inter-mineral diffusion between olivine and chromite. The results of our model will be used to estimate β_{Fe} and β_{Mg}, thus furthering our understanding of inter-mineral diffusion mechanisms.

We modeled the diffusive exchange of Fe and Mg between cumulus minerals using a modified version of the Mathematica code developed by Bai et al. (2019) and Tian et al. (2019) and the diffusion equation of Richter et al. (1999, 2003). We varied the diffusion coefficients (D, m^2/s) as a function of the molar fraction of FeO or MgO (C) in minerals, the position (r) along profiles within grains, and time (t) as:

$$\frac{\partial C(r,t)}{\partial t} = \frac{\partial D}{\partial r} \cdot \frac{\partial C(r,t)}{\partial r} + D\frac{\partial^2 C(r,t)}{\partial r^2},$$

where the crystal center is at $r = 0$ and the interface between olivine and chromite is set at the maximum diffusion length ($r = a$) as restricted by the grain size distributions of olivine and chromite. The mole fraction of FeO or MgO in silicates was varied from the initial concentration before subsolidus exchange at the crystal center, $C_0 = C(0, t)$, to the equilibrated concentration at the crystal rim, $C_a = C(a, t)$.

The initial compositions (C_0) represent the original liquidus chemistry of olivine and chromite. We therefore selected the lowest observed olivine Fo value in harzburgite (82.5; Figure 3.7a) and the highest chromite Mg# in massive chromitite (60; Figure 3.7b) as primitive chemical compositions. The selected olivine has also a Li-Cr isotopic composition similar to the bulk silicate Earth (Bai et al., 2019; Su et al., 2020a). Accounting for the importance of rock type in inter-mineral diffusion, we also

developed an elemental diffusion model based on the relative modal abundances and diffusive proportions (Figure 3.7). Comparison between the model curves and sample compositional ranges constrain the largest degrees of Fe-Mg exchange (C_a). In silicate cumulates (chromite:silicates = 10:90), the diffusion of about half of the chromite Mg content into silicates (Figure 3.7a) would decrease chromite Mg# values to about 30 and only marginally affect silicates Mg#. Conversely, in massive chromitite (chromite:silicates = 10:90), the diffusion of about half of the silicates Fe content into chromite (Figure 3.7b) would increase silicates Mg# values to ~90 and only marginally affect chromite Mg#. These two cases encompass the maximum observed isotopic variations in olivine and chromite (Figure 3.7).

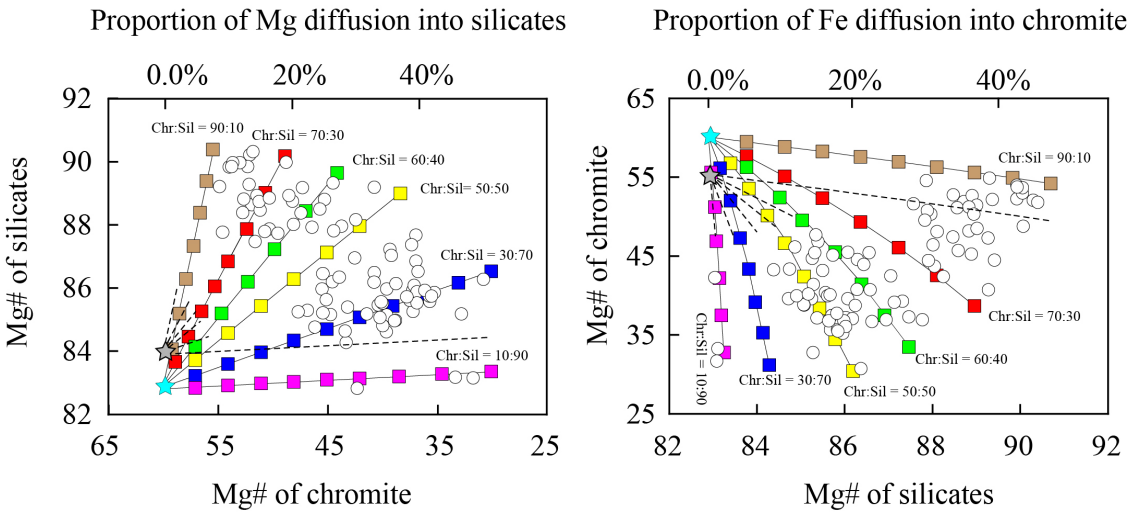

Figure 3.7 Modeling the effect of Fe-Mg exchange on (a) chromite Mg# and (b) silicates Mg. Solid lines are modeled exchanges between different proportions of chromite relative to silicates (Chr:Sil, representing different lithologies), and the square symbols along the lines indicate different proportions of (a) Mg diffusion from chromite to silicates and (b) Fe diffusion from silicates to chromite. White circles are chromite Mg# and silicate Mg# pairs in our samples from the Peridotite Zone, and the cyan stars are the most extreme values observed in our samples, with olivine Fo = 82.5 (harzburgite) and chromite Mg# = 60 (massive chromitite). The gray stars and dashed lines represent (a) higher silicate Mg# and (b) lower chromite Mg# values, respectively, cannot account for all sample compositions.

Based on the initial and equilibrated concentrations (C_0 and C_a, respectively), we could associate the diffusion time (t) with the diffusion length (r). Previous studies and our observations (Figure S9.2 in Appendix 9.1) suggest that olivine grain sizes are 1.0–2.0 mm in silicate cumulates and 1.5–3.0 mm in chromite-bearing cyclic units (Jackson, 1961; Raedeke and McCallum, 1984). Chromite grain sizes are relatively uniform in silicate cumulates, typically from 0.1 to 0.3 mm. Therefore, in our model, we selected the maximum diffusion radii to be a_{Ol} = 1.5 mm and a_{Chr} = 0.15 mm to generate the longest reasonable diffusion time (t) and the most obvious isotopic variations.

Diffusion coefficients are temperature dependent, following an Arrhenius behavior, and become exponentially smaller with decreasing temperature as (Buening and Buseck, 1973; Freer, 1981; Liermann and Ganguly, 2002):

$$D = D_0 \exp\left(-E / RT\right),$$

where D_0 is the diffusion constant, E the activation energy, R the gas constant, and T temperature (K). Considering that Fe-Mg diffusion is anisotropic, and that E and D_0 are crystallographically dependent, we selected average values of E and D_0 parallel to the a- and c-axial directions. We used chromite data from Vogt et al. (2015): E = 139 ± 18 kJ/mol and $\log_{10}D_0$ = –12.33 ± 0.85 m^2/s. For olivine, experimental studies have shown that Fe-Mg diffusion coefficients further depend on pressure (P), oxygen fugacity (fO_2), and olivine composition (X_{Fe}, the mole fraction of fayalite in olivine) (e.g., Dohmen et al., 2007; Dohmen and Chakraborty, 2007; Costa et al., 2008), and can be calculated as:

$$D_{Fe-Mg} = 10^{-9.21} \cdot \left(\frac{fO_2}{10^{-7}}\right)^{1/6} \cdot 10^{3(X_{Fe}-0.1)} \cdot \exp\left(-\frac{201000 + \left(P - 10^5\right) \cdot 7 \cdot 10^{-6}}{RT}\right).$$

We set the intensive properties (P, fO_2, and T) in our model based on previous studies of the Stillwater Complex (e.g., Hess, 1972; Selkin et al., 2008; McCallum et al., 2006; Bai et al., 2019), and detailed parameter selection and calculation process are presented in Appendix 10.1.

For simplicity, we assumed a 1:1 Fe-Mg substitution, as Mg-Mn and Fe-Ni

substitutions are negligible (Tian et al., 2019). In this case, the ratio of the isotopic diffusion coefficients follows a modified version of Graham's law, and is directly related to atomic mass as (Richter et al., 1999):

$$\frac{D_1}{D_2} = \left(\frac{M_2}{M_1}\right)^{\beta},$$

where D_1 and D_2 are the diffusivities and M_1 and M_2 the masses of the two analyzed isotopes of Fe (^{54}Fe and ^{56}Fe, respectively) or Mg (^{24}Mg and ^{26}Mg, respectively). Sio et al. (2013) fit diffusion-generated Fe-Mg chemical and isotopic zonings in olivine using $\beta_{Fe} = 0.27 \pm 0.04$ and $\beta_{Mg} = 0.16 \pm 0.05$. Oeser et al. (2015) estimated lower mean values of $\beta_{Fe} = 0.161$ and $\beta_{Mg} = 0.084$, consistent with the ratio $\beta_{Fe}/\beta_{Mg} \approx 2$ estimated by Van Orman and Krawczynski (2015). Although β values for chromite have never been reported, those of ilmenite with analogous lattice structures are similar to those of olivine. Therefore, we adopted trial values of $\beta_{Fe} = 0.05$, 0.16, and 0.27 and $\beta_{Mg} = 0.03$, 0.08, and 0.16 to estimate the most suitable fractionation factors in our model. These quantitative calculations were computed using Mathematica.

Our model results are plotted as binary δ^{56}Fe and δ^{26}Mg variation diagrams in chromite (Figure 3.8a) and olivine (Figure 3.8b). Most of our analytical data plot within the modeled field, confirming that the observed heavy Fe and light Mg isotopic compositions of olivine and the conjugate isotopic variations in chromite were produced by diffusion-driven kinetic isotope fractionations. The model best fits the observed data for olivine that underwent protracted cooling and inter-mineral diffusion in the layered intrusion when $\beta_{Fe} \approx 0.27$ and $\beta_{Mg} \approx 0.016$ (Figure 3.8a), whereas lower values of $0.03 < \beta_{Fe} < 0.08$ and $0.05 < \beta_{Mg} < 0.16$ fit the modeled chromite curves (Figure 3.8b), possibly reflecting higher D_{Chr} than D_{Ol} values (Vogt et al., 2015). We emphasize that, absent well-constrained isotopic diffusion profiles through the minerals, these values are not unique. Variable boundary environments and more detailed in-situ isotopic analyses would provide further quantitative constraints on the fractionation factor β and the Fe-Mg inter-mineral diffusion process.

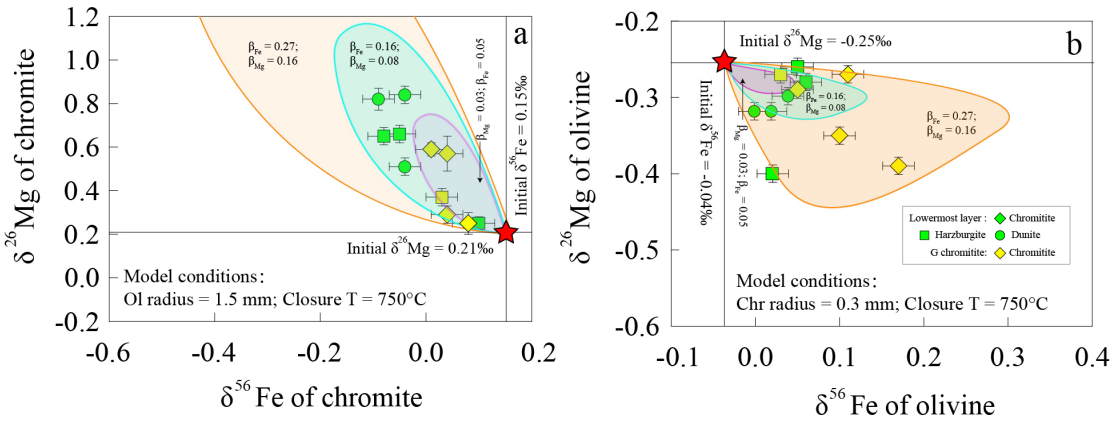

Figure 3.8 Expected variations of (a) chromite and (b) olivine Fe and Mg isotopic compositions as a function of the isotope fractionation factor *β*. Red stars represent the initial isotopic compositions of each mineral. The initial Fe isotopic compositions of chromite and olivine are derived from minerals in equilibrium with mantle peridotite ($\delta^{56}Fe_{Chr}$ = 0.15‰ and $\delta^{56}Fe_{Ol}$ = –0.04‰; Liu et al., 2011; Macris et al., 2015; Zhao et al., 2015, 2017). The initial Mg isotopic composition of olivine is taken as the value of the mean mafic Earth ($\delta^{26}Mg$ = –0.25 ± 0.07‰; Teng et al., 2010), and the initial $\delta^{26}Mg_{Chr}$ = 0.21‰ was calculated using the equilibrium inter-mineral fractionation factor $\Delta^{26}Mg_{Chr\text{-}Ol}$ = 0.46‰ at 750 °C based the observed chromite compositions.

3.6 Plausible Fe-Mg isotope fractionation scenario for the B chromitite

Notably, chromite in the B chromitite of the Stillwater Complex and chromitite from the Luobusa ophiolite plot away from the negative $\delta^{56}Fe$-$\delta^{26}Mg$ trend defined by our samples from the G chromitite and Lowermost layer (Figure 3.5c; Xiao et al., 2016). Furthermore, the inter-mineral isotope fractionation factors of chromite in the B chromitite are distinct from those in other layers. Although we were unable to separate olivine and orthopyroxene in the B chromitite (see section 3.1.2 and Figure 9.1 in Appendix 9.1), we calculated their approximate inter-mineral Fe-Mg isotope fractionation factors as follows. Based on the average olivine Mg isotopic compositions of our samples ($\delta^{26}Mg_{Ol}$ = –0.29‰), the chromite-olivine Mg isotope fractionation factors in the B chromitite range from 0.24 to 0.49‰, well below the calculated equilibrium inter-mineral fractionation line. Even compared to the lightest olivine

δ^{26}Mg values in our samples, inter-mineral Mg isotope fractionation factors in the B chromitite vary from 0.45 to 0.60‰ (Figure 3.4c), slightly below the equilibrium inter-mineral isotope fractionation line. The $\Delta^{56}Fe_{Chr\text{-}Ol}$ values in the B chromitite similarly calculated using the average olivine δ^{56}Fe value in our samples ($\delta^{56}Fe_{Ol}$ = 0.06‰) range from –0.11 to 0.07‰, markedly higher than the $\Delta^{56}Fe_{Chr\text{-}Ol}$ values in other layers (Figure 3.4a). These results indicate that different factors controlled inter-mineral Fe-Mg isotope fractionation in the B chromitite.

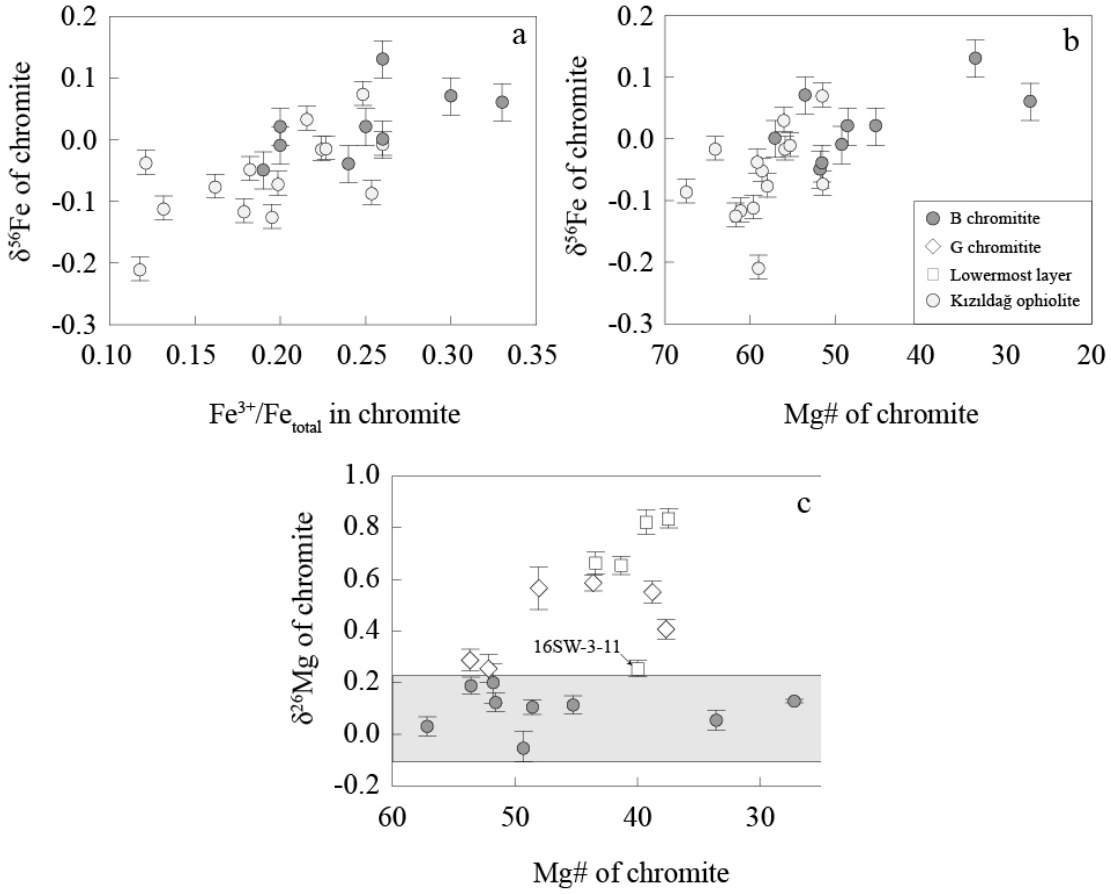

Figure 3.9 Correlation diagrams of the Fe isotopic compositions of chromite in the B chromitite of the Peridotite Zone versus (a) $Fe^{3+}/\sum Fe$ and (b) Mg#, and the Mg isotopic compositions of chromite versus (c) Mg#. Chromite data from the Kizildag ophiolite in (a, b) are from Chen et al. (2015), and the shaded area in (c) indicates the limited Mg isotopic variations in chromite of the B chromitite.

The Fe-Mg isotopic compositions of serpentine should likely be the same as those of the minerals they were altered from (e.g., Scott et al., 2017; Liu et al., 2017). The $\Delta^{26}Mg_{Chr-Ol}$ values of chromite in the B chromitite plot below the calculated equilibrium inter-mineral isotope fractionation line (Figure 3.4c), which may be related to metasomatic in mental xenoliths (Figure 3.4c; Pogge von Strandmann et al., 2011; Young et al., 2009, 2015) and metamorphic processes as discussed in section 5.2.1. The flowing metamorphic fluid orientatedly traverses olivine and chromite, as well as the hydrous phlogopite and clinopyroxene residual may provide us the evidence (Figure S9.1 in Appendix 9.1). Positive correlations between $\delta^{56}Fe$ and $Fe^{3+}/\sum Fe$ (Figure 3.9a) or Mg# (Figure 3.9b) might also suggest a possible influence of metamorphic event on the Fe^{3+} enrichment (Evans and Frost, 1976; McCallum et al., 2006) and isotopic variations of chromite in the B chromitite (Polyakov and Mineev, 2000; Polyakov et al., 2007).

Alternatively, the lighter and constant $\delta^{26}Mg$ (Figure 3.9c; Su et al., 2017; 2019) and variable $\delta^{56}Fe$ (Weyer et al., 2005; Teng et al., 2007, 2008; Dauphas et al., 2010; Bilenker et al., 2017) values of chromite from the B chromitite may indicate the results of equilibrium magmatic differentiation. Open-system magmatic differentiation has been shown to result in more oxidizing conditions higher chromite $Fe^{3+}/\sum Fe$ values (Teng et al., 2008; Zhao et al., 2010; Sossi et al., 2012). Particularly, heavy Fe isotopes are preferentially partitioned into chromite with higher $Fe^{3+}/\sum Fe$ (Figure 3.9a), as reported for ophiolitic samples (Chen et al., 2015). Parameters indicating magmatic differentiation, such as chromite Mg#, are also positively correlated with $\delta^{56}Fe$ in chromite from the B chromitite (Figure 3.9b). Fractional crystallization and accumulation of chromite may explain the isotopically light Mg, instead of the metamorphic process (Figure 3.9c; Su et al., 2017; 2019). Such a mechanism requires that the Fe-Mg isotopic compositions of chromite in the B chromitite represent initial equilibrium isotopic compositions unaffected by subsolidus inter-mineral kinetic fractionation. This would mean that the serpentinization of the silicates must have occurred before the subsolidus stage (Su et al., 2020b), as suggested by the distinct

grain boundaries between serpentinized silicates and fresh chromite grains (Figure S9.1 in Appendix 9.1; Nunes and Tilton, 1971). Anyway, in the absence of reliable isotopic information on coexisting silicates, we cannot exclude other factors to explain why the Fe-Mg isotopic systematics of chromite in the B chromitite differ from those of the adjacent units.

4. Diffusion-driven chromium isotope fractionation in minerals of ultramafic cumulates: elemental and isotopic evidence from the Stillwater Complex.[2]

[2] This chapter is published in Geochimica and Cosmochimia Acta - Bai, Y., Su, B.X., Xiao, Y., Cui, M.M., Charlier, B., 2021. Magnesium and iron isotopic evidence of inter-mineral diffusion in ultramafic cumulates of the Peridotite Zone, Stillwater Complex. Geochimica et Cosmochimica Acta 292, 152-169.

Olivine and pyroxene are the most common silicate minerals in the lithospheric mantle (generally up to >90%), commonly coexisting with chromite in mafic-ultramafic complexes such as layered intrusions and ophiolites, the major hosts of Cr resources on Earth. The kinetics of Cr volume diffusion in olivine (Ito and Ganguly, 2006; Jollands et al., 2017), pyroxene (Ganguly et al., 2007), and chromite (Suzuki et al., 2008; Posner et al., 2016) have been well-documented. Cr diffusion kinetics can yield timescales of magmatic processes and can be used to determine the closure temperatures of the ^{53}Mn-^{53}Cr radiogenic dating system (e.g., Ito and Ganguly, 2006; Ganguly et al., 2007). However, the diffusive behavior of Cr between mineral and melt (mineral to melt or vice versa), the extent of reequilibration, and isotopic fractionations during diffusion are poorly documented. Indeed, both increasing and decreasing core-to-rim Cr zonation patterns have been observed in silicate minerals (Milman-Barris et al., 2008; Foley et al., 2011; Prelević et al., 2013; Bai et al., 2018). The diffusion of Cr from melt to coexisting silicate minerals is supported by observed concentration gradients in minerals (e.g., Drake et al., 1989; Ohtani et al., 1989), whereas the opposite case is supported by silicate-melt Cr partition coefficients that decrease with decreasing temperature or pressure (e.g., Herzberg and O'Hara, 2002).

Recently, high-precision Cr isotopic analytical techniques have been developed using the double-spike method, thermal ionization mass spectrometry (TIMS), and multicollector inductively coupled plasma mass spectrometry (MC-ICP-MS) (see review by Qin and Wang, 2017), revealing that significant Cr isotopic fractionations occur during high-temperature geological processes. Farkaš et al. (2013) and Shen et al. (2015) first observed that mantle-derived chromite grains were isotopically heavier than the average bulk silicate earth (BSE) and ultramafic rocks, suggesting a potential Cr isotopic fractionation during chromite crystallization. Xia et al. (2015) reported significant Cr isotopic variations among globally distributed mantle peridotite xenoliths and Hawaii basalts, implying that Cr isotopes are fractionated during mantle partial melting and metasomatism. Bonnand et al. (2016) observed considerable Cr isotope fractionation in lunar basalts, which they interpreted as resulting from the

crystallization of pyroxene and spinel. Finally, Shen et al. (2018) revealed inter-mineral equilibrium Cr isotopes fractionations in mantle xenoliths.

This study aims to determine the relative role of equilibrium and diffusion-driven fractionations in producing Cr isotopic variations based on new data from ultramafic cumulates of the Stillwater Complex. Large layered mafic-ultramafic intrusions represent critical links in the differentiation of basaltic magma derived by partial melting of the mantle (Helz, 1995), and are expected to show undifferentiated stable isotopic compositions (e.g., Liu et al., 2014; Chen et al., 2014, 2018). Compared to other mafic-ultramafic rock suites, the evolution and differentiation of large layered intrusions are stratigraphically well defined (e.g., Maier et al., 2012; Charlier et al., 2015; Jenkins and Mungall, 2018). Mineral compositional variations are well documented; they are predominantly controlled by fractional crystallization and are modified by reequilibration with trapped liquids and subsolidus elemental diffusion (Jackson, 1961; Roeder et al., 1979; McCallum, 1996). Therefore, silicate minerals in layered intrusions are suitable for studying diffusion-driven stable isotopic fractionations (e.g., Liu et al., 2014; Chen et al., 2014, 2018).

Here we present Cr elemental zoning profiles and isotopic compositions in silicate mineral separates (olivine and orthopyroxene) from the Stillwater Complex, one of the most representative large layered intrusions with world-class chromium deposits (Hess and Smith, 1960; Jackson, 1961; McCallum, 1996). We also analyzed the Cr isotopic compositions of chromite separates to explore the factors controlling inter-mineral Cr isotope fractionation. Finally, we use the elemental and isotopic variations induced by Cr diffusion to constrain the cooling timescale of the Peridotite Zone of the Stillwater Complex.

4.1 Sample and analytical methods

4.1.1 Samples selected

Samples analyzed in this study were collected from the Peridotite Zone of the Ultramafic Series. Fourteen samples, including poikilitic harzburgite and different

types of chromitites, were collected from the cyclic chromitite units of seams B and G in the Benbow area and Mountain View, and seven samples, including dunite, granular harzburgite, and bronzitite, were collected from the un-mineralized lowermost cyclic unit in the Gish area.

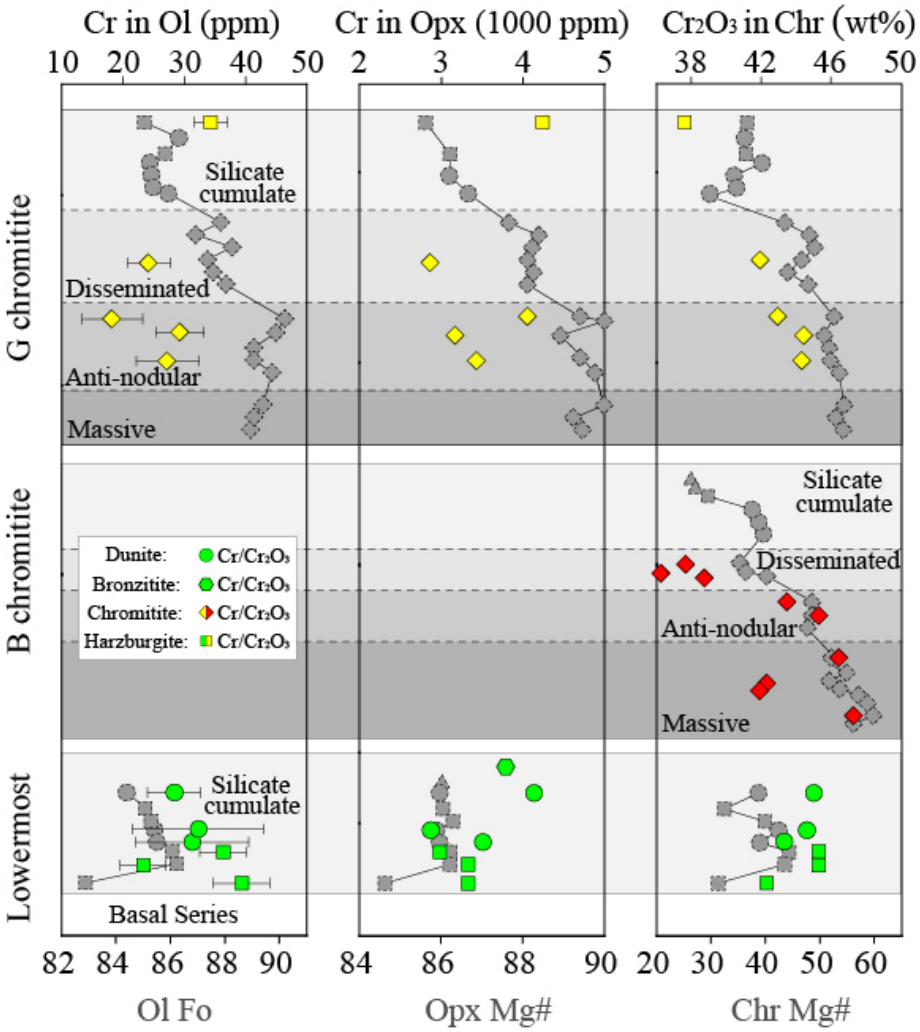

Figure 4.1 Variations of Cr content in olivine and orthopyroxene, and Cr_2O_3 content in chromite. Gray symbols with dashed lines represent the corresponding Fo composition of olivine and Mg# [$Mg^{2+}/(Mg^{2+} + Fe^{2+})$] of orthopyroxene and chromite (see Table S11.1).

Chromite grains in massive and anti-nodular chromitites have the greatest MgO (10.1–12.7 wt%) and Cr_2O_3 contents (42.4–48.6 wt%) and the lowest Al_2O_3 (16.2–20.5 wt%) and FeO contents (21.1–27.3 wt%). Conversely, chromite grains in silicate-dominated cumulates have the greatest Al_2O_3 (17.7–22.6 wt%) and FeO contents (22.1–

40.0 wt%) and the lowest MgO (6.93–10.2 wt%) and Cr_2O_3 contents (35.7–46.8 wt%) (Campbell and Murck, 1993). The most magnesian olivine ($Fo_{87.8–89.9}$) and orthopyroxene ($Mg\#_{88.2–90.0}$) occur in massive and anti-nodular chromitites, whereas more Fe-rich olivine ($Fo_{82.8–86.4}$) and orthopyroxene ($Mg\#_{84.6–86.8}$) occur in the silicate-dominated cumulates (e.g., Jackson, 1961; Raedeke and McCallum, 1984; McCallum, 1996; Figure 4.1). The high Mg# of silicates in the massive and anti-nodular chromitites have been suggested to result from significant elemental diffusion between the silicate minerals and chromite, with Mg diffusing from chromite to silicate minerals and Fe diffusing from silicate minerals to chromite (Jackson, 1961; Roeder et al., 1979). As the effect of elemental diffusion depends on the modal mineral abundances of the rock (Xiao et al., 2016; Bai et al., 2017, 2018), chromites in silicate cumulates and silicate minerals in massive and anti-nodular chromitites are expected to have been the most affected.

4.1.2 Chromium elemental analysis

Selected samples were prepared as 30-μm-thick polished and carbon coated thin sections. The major element compositions of chromite, orthopyroxene, and olivine, as well as Cr_2O_3 profiles in chromite and orthopyroxene, were determined by wavelength-dispersive spectrometry (WDS) using a JEOL JXA8100 electron probe at the State Key Laboratory of Lithospheric Evolution, Institute of Geology and Geophysics, Chinese Academy of Sciences, Beijing, China. Analyses were performed with an accelerating voltage of 15 kV, 12 nA beam current, 5 μm beam spot size, 10–30 s dwell time, and 11 mm working distance. A LIFH crystal was used for Cr, Mn, Fe, and Ni analyses, a PETJ crystal for K, Ca, and Ti, and a TAP crystal for Na, Mg, Al, and Si. Standards used were albite for Na, diopside for Si, Ca, and Mg, hematite and synthetic Cr_2O_3 for Cr, synthetic TiO_2 for Ti, orthoclase for K, synthetic Al_2O_3 for Al, synthetic MnO for Mn, and synthetic NiO for Ni. K(α) lines were selected for analysis, and detection limits were within ~0.008–0.02 wt% (1σ). Concentration profiles were obtained at 10–15 μm increments. Matrix effects were corrected by a program based on the ZAF procedure.

The bulk Cr concentrations and core-to-rim Cr concentration profiles of olivines were determined via laser ablation ICP-MS (LA-ICP-MS) using a 193 nm Coherent COMPex Pro ArF Excimer laser coupled to an Agilent 7500 ICP-MS at the Institute of Geology and Geophysics, Chinese Academy of Sciences, Beijing, China. Prior to analysis, thin sections were treated with 3% HNO_3 followed by de-ionized water and ethylene to remove the carbon coating. We used an approach similar to that of Wu et al. (2018), and isotopes were measured in peak-jumping mode with a repetition rate of 6 Hz. To correct for time-dependent data drift, standards were analyzed after every eight sample analyses. We used ^{53}Cr to determine Cr contents. Spectral interferences for ^{53}Cr are mainly from plasma and atmospheric gases (e.g., Ar, O_2, H_2); thus, each analysis was followed by a 20-s gas-blank measurement and these interferences were effectively corrected by gas-blank subtraction. Because of the relatively low abundance of Cr in olivine, we used a relative large laser diameter of 80 μm to achieve a sufficiently intense ^{53}Cr signal. The laser energy density was ~5 J/cm^{-2}. Helium was used as the ablation gas to improve the transport efficiency of the ablated aerosols. National Institute of Standards and Technology (NIST) reference materials NIST610 and NIST612 (GeoReM: http://georem.mpch-mainz.gwdg.de/) were used as external standards to produce calibration curves. Calibration was performed using NIST612 as an external standard, and the Mg contents of olivine served as internal standards. Off-line data processing was performed using GLITTER 4.0 (Griffin, 2008). The accuracies of Cr and other trace element contents were better than 5% (1 RSD) with a precision of 10%.

The average Cr concentrations of orthopyroxene and olivine and the Cr_2O_3 contents of chromite in each sample, are reported in Table 4.1, and the other major element compositions of these minerals and compositional profiles are provided in the Appendix 10.

4.1.3 Chromium isotopic analysis

Cumulate rocks were crushed to ~250–400 μm and fresh mineral grains were handpicked under a binocular microscope. We followed the dissolution procedure described in detail by Qin et al. (2010) and briefly summarized here. Olivine and orthopyroxene separates were dissolved overnight in capped Savillex beakers by a mixture of HF, HCl, and HNO_3 at 130 °C on a hot plate in a laminar flow exhaust hood. Chromite separates were ground to a very fine powder and dissolved in concentrated 3:1 HF-HNO_3 in a microwave oven at increasing temperatures of 180, 210, 220, and 225 °C at half hour intervals. After complete digestion, the Cr concentrations of the sample solutions were analyzed by ICP-MS to ensure that sample aliquots containing 1 μg Cr could be prepared and mixed with a 1 ml ^{50}Cr-^{54}Cr double spike (^{50}Cr and ^{54}Cr concentrations of 2.716 and 1.742 nmol/g, respectively). The detailed double spike procedure was reported in Han et al. (2012). The sample-spike mixture was dried completely, mixed with 0.2 ml 6 N HCl, and heated at 130 °C for 2–3 h before chromatographic separation by a two-step cation exchange chromatography procedure (Qin et al., 2010) using Bio-Rad 200–400 mesh AG50-X8 resin in both columns. Procedural blanks were generally less than 3 ng, which was negligible in all cases.

Chromium isotopic analyses of mineral separates were performed using a Thermo-Fisher Neptune Plus MC-ICP-MS at the CAS Key Laboratory of Crust-mantle Materials and Environments, University of Science and Technology of China, Hefei. The medium- to high-resolution modes were used during analyses of chromium isotopes ($5{,}500 < \Delta M/M < 11{,}000$, Bonnand et al., 2016) to resolve polyatomic interferences, and the desolvator was operated with only Ar gas (i.e., without the addition of N_2) to minimize polyatomic interferences from $^{40}Ar^{14}N^+$ and $^{40}Ar^{16}O^+$. During each analytical session, the spiked internal standard (SCP) was analyzed after every four to five sample analyses to ensure instrumental stability. Most samples were analyzed two or more times during a single analytical session. The reported uncertainties for individual sample analyses are conservatively defined as the largest of the 2SD uncertainties of replicate sample measurements, the 2SD uncertainties of replicate standard measurements in the same session, or the long-term reproducibility

of the peridotite standard JP-1. Chromium isotopic data are expressed relative to NIST standard reference material (SRM) 979 as $\delta^{53}Cr$ [‰] = $[(^{53}Cr/^{52}Cr)_{sample}/(^{53}Cr/^{52}Cr)_{SRM\ 979} - 1] \times 1{,}000$. The spiked NIST SRM 3112a was analyzed at the beginning of each session; we obtained an average $\delta^{53}Cr$ value of –0.09 ± 0.03‰ (*n* = 9, 2SD), consistent with the value of –0.07 ± 0.05‰ reported by Schoenberg et al. (2008). The average Cr isotopic composition of peridotite standard JP-1 (–0.11 ± 0.03‰, *n* = 9) was also in agreement with published values (–0.13 ± 0.02‰; Bonnand et al., 2016).

4.2 Results

4.2.1 Elemental Cr concentrations

Average olivine Cr concentrations per sample range from 18 to 39 ppm (Table 4.1), and olivine grains from silicate cumulates commonly have lower Cr contents than those from chromitites (Figure 4.1). Average orthopyroxene Cr concentrations per sample are higher than those of olivine, ranging from 2,778 to 4,239 ppm (Table 4.1), and are not distinguishable based on lithology (Figure 4.1). Systematic Cr content variations were observed in profiles traversing silicate minerals. Olivine Cr contents are highest in their cores (~60 ppm) and decrease to ~20 ppm near their rims (Figure 4.2a, b). The Cr concentrations of orthopyroxene grains similarly decrease by up to a factor of two from their cores (4,970 and 4,620 ppm in samples 16SW-3-3 and 16SW-3-5, respectively) toward their grain boundaries (2,690 and 2,440 ppm, respectively; Figure 4.2b). Average chromite Cr_2O_3 contents per sample vary markedly from 36.8 to 47.8 wt% (Table 4.1), with the highest values observed in massive chromitites and the lowest in silicate cumulates (Figure 4.1), consistent with previous studies (e.g., Campbell and Murck, 1993). Chromite Cr_2O_3 concentration profiles are homogenous in each sample, with variations commonly less than 1 wt% (Table S11.2).

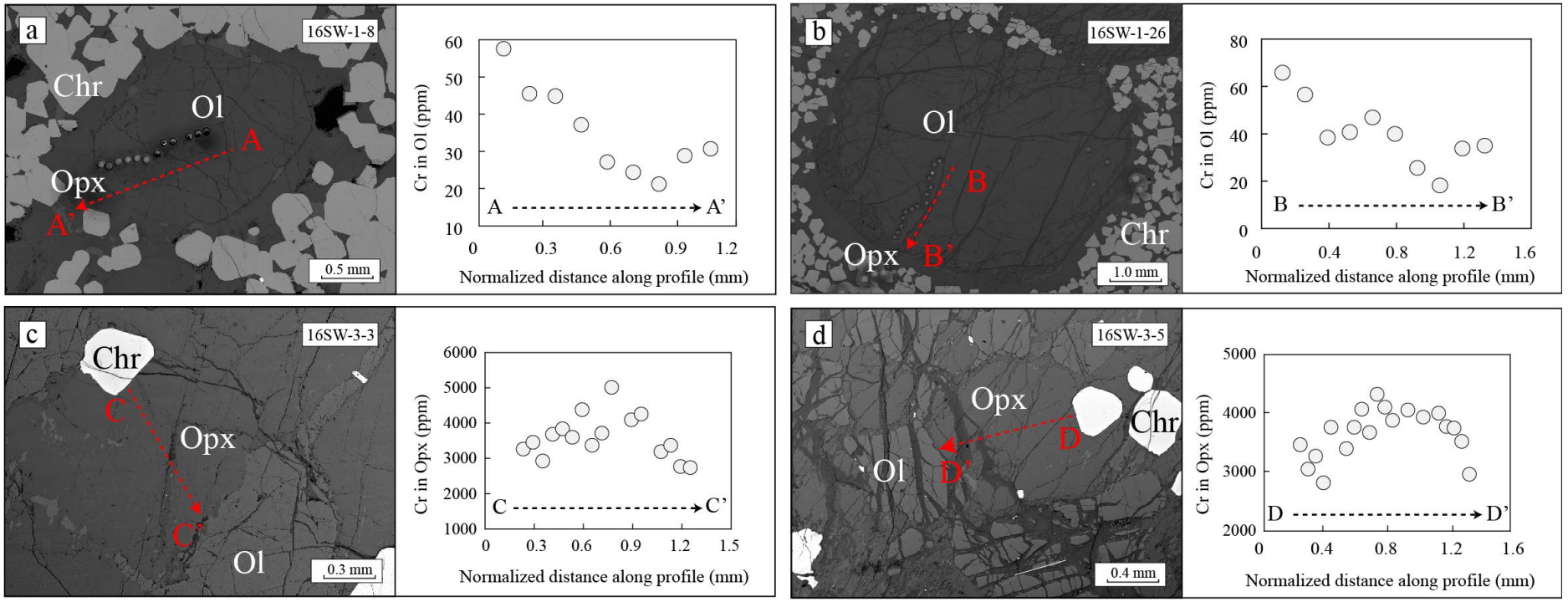

Figure 4.2 Core-to-rim chromium concentration profiles in olivine extended to traverse adjacent orthopyroxene in (a) sample 16SW-1-8 (anti-nodular chromitite), (b) sample 16SW-1-26 (anti-nodular chromitite), (c) sample 16SW-3-3 (dunite), and (d) sample 16SW-3-3 (granular harzburgite).

4.2.2 Cr isotopes

The $\delta^{53}Cr$ values of chromites in the different rock suites and layers are extremely restricted, ranging from –0.07 to –0.23‰ (Table 4.1), similar to spinel from other mafic-ultramafic rock suites and mantle xenoliths (Figure 4.3; Farkaš et al., 2013; Xia et al., 2017; Shen et al., 2018; Chen et al., 2019). This is in agreement with the restricted $\delta^{53}Cr$ values (–0.12 ± 0.10‰) reported for igneous rocks from various tectonic settings and with varying chemical parameters (Schoenberg et al., 2008). In addition, chromite $\delta^{53}Cr$ values are roughly consistent with the whole-rock values, as observed for ophiolites (Farkaš et al., 2013; Shen et al., 2015), mantle xenoliths (Xia et al., 2017), other types of ultramafic/mafic intrusions (Farkaš et al., 2013), and meteorites (e.g., Moynier et al., 2011; Schiller et al., 2014, Schoenberg et al., 2016).

In contrast to chromite, olivine and orthopyroxene $\delta^{53}Cr$ values show variations from –0.09 to 0.25‰ and –0.11 to 0.07‰, respectively (Figure 4.3). Olivine grains have higher and more variable $\delta^{53}Cr$ values than orthopyroxene, and almost all silicate minerals in the Stillwater Complex have higher $\delta^{53}Cr$ values than chromite. These characteristics are opposite the inter-mineral equilibrium fractionations observed in mantle xenoliths, for which $\delta^{53}Cr_{Spl} > \delta^{53}Cr_{Opx} > \delta^{53}Cr_{Ol}$ (Xia et al., 2017; Shen et al., 2018).

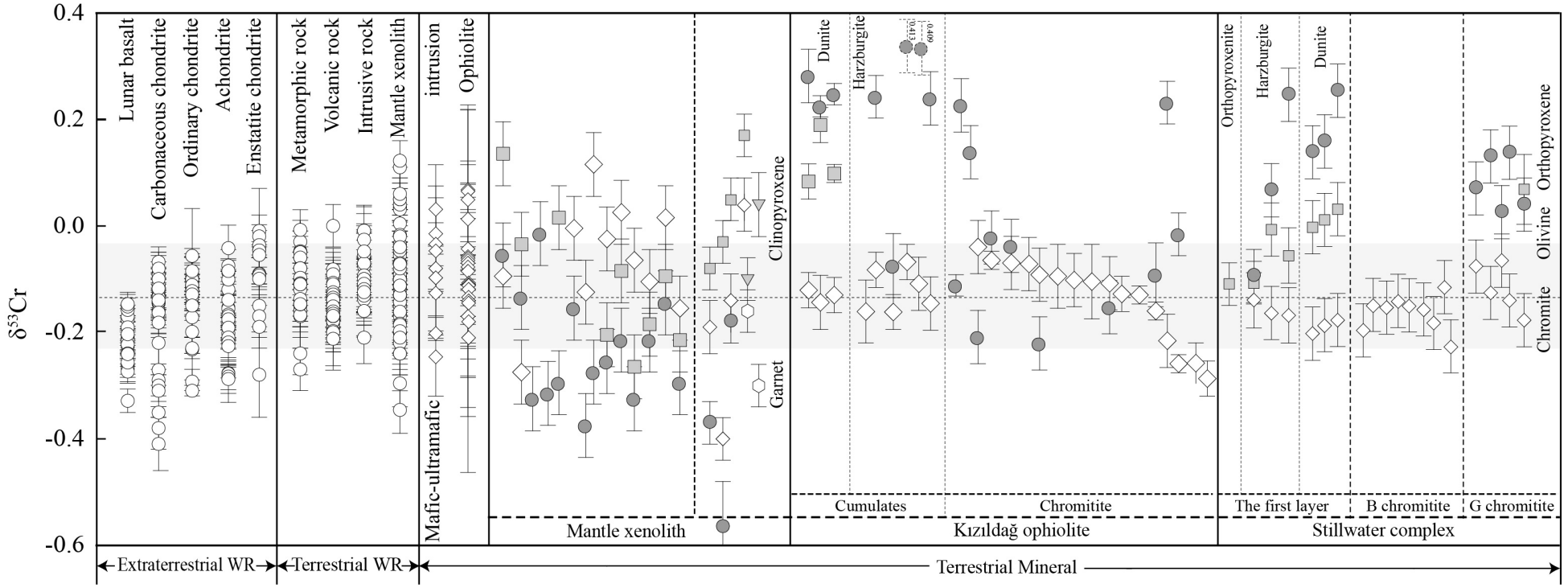

Figure 4.3 Chromium isotopic compositions of olivine, orthopyroxene, and chromite in the Stillwater Complex (far right panel) compared to published terrestrial mineral and whole-rock data (central panels) and extraterrestrial whole-rock data (far left panel). Circles represent olivine, squares represent orthopyroxene, and diamonds represent chromite. Silicate mineral $\delta^{53}Cr$ values are from Xia et al. (2017), Shen et al. (2018), and Chen et al. (2019), and $\delta^{53}Cr$ values of chromite in other mafic-ultramafic intrusions and ophiolites are from Farkaš et al. (2013) and Shen et al. (2015). Terrestrial and extraterrestrial whole-rock $\delta^{53}Cr$ values are from Moynier et al. (2011), Farkaš et al. (2013), Bonnand et al. (2016), and Schoenberg et al. (2008, 2016). The range of BSE values is from Schoenberg et al. (2008). Reported errors are 2SE.

Table 4.1 Chromium concentration and isotopic compositions of mineral separates in rocks from the Stillwater Complex

Location	Samples	Lithology	Cr (ppm)	Standard deviation	$\delta^{53}Cr$ (‰)	2σ	Cr (ppm)	Standard deviation	$\delta^{53}Cr$ (‰)	2σ	Cr_2O_3 (wt%)	$\delta^{53}Cr$ (‰)	2σ
				olivine				orthopyroxene				chromite	
Lowermost layer	16SW-3-4	Dunite	23	3.70	0.14	0.05	3871	413	0.00	0.05	44.87	-0.20	0.05
Lowermost layer	16SW-3-3	Dunite	28	4.30	0.26	0.05	3586	225	0.03	0.05	45.38	-0.18	0.05
Lowermost layer	16SW-3-2	Dunite	36	3.80	0.16	0.05	3767	226	0.01	0.05	44.52	-0.19	0.05
Lowermost layer	16SW-3-9	Harzburgite	32	10.7	0.25	0.05	4134	319	-0.06	0.05	45.82	-0.17	0.05
Lowermost layer	16SW-3-5	Harzburgite	31	9.20	0.07	0.05	3852	246	-0.01	0.05	44.47	-0.16	0.05
Lowermost layer	16SW-3-11	Harzburgite	39	4.60	-0.09	0.05	3416	397	-0.11	0.04	44.23	-0.14	0.05
Lowermost layer	16SW-3-6	Orthopyroxenite					3550	479	-0.11	0.04			
G chromitite	16SW-1-15	Harzburgite	34	2.70	0.04	0.05	3109	212	0.07	0.07	39.62	-0.18	0.05
G chromitite	16SW-1-9	Disseminated chromitite	24	3.50	0.14	0.05	3230	333			42.44	-0.14	0.05
G chromitite	16SW-1-27	Disseminated chromitite	18	4.90	0.03	0.05	3729	247			43.38	-0.07	0.05
G chromitite	16SW-1-8	Anti-nodular chromitite	29	3.90	0.13	0.05	3050	518			45.13	-0.13	0.05
G chromitite	16SW-1-26	Anti-nodular chromitite	27	5.10	0.07	0.05	3265	384			44.84	-0.08	0.05
B chromitite	16SW-2-21	Disseminated chromitite									36.78	-0.23	0.05
B chromitite	16SW-2-12	Disseminated chromitite									45.69	-0.11	0.05
B chromitite	16SW-2-4	Disseminated chromitite									40.46	-0.16	0.05
B chromitite	16SW-2-17	Disseminated chromitite									43.94	-0.20	0.05
B chromitite	16SW-2-8	Disseminated chromitite									46.47	-0.15	0.05
B chromitite	16SW-2-14	Anti-nodular chromitite									47.11	-0.14	0.05
B chromitite	16SW-2-13	Massive chromitite									43.12	-0.18	0.05
B chromitite	16SW-2-15	Massive chromitite									47.78	-0.15	0.05
B chromitite	16SW-2-6	Massive chromitite									42.42	-0.15	0.05

4.1 Equilibrium chromium isotopic fractionation

Chromium isotopic variations in olivine, orthopyroxene, and chromite may result from either equilibrium fractionation or diffusion-driven kinetic fractionation. In this section, we first discuss the mechanism governing the observed Cr isotopic variations in these minerals during magmatic processes. Then, we explore potential petrologic applications.

The restricted range of chromite δ^{53}Cr values in our results (–0.23 to –0.07‰) overlap the narrow range reported for the BSE (δ^{53}Cr = –0.22 to –0.02‰; Schoenberg et al., 2008). However, we note chromite Cr isotopic variations in our data, specifically those from the B and G chromite seams (Figure 4.4a, b). Chemical exchanges play an important role in modifying isotopic compositions (e.g., for Fe and Mg isotopes; see Teng et al., 2011; Chen et al, 2018), but the δ^{53}Cr values of chromite grains are expected to be insensitive to chemical exchanges due to the huge Cr concentrations in chromite relative to other phases (e.g., Drake et al., 1989; Ohtani et al., 1989). Chromites are thus expected to maintain their original Cr isotopic compositions during cooling.

Some Cr isotopic variations in chromite may be induced by magmatic differentiation, as observed in ophiolitic samples (Chen et al., 2019) and terrestrial and lunar basalts (Bonnand et al., 2016; Xia et al., 2017). During differentiation, heavier Cr isotopes are preferentially partitioned into chromite and lighter isotopes into the residual melt (Farkaš et al., 2013; Shen et al., 2015, 2018; Xia et al., 2017). The range of Cr isotopic compositions observed in chromites of this study (Figure 4.4a, b) could have been induced by abundant chromite crystallization in the B and G chromite seams. Indeed, massive chromitite crystallization at the base of every cyclic chromitite unit (Raedeke and McCallum, 1984; McCallum, 1996) could have enriched the residual melt in light Cr isotopes. Chromite grains that subsequently crystallized from the residual melt (i.e., in anti-nodular and disseminated chromitites and silicate cumulates) would naturally have lighter Cr isotopic compositions. The δ^{53}Cr values of chromite, especially in the B and G chromite seams, correlate negatively with indicators of magmatic differentiation, such as chromite Mg# (Figure 4.4a) and TiO_2 content (Figure

4.4b) (e.g., Barnes and Roeder, 2001; Bai et al., 2017). This provides further evidence that the observed Cr isotopic variations could have been induced by chromite fractionation during magmatic differentiation.

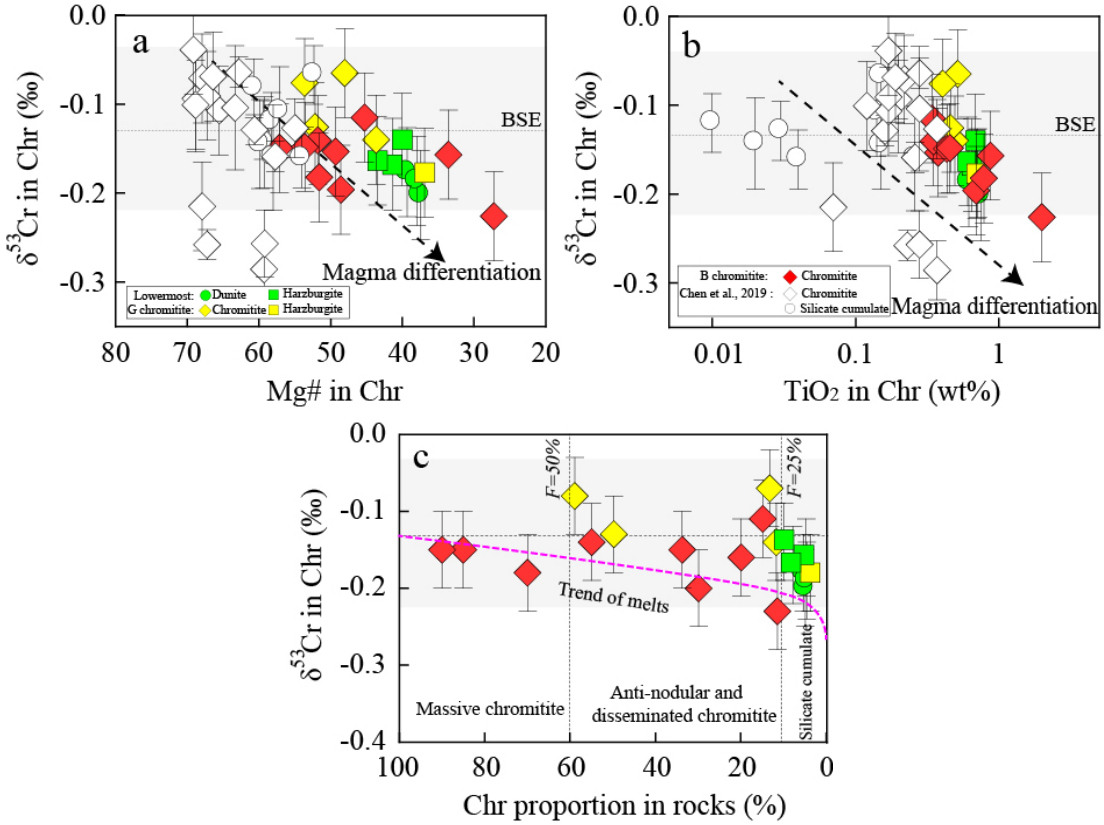

Figure 4.4 Chromite Cr isotopic compositions compared to magma differentiation trends: (a) chromite Mg# and (b) chromite TiO_2 content. Dashed lines represent the trend of magma differentiation. (c) The calculated trend of the Cr isotopic evolution of the melt during fractional crystallization of chromite. The horizontal axis represents the chromite proportion in different samples, which are calculated by mass balance (Table S11.4). *F* is the fraction of Cr in the residual melt relative to that in the primary melt. The isotopic evolution of the melt is calculated from Shen et al. (2018). The range of BSE values is from Schoenberg et al. (2008).

The massive chromitites formed at the base of each cyclic sequence have the closest Cr isotopic compositions to the BSE value (Figure 4.4c). Interestingly, a few anti-nodular and disseminated chromitites are isotopically heavier than the massive

chromitites (Figure 4.4c), although, as discussed above, they should be isotopically lighter with $\delta^{53}Cr$ values between those of the massive chromitites and the residual melt. This is hard to reconcile in a closed magmatic system, and contamination by isotopically heavy Si-rich sedimentary rocks might have produced the elevated $\delta^{53}Cr$ values in those chromitites (e.g., Qin and Wang, 2017). The residual melt from which the anti-nodular and disseminated chromitites formed had a lower Cr content than the primitive melt that produced the massive chromitites. Therefore, the Cr isotopic composition of the Cr-poor residual melt would have been more easily influenced by such sedimentary rocks, such that anti-nodular and disseminated chromitites that formed later would be isotopically heavier than massive chromitites that had formed earlier in the sequence. The Cr isotopic compositions of chromites thus show that the injected primitive melt and assimilation of the surrounding rocks are two factors responsible for the formation of the isotopically distinct chromitites in the Stillwater Complex. This conclusion is supported by the presence of crust-derived inclusions in those lithologies (Spandler et al., 2005) and results from chemical modeling of the parent magma of the Peridotite Zone (Jenkins and Mungall, 2018).

4.2 Diffusion-driven kinetic chromium isotopic fractionation

Theoretical predictions (Moynier et al., 2011; Farkaš et al., 2013; Shen et al., 2015, 2018) and data from mantle xenoliths (Figure 4.3; Xia et al., 2017) show that mineral-specific Cr isotopic compositions attained by equilibrium inter-mineral Cr isotopic fractionation should follow the general order $\delta^{53}Cr_{Spl} > \delta^{53}Cr_{Opx} > \delta^{53}Cr_{Ol}$. Inter-mineral fractionation factors are also controlled by temperature and oxygen fugacity (Shen et al., 2018), which affect the charge and coordination environment of Cr (e.g., Polyakov and Mineev, 2000; Polyakov et al., 2007). However, we observed the reverse order of $\delta^{53}Cr_{Ol} \geq \delta^{53}Cr_{Opx} > \delta^{53}Cr_{Chr}$ (Figure 4.3), and mineral pairs plot far from the equilibrium inter-mineral isotopic fractionation lines defined for mantle xenoliths by Xia et al. (2017) and Shen et al. (2018) (Figure 4.5), indicating disequilibrium fractionation in our samples.

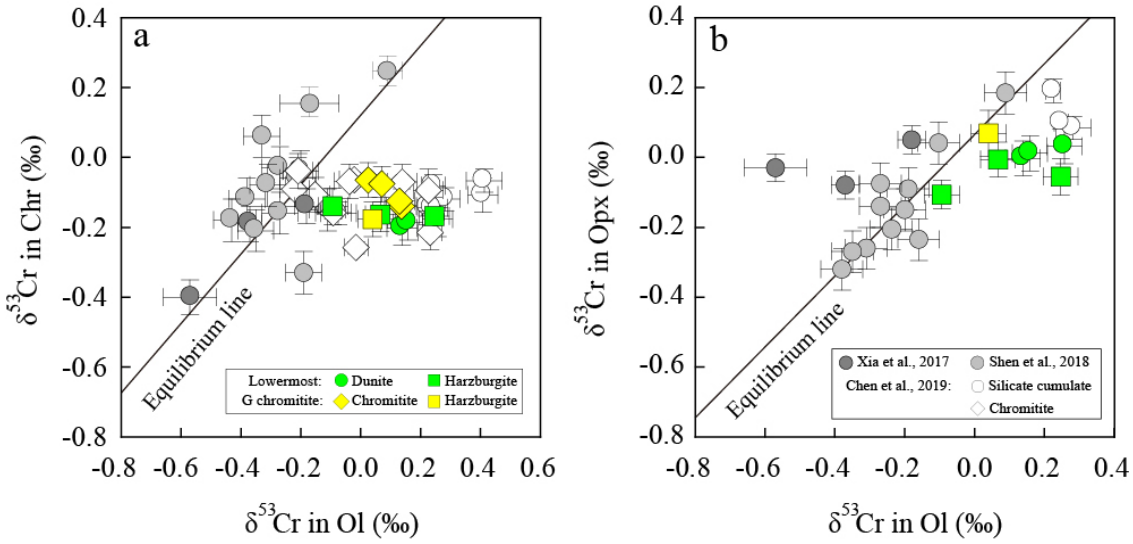

Figure 4.5 Inter-mineral Cr isotopic fractionations between (a) olivine and chromite and (b) olivine and orthopyroxene. Solid lines represent the equilibrium fractionation lines defined from mineral pairs in mantle xenoliths (Xia et al., 2017; Shen et al., 2018).

Significant disequilibrium isotopic fractionations have been observed during magmatic processes in a variety of environments for elements including Li, Fe, and Mg (e.g., Teng et al., 2011; Oeser et al., 2015; Collinet et al., 2017). Light isotopes diffuse faster than heavy ones during elemental diffusion (Richter et al., 2009), therefore subsolidus Cr diffusion should also result in disequilibrium isotopic fractionation via Soret (e.g., Richter et al., 2009; Huang et al., 2010) or chemical diffusion (e.g., Richter et al., 2009; Teng et al., 2011). Soret diffusion could produce large Cr isotopic fractionations, with heavy Cr isotopes preferentially diffusing down the thermal gradient. However, Soret diffusion cannot be responsible for the heavy Cr isotopic compositions observed here in silicate minerals because thermal diffusivity (Lesher and Walker, 1986) is dozens of orders of magnitude faster than that of elemental Cr in minerals (Ganguly et al., 2007; Posner et al., 2016; Jollands et al., 2017). It is thus reasonable to assume that no measurable or long-lasting temperature gradient can occur at the grain scale. Hence, it is more likely that the kinetic mechanisms of Cr diffusion derive from chemical diffusion.

Chemical diffusion during crystal growth is often induced by the concentration gradients caused by the changing composition of the equilibrium melt, as typically inferred from elemental zonings in mineral (Preβ et al., 1986; Bai et al., 2018; Guotana et al., 2018). Isotopic evidence of Cr chemical diffusion has also been reported during mantle processes in which Cr diffuses from high-Cr melt to adjacent peridotites (Xia et al., 2017), imprinting light Cr isotopic signatures into the rock-forming minerals (Figure 4.5). This is most obviously observed in olivine grains with $\delta^{53}Cr$ values (and Cr concentrations) lower than those of spinel (Figure 4.5a) and orthopyroxene (Figure 4.5b). However, Cr diffusion from melt to silicate minerals could cause lighter Cr isotopic compositions in the silicate minerals (Figure 4.3) and decreasing Cr contents from their cores to rims (Figure 4.2). Alternatively, chemical diffusion can occur due to the elemental disequilibrium induced by variable physicochemical states. The compatibility of Cr in olivine and orthopyroxene are commonly inconstant (e.g., $D_{Cr}^{Opx/melt}$ = 0.55 – 2.2, $D_{Cr}^{Ol/melt}$ = 0.45 – 1.3; Kennedy et al., 1993). Specifically, the solubility of Cr in silicate minerals decreases with decreasing temperature (Papike et al., 2005; Jollands et al., 2018), and Cr should diffuse from silicate minerals to the melt during cooling. Grain-boundary diffusion is also an order of magnitude faster than volume diffusion, and both occur in minerals (Freer, 1981; Ganguly, 2002). Accordingly, silicate minerals in our samples show decreasing core-to-rim Cr profiles (Figure 4.1) and have heavy Cr isotopic compositions that plot away from the equilibrium fractionation line (Figure 4.5).

Inter-mineral Cr isotopic fractionation factors ($\Delta^{53}Cr_{A\text{-}B} = \delta^{53}Cr_A - \delta^{53}Cr_B$, where A and B are two mineral phases) were estimated by Shen et al. (2018). Overall, our samples show disequilibrium isotopic fractionations (Figure 4.6). Chromite-olivine pairs in silicate cumulates tend to have larger fractionation factors than those in chromitites (Figure 4.6a). This may be attributed to migration of the interstitial melt. Chromitites generally form by the rapid sorting (sinking) and accumulation of chromite, and efficient compaction of the earliest accumulated chromitites will cause the upward migration of any interstitial melt (Raedeke and McCallum, 1984; Boudreau, 2016).

Consequently, silicate minerals in chromitites are likely less affected by Cr diffusion in the interstitial melt (Manoochehri and Schmidt, 2014; Jenkins and Mungall, 2018). On the other hand, if the interstitial melt maintains elemental exchange with the parental magma of the silicate cumulates overlying the chromitites, the prolonged exchange between the two melts would generate larger fractionations between minerals of the two lithologies. The sole exception in our data is sample 16SW-3-11, which is located close to the chilled margin of the Basal Series and thus cooled rapidly without undergoing protracted diffusion. This sample thus preserves relatively primary Cr isotopic compositions and displays the lowest isotopic fractionation factor (Figure 4.6).

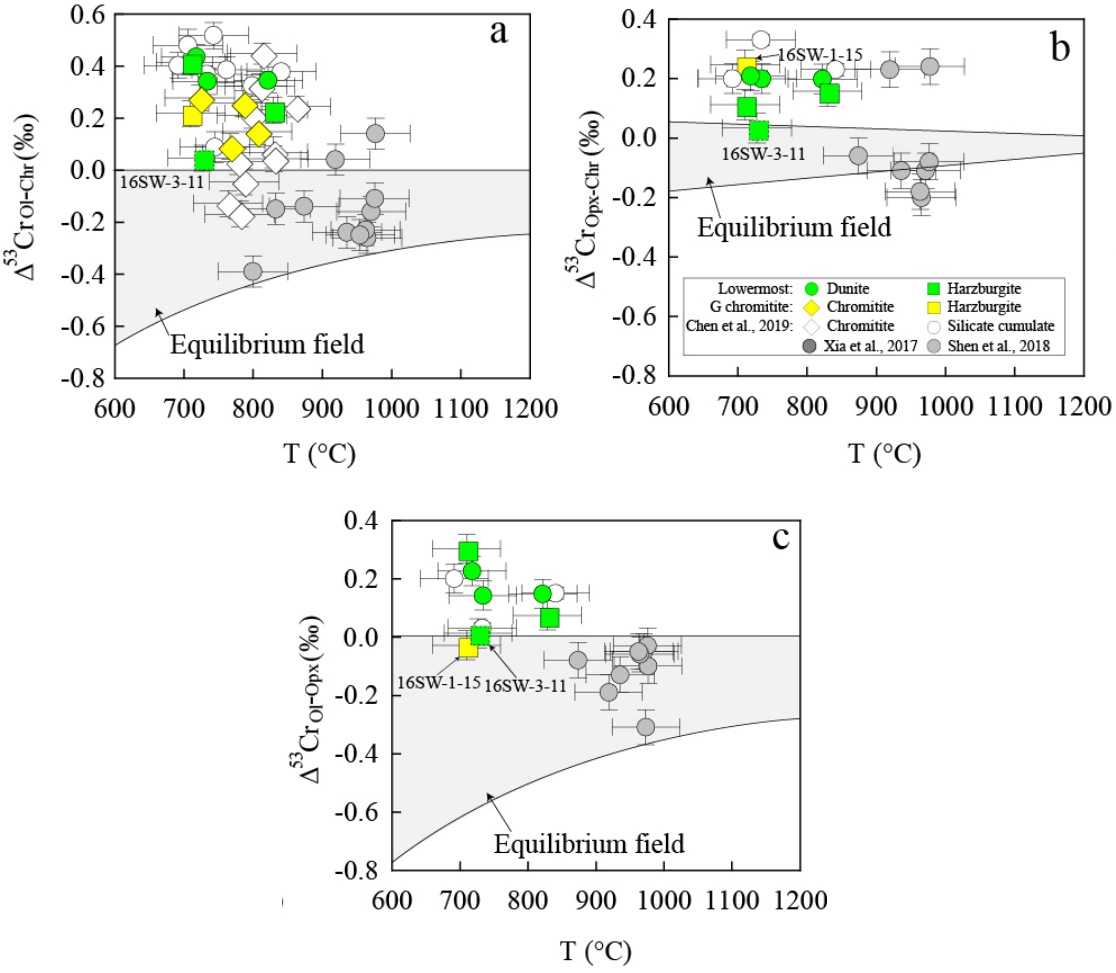

Figure 4.6 Calculated (a) olivine-chromite, (b) orthopyroxene-chromite, and (c) olivine-orthopyroxene inter-mineral equilibrium Cr isotopic fractionation factors as a function of temperature in the Stillwater Complex, compared with samples from Shen et al. (2018) and Chen et al. (2019). The gray field denotes isotopic fractionations arising from equilibrium

processes (Shen et al., 2018).

The characteristic $\delta^{53}Cr_{Ol} > \delta^{53}Cr_{Opx}$ values between olivine and granular orthopyroxene may be due to the low Cr contents of olivine, which could have been significantly affected by extrinsic heavy Cr isotopes. Orthopyroxenes in the poikilitic harzburgite sample 16SW-1-15 have Cr isotopic compositions similar to those of olivine from the same sample. This is expected because the poikilitic orthopyroxene formed from the reaction between olivine and trapped melt (Jackson, 1961; Barnes, 1986). Poikilitic orthopyroxenes thereby inherited the Cr isotopic compositions of their precedent olivines, i.e., heavier $\delta^{53}Cr$ values than granular orthopyroxenes.

4.3 Constraints on the cooling time of the Stillwater Complex

Li, Fe, and Mg elemental and isotopic zonings induced by inter-mineral disequilibrium are widely observed in intrusive rocks (e.g., Chen et al., 2014; Xiao et al., 2016), volcanic rocks (e.g., Teng et al., 2011), and meteorites (e.g., Collinet et al., 2017), but only constrain cooling histories over short time scales, such as for volcanic rocks and meteorites (Teng et al., 2011; Collinet et al., 2017). For magmatic processes with longer cooling periods, for instance in intrusive rocks, few of the aforementioned elements are zoned, although their isotopic compositions can show evidence of inter-mineral diffusion (Xiao et al., 2016). Zoning patterns of low-valence elements are generally homogenized by rapid diffusion during prolonged subsolidus processes (Yang and Seccombe, 1993). In contrast, some high-valence elements, such as Ti and Si, are not re-equilibrated due to their extremely low diffusivities (Suzuki et al., 2008).

Chromium diffuses slower than Fe, Mg, and Li, but faster than Ti and Si in silicate minerals (e.g., Ito and Ganguly, 2006; Ganguly et al., 2007; Posner et al., 2016), and magmatic minerals thus commonly present Cr zoning patterns. Indeed, Cr diffusion profiles in olivine, orthopyroxene, and spinel have been used to calculate the cooling rates of meteorites (e.g., Lugmair and Shukolyukov, 1998; Ito and Ganguly, 2006). Here, we similarly use Cr diffusion profiles to constrain the cooling history of the Peridotite

Zone in the Stillwater magma body.

We developed a simple diffusion model for olivine and orthopyroxene using Mathematica. We use the one-dimensional diffusion equation of Richter et al. (1999, 2003), which is a function of the Cr concentration (C) in olivine or orthopyroxene, the position (r) along the profile, and time (t):

$$\frac{\partial C(r,t)}{\partial t} = \frac{\partial D}{\partial r} \cdot \frac{\partial C(r,t)}{\partial r} + D \frac{\partial^2 C(r,t)}{\partial r^2}$$

Elemental Cr diffusion coefficients (D) in olivine and orthopyroxene are well known to follow an Arrhenius behavior, and become exponentially smaller with decreasing temperature (Ito and Ganguly, 2006; Ganguly et al., 2007), expressed as:

$$D = D_0 \exp(-E / RT)$$

where D_0 is the diffusion constant, E the activation energy, R the gas constant, and T the temperature (K). In addition, Cr diffusion in olivine and orthopyroxene is anisotropic. Here we assume that Cr diffusion parallel to different crystallographic axes has different activation energies, and that D_0 is also strongly dependent on the crystallographic axis. Accordingly, we selected average data for E and D_0 parallel to the a- and c-axes to represent their activation energies and diffusion constants in olivine (Ito and Gauguly, 2006) and orthopyroxene (Gauguly et al., 2007).

The closure temperature (T_c) is defined as the temperature at which diffusion effectively ceases during cooling (Dodson, 1973). Ito and Gauguly (2006) and Gauguly et al. (2007) demonstrated that T_c for Cr in olivine and orthopyroxene is a function of the initial temperature (T_0), grain size, and cooling rate according to the formulation of Ganguly and Tirone (1999):

$$\frac{E}{RT_c} = \ln\left(-\frac{A' R T_c^2 D_0}{E (dT/dt)_{@T_c} a^2} \right)$$

where $(dT/dt)_{Tc}$ is the cooling rate at T_c and a is the radius of olivine grains, set to 500, 1,000, and 2,000 μm for our samples. The function A' can be expressed as $A' = A \exp(g)$, where A is a geometric factor given by $A = e^{G}$ (Dodson, 1973), and G = 4.0066 for spheres, 3.29506 for cylinders, and 2.15821 for plane sheets. The term

g, which is referred to as a "memory function", is a function of a dimensionless parameter, M, given by Dodson (1973) as:

$$M = \frac{RD(T_0)}{E\eta a^2}$$

where η is a cooling time constant with units $K^{-1}\,t^{-1}$. The values of g for specific values of M are tabulated in Ganguly and Tirone (1999, 2001). In the above equation, $D(T_0)$ is the diffusion coefficient at the peak (initial) temperature, which makes T_c dependent on T_0. We assume that cooling was asymptotic, described by:

$$\frac{1}{T} = \frac{1}{T_0} + \eta t$$

The thermal models developed by Hess (1972) for the Stillwater Complex assumed a T_0 value around 1200 °C. Melting experiments performed on samples from the Stillwater Complex showed that olivine was the first phase in the crystallization sequence, with a liquidus temperature of 1200 °C (Helz, 1995). This temperature is further supported by the presence of RuS_2 in the Peridotite Zone, which is stable at or below approximately 1200 °C (Talkington and Lipin, 1986). Thus, we set T_0 in our model to 1200 °C. This assumes that the Stillwater magma was injected as a single sill at 1200 °C into basement rocks at 300 °C, and that the magma cooled below its solidus (e.g., Selkin et al., 2000). Most mineral grains are assumed to have crystallized from the melt and settled into cumulate piles at this initial cooling temperature. We use the cooling rate at any temperature, T', instead of that at T_c to obtain curves for T_c vs. cooling rate for specific values of T_0 and a (Figure 4.7).

We calculate the diffusion coefficients of ^{52}Cr and ^{53}Cr using a modified version of Graham's low for molten oxides and crystals (Richter et al., 1999):

$$\frac{D_1}{D_2} = \left(\frac{M_2}{M_1}\right)^{\beta}$$

where D_1 and D_2 are the diffusivities and M_1 and M_2 the masses of the two analyzed Cr isotopes. β is the isotopic fractionation factor, which remains to be determined for Cr diffusion in olivine and orthopyroxene; we set it to ~0.16, similar to the latest empirical

results for Fe isotopes (Sio et al., 2018). This value can be used to describe diffusion along all major crystallographic axes.

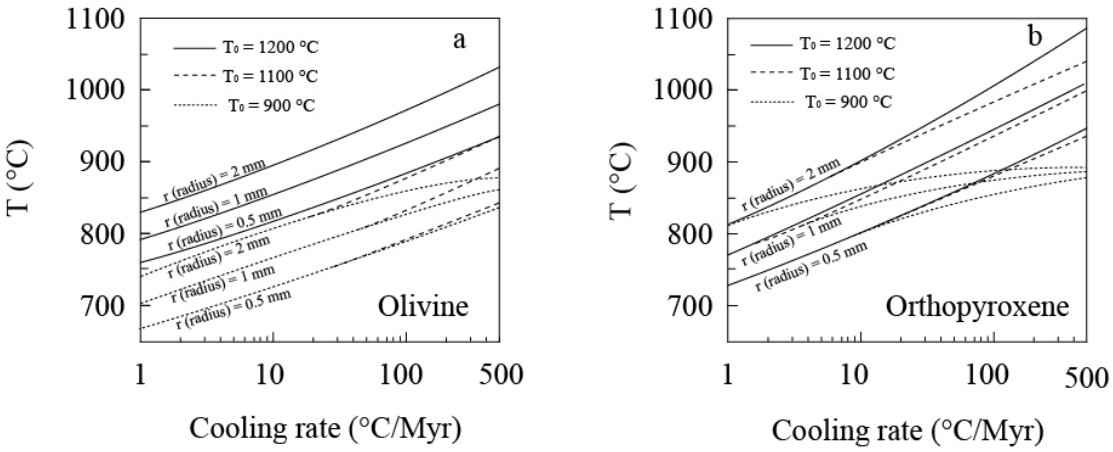

Figure 4.7 Closure temperature (T_c) of Cr diffusion in olivine and orthopyroxene as a function of the initial temperature (T_0), cooling rate, and grain size. The cooling trends for T_0 = 1100 and 900 °C in olivine and orthopyroxene are from Ito and Ganguly (2006) and Ganguly et al. (2007).

The initial Cr concentration C_0 is variable in our samples, and we varied its value from 60 to 20 ppm in olivine and from 6,000 to 3,000 ppm in orthopyroxene. The calculated closure temperatures (T_c = 790 °C for olivine and 760 °C for orthopyroxene) for grains of radius a = 1,000 μm were adopted in the diffusion model. Thus, we obtain the Cr concentrations and isotopic compositions at any position along the grain radius and at different cooling times using the temperature-dependent Cr diffusion constants; the average concentrations and isotopic compositions are obtained by integration over the grain radius. We explored various cooling times, which yielded different average Cr concentrations and isotopic compositions, and the various initial Cr concentrations in the minerals produced different trend lines depending on the cooling time (Figure 4.8). We plotted all our analytical data to compare with these model results, and we find that most of our samples are confined to within the trend lines of 10 to 100 kyr cooling times.

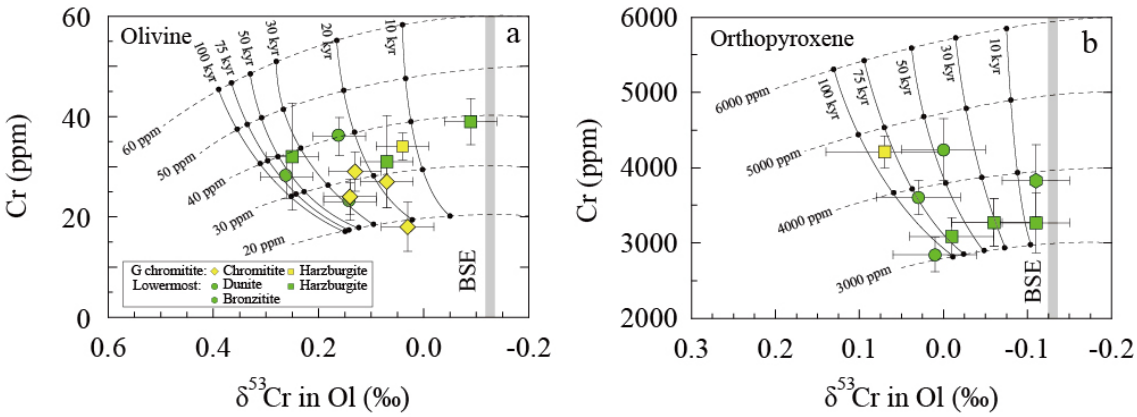

Figure 4.8 Modeled Cr contents and isotopic compositions in olivine and orthopyroxene as a function of cooling time. The Cr concentration and isotopic profiles were obtained using the Mathematica diffusion model developed in the text, and average Cr concentrations and isotopic compositions are calculated by integration over the grain radius. Dashed horizontal lines represent the calculated evolution of Cr contents and isotopic compositions, and the solid lines represent cooling times for different initial Cr concentrations. Model results are compared to the observed Cr concentrations and isotopic compositions of olivine and orthopyroxene, which restrict the cooling times to 10–100 kyr. The BSE value is from Schoenberg et al. (2008).

4.4 Petrogenetic applications

Hess (1972) conducted the earliest study on the cooling history of the Stillwater Complex. They calculated the rate of heat loss from the magma using likely values of thermal diffusion and depth of burial, and estimated the cooling rate of the 2 km-thick rock unit to be about 1 °C/kyr. The cooling history of the Stillwater Complex was then commonly calculated based on Fe-Mg elemental exchange. Cooling rates of 1–50 °C/Myr were obtained using intercrystalline Fe-Mg exchange between pyroxenes (Domeneghetti et al., 2001; McCallum et al., 2006). However, this value has a large uncertainty and is much slower than the computed cooling rate for a terrestrial intrusion (Irvine, 1970; McCallum et al., 2006). The Stillwater Complex was exposed to a low-grade (greenschist facies) metamorphic event at 1.7 Ga. Heating associated with this metamorphic event may have induced intracrystalline redistribution of Fe and Mg, and it is likely that such slow cooling rates reflect this late low-temperature heating event.

Micron-scale oscillatory zonings in plagioclase were also used to determine the cooling rate of the Stillwater Complex based on CaAl-NaSi diffusion in plagioclase feldspar (Grove et al., 1984), and their results showed that cooling from 1200 to 1000 °C required around 100 kyr. Recently, Selkin et al. (2006) used a 1-D finite difference conductive cooling model based on an analytic half-space model to estimate the cooling history of the Stillwater Complex. Their results for sites at the top of the Stillwater Complex, where the heat should have been conductively consumed by the surrounding rocks (Coogan et al., 2002), suggest that it may take as little as 20 kyr to cool from 1200 to 580 °C. However, for sites at the bottom of the complex (e.g., the Peridotite Zone) where diffusive cooling dominates, their results suggest that the minimum closure temperature would have been reached about 1 Myr later than at sites near the top of the pluton.

According to our model, the Peridotite Zone of the Stillwater Complex more likely cooled within 10–100 kyr. This result is consistent with the convective cooling time Selkin et al. (2006) obtained for the top of the layered intrusion. This rapid cooling rate may provide evidence that convective cooling was active during cooling of the Peridotite Zone, a mechanism that increases cooling rates by nearly an order of magnitude compared to diffusive cooling (Coogan et al., 2002). Our results thus suggest that the intrusion was not constructed in a strictly sequential stratigraphic order from the base (oldest) to the top (youngest), in agreement with Wall et al. (2018). The parental magma of the Peridotite Zone may have been injected directly into a cooled, crystallized sill. This emplacement mechanism would have enabled rapid convective thermal dissipation (Scoon and Costin, 2018).

5. Petrogenesis of the Ultramafic Zone of the Stillwater Complex in North America: constraints from mineral chemistry and stable isotopes of Li and O[3]

[3] This chapter is published in Contributions to Mineralogy and Petrology - Su, B.X., Bai, Y., Cui, M.M., Wang, J., Xiao, Y., Lenaz, D., Sakyi, P.A., Robinson, P.T., 2020. Petrogenesis of the Ultramafic Zone of the Stillwater Complex in North America: Constraints from mineral chemistry and stable isotopes of Li and O. Contributions to Mineralogy and Petrology 175, 68. https://doi.org/10.1007/s00410-020-01707-y

It has been suggested that parental magmas of large mafic-ultramafic layered intrusions worldwide vary in composition due to different mixing proportions, consequently leading to chemical disequilibrium between the magmas and crystallizing minerals (e.g., Bushveld, Mondal and Mathez 2007; Stillwater, McCallum 1996, 2002). This results in compositional variations and modifications in minerals via re-equilibration and interaction (Pagé et al. 2011). Further interaction or chemical diffusion may also occur between crystallized minerals and interstitial liquids (Raedeke and McCallum 1984; Lenaz et al. 2012) and between subsolidus mineral phases, such as olivine and chromite during solidification and cooling (Jackson 1961; McCallum 2002; Bai et al. 2019). The extent of such interactions depends largely on the spatial migration of the melts; O'Driscoll et al. (2009) proposed downward infiltration of a melt during the formation of layers in such intrusions, whereas others have argued for upward-percolation of the melts (Kaufmann et al. 2018) owing to compaction of the underlying crystal pile (Irvine 1980) or a temperature gradient-driven flux (Latypov et al. 2008). Thus, the cooling and crystallization history of large layered intrusions is long, complex, and involves multiple injections of primitive magma into an evolving and fractionating magma chamber. These processes would have modified the primary melt compositions and the constituent minerals, making it difficult to identify a clear parental magma. Moreover, much of the mineralogical evidence for mineral-interstitial melt interactions would likely have been obliterated during late post-magmatic textural maturation and recrystallization (Pagé et al. 2011). These considerations have led to several hypotheses for the formation of stratiform chromitite layers in layered intrusions including magma mixing (Irvine 1975; Horan et al. 2001; Spandler et al. 2005), mechanical sorting (Cooper 1990; Mondal and Mathez 2007; Maier et al. 2012; Mungall et al. 2016; Jenkins and Mungall 2018), fluid immiscibility (McDonald 1965; Spandler et al. 2005) and incongruent melting (Boudreau 2016).

Because lithium (Li) and incompatible trace elements are sensitive to changing magma compositions, fluid activity and limited Li diffusion between silicates and chromite (Lambert and Simmons 1987; Eiler et al. 1995; Su et al. 2016, 2018;

Tomascak et al. 2016), integration of such data and oxygen (O) isotopes may shed new light on the formation of large layered mafic–ultramafic intrusions. In this study, we conducted in situ analyses of major and trace elements and Li and O isotopes of major silicate minerals from the Ultramafic Zone of the Stillwater Complex following petrographical and mineralogical investigations. These datasets, together with the Cr isotope data from the same samples in Bai et al. (2019), are used to identify elemental and isotopic variations in different rock types and to constrain potential melt/fluid activity as well as chemical interactions between various components.

5.1 Sample description and analytical methods

5.1.1 Sample description

The samples in this study were collected mainly from the peridotite subzone of the Ultramafic Zone. Six samples were collected from the cyclic chromitite unit of seam G in the Mountain View section, and seven samples were collected from the unmineralized lowermost cyclic unit in the Gish area (Figs. 5.1a; Table S12.1 in Appendix 12). One basal harzburgite sample was also collected from the contact between the Basal Zone and the Ultramafic Zone. The principal rock types vary from poikilitic harzburgite and dunite to chromitite and bronzitite (Figure 5.1b–g). They are mostly composed of olivine, orthopyroxene and chromite with varying amounts of plagioclase and clinopyroxene. Plagioclase is absent or less abundant in the chromitites than in the harzburgites. Previous studies (Jones et al. 1960; Campbell and Murck 1993; Jenkins and Mungall 2018), and our Figure 5.1, show that orthopyroxene, clinopyroxene, and plagioclase mainly occur as oikocrysts including olivine and chromite chadacrysts in the peridotite subzone of the Stillwater Complex. The crystallization sequence is olivine → chromite → orthopyroxene (→ plagioclase → clinopyroxene). Note that it is difficult to determine the crystallization order of the last two members of the sequence solely from the ultramafic rocks. There are some field outcrops and hand specimens in which plagioclase follows orthopyroxene and clinopyroxene follows plagioclase (Jackson 1961; McCallum 1996, 2002).

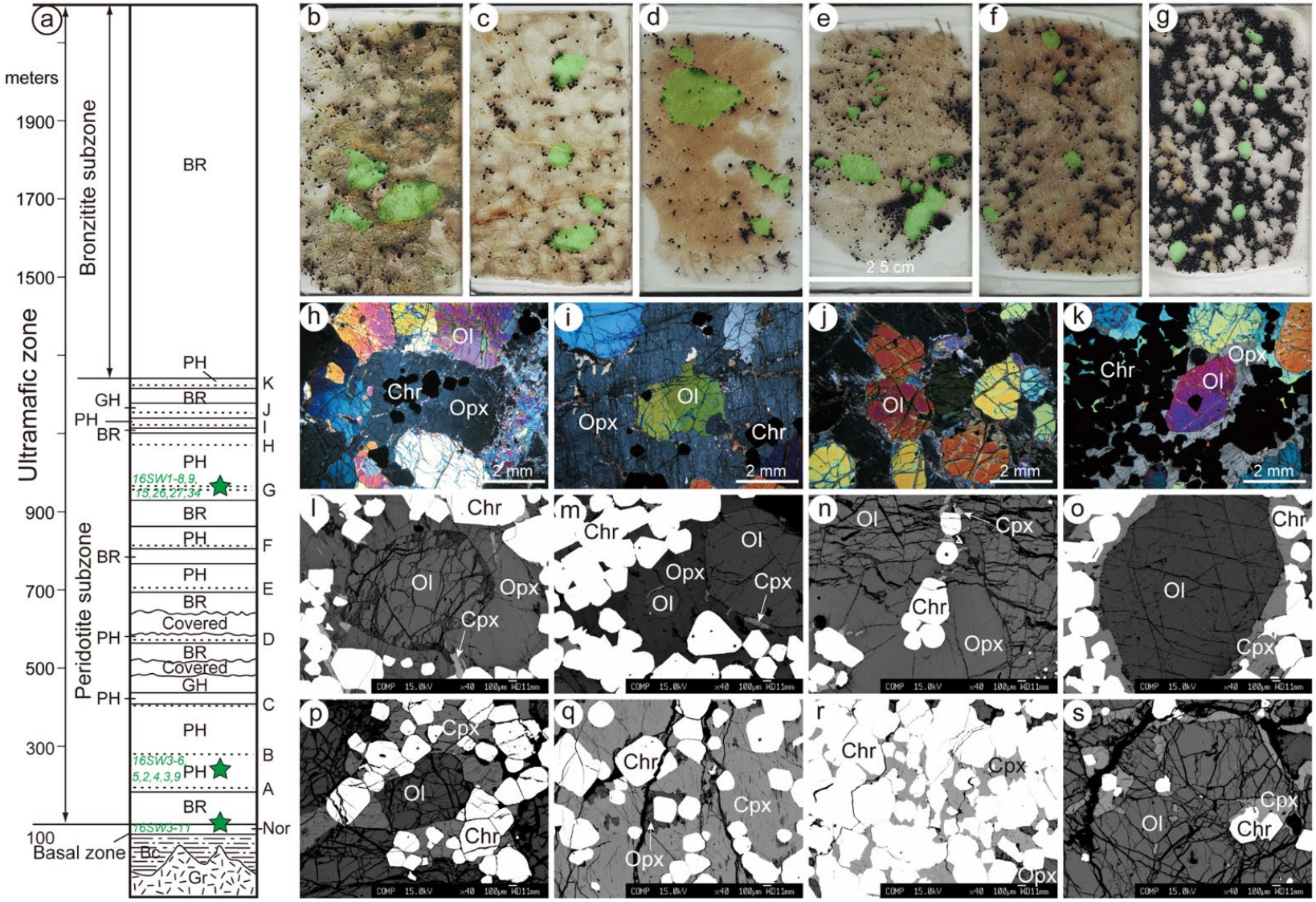
a
meters
1900
1700
1500
900
700
500
300
100
Ultramafic zone
Bronzitite subzone
Peridotite subzone
Basal zone
BR
PH
GH
Covered
16SW1-8,9, 15,26,27,34
16SW3-6, 5,2,4,3,9
16SW3-11
Bc
Gr
K
J
I
H
G
F
E
D
C
B
A
Nor
b
c
d
e
f
g
2.5 cm
h
i
j
k
Ol
Chr
Opx
2 mm
l
m
n
o
Cpx
p
q
r
s

Figure 5.1 (a) Generalized columnar section of the Ultramafic Zone, eastern part of the Stillwater Complex (after McCallum 1996) with sample locations (star symbol). BR bronzitite, Bc basement complex, Gr granite, GH granular harzburgite, Nor norite, PH poikilitic harzburgite. (b–g) Scanned images of thin-sections of the Stillwater samples showing distribution and relation of minerals and general variations of crystal size from harzburgite (b–c) and dunite (d–e) to chromitite (f–g); (h) harzburgite sample 16SW3-5 showing chromite (Chr) enclosed in orthopyroxene (Opx); (i) harzburgite sample 16SW3-9 showing orthopyroxene poikilitic crystals enclosing rounded olivine (Ol); (j) dunite sample 16SW3-3 showing equigranular olivine; (k) chromitite sample 16SW1-8 showing euhedral chromite and rounded olivine grain within poikilitic orthopyroxene; (l) chromitite sample 16SW1-26 showing tiny clinopyroxene (Cpx) in orthopyroxene, which encloses chromite and olivine; (m) chromitite sample 16SW1-8 showing olivine grains in variable size within orthopyroxene; (n) chromitite sample 16SW1-34 showing occurrence of euhedral chromite grains within olivine and orthopyroxene associated with minor clinopyroxene; (o) chromitite sample 16SW1-8 showing well-defined boundary between olivine and clinopyroxene; (p) chromitite sample 16SW1-9 showing clinopyroxene poikilitic crystal enclosing chromite and olivine and fracture development in chromite; (q) chromitite sample 16SW1-27 showing residual orthopyroxene poikilitic crystal in large clinopyroxene grain; (r) chromitite sample 16SW1-26 showing altered boundaries of chromite enclosed in clinopyroxene; (s) chromitite sample 16SW1-27 showing clinopyroxene-chromite association within or surrounding olivine.

Poikilitic harzburgite: Harzburgites in the Ultramafic Zone are coarse-grained rocks with either granular or poikilitic textures (Howland et al. 1949; Jones et al. 1960). The granular harzburgites comprise only a small stratigraphic proportion (Figure 5.1a) and consist chiefly of olivine and pyroxene grains which may exceed 1 cm in length. Plagioclase, chromite, biotite and even apatite are locally present as interstitial accessory minerals (Howland et al. 1949). The poikilitic harzburgite occurs mostly in the peridotite subzone where it hosts most of the economic chromitites (Figure 5.1a). This variety occurs on both sides of the chromite seams, and in some places, merges gradually into chromitite (Peoples and Howland 1940). The poikilitic harzburgites contain the same minerals as the granular varieties, but are characterized by relatively large, skeletal or poikilitic crystals enclosing rounded grains of olivine (Figure 5.1h, i). Interstitial plagioclase is usually present and can constitute up to 15% of the rock, whereas small, black chromite grains are enclosed in both the plagioclase and orthopyroxene (Figure 5.1i).

Dunite: Dunite bodies, together with olivine-rich harzburgite and coarse-grained pyroxenite, typically occur in the lower part of the Ultramafic Zone, where they cut and locally obscure the primary layers of bronzitite and harzburgite (Peoples and Howland 1940; Jones et al. 1960). Gradations from dunite through harzburgite into layered bronzitite have also been observed in a few outcrops (Jones et al. 1960). Olivine crystals in the layered dunites studied here are variable in size from mm to cm (Figure 5.1d, e, j). Orthopyroxene crystals are present as skeletal oikocrystals making up a very small proportion of the rock. Chromite is ubiquitous in the dunites, whereas plagioclase is rare.

Chromitite: In the Stillwater Complex, the chromite deposits are generally found with the poikilitic harzburgite (Peoples and Howland 1940; Jones et al. 1960) in the lower part of individual cyclic units. There are almost continuous gradations in places from nearly pure chromite to harzburgite with scattered chromite crystals (Jackson 1970; Cooper 1997). In chromitite, chromite and olivine are equigranular with various proportions (Figure 5.1f, g), and orthopyroxene occurs as oikocrysts including olivine

and chromite chadacrysts (Figure 5.1k–n). Olivine grains are relatively uniform in grain size compared to those in the silicate rocks (Figure 5.1g). Clinopyroxene may also be present as smaller poikilitic grains in some samples (Figure 5.1o–r) or as swarm-like grains associated with chromite within orthopyroxene (Figure 5.1l–n) or olivine (Figure 5.1s). It should be noted that the chromite grains enclosed in clinopyroxene show well-developed fractures (Figure 5.1p, q) and smoothed or poorly defined boundaries (Figure 5.1o–r) relative to those in orthopyroxene. The silicate minerals are mostly well preserved in disseminated chromitites, whereas they are partially or completely serpentinized in massive chromitites. It is also noticeable that olivine crystals in the studied samples are typically anhedral and exhibit peritectic texture with orthopyroxene rims (Figure 5.1b–n) and rarely show direct contact with chromite. In addition, the chromitite layers are commonly associated with mafic pegmatite layers (Jones et al. 1960). Those pegmatites associated with the chromitite horizons are stratiform or locally cross-cut other layers, and they contain all combinations of minerals found in the Ultramafic Zone (Jenkins and Mungall 2018).

5.1.2 Analytical methods

Olivine, orthopyroxene and clinopyroxene grains were handpicked under a binocular microscope, and together with reference materials were mounted in epoxy. The mount was then polished to expose the crystals, which were identified using both transmitted and reflected light images. The minerals were first analyzed for major elements using an electron probe microanalyzer (EPMA) followed by oxygen and then Li isotopes with a Cameca IMS-1280 secondary ion mass spectrometry (SIMS). Finally, trace elements were measured using laser ablation inductively coupled plasma mass spectrometry (LA-ICP-MS). The same spots of the mineral grains were selected for all measurements to yield corresponding element and isotope data. All analyses were conducted at the Institute of Geology and Geophysics, Chinese Academy of Sciences.

The major element analyses were carried out using a JEOL JXA8100 EPMA at an accelerating voltage of 15 kV and 10 nA beam current, 5 μm beam spot and 10–30 s

counting time on peak. Natural and synthetic mineral standards were used for calibration. A program based on the ZAF procedure was used for matrix corrections. Typical analytical uncertainty for all of the elements analyzed was better than 1.5%.

The SIMS oxygen isotope analyses of minerals were conducted using Cs^+ ions as a primary beam with ~ 10 μm diameter, and ~2 nA in intensity. The ^{16}O and ^{18}O ions are detected simultaneously by two faraday cups, and the signals were amplified by 10E10 ohm and 10E11 ohm resistors, respectively. A normal electron gun was used to compensate for the charging effect in the bombarded area. The entrance slit was set at ~120 μm; the field aperture at 6000 × 6000 μm^2; the energy slit at 40 eV, and the exit slit at ~500 μm. The magnification of the transfer system was configured as ~ 133. Each analysis consisted of pre-sputtering, beam centering, and signal collecting. The collecting process consisted of 16 cycles, each of which took 4 s. The $^{18}O/^{16}O$ ratios were normalized to VSMOW and expressed as $\delta^{18}O$. Standards used to correct instrument mass fractionation included olivine 06JY06OL ($\delta^{18}O$ = 5.20‰), orthopyroxene 06JY34OPX ($\delta^{18}O$ = 5.64‰) and clinopyroxene 06JY31CPX ($\delta^{18}O$ = 5.19‰) (Tang et al. 2019). Detailed analytical procedures are described by Li et al. (2010) and Tang et al. (2015, 2019).

After the oxygen isotope analyses, the same mount was again polished to remove the analytical spots and vacuumcoated with high-purity gold for Li isotope analyses. The O-primary ion beam was accelerated at 13 kV, with an intensity of about 15–30 nA. The elliptical spot was approximately 20 × 30 μm in size. Positive secondary ions were measured on an ion multiplier in pulse counting mode, with a mass resolution (M/DM) of 1500 and an energy slit open at 40 eV without any energy offset. A 60-s pre-sputtering with raster was applied before analysis. The secondary ion beam position in apertures, as well as the magnetic field and the energy offset, were automatically centered before each measurement. Eighty cycles were measured with counting times of 7 and 2 s for ^6Li and ^7Li, respectively. The measured δ^7Li values are given as δ^7Li ($[(^7Li/^6Li)sample/ (^7Li/^6Li)L\text{-}SVEC - 1] \times 1000$] relative to units of the standard NIST SRM 8545 (L-SVEC) with $^7Li/^6Li$ of 12.0192. The same standards as in oxygen isotope

analyses were used to correct instrument mass fractionation. The olivine standard 06JY06OL has a Mg# (100 × Mg/(Mg+ Fe)) value of 89.6, Li concentration of 2.23 ppm and δ^7Li of 5.34‰; the orthopyroxene standard 06JY34OPX has a Mg# of 92.1, Li concentration of 1.07 ppm and δ^7Li of −0.77‰; and the clinopyroxene standard 06JY31CPX has a Mg# of 91.1, Li concentration of 1.16 ppm and δ^7Li of −2.37‰ (Su et al. 2015). Lithium concentrations of the samples were calculated on the basis of $^7Li^+$ count rates (cps/nA) relative to the standard. The detection limit of Li was <1 ppb and uncertainties were mostly <0.90 ppm (1 σ). The internal errors of the Li isotopic compositions for both the standard and the olivine samples are less than 1.20‰ (1se). Matrix effects, in which δ^7Li increases by 1.0‰ for each mole percent decrease in the Mg# of olivine (Su et al. 2015), were considered for calibration. Detailed analytical procedures are described in Su et al. (2015, 2018).

After removing the gold coating on the mount, trace element compositions were determined with a 193 nm Coherent COMPex Pro ArF Excimer laser coupled to an Agilent 7500a ICP-MS. Each analysis was performed using 80 μm-diameter ablating spots at 6 Hz with an energy of ~100 mJ per pulse for 45 s after measuring the gas blank for 20 s. References materials NIST610 and NIST612 were used as external standards to produce calibration curves. Every eight analyses were followed by two analyses of the standards to correct for time-dependent drift. Calibration was performed using NIST612 as an external standard. Offline data processing was performed with the GLITTER 4.0 program using Mg for olivine and Si for orthopyroxene and clinopyroxene as internal standards, which were obtained by EPMA and shown in Table S12.2 of Appendix 12.

5.2 Results

All the rocks studied here are from the layer of poikilitic harzburgite containing chromite layer G (Figure 5.1). The samples include five chromitites and one harzburgite from the G chromitite layer and four harzburgites and two dunites from the silicate layer of the lower part of the peridotite subzone and its contact with basal zone (referred to

as the lowermost layer). Mineral compositional differences among the samples (Figs. 5.2, 5.3, 5.4) basically reflect variations between these two layers.

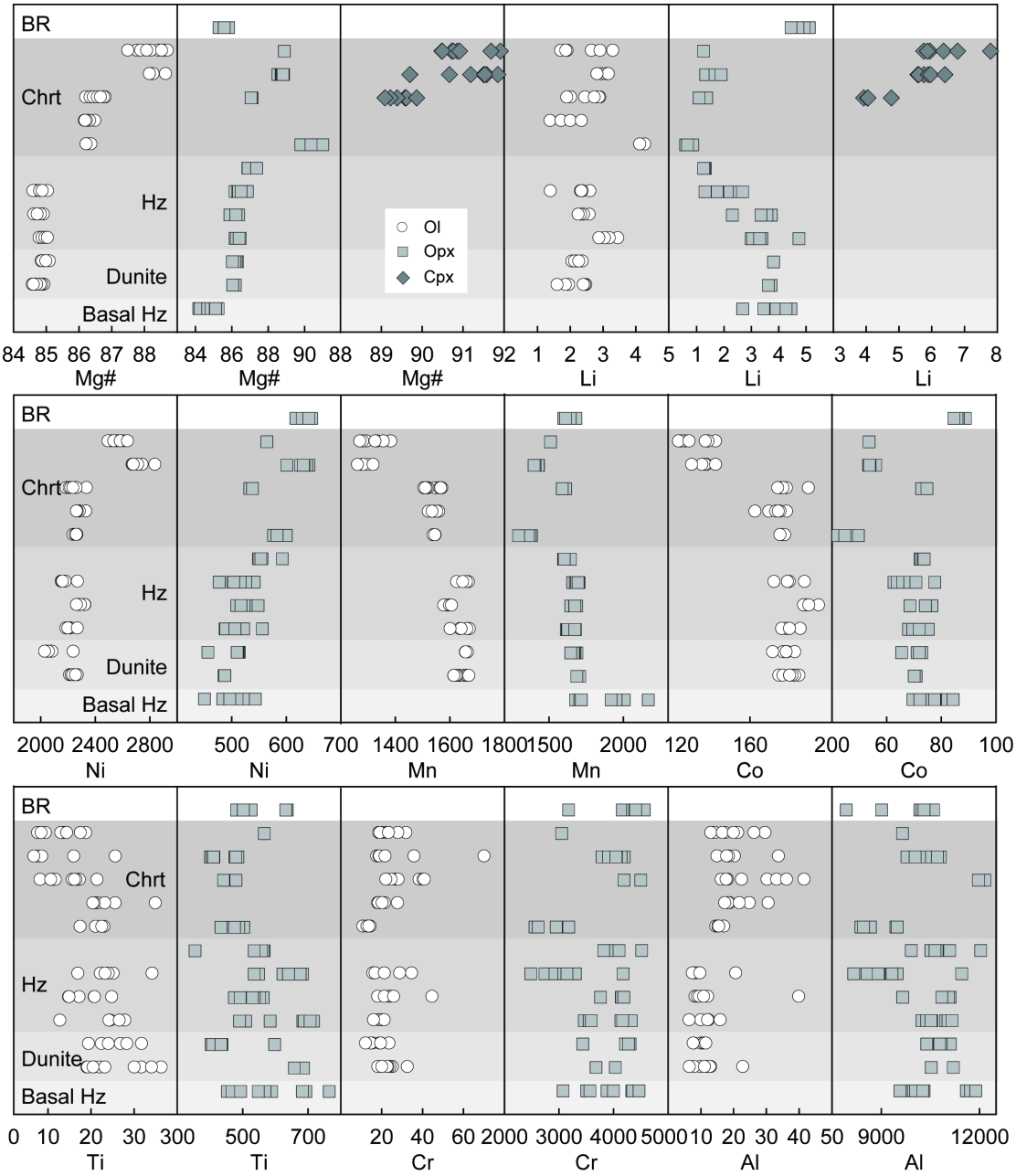

Figure 5.2 Major and trace element compositions of minerals in the stratigraphic section of the Ultramafic Zone of the Stillwater Complex. BR bronzitite, Chrt chromitite, Hz harzburgite

5.2.1 Major and trace elements

Elemental compositions of olivine, orthopyroxene and clinopyroxene in the rocks from the Stillwater Complex are illustrated in Figure 5.2. Olivine and orthopyroxene in

silicate rocks from the lowermost layer have lower Mg# values of 84–85 and 84–87, respectively, than those in the G chromitite (olivine Mg# = 86–89; orthopyroxene Mg# = 87–91), whereas clinopyroxene in chromitites has higher Mg# values of 89–92 (Table S12.2 in Appendix 12). These Mg# values overlap those of published datasets from the Stillwater Complex (Raedeke and McCallum 1984; Campbell and Murck 1993; McCallum 2002). The Li contents in olivine are relatively uniform in a range of 1–3 ppm; orthopyroxene shows highly variable Li contents from 0.5 to 5 ppm, with the lowest contents in orthopyroxene from the chromitite samples. Clinopyroxene grains in the three analyzed chromitite samples have the highest Li contents of 4–8 ppm (Table S12.2 in Appendix 12).

Transition elements in both olivine and orthopyroxene are distinctly different between the lowermost silicate layer and the G chromitite. The chromitites have overall larger variations and higher Ni concentrations in olivine and orthopyroxene than their counterparts in the harzburgites and dunites, whereas Mn, Co and Ti concentrations are lower (Figure 5.2). Cr concentrations in both olivine and orthopyroxene overlap values in different rocks types. The basal harzburgite and bronzitite samples commonly display maximum or minimum concentrations in these transition elements as well as in Mg# and Li content. In addition, olivine in chromitite has clearly higher Al contents than those in harzburgite and dunite, whereas Al concentrations in orthopyroxene show large inter- and intra-sample variations in all rock types (Figure 5.2).

Trace element concentrations of orthopyroxene obtained in this study (Table S12.2 in Appendix 12) are at the same levels as those in the Ultramafic Zone of the Stillwater Complex (Lambert and Simmons 1987) and those from the chromitite layers of the Bushveld Complex as given in Kaufmann et al. (2018) and Yang et al. (2019). Briefly, all these orthopyroxene crystals are characterized by relative enrichment in the heavy rare earth elements (HREE) relative to the light rare earth elements (LREE) and show large LREE variations (Figure 5.3a, b). Orthopyroxene grains in the harzburgites and bronzitites (Figure 5.3a) show remarkably negative Eu anomalies, as noted in the literature (Lambert and Simmons 1987), whereas grains in the dunites and

chromitites show no or weakly negative Eu anomalies (Figure 5.3b). The LREE concentrations of orthopyroxene are most enriched in bronzitite, the most depleted and variable in chromitite, and moderate in harzburgite and dunite. Clinopyroxene grains from the three chromitite samples show flat REE patterns with uniform LREE concentrations relative to HREE and slightly positive or negative Eu anomalies (Figure 5.3c), which are similar to those in chromitite from the Bushveld Complex (Yang et al. 2019).

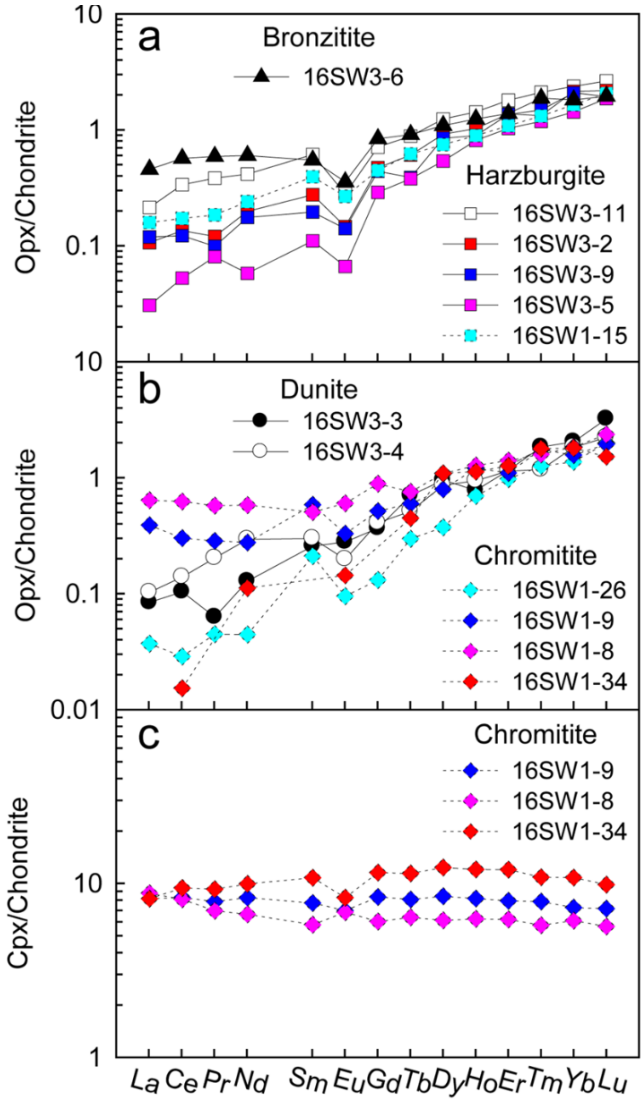

Figure 5.3 Chondrite-normalized rare earth element patterns of orthopyroxene (a, b) and clinopyroxene (c) in rocks from the Ultramafic Zone of the Stillwater Complex. Samples from the G chromitite zone are indicated in dashed lines, and samples from the lowermost layer in solid lines. Chondrite normalizing values are from Anders and Grevesse (1989)

5.2.2 Li and O isotopic compositions

Lithium isotopic compositions are highly variable with a decreasing δ^7Li order of olivine (4–26‰) > orthopyroxene (−13 to 7‰) > clinopyroxene (−14 to −6‰). The dunites and harzburgites from the lowermost layer and one harzburgite sample from the G chromitite have overlapping δ^7Li ranges in olivine and restricted δ^7Li variations in orthopyroxene, considerably higher than their counterparts in the G chromitites, whereas the orthopyroxene grains in the basal harzburgite and bronzitite have the lowest δ^7Li values (Figure 6a).

In contrast to Li isotopes, oxygen isotopic compositions are rather homogeneous in olivine, orthopyroxene and clinopyroxene. Regardless of the host lithology, olivine has limited δ^{18}O variation from 4.91 to 5.72‰ (except for one analysis of 4.45‰), overlapping the δ^{18}O values of clinopyroxene (4.64–5.86‰) and orthopyroxene (5.11–5.87‰) (Table 5.1), slightly lower than the values of orthopyroxene (5.7, 5.9 and 6.4‰) in mafic rocks of the Stillwater Complex (Dunn 1986) (Figure 5.4b).

For convenience in the following discussion, Cr isotopic compositions reported in Bai et al. (2019) are also illustrated in Figure 5.4c. Except for the basal harzburgite sample 16SW3-11 which has similar δ^{53}Cr values in all its minerals, all the analyzed samples exhibit significant isotope fractionation between chromite and silicates. Olivine has higher δ^{53}Cr values and larger variations than coexisting orthopyroxene, whereas δ^{53}Cr values in chromite are uniform within analytical uncertainty (Bai et al. 2019).

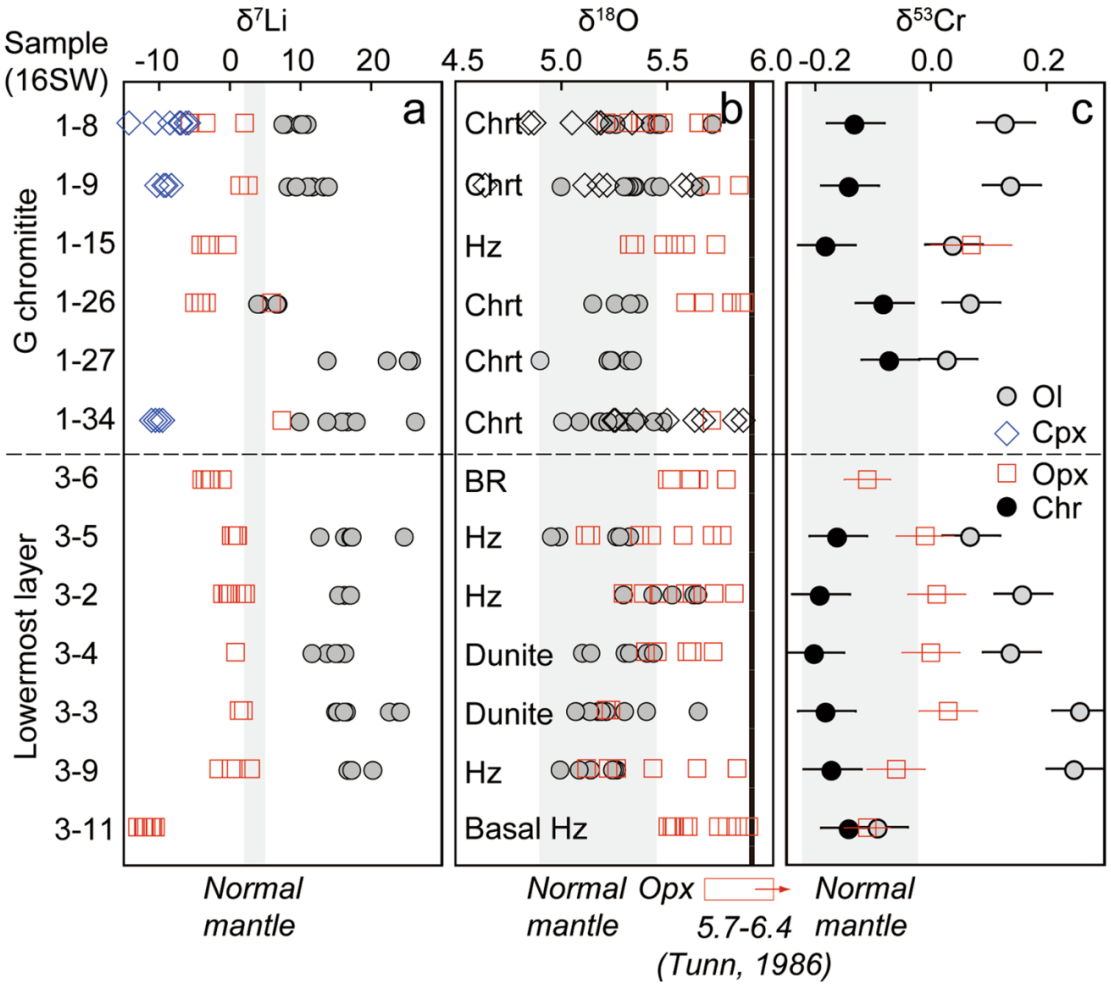

Figure 5.4 Li–O–Cr isotopic compositions of minerals in the stratigraphic section of the Ultramafic Zone of the Stillwater Complex. Oxygen isotopic compositions of orthopyroxene in peridotites of the Ultramafic Zone of the Stillwater Complex from Dunn (1986) are also plotted for comparison. The Cr isotopic data are from Bai et al. (2019). Normal mantle ranges of δ^{7}Li (2.0–5.0‰), δ^{18}O (4.90–5.46‰) and δ^{53}Cr (−0.22 to −0.02‰) are from Elliott et al. (2006), Mattey et al. (1994), and Schoenberg et al. (2008), respectively. The bold black line in (b) represents a calculated δ^{18}O value of 5.9‰ for the parental magma of the Stillwater Complex (Dunn 1986).

5.3 Effects of subsolidus element exchange on disequilibrated isotopic fractionations between minerals

The subsolidus element exchange between minerals is presumably extensive in the long cooling history of large layered intrusions (McCallum 2002; Schulte et al. 2010),

and its effects on minerals depend on their composition and modal proportion (Jackson 1969; Xiao et al. 2016). Theoretically, the primary compositions of silicates are retained in silicate rocks whereas the silicates in chromitite have undergone extensive subsolidus exchange with chromite (Irvine 1967; Mondal et al. 2006; Mukherjee et al. 2010). In chromitites, olivine and pyroxenes reach their maximum Mg#s and Ni contents and their minimum Mn, Co and Ti contents (Figure 5.2), whereas the reverse compositions were observed in the associated chromite (Campbell and Murck 1993; Schulte et al. 2010). This is consistent with chemical exchange between silicate and chromite because elements such as Mg and Ni in chromite are relatively incompatible compared to Fe, Mn, Co, and Ti (Su et al. 2019).

Likewise, Cr is a major component in chromite but is typically present only as a trace to minor element in olivine and pyroxenes. Its diffusion from silicates to chromite should lead to negligible fractionation of Cr isotopes in chromite but significant fractionation in silicates, particularly for those in chromitites. This prediction, however, contradicts the measured inter-mineral δ^{53}Cr fractionations of silicate rocks > chromitites (Figure 5.4c; Bai et al. 2019). Moreover, in our basal harzburgite and bronzitite samples, identical δ^{53}Cr values in orthopyroxene and olivine to chromite (Figure 5.4) cannot be attributed to subsolidus element exchange between them.

The presence of orthopyroxene between olivine and chromite implies that in subsolidus exchange between olivine and chromite, if occurred, would have been impeded by the orthopyroxene mantles around the olivine grains. Because there are extremely low Li contents in chromite (Su et al. 2016, 2018), the occurence of Li in olivine would reflect isotopic exchange between orthopyroxene and olivine. Because of higher partition coefficient of Li in olivine than in orthopyroxene (Seitz and Woodland 2000), Li is expected to diffuse from orthopyroxene to olivine, resulting in Li depletion and δ^{7}Li elevation in orthopyroxene and the reverse in olivine as ^{6}Li diffuses faster than ^{7}Li (Richter et al. 2003).

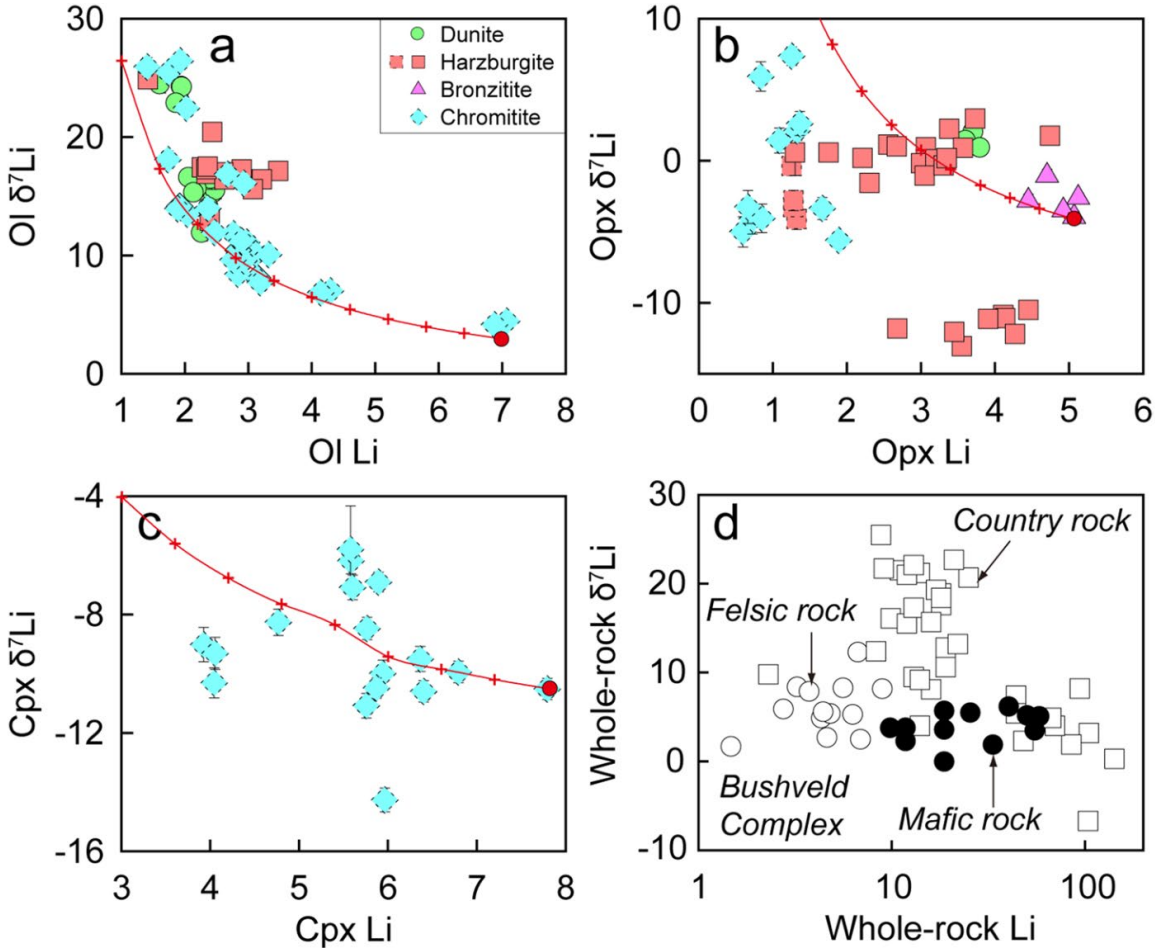

Figure 5.5 Correlation diagrams of Li and δ7Li for olivine (a), orthopyroxene (b) and clinopyroxene (c) in rocks from the Ultramafic Zone of the Stillwater Complex, with comparison of data from the Bushveld Complex (Ireland and Penniston-Dorland 2015) (d). Red solid line with stars in (a–c) is the modeling result of Li diffusion between solid phases and interstitial liquid using a Rayleigh distillation process. Initial compositions of olivine are assumed as 7 ppm Li and 3.0‰ δ^7Li, and the compositions of the interstitial liquid are the mean values of orthopyroxene (Li = 3 ppm; δ^7Li = −2.0‰). Initial compositions of orthopyroxene are assumed as 5 ppm Li and −4.0‰ δ^7Li of the Li-richest analysis, and the compositions of the interstitial liquid are 4 ppm Li and −11.6‰ δ^7Li of the δ^7Li-lowest analysis. Initial compositions of clinopyroxene are assumed as 7.8 ppm Li and −10.5‰ δ^7Li of the Li-richest analysis, and the compositions of the interstitial liquid are 6 ppm Li and −14.3‰ δ^7Li of the δ^7Li-lowest analysis. Samples from the G chromitite zone are indicated in dashed symbols, and samples from the lowermost layer in solid symbols.

It is, however, opposite to the obtained data (Figs. 5.5a, b, 5.6a, b), particularly, in some of our samples olivine has more variable and higher δ^7Li values than orthopyroxene (Figure 5.2a), although Li contents and δ^7Li values of olivine plot along the modeling results of diffusion process (Figure 5.5a). The relationship can apply to compositional variations between poikilitic clinopyroxene and olivine (Figs. 1o–s, 5.5c, 5.6c). Most olivine grains exhibit Li enrichment and δ^7Li depletion in their rims relative to their cores (Figure 5.7), consistent with expected trends of ingressive diffusion. However, Li contents and δ^7Li values of orthopyroxene and clinopyroxene in similar rimcore profiles (Figure 5.7) and their distributions in the entire dataset are totally inconsistent with experimental diffusion trends (Figure 5.5b, c). Therefore, the compositional variations of the minerals in the Ultramafic Zone of the Stillwater Complex cannot be explained solely by subsolidus element exchange, and complex δ^7Li profiles in olivine grains at inter- and intra-sample scales suggest additional processes to account for their compositional characteristics.

5.4 Effects of crustal contamination on mineral Li and O isotopic compositions

The properties of Li, a moderately incompatible and fluidmobile element with a mass difference of ~17% between the two stable isotopes (^{6}Li and ^{7}Li), make it a useful tracer for various melt/fluid–rock interactions (Chan et al. 1992; Su et al. 2014, 2018). Crustal contamination in mantle-derived magmas can be identified by Li isotope systematics, because crustal rocks typically have higher Li concentrations (several to hundreds ppm) and more variable but overall higher δ^7Li values than mantle rocks (Tomascak et al. 2016). Studies of the Bushveld Complex revealed that involvement of country rocks resulted in significant elevation of Li concentrations in mafic rocks (Li > 10 ppm) and felsic ones (Li< 10 ppm) but only slight δ^7Li variations in bulk rock samples (Figure 5.5d) (Ireland and Penniston-Dorland 2015). Since olivine and pyroxene are the major hosts of Li in the studied rocks from the Stillwater Complex, their <7 ppm Li concentrations and large δ^7Li variations (Figure 5.5a–c) could approximately represent whole-rock compositions and are apparently inconsistent with

indicators of contamination in the Bushveld Complex. The negative correlation between Li and δ^7Li in the olivine (Figure 5.5a) and the lack of their correlations in either orthopyroxene or clinopyroxene (Figure 5.5b, c) in the Stillwater Complex suggest insignificant effects of crustal contamination on their Li isotope systematics.

Previous studies of O isotopes of the Stillwater Complex revealed that the intrusion has retained its magmatic isotopic composition with a calculated δ^{18}O value of 5.9‰ (Dunn 1986), agreeing well with mantle-derived melts (~5.7‰, Eiler 2001). These values show that most of the isotopic variations within the complex can be accounted for by simple fractional crystallization (Dunn, 1986). The δ^{18}O ranges of both olivine and pyroxenes in the Ultramafic Zone of the complex are between normal mantle values and those estimated for the entire complex (Figure 5.4b), indicating negligible effects of crustal contamination on O isotope systematics. The O isotopic compositions of these minerals do not co-vary with δ^7Li values (Figure 5.6a–c), which is inconsistent with the contamination trend defined from the studies of the Bushveld Complex (Figure 5.6d; Ireland and Penniston-Dorland 2015). Hence, crustal contamination, if it occurred, did not significantly modify the Li and O isotopic compositions of the parental magma of the Stillwater Complex. In addition, large inter-sample δ^7Li and intra- and inter-sample δ^{18}O variations of orthopyroxene and clinopyroxene cannot be explained by incongruent melting, which would not produce Li and O isotopic fractionation but significant Li depletion.

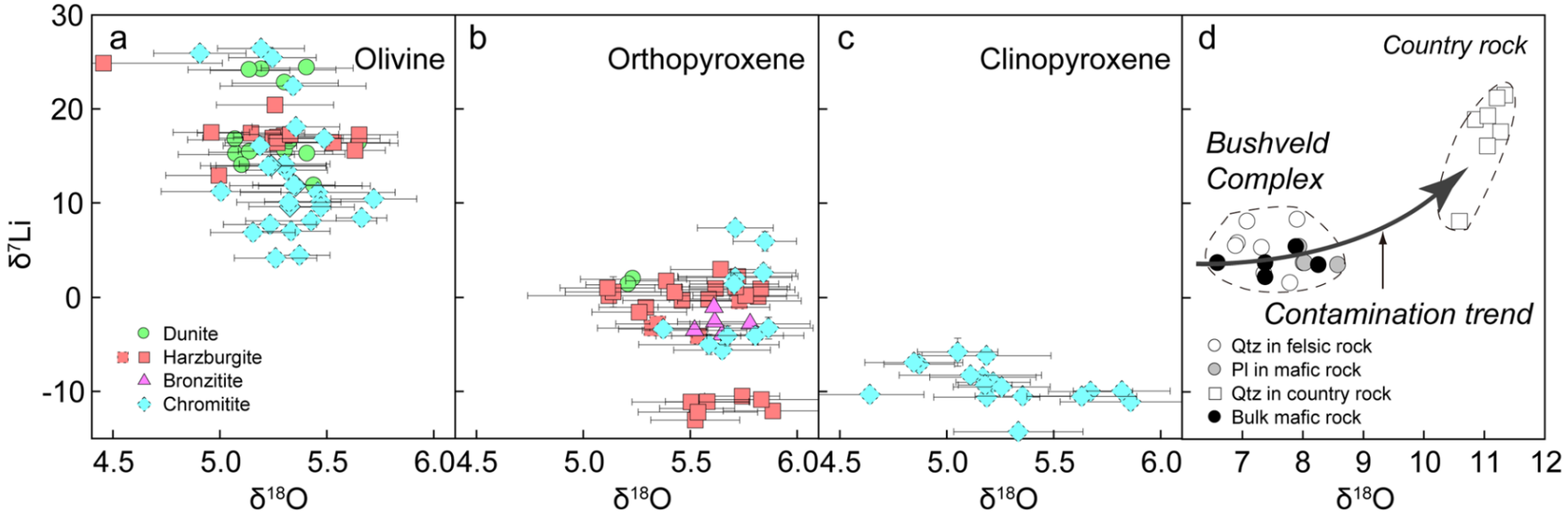

Figure 5.6 Correlation diagrams of $\delta^{18}O$ and $\delta^{7}Li$ for olivine (a), orthopyroxene (b) and clinopyroxene (c) in rocks from the Ultramafic Zone of the Stillwater Complex, with comparison of data from the Bushveld Complex (Ireland and Penniston-Dorland 2015) (d). Samples from the G chromitite zone are indicated in dashed symbols, and samples from the lowermost layer in solid symbols.

5.5 Links between mineral composition, mineral assemblage and crystal size, and controls of magma differentiation

Compositionally, there are no observable variations in terms of element concentrations and Li and O isotopes in olivine from the Stillwater harzburgites and dunites, but abrupt changes, particularly in Mg#, transition metal element contents, and Li and Cr isotopes, are obvious between silicate rocks and chromitite seams (Figs. 5.2, 5.4), probably related to cooling and re-equilibration between minerals and/ or interstitial liquids. Correspondingly, in transitions from chromitite and dunite to poikilitic harzburgite and bronzitite chromite and olivine abundances generally show gradually decreasing trends whereas orthopyroxene, clinopyroxene and plagioclase increase. The average chromite crystal size increases uniformly upward from the base within an individual cyclic unit (Figure 1g; Boudreau 2011), but then decreases abruptly directly above the chromitite seam. From there it increases monotonically to the top of the unit (Figs. 1; Cooper 1990). In general, increases in olivine crystal size are most conspicuous in poikilitic harzburgites and some dunites (Figure 1b–e; Boudreau 2011). These links between mineral assemblage, crystal size and chemical composition are also compatible to field observations. A regular decrease in the size and abundance of orthopyroxene oikocrysts in olivine-rich rocks occurs near gradational contacts or, more rarely, sharp contacts between dunite and poikilitic harzburgite over a meter scale (Jones et al. 1960; Jackson 1961; Jenkins and Mungall 2018). The sharp physical contact and the abrupt chemical changes have been related to breaks in injection of magma into the chamber (Jackson 1970) or truncation of the previous cyclic unit by a low-angle magmatic unconformity (Cooper 1997). Both explanations imply distinct parental magmas or various postcumulus modifications for chromitites and silicate rocks or abrupt compositional changes of a single magma pulse during formation of an individual unit.

The inter-lithological compositional differences might also be controlled by crystallization sequence and the spatial relations of minerals. This inference is supported by a lack of negative Eu anomalies and slight LREE enrichment in

orthopyroxene and clinopyroxene in some chromitite samples (e.g., 16SW1-8; Figure 5.3b, c) in which plagioclase is absent, because plagioclase normally accommodates large amounts of LREE and Eu (Lambert and Simmons 1987). Consequently, REE patterns of orthopyroxene in harzburgite and bronzitite (Figure 5.3a) suggest that these rocks formed from an evolved magma which had previously experienced plagioclase fractionation. In a few chromitite samples LREE depletion and Eu anomalies of their pyroxenes (Figure 5.3b, c; Lambert and Simmons 1987) suggest that the parental magmas of these chromitites experienced concurrent crystallization of plagioclase (McCallum 1996) or mixing with an evolved magma.

Isotopically, the generally decreasing trend of δ^7Li values (and the increasing trend of Li contents in the lowermost layer) from olivine to orthopyroxene and clinopyroxene (Figure 5.6a–c) is consistent with magma differentiation, which normally results in Li increasing and 6Li enrichment in evolving melts (Su et al. 2017), and further confirms the crystallization order of these coexisting minerals. The Li content and δ^7Li co-variations in rim-core profile analyses of orthopyroxene and clinopyroxene (Figure 5.7) reveal their growth from evolving magmas. Taking into account intersample variations, δ^7Li values in olivine, although negatively correlated with Li concentrations as a whole, show larger variations in chromitite than in silicate rocks (Figure 5.5a). This indicates formation from distinct parental magmas or various post-cumulus modifications. Moreover, the absence of correlations between Li and δ^7Li in orthopyroxene and clinopyroxene (Figure 5.5b, c) is compatible with crystallization from different parental magmas.

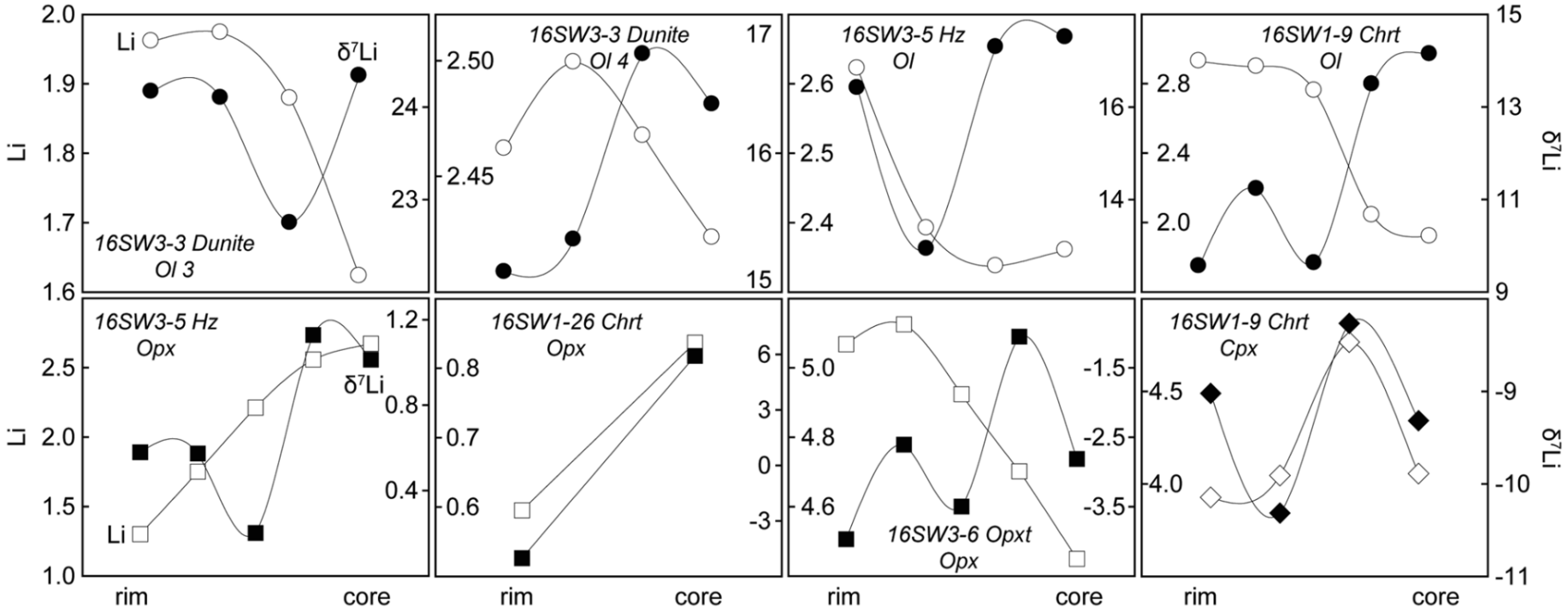

Figure 5.7 Representative rim-core profile analyses of Li elemental and isotopic compositions of mineral grains in rocks from the Ultramafic Zone of the Stillwater Complex.

5.6 Formation of poikilitic pyroxenes

The above discrepancies are closely related to the formation of orthopyroxene and clinopyroxene oikocrysts in large layered intrusions. The formation of poikilitic textures is dependent on differences in the nucleation rate and/or the growth rate of the different minerals; oikocrysts form if one mineral has a lower nucleation rate but higher growth rate than co-accumulating crystals of another phase (Kaufmann et al. 2018). Three main hypotheses have been proposed: (1) Oikocrysts form in the post-cumulus stage by solidification of interstitial liquid (e.g., Wager et al. 1960); (2) they are cotectic grains lacking compositional zonation but having compositions typical of primocrysts of the same phase (Barnes et al. 2016). (3) Pyroxene oikocrysts form by reactive replacement of olivine primocrysts by upward-percolating melts, followed by poikilitic overgrowth of oikocryst cores from a more primitive melt (Kaufmann et al. 2018).

The occurrence and morphological features of chromite and olivine in ultramafic rocks show that they are cumulus phases (Figure 1b–s; Jackson 1961; McCallum 1996; Cooper 1997). The nature of contacts between chromite and olivine through orthopyroxene or clinopyroxene does not always fit the classic cumulus model. For example, most chromite grains in the Ultramafic Zone are surrounded by pyroxenes and the abundance of chromite in different sections varies. Where chromite is concentrated in thin and massive layers, the interstitial mineral is largely orthopyroxene, whereas where chromite is less abundant, olivine is more abundant (Howland et al. 1949). These characteristics suggest that chromite and olivine did not crystallize simultaneously in cotectic proportions, rather the chromite grains appear to have been transported by liquids, from which the pyroxenes crystallized, and were then emplaced within cumulus olivine piles. The intrusion of chromite-rich liquids physiochemically modified the olivine grains before their complete solidification. The olivine crystals were smoothed to round shapes (Figure 1b–s), and the presence of tiny olivine remnants in pyroxene (Figure 1m) indicates reaction replacement. The reaction should have been less extensive than that observed in the Bushveld complex, where orthopyroxene oikocrysts are larger but contain fewer remnants of olivine (Kaufmann et al. 2018). The

narrow variation of intra-grain Li isotopic compositions (Figs. 5.4a, 5.7) and the absence of a negative correlation between δ7Li and Li abundance (Figure 5.5b, c) in the pyroxenes reflect no significant elemental diffusion after crystallization. We thus conclude that poikilitic pyroxenes formed from a chromite-saturated liquid, which added an external component to cumulus olivine piles and resulted in replacive reaction of the olivine.

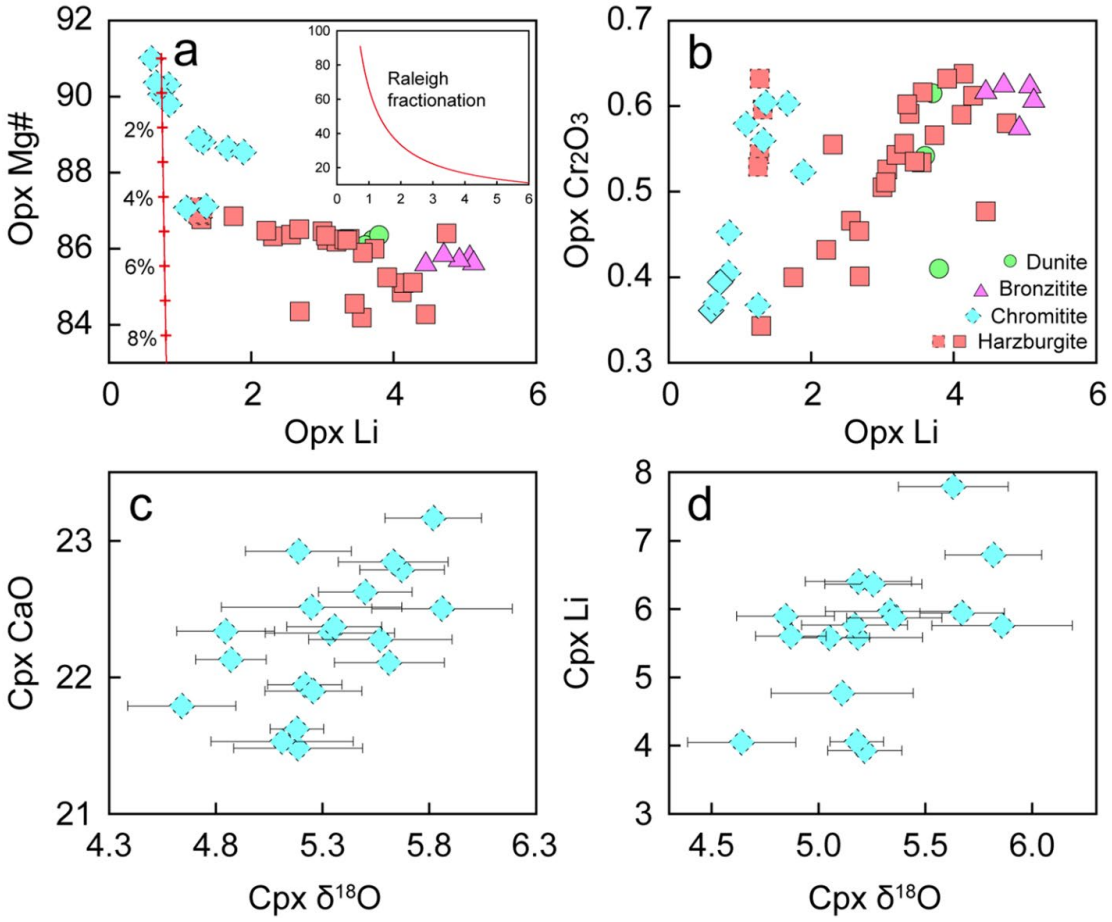

Figure 5.8 Correlation diagrams of Li vs. Mg# (a) and Cr_2O_3 (b) for orthopyroxene and $\delta^{18}O$ vs. CaO (c) and Li (d) for clinopyroxene in rocks from the Ultramafic Zone of the Stillwater Complex. Raleigh fractionation calculation shown in a indicates that orthopyroxene crystallized from compositionally varying melts. Samples from the G chromitite zone are indicated in dashed symbols, and samples from the lowermost layer in solid symbols.

The compositions of pyroxene crystallized from chromite-rich magma would depend on competition for elements posed by the co-precipitating chromite. The most

intense competitions will be for Fe, Cr, Al, and Mg rather than Ca, Li and O owing to their contrasting partition coefficients between chromite and pyroxenes (Schulte et al. 2010). As a consequence, in a given cycle in the Stillwater Complex from chromitite through harzburgite to bronzitite, orthopyroxenes show significant Li increases with only small changes in Mg# (Figure 5.8a), whereas a generally positive correlation between Li and Cr_2O_3 (Figure 5.8b) reflects decreasing competition for Cr due to lower chromite crystallization. These relationships are further supported by positive correlations between $\delta^{18}O$ values and CaO and Li concentrations in the clinopyroxene (Figure 5.8c, d). Similarly, because chromite structurally contains very minor or no REE, its crystallization would have negligible effect on the overall REE abundance. The increasing enrichment of LREE in orthopyroxene from chromitite to bronzitite (Figure 5.3a, b) reflects a trend of fractional crystallization or compositional change of the parental magma. The Li isotopic compositions of the orthopyroxene are homogeneous in individual samples but are heterogeneous on a larger scale (Figure 5.4a), further suggesting that the melts, from which orthopyroxene crystallized, had locally uniform δ^7Li values but highly varying within the magma chamber. Compositional changes in the melts were likely due to mixing between fractionated magma and newly injected primitive melts because the variations in $\delta^{18}O$ of the orthopyroxene fluctuate between normal mantle values and those of the estimated parental magma of the Stillwater Complex (Figure 5.4b). This inference receives further support from an apparent shift of the orthopyroxene data from Raleigh fractionation line (Figure 5.8a).

5.7 Reaction between interstitial liquids and cumulus minerals

Olivine grains in the Stillwater chromitites have larger compositional variations, particularly in terms of major and trace elements (Figure 5.2) and Li, O and Cr isotopes (Figs. 5.4, 5.5a, 5.6a) than those in the silicate rocks. This indicates complex processes involved in the olivine formation. For a given sample, olivine displays more variable and higher δ^7Li but lower $\delta^{18}O$ values than orthopyroxene, indicating that olivine

experienced more extensive post-crystallization compositional modification than the orthopyroxene. Modeling results assuming the highest-Li analysis as initial compositions of olivine and mean values of orthopyroxene as the compositions of interstitial liquid demonstrate that negative correlations between Li and δ^7Li in olivine can be attributed to kinetic diffusion with interstitial liquid (Figure 5.5a).

The observed positive correlation between δ^7Li and δ^{53}Cr values in olivine (Figure 5.9a) would not have been generated by Cr diffusion from olivine to chromite (Xia et al. 2017; Bai et al. 2019). Instead, Cr isotopic changes of the reacting liquids due to chromite crystallization were more likely responsible for the δ^{53}Cr variations in the olivine, which is evident from the positive correlation between chromite δ^{53}Cr and olivine δ^7Li (Figure 5.9b). Constant δ^{18}O values in olivine showing no correlation with either δ^{53}Cr or δ^7Li indicate no visible modification (Figs. 5.5a, 5.9c) in O isotopes in olivine during its reaction with the liquids, which were probably newly injected primitive magma (Raedeke and McCallum 1984; Campbell and Murck 1993; Lipin 1993; Cawthorn et al. 2005). The absence of co-variations between δ^7Li, δ^{18}O and δ^{53}Cr values in pyroxenes, chromite and olivine (Figs. 5.5b, c, 5.9d–f) further confirms the isotopic variations are related to the reacting liquid. Development of fractures and poorly-defined grain boundaries of some chromite grains enclosed within clinopyroxene (Figure 1p–r) demonstrates physical as well as composition modification by the liquids. Low δ^{18}O values (2.2 and 3.2‰) of chromite from the Stillwater Complex reported by Mondal et al. (2003) are consistent with high-temperature alteration.

The interstitial liquid, from which pyroxenes mainly crystallized, reacted with the olivine and significantly modified its chemical composition (Barnes 1986) (Figure 5.4). Simultaneously the compositions of the interstitial liquid were also modified. As the chromite grains collected hydrous fluids on their crystal surfaces due to the wetting property of chromite (Matveev and Ballhaus 2002), chromite compaction would lead to expelling of the hydrous fluids and outward penetration or upward transportation (Su et al. 2020). Outward penetration yielded additional modification on olivine

compositions and occasionally on chromite. The fluids are believed to have been the parent magma of clinopyroxene and some hydrous minerals in stratiform and podiform chromitites (McDonald 1965; Matveev and Ballhaus 2002; Boudreau 2016; Johan et al. 2017; Su et al. 2019, 2020), and, thus, they were likely sources of clinopyroxene crystals in chromite seams and pegmatites in the Stillwater Complex. During formation of the harzburgite and bronzitite layers, infiltration of upward ascending hydrous fluids from the chromite seams would have enhanced chemical exchange between cumulus minerals (Bai et al. 2019; Su et al. 2020). The evolved magma after separation from the ultramafic cumulates would have become a new starting point of a repeated process of magma mixing and subsequent formation of a new cyclic unit.

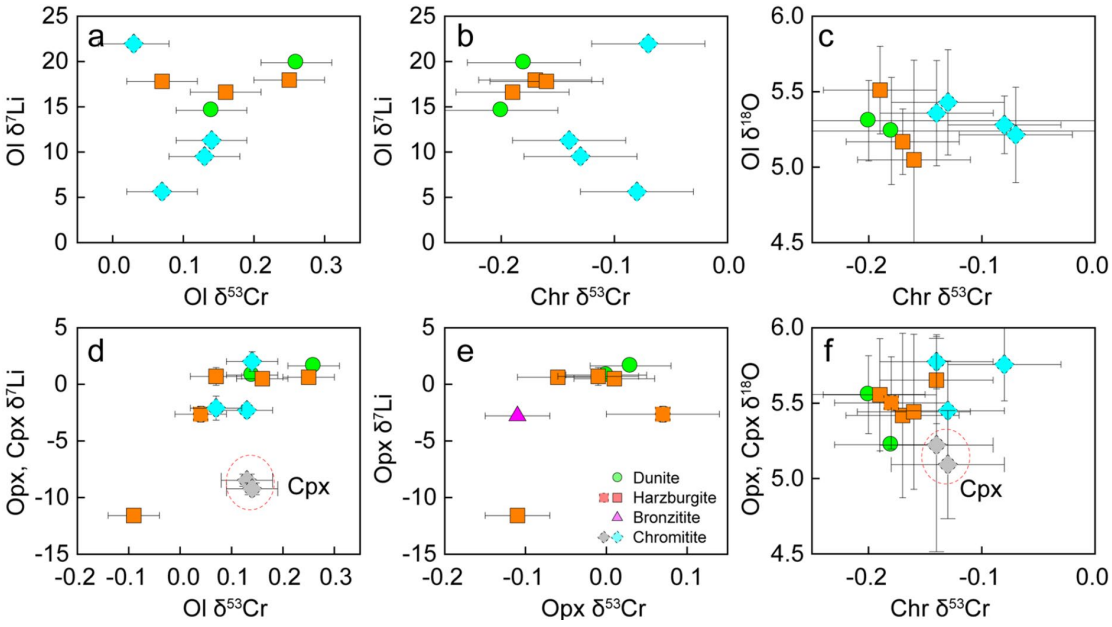

Figure 5.9 Multiple correlation diagrams of average $\delta^{18}O$, average $\delta^{7}Li$ and $\delta^{53}Cr$ values for minerals in rocks from the Ultramafic Zone of the Stillwater Complex. Clinopyroxene data are indicated in gray in plots (d) and (f). Samples from the G chromitite zone are indicated in dashed symbols, and samples from the lowermost layer in solid symbols.

6. FTIR study of H_2O in silicate minerals and mineral inclusions in chromite from the peridotite zone of the Stillwater complex (Montana, USA): Evidence for chromitite formation in an H_2O-rich environment[4]

[4] This chapter is published in The Geological Society of America Bulletin - Bai, Y., Cui, M. M., Su, B. X., Liu, X., Xiao, Y., Robinson, P. T., Gu, X. Y. 2023. FTIR study of H_2O in silicate minerals and mineral inclusions in chromite from the peridotite zone of the Stillwater complex (Montana, USA): Evidence for chromitite formation in an H_2O-rich environment. GSA Bulletin. doi.org/10.1130/B36733.1

Chromitite seams within layered intrusions host most of the world's chromium reserves. The formation mechanism of these nearly monomineralic chromite deposits has been extensively studied but remains unresolved. The most widely accepted models involve mixing of fractionated and primitive magmas (e.g., Irivine, 1975, 1977; Raedeke and McCallum, 1984; Campbell and Murck, 1993; Cawthorn et al., 2005; Eales and Costin, 2012; Jenkins and Mungall, 2018) and assimilation of silica-rich country rock (e.g., Alapieti et al., 1989; Horan et al., 2001; Spandler et al., 2005). These processes are thought to move the ambient melts to the stability field of chromite allowing it to crystallize as the sole liquidus phase. Drop or increase in pressure and oxygen fugacity have also been proposed to expand the field of monomineralic chromite crystallization (e.g., Lipin, 1993; Latypov et al., 2018). The major problem with all these models is that crystallization of chromite alone would rapidly consume the limited chromium in a silicate melt causing crystallization to shift rapidly towards multiphase cotectic equilibrium. In this case, most of the chromite grains would soon crystallize coevally with silicate minerals producing chromite-rich dunites and peridotites rather than nearly monomineralic chromitite seams (Pebane and Latypov, 2017; Latypov and Chistyakova, 2020).

For many years, it was thought that substantial annealing and overgrowth of settled chromite grains could increase the volume of chromite in single layers to form nearly monomineralic chromitite seams (e.g., Hess, 1960; Jackson, 1961; Eales, 1987; Campbell and Murck, 1993). However, the minor amount of chromium in late interstitial melts would likely cause coarsening of individual grains rather than increasing the modal percent of chromite. Nicholson and Mathez (1991) proposed that incongruent melting of a chromite-orthopyroxene-olivine mush would preferentially remove the silicate minerals leaving chromite as a residual mineral to form nearly the chromitites (Mathez et al., 1997; O'Driscoll et al., 2009). Another model highlights the significance of fluids in the melts of the layered intrusion, based on the presence of hydrous melt inclusions in chromite and olivine from rocks of the Ultramafic Series (e.g., Spandler et al., 2005; Boudreau, 2016, 2019). On the other hand, Jenkins and

Mungall (2018) suggested that chromite and olivine begin to precipitate in deep, magma sources, and are then carried upward by low-viscosity melts or liquids in the conduit. The chromite would settle preferentially from the rising melts, and be deposited as a cumulate pile that then could undergo spontaneous mechanical sorting to form nearly monomineralic chromitite layers (Forien et al., 2015; Pebane and Latypov, 2017; Latypov and Chistyakova, 2020). Currently, the presence of low-viscosity melts or liquids in mafic magma chambers is commonly considered to be a critical factor in the formation of chromitite seams (e.g., Maier et al., 2013; Boudreau, 2016; Mungall et al., 2015; Mukherjee et al., 2017; Jenkins and Mungall, 2018; Veksler and Hou, 2020).

The discovery of hydrous mineral inclusions in chromite grains attests to the presence of fluids in the parental magmas of podiform chromitites (e.g., Lorand and Ceuleneer, 1989; Melcher et al., 1997; Liu et al., 2019; Su et al., 2020a). Such fluids can enhance the migration and convergence of chromite grains by flotation or sinking (e.g., Edwards, 2000; Matveev and Ballhaus, 2002; Li et al., 2005; Feig et al., 2010; Johan et al., 2017; Rollinson et al., 2018; Friedrich et al., 2019; Su et al., 2020a, 2021), leading to formation of chromitite seams. Cl-rich apatite inclusions in olivine and interstitial amphibole are also considered to furnish evidence that the chromitites formed from hydrous parental magmas (Page and Zientek, 1987; Nicholson and Mathez, 1991; Boudreau, 2016; Wang et al., 2020). Sufficient fluids in a melt can change the olivine-orthopyroxene cotectic equilibrium to a peritectic relationship (Boudreau, 2016), which suggests that poikilitic harzburgite, the typical host of the chromite, crystallized from fluid-enriched magmas (Jackson, 1961; Kaufmann et al., 2018; Su et al., 2020b).

Various primary mineral and fluid inclusions entrapped in chromite are valuable in documenting characteristics of chromitite parent magmas and their conditions, such as temperature and oxygen fugacity responsible for the agglomeration of chromite grains (e.g., Melcher et al., 1997; Zhou et al., 2014; Liu et al., 2019). In this paper, we focus on mineral inclusions in chromite grains from the chromitite seams of the Stillwater Complex, a typical large layered intrusion worldwide. The morphology,

texture and chemical compositions of these inclusions are documented to investigate the hydrous nature of the parent magma, and to provide comparisons of silicate minerals in the matrix of the chromitites and the overlying cumulates with similar minerals included in chromite. A theoretical maximum H_2O-solubility for the parent magma of the Peridotite Zone of the complex was modeled to compare with calculated H_2O contents based on FTIR measurements of minerals. Finally, we propose an appropriate mechanism for the mechanical sorting of chromite grains to explain the origin of the numerous, nearly monomineralic chromitite seams in the Stillwater Complex.

6.1 Sample description and analytical methods

6.1.1 Sample description

Hundreds of individual polymineralic inclusions in chromite grains from different types of samples were also described here for their distribution and morphology during the investigations of the polished thin sections of collected samples (analytical conditions of back-scattered electron images are presented in Table S13.1 in the Appendix 13). The inclusions are abundant, commonly occurring in up to 10% of the chromite grains (Figure 6.1 and Figure S12.1 in Appendix 12). They typically occur in the cores and mantles of the chromite grains (Figure 6.1a-f) as single features (Figure 6.1a-b), or as small clusters (Figure 6.1c-h). In the latter case, inclusions may comprise up to 30% of the surface of the host grain (Figure 6.1g). Most of the inclusions range from 0.01 to 0.1 mm in size, and when they occur in clusters the central inclusion is typically the largest (Figure 6.1h). Several silicate phases can be recognized in most inclusions, locally accompanied by minor apatite and sulfides (Figure 6.1 and Figure S12.2 in Appendix 12). Orthopyroxene, hornblende and plagioclase +/– phlogopite are the most common silicate phases (Figure 6.1i-p). Most inclusions are circular (Figure 6.1i, g) or polygonal (Figure 6.1k, l) and typically have sharp boundaries with the host. However, in some cases the host chromite may extend into an inclusion (e.g., Figure 6.1m), producing irregular or rugged boundaries (Figure 6.1m, n) marked by irregular minute inclusions (Figure 6.1o, p). Similar textural features of inclusions have also been

reported in the Merensky Reef of the Bushveld Complex (McDonald, 1965; Li et al., 2005) and in a massive chromitite layer of the Jacurici Complex (Friedrich et al., 2019).

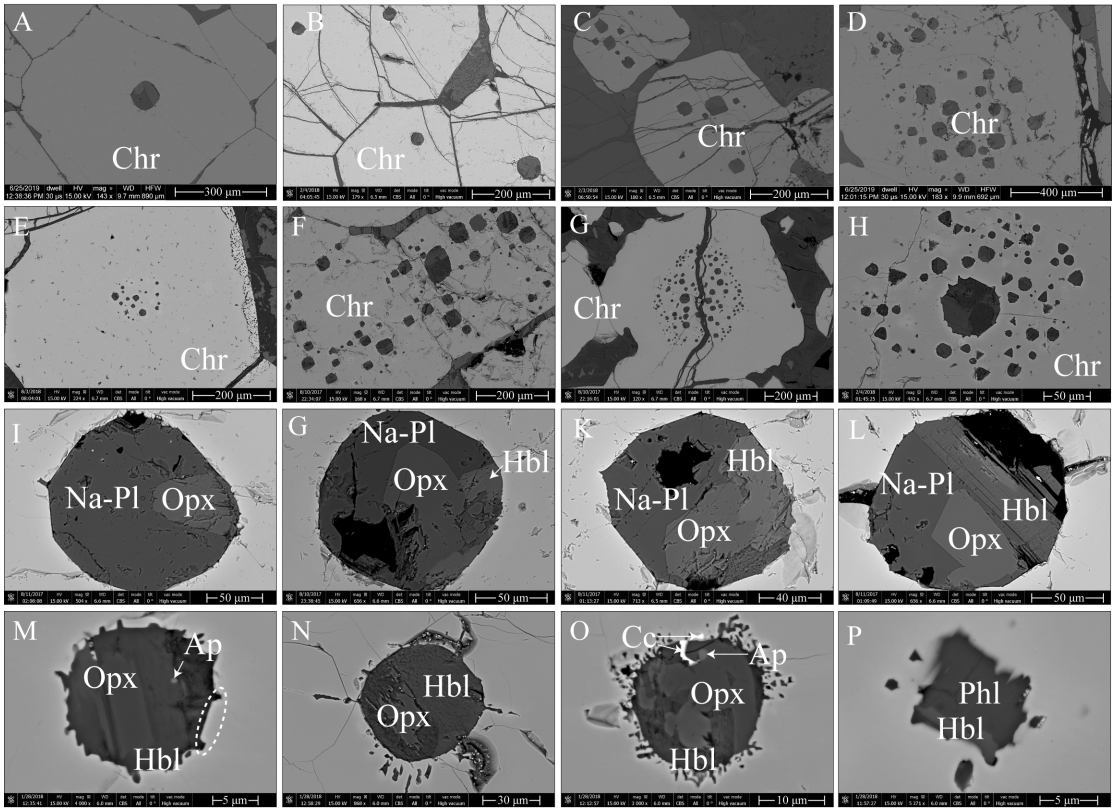

Figure 6.1 (a-h) Back-scattered electron images showing the distribution of polymineralic and central-located inclusions in chromite from the Stillwater Complex. (i-p) Details of back-scattered electron images showing morphology, texture and mineral assemblage of multiphase inclusions in chromite from the Stillwater Complex. The enclosed area in 'e' indicates that the chromite is projected into the margins of the inclusions, generating the bright halos than the main chromite circling inclusions. Abbreviations: Na-Pl, plagioclase; Hbl, hornblende; Cc, chalcocite; Ap, apatite; Phl, phlogopite. Some single-phase silicate inclusions also present at the margins of chromite grains, and the detailed descriptions are given in the Figure S12.3 in Appendix 12.

6.2.2 Analytical methods

Major element analysis of minerals: The major elemental compositions of the host chromite grains and their mineral inclusions, as well as interstitial silicate minerals, were determined with a JEOL JXA8100 electron microprobe at IGGCAS. Analyses were performed with an accelerating voltage of 15 kV, 12 nA beam current and 5 μm beam diameter with 10-30 s dwell time, and 11 mm working distance. Standards were albite for Na, diopside for Si, Ca and Mg, hematite and synthetic Cr_2O_3 for Cr, synthetic TiO_2 for Ti, orthoclase for K, synthetic Al_2O_3 for Al, synthetic MnO for Mn and synthetic NiO for Ni. K(α) lines were selected for analysis, and the detection limits were within ~0.008-0.02 wt% (1σ). Matrix effects were corrected with a ZAF-based program. The results are plotted in Figure 6.2 and the data are presented in Table S13.2 in the Appendix 13.

Water contents of silicate minerals: The water contents of olivine, clinopyroxene, and orthopyroxene in sixteen representative samples, including dunite, bronzitite, granular and poikilitic harzburgite, as well as different types of chromitites, were analyzed by Fourier-transform Infrared Spectroscopy (FTIR). These samples were prepared as double-polished thin sections with thicknesses of ~0.2 mm, and the cross polarized light of analyzed thin sections have been showed in Figure S12.4 in Appendix 12. Infrared unpolarized spectra were obtained at wave-lengths from 2500 to 4000 cm^{-1} (Figure 6.3) on a Nicolet FTIR spectrometer IS50 coupled with a Continuum microscope at Zhejiang University, using a KBr beam-splitter and a liquid-nitrogen cooled MCT-A detector. The entire instrument was continuously flushed with dry nitrogen during analysis. 256 scans were accumulated at a resolution of 4 cm^{-1}. A square aperture (30×30 to 100×100 μm^2) was used and adjusted depending on the mineral grain size and quality. Most of the spectra were collected close to the cores of the grains, through optically clear pathways. While three large olivine and orthopyroxene grains were chosen to make core-rim measurements to check the intragranular water distribution homogeneity and the subsolidus re-equilibration among these minerals (Table 6.1).

A modified form of the Beer-Lambert law was used to calculate the H_2O contents:

$$c = A/\varepsilon t\gamma$$

in which c is the content of hydrogen species (H_2O in ppm), A is the integrated area (cm^{-2}) of absorption bands in the region of interest, ε is the molar absorption coefficient (ppm^{-1} cm^{-2}), and t is the thickness (cm). OH absorption bands were integrated between 3000 and 4000 cm^{-1} for olivine, and 2600 to 4000 cm^{-1} for pyroxene and multiplied by 3 to obtain A values. The integral specific coefficients of 5.32 ppm^{-1} cm^{-2} for olivine, 7.09 ppm^{-1} cm^{-2} for clinopyroxene and of 15.6 ppm^{-1} cm^{-2} for orthopyroxene were used to calculate H_2O contents (Bell et al., 1995; Kovács et al., 2010). Uncertainties during the FTIR measurements and the calculated results may come from: (1) using unpolarized infrared beams on unoriented minerals (< 10%) (Libowitzky and Rossman, 1996); (2) baseline correction (< 5%); (3) variable sample thickness (< 3%); and (4) differences between the absorption coefficients (< 20%) of our samples and those of samples used by Bell et al. (1995) due to differences in composition. Baseline corrections were carried out by hand at least three times for each spectrum, the uncertainty was less than 5% and the average corrected spectrum was used to calculate the water content. Thickness was measured using a digital micrometer and reported as the average of 30-40 measurements covering the entire section. Thus, the total uncertainty is estimated to be less than 15-30%. The potential bias given by the crystallographic orientation of the silicates may also provide the possible uncertainties for the result. To minimize possible uncertainties from the unpolarized determination of these optically anisotropic minerals, we typically analyzed more than 10 different grains of each mineral in the same samples and used the average value to define the water content of that mineral in that sample (Asimow et al., 2006; Grant et al., 2007). Repeated analysis the framework of randomly oriented silicates in mesocumulate and heteradcumulate textures can effectively eliminate the uncertainty caused by the crystallographic orientation. The analysis results are plotted in Figure 6 showing the dispersions and ranges, and the calculated water concentration averages of minerals are

reported in Table 6.1.

Table 6.1 Water contents of minerals and calculated H_2O contents in whole-rocks from the Stillwater Complex.

Samples	Rock types	Minerals	H_2O (ppm)	Grain No.	Minerals	H_2O (ppm)	Grain No.	Minerals	H_2O (ppm)	Grain No.	H_2O contents in magma (wt.%)
Samples from the G chromitite layer outcropped in Mountain View area:											
16SW1-7	Bronzitite	Ol			Opx	39.4	13	Cpx	489	13	4.26 ~4.94
16SW1-11	Dunite	Ol	34.8	10				Cpx	144	12	1.25~1.45
16SW1-19	Dunite	Ol	40.3	12							
16SW1-17	Harzburgite	Ol-core	26.8	8	Opx-core	29.1	9				
		Ol-rim	22.2	3	Opx-rim	33.2	4				
16SW1-9	Disseminated chromitite	Ol	28.8	12	Opx	45.3	7	Cpx	192	7	1.67~1.94
16SW1-14	Disseminated chromitite	Ol	20.6	10	Opx	31.2	10				
16SW1-8	Anti-nodular chromitite	Ol-core	20	8	Opx-core	40.9	7				
		Ol-rim	18.4	5	Opx-rim	38.7	2				
16SW1-35	Anti-nodular chromitite	Ol	23.3	10	Opx	37.7	12				
16SW1-16	Anti-nodular chromitite	Ol	23.5	12	Opx	31.9	10				
16SW1-32	Massive chromitite	Ol	27.6	7	Opx	30.1	6				
16SW1-30	Massive chromitite	Ol	30.4	9	Opx	34.5	7	Cpx	292	4	2.54~2.95
Samples from the Lowermost layer outcropped in Gish area:											
16SW3-7	Bronzitite	Ol			Opx	41.3	11	Cpx	356	10	3.09~3.59
16SW3-4	Dunite	Ol	54.7	7							
16SW3-3	Dunite	Ol-core	38.6	9	Opx-core	30.2	8				
		Ol-rim	34.2	4	Opx-rim	32.8	4				
16SW3-5	Harzburgite	Ol	32.5	11	Opx	28.3	10				
16SW3-9	Harzburgite	Ol	25.7	10	Opx	26.3	11				

6.2. Results

6.2.1 Compositional differences between interstitial silicate minerals in the chromitite layers and those in inclusions of chromite

Orthopyroxene is the most common intercumulus phase coexisting with chromite in the chromitite seams. It is typically highly magnesian with Mg numbers ranging from 87.7 to 91.9 in our samples and total alkali contents (Na_2O+K_2O) are, always less than 0.06 wt% (Figure 6.2a). Minor amounts of plagioclase and phlogopite also occur as intercumulus phases in the chromitites. The interstitial plagioclase in the chromitites has compositions of $An_{80.5-42.2}$ and has Na numbers (100Na/(K+Na)) ranging from 4 to 11 (Figure 6.2b, c). Interstitial phlogopite in the chromitites has MgO contents of 19.0 to 23.2 wt% (Figure 6.2c). In contrast, the compositions of these phases are significantly different in the inclusions of the chromite. For example, the orthopyroxene in the inclusions of the chromite is somewhat more magnesian with Mg numbers of 88.8-95.1 and has total alkalis up to 0.7 wt% and the plagioclase in the inclusions of the chromite is nearly pure albite ($An_{0.1-2.1}$) with Na numbers of 19.5 to 57.8. The very sparse phlogopite grains in the inclusions of chromite have 21.3-26.9 wt% MgO and Na numbers of 2-64.

Hornblende is absent in the Peridotite Zone in the Mountain View area of the complex but does occur locally in rocks of the Banded Series, especially in olivine-bearing subzones. Hornblende commonly coexists with plagioclase and quartz in veins, cutting troctolite bodies in the upper sequences of the Complex. Boudreau et al. (1986) reported that these hornblende grains typically have low MgO (16.8 to 18.3 wt%) and (Na_2O+K_2O) (2.13 to 2.78 wt%), and high CaO contents (11.2 to 13.4 wt%) and Si cation contents (6.23 to 6.70) (Figure 6.2d, e). We identified two types of hornblende occurring as inclusions in chromite grains with distinctly different compositions; one has extremely low CaO (<0.56 wt%) and higher Si cation contents (4.78-6.25 wt%), whereas the other had much higher CaO (2.20-11.8 wt%) but lower Si cation contents (2.10-5.26) (Figure 6.2d). However, both have higher total alkalis (2.03-7.10 wt%) and MgO (4.1-12.1 wt%) contents than hornblende from the upper sequences (Figure 6.2e).

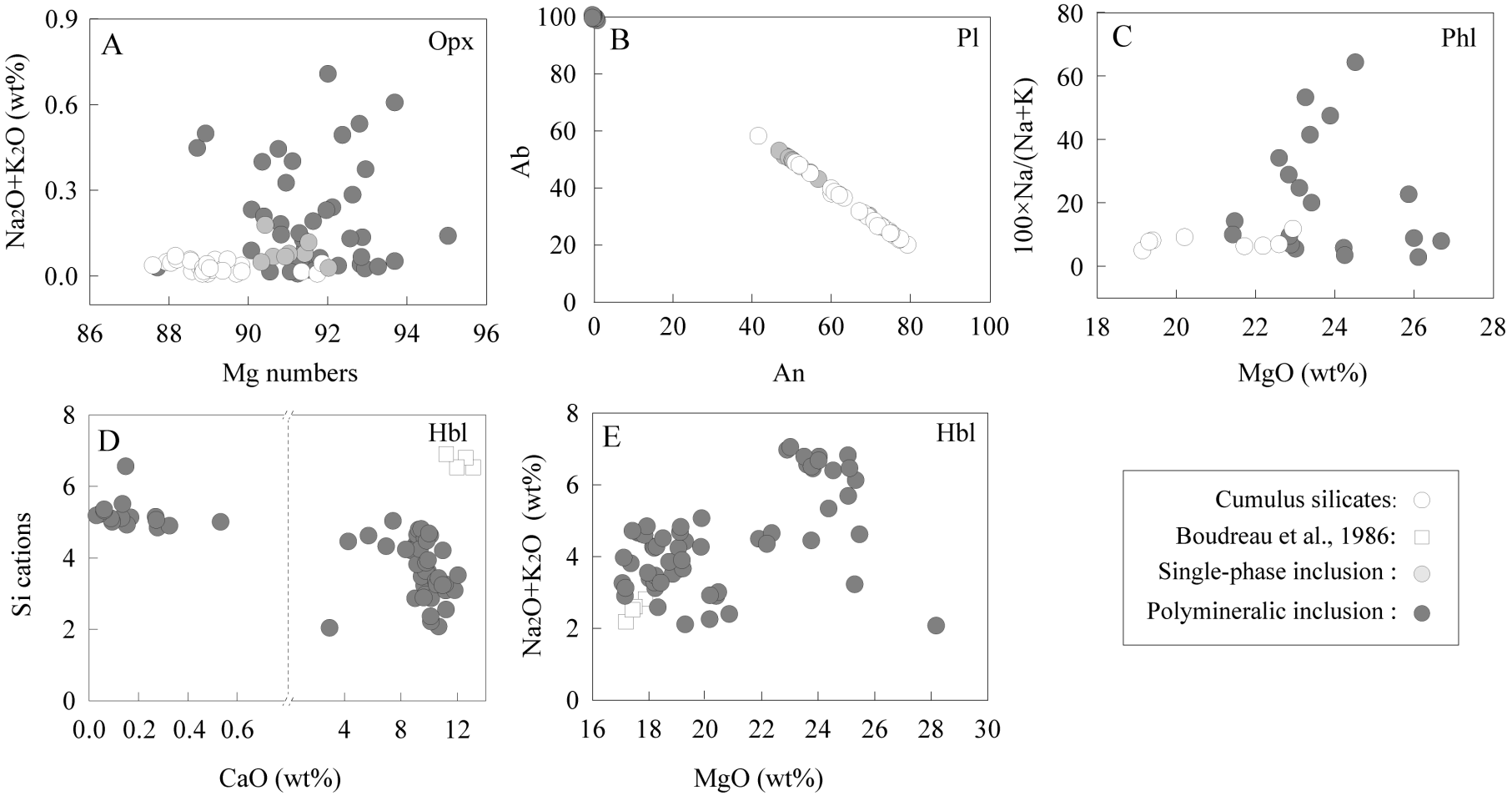

Figure 6.2 Compositional variations of silicate inclusions compared to those minerals in the matrix of chromitites or upper rock sequences from the Stillwater Complex.

6.2.2 H_2O contents of nominally anhydrous phases

FTIR spectra could provide us information as to where the H_2O sits within the crystal lattice. All measured clinopyroxene grains display several characteristic OH stretching-related absorption bands at 3460, 3540 and 3630 cm^{-1} (Figure 6.3a), olivine grains display characteristic OH absorption bands at 3596, 3572 and 3525 cm^{-1} (Figure 6.3b), that match those reported in other ultramafic rocks (e.g., Hao et al., 2014; Li et al., 2018). These FTIR spectras also show no sharp OH peaks greater than 3660 cm^{-1} or broad OH peaks around 3400 cm^{-1}, excluding the influence of secondary hydrous minerals or fluid inclusions formed during alteration (Figure 6.3). Orthopyroxene in harzburgite and dunite with granular texture have commonly documented prominent OH-absorption peaks at 3420, 3520 and 3590 cm^{-1} (Figure 6.3c), and these positions are similar to those reported in earlier studies of mantle peridotites (Bell and Rossman, 1992; Stalder and Skogby, 2002), and interpreted as resulting from the vibration of structural OH. In contrast, orthopyroxene in chromitite with poikilitic texture only has one OH-absorption band peaks at 3420 cm^{-1}. The variation in the relative intensity of these absorption bands is likely to be related to the composition of two types of orthopyroxene.

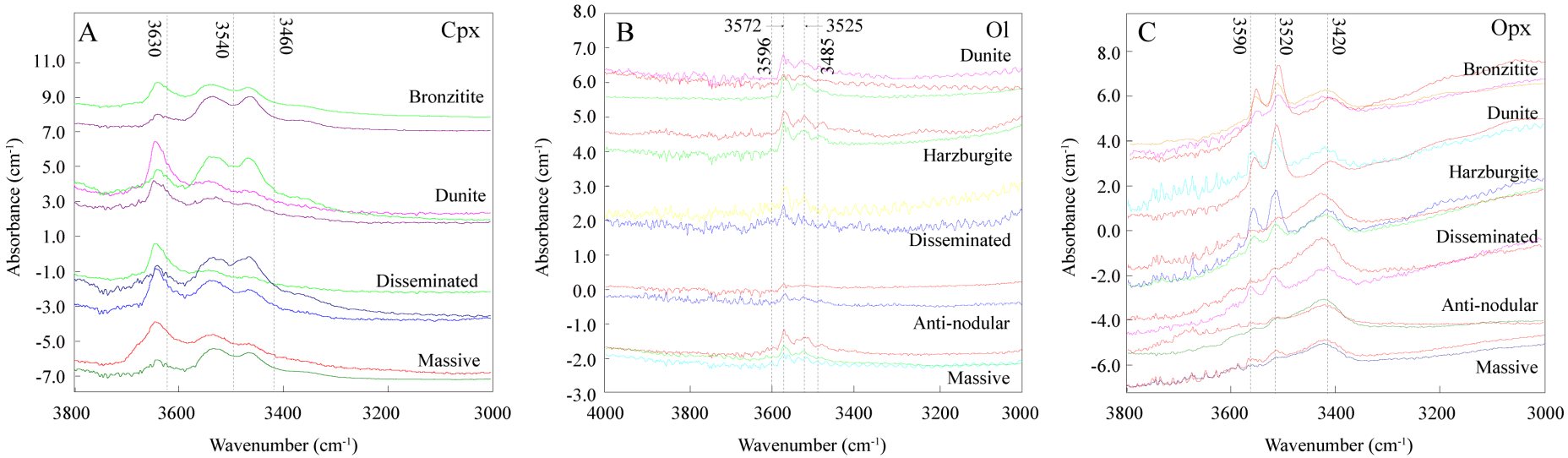

Figure 6.3 Representative unpolarized IR absorption spectra for (a) clinopyroxene, (b) olivine, and (c) orthopyroxene from the Stillwater Complex. The spectra are shown without baseline correction, and the dash lines indicate the wave numbers of absorbing peak. The absorbances of all spectra are normalized to 1 cm thickness. All of the obtained spectra are provided in Figure S12.5 in Appendix 12, and the ratios between the amplitude of the different peaks show variably crystallographic orientations.

The measured H_2O contents for olivine and orthopyroxene from Stillwater are ranging from 20.0 to 54.7 ppm and 26.3 to 45.3 ppm, respectively (Table 6.1; Figure 6.4). Olivine and orthopyroxene from the silicate cumulates have similar H_2O contents, which increase from the harzburgites to dunites to bronzitites. However, different trends in H_2O contents in olivine and orthopyroxene are apparent in the chromitites. The H_2O in olivine from chromitite (20.0-30.4 ppm) is lower than that for olivine from the silicate cumulates (25.7-54.7 ppm), whereas H_2O in orthopyroxene from the chromitites (30.1-45.3 ppm) is higher than in orthopyroxene from the cumulates (26.3-41.3 ppm). The H_2O contents of clinopyroxene range from 143.8 to 489.4 ppm (Table 6.1), which are a little lower than the values obtained in clinopyroxene from the Rum complexes (149 to 820 ppm; Libowitzky and Rossman, 1997; Mattsson et al., 2014; Weis et al., 2018) and Panzhihua complexes (411 to 775 ppm; Zhang et al., 2014; Wang and Zhang, 2015). In addition, clinopyroxene grains in Bronzitite have much higher H_2O contents compared to dunite and chromitite, showing the similar trends with coexisting orthopyroxene (Figure 6.4).

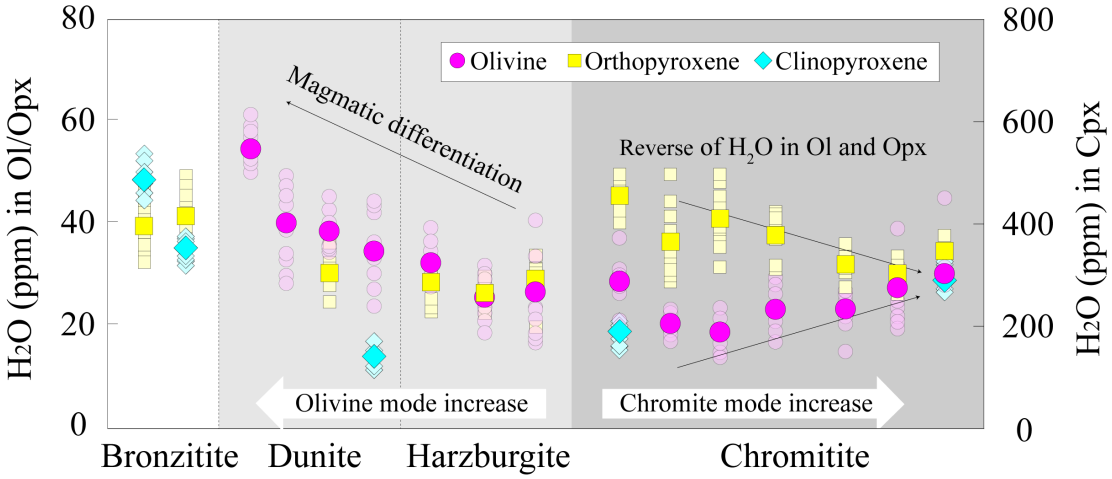

Figure 6.4 Analysis H_2O contents in silicate minerals from chromitites and silicate cumulates in the Stillwater Complex. The chromite and olivine mode references to Bai et al. (2019), and the arrows indicate the trend of H_2O contents along with the increasing chromite or olivine mode. All of the analysis results are plotted as smaller and translucent symbols, showing the ranges and dispersions. The calculated average values in Table 6.1 are plotted in bigger and solid symbols.

6.3 Hydrous interstitial melts surround chromite: implications from inclusion mineralogy

Some of reported properties of parental magmas of stratiform and podiform chromitites, such as Si and Mg compositions and water contents, were deduced from minerals or melt inclusions in chromite grains (e.g., Melcher et al., 1997, Spandler et al., 2005). More recent studies, however, showed that the inclusions in chromite grains could only record the residual melts (Spandler et al., 2007; Johan et al., 2017). Any evolved melt droplets adhering to a chromite grain could be trapped as an inclusion during this process. The silicates, containing orthopyroxene, plagioclase with some H_2O-bearing minerals, such as hornblende and phlogopite, occurring in inclusions of chromite mainly serve as the interstitial mineral phases in chromitite (Figure 6.1). Olivine is the major cumulus phase coexisting with chromite in the Stillwater chromitites, but it does not appear in the inclusions of chromite. That may be due to the reaction of olivine + liquid = orthopyroxene, in which olivine is consumed and replaced by orthopyroxene overgrowths in the inclusions (Morse, 1979; Zellmer et al., 2016).

The high Mg numbers of silicates in the inclusions of chromite could be related to subsolidus diffusion, with Mg diffusing from the host chromite to silicates in the inclusion and Fe moving in the opposite direction (Figure 6.2a, c, e; Scowen et al., 1991; Xiao et al., 2016; Bai et al., 2017, 2018). However, according to the experimental results of Botcharnikov et al. (2008), high Mg numbers of these minerals could also reflect increasing H_2O-activity in the magmas, and higher Mg numbers of silicate minerals in inclusions of chromite might have crystallized from hydrous melts. On the other hand, the fluid-mobile elements, such as Na and K that are significantly richer in the orthopyroxene and hornblende from the inclusions in chromite than those minerals serve as the interstitial mineral phases in the chromitites would be unaffected by subsolidus processes and thus keep their primary contents (Figure 6.2a, e; Spandler et al., 2005). Na-rich phlogopite (aspidolite) is a ubiquitous part of this assemblage in chromite-hosted melt inclusions. Luth (1967) and Carman (1974) suggested that such high-Na phlogopite could have formed by the reaction between olivine and fluid-

enriched melts and that high-K phlogopite could have formed by the reaction between orthopyroxene and fluid-enriched melts. Li et al. (2005) reported a similar co-existence of high-K and high-Na phlogopite in inclusions in chromite from the Bushveld Complex. Clinopyroxene, which is absent in inclusions of the Stillwater chromite grains, may have been replaced by the abundant hornblende. The hornblende stability field is rather limited and is constrained by reactions involving clinopyroxene + liquid ± plagioclase and orthopyroxene + liquid ± plagioclase (McNeil and Edgar, 1987; Nandedkar et al., 2014). The surplus H_2O in melts from which the inclusions formed suppressed clinopyroxene and orthopyroxene and led to the crystallization of high-Ca and low-Ca hornblende, respectively (Figure 7.2d; Cawthorn and O'Hara, 1976). Crystallization of high-Ca hornblende grains from the early melts trapped in the inclusions could have exhausted the Ca in the melts, thereby shifting the plagioclase to more Na-rich varieties (Figure 6.2b).

Sixteen inclusions in chromite were selected for volume-area analysis to calculate the bulk inclusion compositions. The volume percentages of individual minerals in the inclusions were converted to weight percentages using the medium densities of the minerals given by Deer et al. (1992). The average modal compositions of the inclusions are 26% orthopyroxene, 31% hornblende, 41% albite. Other minor phases such as apatite, phlogopite and sulfides together comprise < 2% of the inclusions. The bulk compositions of the inclusions and the average compositions of the minerals are given in Table S14.3 in the Appendix 14, and the results are characterized by low CaO (2.32 wt%) and FeO (2.68 wt%) and high MgO (15.4 wt%), Na_2O (5.56 wt%), and H_2O (2.60 wt%). These values are also inconsistent with those of many previously proposed parental magmas for the Stillwater Complex or the Ultramafic Series (Table S13.3). Therefore, the chemical compositions of polymineralic inclusions are not reliable indicators of the conditions and compositions of the parental magma, instead, can only provide insights into the characteristics of interstitial melts surrounding chromite.

6.3 Fluid-enriched interstitial melts indicated by H_2O contents of silicate minerals

6.3.1 Water contents of the melts for Stillwater chromitite

Boudreau et al. (1997) was the first to suggest that the Stillwater Complex and other high-Cl layered intrusions (e.g., Bushveld Complex) crystallized from magmas with > 1 wt% H_2O that was derived from a metasomatized, previously depleted mantle. Once the partition coefficient of H_2O between clinopyroxene and melt was established ($D_{H_2O}^{Cpx/melt} = 0.0115 \pm 0.0016$; Novella et al., 2014), it was used to calculate H_2O contents of gabbro veins of the Rum Complex (1.98 to 2.71 wt%; Mattsson, 2014), and the Panzhihua layered intrusion (up to 3.0 wt%; Zhang et al., 2014; Wang and Zhang, 2015). These gabbro veins may represent residual intercumulus fluids (Butcher, 1985) or residual magmas of the troctolite matrix (Donaldson, 1975), rather than parental magmas of the associated chromitites.

In this study, we found a range of H_2O contents (143.8 to 489.4 ppm) in clinopyroxene from the chromitites and overlying silicate cumulates of the Stillwater Complex, and the equilibrated H_2O contents in corresponding samples range from 1.25 to 4.94 wt% (Table 6.1). The H_2O contents decrease upward in a section across a chromitite layer from 2.54 to 2.95 wt% in the basal massive chromitite, to disseminated chromitite with 1.67 to 1.94 wt%, to the overlying dunite with 1.25 to 1.45 wt%. Late-crystallized bronzitite has the highest H_2O contents (4.26-4.94 wt%), which confirms a trend of increasing H_2O with increasing magmatic differentiation (Naumov et al., 2010; Plank et al., 2013).

Water contents of mafic melts generated in a variety of tectonic settings are variable (Dixon et al., 1997; Naumov et al., 2010; Weis et al., 2015). The melts of the Stillwater chromitites have high water content, even surpassing those of island arc (average 1.80 wt%) and active continental margin (average 1.96 wt%) magmas. Most layered intrusions, such as the Stillwater, Bushveld, Skaergaard, Panzhihua, and Rum complexes, were generated in stable continental settings (e.g., Hamlyn and Keay, 1986; Emeleus et al., 1996; Boudreau et al., 1997), making it difficult to understand how their parental magmas became enriched in H_2O (e.g., Dixon et al., 2004; Li et al., 2018). Spandler et al. (2005) and Mattsson (2014) suggested that the H_2O originated from

partial melting of crystallized mafic wall rocks and associated fractional crystallization in a deep reservoir. Nicholson and Mathez (1991) and Li et al. (2005) proposed that the excess H_2O in the Bushveld Complex was derived from migration and accumulation of cumulate bronzitite, which has high H_2O, but this does not address the origin of the high-H_2O parental melts. Therefore, the measured high H_2O contents should be also identified as interstitial fluids.

6.3.2 Heterogeneous distribution of H_2O between chromitites and silicate cumulates

We report here for the first time H_2O contents of olivine and orthopyroxene from a layered intrusion. The two phases have similar H_2O contents in silicate cumulates, and both increase in H_2O with increasing magmatic differentiation (Figure 7.4). However, these two phases have different H_2O compositions in the chromitite samples. The poikilitic orthopyroxene surrounding chromite grains has higher H_2O contents (30.1-45.3 ppm) than orthopyroxene in the silicate cumulates (26.3-30.2 ppm), whereas olivine oikocrysts in the chromitite have significantly lower values (20.0-30.4 ppm) than olivine in the dunite and harzburgite (25.7-54.7 ppm). These trends are also associated with the chromite mode in chromitite, suggesting a heterogeneous fluids distribution induced by chromite crystallization.

Hurwitz and Navon (1994) showed that two rhyolitic obsidians, one with 1% and the other with 20% of Fe-Ti oxide microlites, were similar except that the latter contained separate fluids phases. These authors suggested that the oxide microlites had attracted fluids to themselves to reduce surface energies, causing a redistribution of H_2O in the original melts leading to local H_2O-supersaturation. Cichy et al. (2011) later investigated different mineral microlites, such as amphibole, pyroxene and oxides, and found that only oxides in melts could produce local H_2O-supersaturation. Thermodynamic experiments conducted by Matveev and Ballhaus (2002) suggested that chromite can attract fluids phases during its growth, thereby lowering H_2O contents in olivine residing in the residual melts. Such a process operating in the Peridotite Zone

of the Stillwater Complex could have caused accumulation of fluids in zones containing abundant chromite, thereby generating high H_2O contents in silicate minerals surrounding the chromite grains. This would have caused depletion of fluids in the residual melt such that the silicate minerals crystallizing from the melt would have reduced H_2O contents (Gualda and Ghiorso, 2013).

Redistribution of H_2O in melts induced by crystallization of chromite or other oxides has been suggested in podiform chromitites and magnetite deposits (e.g., Melcher et al., 1997; Knipping et al., 2015, 2019; Pleše et al., 2019; Su et al., 2020a). In this model, the fluids in mafic magmas would have been inherited from the wall rocks or overlying cumulates as previously suggested (Li et al., 2005; Spandler et al., 2005; Mattsson, 2014). We suggest that such a process may be the principal mechanism for the formation of fluid-enriched circumstances for chromite.

6.4 Model based on the high fluids facilitated the concentration of chromite to form chromitite seam

It was thought that fluids in podiform chromitite could be collected on the chromite surfaces during crystallization allow chromite grains to rise via decreasing density in the form of assembly, thus promoting their gathering and concentration (e.g., Melcher et al., 1997; Matveev and Ballhaus, 2002; Su et al., 2020a). The enriched fluids in stratiform chromitite induced by redistribution might also propose a similar mechanism for the mechanical sorting of chromite grains to explain the origin of chromitite seams:

1) The effect of temperature changes on the solubility of H_2O in melts is negligible under low pressure (Dixon et al., 1995; Fiege et al., 2014), and the H_2O solubility in melts is influenced primarily by pressure (Bottinga and Javoy, 1990). Rapid decompression leads to high ΔP, which could greatly reduce the maximum H_2O solubility in a melt (Hurwitz and Navon, 1994; Witham et al., 2012). Layered intrusions represent lower crustal storage of mafic magma derived by partial melting of the uppermost mantle (e.g., Latypov et al., 2018; Latypov and Chistyakova, 2020). A thermal model of the Stillwater Complex proposed by Helz (1995) suggested that melts

ascending from a mantle source were injected into a shallow crustal chamber (McCallum and O'Brien, 1999; Labotka and Kath, 2001; Thomson, 2008). As a consequence, the fluids would be exsolved and segregated as "bubbles" (Bottinga and Javoy, 1990; Sparks et al., 1994; Ballhaus et al., 1998, 2015; Knipping et al., 2015, 2019). The bubbles are not pure H_2O but can also contain some silicate melt, metal oxide solute, and other volatiles (Ballhaus, 1998; Ballhaus et al., 2015; Giachetti et al., 2019).

2) Mounting evidence indicated that the mantle-derived melts would be expected to crystallize numerous chromite and silicate microlites before ascending to shallow-level chambers (e.g., Eales and Costin, 2012; Chistyakova et al., 2015; Mukherjee et al., 2017). Small quantities of olivine and perhaps orthopyroxene microlites may also precipitate from the magma, leading to a crystal-rich slurry composed of silicate and chromite microlites. Compared to silicates, which are dominated by Si-O ions with a tetrahedral structure, chromite is dominated by complex cations consisting of Ti^{4+}, Cr^{3+}, Al^{3+} and Fe^{3+}. Therefore, chromite microlites will have a stronger attraction for bubbles than silicate grains (Matveev and Ballhaus, 2002; Gualda and Ghiorso, 2007; Edmonds et al., 2015). The relative movements and attachments between ascending bubbles and sinking microlites, and chromite microlites are evenly distributed on the surface of bubble, developing the chromite-bubble assembly (Figure 6.5a; e.g., Pleše et al., 2019).

3) Numerous experiments and simulations have confirmed that attachment of microlites on bubbles is strong enough to efficiently float microlites of magnetite and ilmenite with densities of 5.15 g/cm^3 and 4.7 g/cm^3, respectively in felsic melts with densities of 2.6-2.7 g/cm^3 (Melcher et al., 1997; Knipping et al., 2015, 2019; Ballhaus et al., 2015; Mungall et al., 2015; Pleše et al., 2019), providing a mechanism for generating high-density magnetite monomineralic layers that overlie less dense cumulates in layered intrusions. Chromite has an even lower density (4.6 g/cm^3) than magnetite and ilmenite, and silicate melts are heavier than felsic melts due to their higher proportions of mafic-ultramafic components. Thus, we suggest that chromite microlites can rise through silicate melts when they are attached to bubbles.

4) After assembly of the bubbles with partial or complete coatings of chromite microlites, they can be injected into a shallower magma chamber, triggering lateral movements of the slurries (Figure 6.5). Most of the bubbles will continue to expand under the lowering pressures, causing disaggregation of the coatings of chromite microlites (Figure 6.5b). The microlites are then free to settle through the slurry by kinetic sieving; that is, downward settling of small and dense chromite grains through the melt to collect at the base of the slurries (Maier et al., 2013; Mukherjee et al., 2017; Jenkins and Mungall, 2018). In this model, chromite grains accumulate before the silicate minerals, giving rise to a nearly monomineralic chromite layer, that has a sharp contact with the underlying cumulate pile and serves as the base of a new cycle (Figure 6.5c).

6.5 The fate of fluids in the bubbles

Fluids in the bubbles could reduce the liquidus temperature of silicate minerals (Ford et al., 1972; Sisson and Grove, 1993; Gaetani and Grove, 1998; Feig et al., 2010), and the melts in bubbles would thus remain fluids until nearly all the chromite has crystallized. This interpretation is supported by the central location of inclusions in chromite grains (e.g., Figure 6.1a) and their polygonal shapes which would have been controlled by the chromite (e.g., Figure 6.1k, l). The inward growth of chromite into some of the inclusions is shown by a projection of skeletal grains through the outer rim (Figure 7.5b; Chalmers, 1964; Greenbaum, 1977), generating the rugged borders between many inclusions and their host (e.g., Figure 6.1m). As the last step, fluids accumulating in the inclusion-bearing chromite grains, would produce hydrated minerals, such as hornblende, phlogopite and apatite (Figure 6.1i-l).

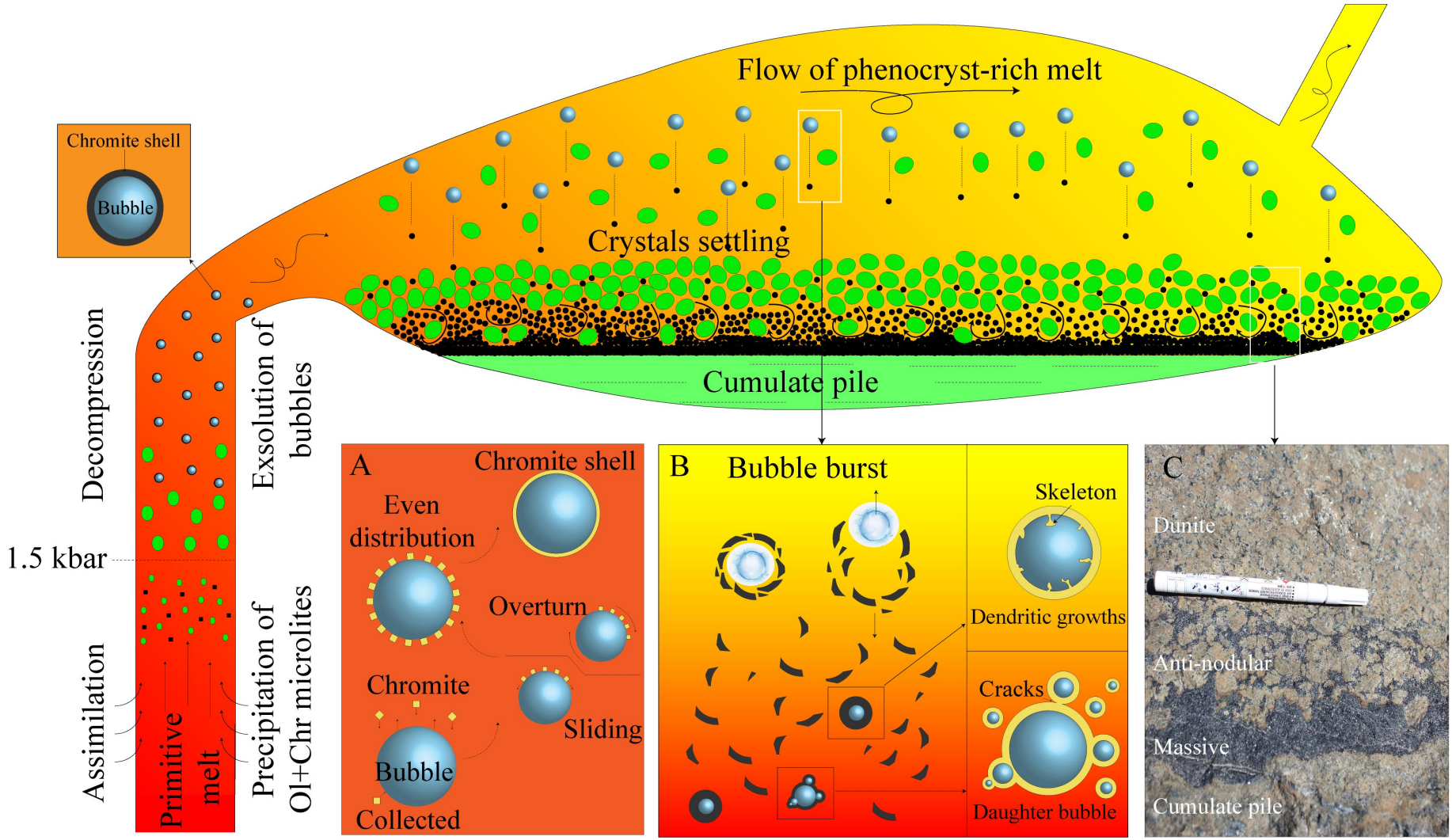
Chromite shell
Bubble
Flow of phenocryst-rich melt
Crystals settling
Cumulate pile
Decompression
Exsolution of bubbles
1.5 kbar
Assimilation
Primitive melt
Precipitation of Ol+Chr microlites
A
Chromite shell
Even distribution
Overturn
Chromite
Sliding
Bubble
Collected
B
Bubble burst
Skeleton
Dendritic growths
Cracks
Daughter bubble
C
Dunite
Anti-nodular
Massive
Cumulate pile

Figure 6.5 Simplified diagram showing the possible model for the formation of anchimonomineralic chromitite seams in the Stillwater Complex: (a) Summary of the development of chromite-bubble aggregation. Both the bubbles and microlites would be suspended in melts at the early stage of magmatic differentiation, but with the ascension of the low-density bubbles and sinking of the high-density chromite microlites the magmas would intermingle, facilitating their collision and attachment of the chromite microlites. Either by overturn of mechanically unstable magma or via downward sliding by surface tension forces, the chromite microlites would be evenly distributed on the surface of the bubble, and further growth would likely link the microlites until a thin, but solid, crust of chromite developed, essentially trapping the bubbles inside; (b) The bubble burst and chromite settled. A few bubbles with thicker coatings of microlites may also settle into the chromite layer and become inclusions in larger annealed grains (Figure 6.1). This process is consistent with the experiments of Knipping et al. (2019) and Pleše et al. (2019), in which developing bubbles can range in size from 10 to 100 μm under geologically relevant magmatic conditions, and could explain the silicate (formerly melt) inclusions observed in our chromite grains (Figure 6.1). Cracks may have formed in some melt inclusions induced by decreasing ambient pressure during upward migration of the magmas, allowing fluids to leak into the immediate surroundings and develop some daughter inclusions around the central large one (Figure 6.1h). The inward dendritic growth of chromite lead to skeletons projected into inclusions generating the rugged borders, and some liquids could leak from the cracks of inclusions developing some daughter inclusions around the centrally big one; (c) Photograph of contact among the cumulate pile, chromitite seams, anti-nodular chromitite and dunite. Once the heavier chromite microlites and crystals have settled into a basal layer, the remaining silicate minerals would accumulate on top of the chromitite seam. Later flow of the remaining melts could shift the silicate minerals laterally, some of which might mix with the chromite-rich flurry to generate the observed anti-nodular chromitites. Such turbulence would only affect the narrow contact zone between the chromitite seams and overlying silicate cumulates, forming the rugged boundary between the two. Crystallization of the remaining magma would generate the layers of dunite, harzburgite, and bronzitite with only sparse chromite grains. These sequences would persist until emplacement of the next pulse of magma.

On the other hand, abundant fluids enclosed in chromite shells may be released when the shell breaks, and compaction of the crystal mush would drive the fluids upward (Raedeke and McCallum, 1984; McCallum, 1996). This process may be responsible for the discordant pegmatitic bodies in the Stillwater Complex that appear to replace or cut the original modal layering (Emeleus et al., 1996; Boudreau et al., 1997). Some of the residual fluids could act as precursors of the interstitial clinopyroxene and phlogopite locally surrounding chromite grains (Figure 6.6a, b). Some vapors could also surround the chromite, representing the alteration induced by residual fluids (Figure 6.6c). Fluids can also enter early formed olivine and chromite, to later form rod-like inclusions during subsolidus re-equilibration (Figure 6.6d; Xiong et al., 2017; Liang et al., 2018). Any excess fluids excluded from these minerals would adhere to the ambient chromite and olivine, generating the ragged boundary described earlier (Figure 6.6e) and serpentinization of the olivine (Figure 6.6f). Also, any fluids remaining in the overlying silicate cumulates would alter all the silicate minerals (Figure 6.6g), providing an important means of prospecting for chromitite layers (He et al., 2014, 2018). Besides, the fluids released by chromite and liberated fluids in layered intrusions will greatly enhance subsolidus elemental diffusion (Bai et al., 2019, 2020; Su et al., 2020b) and the formation of PGE deposits (Leroy, 1985; Boudreau and McCallum, 1992; Boudreau, 2016; Latypov et al., 2017).

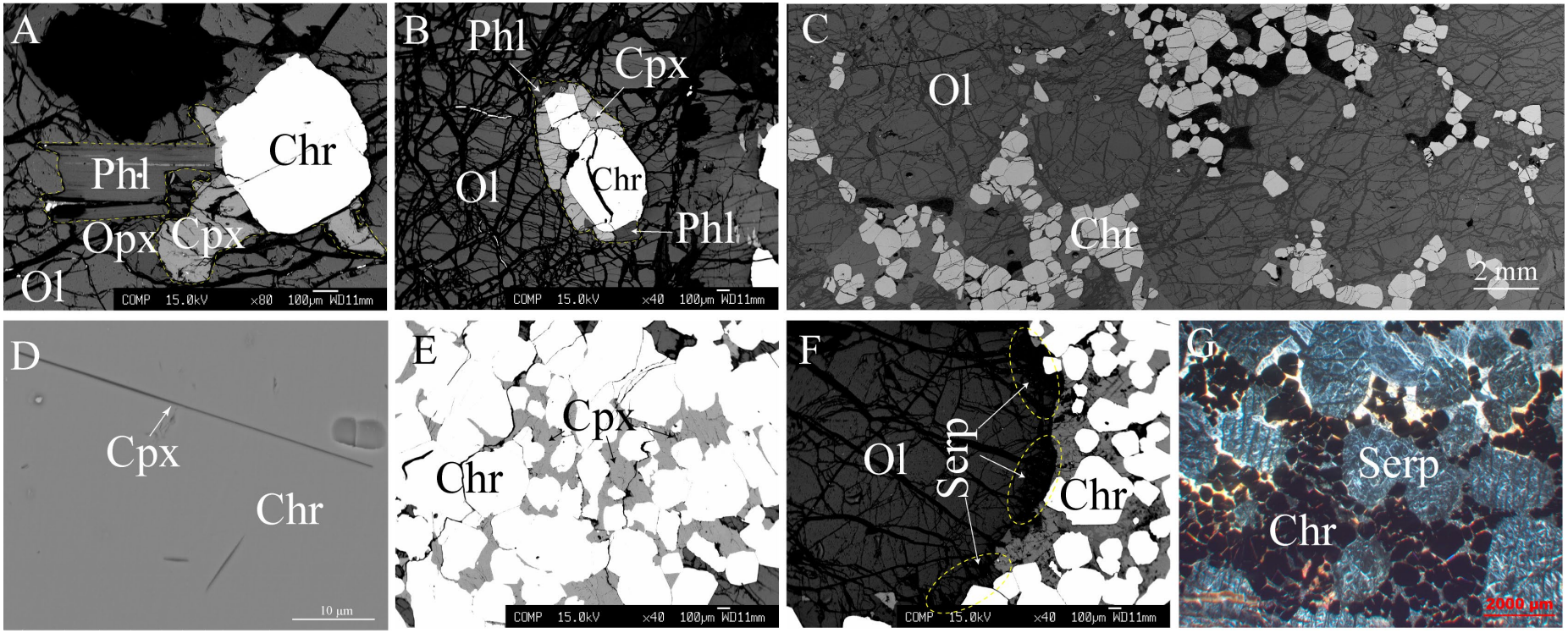

Figure 6.6 Back-scattered electron (a-c, e-f) and cross-polarized optical (f) Images of samples from the Stillwater Complex, and the exsolution textures of clinopyroxene in chromite from the Kızıldağ ophiolite (Liang et al., 2018): (a-b) Phlogopite and clinopyroxene surrounding chromite; (c) Vapors around chromite grains; (d) Exsolution textures of clinopyroxene in chromite; (e) Ragged boundary of chromite wetted by intercumulus clinopyroxene; (f) Selective alteration of olivine adjacent to chromite; (g) Extensive alteration on silicate minerals.

7. Conclusions

Based on a detailed mineralogical, petrological, and geochemical analysis of the Stillwater Complex, USA, examines the effects of different diffusion mechanisms on the non-traditional stable isotope composition for crystalline minerals. The main findings and conclusions of the paper are as follows:

1) Mg-Fe isotopes are negatively correlated between silicate and chromite cumulus minerals, and the conjugate isotopic variations in silicates and chromite indicate kinetic isotope fractionation during inter-mineral diffusion. Our dataset highlights significant intermineral isotope fractionations that are inconsistent with high-temperature equilibrium isotopic partitioning. Instead, our isotopic data reflect kinetic effects associated with inter-mineral diffusion and variable degrees of chemical re-equilibration during the protracted cooling of the Stillwater Complex and other mafic-ultramafic complexes.

2) Evolving chromite Cr isotopic compositions may be a geochemical indicator of magmatic differentiation. We suggest that magma replenishment and wall rock contamination contributed to the formation of chromitites. Disequilibrium inter-mineral isotopic fractionations induced by Cr diffusion from the crystals to the melt. The observed Cr elemental zonings and isotopic compositions in our samples suggest that the Peridotite Zone of the Stillwater magma cooled to the Cr diffusive closure temperature within 10 to 100 kyr. Chromium elemental and isotopic analyses are thus useful in constraining the cooling times of persistent magma systems.

3) The general Li and O isotopic compositions and inter-mineral and inter-sample isotopic variations are correlated with mineral assemblages, crystal sizes and major and trace element compositions, suggesting various reactions between interstitial liquids, from which pyroxenes crystallized, and the cumulus minerals. Integration of rare earth element patterns and Cr isotope variations indicates that compositional changes in the interstitial liquids were the main controlling factor, in addition to mineral fractionation and subsolidus chemical exchange, on the mineral compositions. Hydrous fluids collected on the surfaces of chromite grains provided a critical medium for extensive

chemical exchange between chromite and olivine, and their release might have contributed to generation of hydrous minerals and pegmatites in the Stillwater Complex. Mixing between fractionated magma and a newly injected primitive melt can account for the compositional changes in the interstitial liquids.

4) The appearance of hydrous minerals in the inclusions and their compositional variations are consistent with crystallization in fluid-rich melts. The water contents calculated by the FTIR measurements indicate that the H_2O contents in the cumulate rocks increased with increasing chromite mode and decreased in coexisting olivine and orthopyroxene. These variations in the chromitites provide a guide to H_2O redistribution induced by chromite crystallization. The fluids play an important role in sorting and accumulating chromite from basaltic magma, and we provide a plausible mechanical sorting process for the nearly monomineralic chromitite seams. Chromite and associated orthopyroxene that crystallized from the fluid-rich melts and olivine that crystallized in fluid-extracted melts would inherit information on the melt compositions and conditions.

8. References

Abdallah S, Ali S, Obeid MA. Geochemistry of an Alaskan-type mafic-ultramafic complex in eastern desert, Egypt: New insights and constraints on the Neoproterozoic island arc magmatism[J]. Geoscience Frontiers, 2019, 10(3): 150-164.

Abzalov MZ. Chrome-spinels in gabbro-wehrlite intrusions of the Pechenga area, Kola Peninsula, Russia: Emphasis on alteration features[J]. Lithos, 1998, 4: 109-134.

Agata T, Adachi M. Chrome spinel in normal MORB-type greenstones from the Paleozoic-Mesozoic Mino Terrane, east Takayama area, central Japan: Crystallization course with a U-turn[J]. Island Arc, 2014, 23: 62-73.

Agata T, Hattori I. Chromite in greenstone lavas from the Kanakasu area, Nanjo Massif of the Mesozoic Mino terrane, central Japan[J]. Mineralogical Magazine, 2002, 66(4): 575-590.

Agata T. Chrome spinels from the Oura layered igneous complex, central Japan[J]. Lithos, 1988, 21: 97-108.

Ahmed AH, Helmy HM, Arai S, et al. Magmatic unmixing in spinel from late Precambrian concentrically-zoned mafic-ultramafic intrusions, eastern desert, Egypt[J]. Lithos, 2008, 104(1-4): 85-98.

Ahmed AH, Surour AA. Fluid-related modifications of Cr-spinel and olivine from ophiolitic peridotites by contact metamorphism of granitic intrusions in the Ablah area, Saudi Arabia[J]. Journal of Journal of Asian Earth Sciencesences, 2016, 12: 58-79.

Alapieti TT, Filén BA, Lahtinen JJ., et al. Early Proterozoic layered intrusions in the northeastern part of the Fennoscandian Shield[J]. Mineralogy and Petrology, 1990, 42(1): 1-22.

Alapieti TT, Kujanpaa J, Lahtinen JJ, et al. The Kemi stratiform chromitite deposit, northern Finland[J]. Economic Geology, 1989, 84(5): 1057-1077.

Albert C, Williams HM, Kaufmann F, et al. Iron isotope fractionation during magmatic evolution and implications for isotope disequilibrium in the Bushveld Complex[C]. AGU Fall Meeting, 2019, V23E-0215.

Allan JF, Batiza R, Perfit MR, et al. Petrology of lavas from the Lamont seamount chain and adjacent east Pacific rise, 10° N[J]. Journal of Petrology, 1989, 30: 1245-1298.

Allan JF, Sack RO, Batiza R. Cr-rich spinels as petrogenetic indicators; MORB-type lavas from the

Lamont seamount chain, eastern Pacific[J]. American Mineralogist, 1988, 43(1): 6-16.

Arai S, Uesugi J, Ahmed AH. Upper crustal podiform chromitite from the northern Oman ophiolite as the stratigraphically shallowest chromitite in ophiolite and its implication for Cr concentration[J]. Contributions to Mineralogy and Petrology, 2004, 147(2): 145-154.

Armienti P, Innocenti F, Pareschi MT, et al. 1991. Crystal population density in not stationary volcanic systems: estimate of olivine growth rate in basalts of Lanzarote (Canary Islands)[J]. 1991, 44(3-4): 181-196.

Aswad KJ, Aziz NR, Koyi HA. Cr-spinel compositions in serpentinites and their implications for the petrotectonic history of the Zagros Suture Zone, Kurdistan Region, Iraq[J]. Geological Magazine, 2011, 148(5-6): 802-818.

Bai Y, Su BX, Chen C, et al. Base metal mineral segregation and Fe-Mg exchange inducing extreme compositions of olivine and chromite from the Xiadong Alaskan-type complex in the southern part of the Central Asian Orogenic Belt[J]. Ore Geology Reviews, 2017, 90: 184-192.

Bai Y, Su BX, Xiao Y, et al. Chromium inter-mineral diffusion in ultramafic cumulates: elemental and isotopic evidence from the Stillwater Complex[J]. Geochimica et Cosmochimica Acta, 2019, 263: 167-181.

Bai Y, Su BX, Xiao Y, et al. Origin of reverse zoned Cr-spinels from the Paleoproterozoic Yanmenguan mafic-ultramafic complex in the North China Craton[J]. Minerals, 2018, 8(2): 62-77.

Ballhaus C, Berry RF, Green DH. High pressure experimental calibration of the olivine-orthopyroxene-spinel oxygen geobarometer: implications for the oxidation state of the upper mantle[J]. Contributions to Mineralogy and Petrology, 1991, 107: 27-40.

Ballhaus C, Fonseca RO, Münker C, et al. Spheroidal textures in igneous rocks-Textural consequences of H_2O saturation in basaltic melts[J]. Geochimica et Cosmochimica Acta, 2015, 167: 241-252.

Ballhaus C. Origin of podiform chromite deposits by magma mingling[J]. Earth and Planetary Science Letters, 1998, 156(3-4): 185-193.

Ballhaus C. Redox state of lithospheric and asthenospheric upper mantle[J]. Contributions to Mineralogy and Petrology, 1993, 114(3): 331-348.

Barnes SJ, Naldrett AJ, Gorton MP. The origin of the fractionation of platinum-group elements in terrestrial magmas[J]. Chemical Geology, 1985, 53(3):303-323.

Barnes SJ, Pagé P, Prichard HM, et al. Chalcophile and platinum-group element distribution in the Ultramafic Series of the Stillwater Complex, MT, USA-Implications for processes enriching chromite layers in Os, Ir, Ru, and Rh[J]. Mineralium Deposita, 2015, 51: 25-47.

Barnes SJ, Roeder PL. The range of spinel compositions in terrestrial mafic and ultramafic rocks[J]. Journal of Petrology, 2001, 42: 2279-2302.

Barnes SJ. Chromite in Komatiites, II. Modification during Greenschist to Mid-Amphibolite Facies Metamorphism[J]. Journal of Petrology, 2000, 41(3): 387-409.

Barnes SJ. The effect of trapped liquid crystallization on cumulus mineral compositions in layered intrusions[J]. Contributions to Mineralogy and Petrology, 1986, 93(4): 524-531.

Barra F, Gervilla F, Hernández E, et al. Alteration patterns of chromian spinels from La Cabaña peridotite, south-central Chile[J]. Mineralogy and Petrology, 2014, 108(6): 819-836.

Beard JS, Lofgren GE. Dehydration melting and water-saturated melting of basaltic and andesitic greenstones and amphibolites at 1, 3, and 6.9 kbr[J]. Journal of Petrology, 1991, 32: 365-401.

Bell BR, Claydon RV. The cumulus and post-cumulus evolution of chrome-spinels in ultrabasic layered intrusions: evidence from the Cuillin Igneous Complex, Isle of Skye, Scotland[J]. Contributions to Mineralogy and Petrology, 1992, 112(2): 242-253.

Bilenker LD, VanTongeren JA, Lundstrom CC, et al. Iron isotopic evolution during fractional crystallization of the uppermost Bushveld Complex layered mafic intrusion[J]. Geochemistry, Geophysics, Geosystems, 2017, 18: 956-972.

Bonnand P, Parkinson IJ, Anand M. Mass dependent fractionation of stable chromium isotopes in mare basalts: Implications for the formation and the differentiation of the Moon[J]. Geochimica et Cosmochimica Acta, 2016, 175(20): 208-221.

Botcharnikov RE, Almeev RR, Koepke J, et al. Phase relations and liquid lines of descent in hydrous ferrobasal-implications for the Skaergaard intrusion and Columbia River flood basalts[J]. Journal of Petrology, 2008, 49(9): 1687-1727.

Bottinga Y, Javoy M. MORB degassing: Bubble growth and ascent[J]. Chemical Geology, 1990, 81(4): 255-270.

Boudreau AE, Mathez EA, McCallum IS. Halogen geochemistry of the Stillwater and Bushveld Complexes: evidence for transport of the platinum-group elements by Cl-rich fluids[J]. Journal of Petrology, 1986, 27(4): 967-986.

Boudreau AE, McCallum IS. Investigations of the Stillwater Complex; III, The Picket Pin Pt/Pd deposit[J]. Economic Geology, 1953, 81(8): 1953-1975.

Boudreau AE, McCallum IS. Concentration of platinum-group elements by magmatic fluids in layered intrusions[J]. Economic Geology, 1992, 87(7): 1830-1848.

Boudreau AE, McCallum IS. Investigations of the Stillwater Complex: Part V. Apatites as indicators of evolving fluid composition[J]. Contributions to Mineralogy and Petrology, 1989, 102(2): 138-153.

Boudreau AE, Stewart MA, Spivack AJ. Stable Cl isotopes and origin of high-Cl magmas of the Stillwater Complex, Montana[J]. Geology, 1997, 25: 791-794.

Boudreau AE. Hydromagmatic processes and platinum-group element deposits in layered intrusions[M]. Cambridge: Cambridge University Press, 2019.

Boudreau AE. Pattern formation during crystallization and the formation of fine-scale layering[J]. Origins of Igneous layering, 1987, 196: 453-471.

Boudreau AE. The Stillwater Complex, Montana-Overview and the significance of volatiles[J]. Mineralogical Magazine, 2016, 80: 585-637.

Brearley M, Scarfe CM. Dissolution rates of upper mantle minerals in an alkali basalt melt at high pressure: An experimental study and implications for ultramafic xenolith survival[J]. Journal of Petrology, 1986, 27: 1157-1182.

Brenan JM, Caciagli NC. Fe-Ni exchange between olivine and sulphide liquid: Implications for oxygen barometry in sulphide-saturated magmas[J]. Geochimica et Cosmochimica Acta, 2000, 64(2): 307-320.

Burnham CW. Water and magmas: a mixing model[J]. Geochimica et Cosmochimica Acta, 1975, 39: 1077-1084.

Cameron EN. Evolution of the Lower Critical Zone, central sector, eastern Bushveld Complex, and its chromite deposits[J]. Economic Geology, 1980, 75: 845-871.

Cameron EN. Postcumulus and subsolidus equilibration of chromite and coexisting silicates in the

eastern Bushveld Complex[J]. Geochimica et Cosmochimica Acta 1975, 39: 1021-1033.

Campbell IH, Murck BW. Petrology of the G and H chromitite zones in the Mountain View area of the Stillwater Complex, Montana[J]. Journal of Petrology, 1993, 34: 291-316.

Cawthorn RG, Barnes SJ, Ballhaus C, et al. Platinum-group element, chromium, and vanadium deposits in mafic and ultramafic rocks[J]. Economic Geology, 2005, 100: 215-249.

Cawthorn RG, O'Hara MJ. Amphibole fractionation in calc-alkaline magma genesis[J]. American Journal of Science, 1976, 276: 309-329.

Cawthorn RG. Layered Intrusions[J]. Developments in Petrology, 1996, 15: 531.

Ceuleneer G. Mantle mapped in the desert[J]. Nature, 2004, 432: 156-157.

Chakraborty S, Ganguly J. Cation diffusion in aluminosilicate garnets: experimental determination in spessartine-almandine diffusion couples, evaluation of effective binary diffusion coefficients, and applications[J]. Contributions to Mineralogy and Petrology, 1992, 111(1): 74-86.

Chalmers B. Principles of Solidification[M]. New York: John Wiley and Sons, 1964.

Chen B, Suzuki K, Tian W, et al. Geochemistry and Os-Nd-Sr isotopes of the Gaositai Alaskan-type ultramafic complex from the northern North China Craton: Implications for mantle-crust interaction[J]. Contributions to Mineralogy and Petrology, 2009, 158(5): 683-702.

Chen C, Su BX, Uysal I, et al. Iron isotopic constraints on the origin of peridotite and chromitite in the Kızıldağ ophiolite, southern Turkey[J]. Chemical Geology, 2015, 417: 115-124.

Chen C, Su BX, Xiao Y, et al. High-temperature chromium isotope fractionation and its implications: Constraints from Kızıldağ ophiolite, SE Turkey[J]. Lithos, 2019, 342: 361-369.

Chen LM, Song XY, Zhu XK, et al. Iron isotope fractionation during crystallization and sub-solidus re-equilibration: Constraints from the Baima mafic layered intrusion, SW China[J]. Chemical Geology, 2014, 380: 97-109.

Chen LM, Teng FZ, Song XY, et al. Magnesium isotopic evidence for chemical disequilibrium among cumulus minerals in layered mafic intrusion[J]. Earth and Planetary Science Letters, 2018, 487: 74-83.

Clark T. Oxide minerals in the Turnagain ultramafic complex, northwestern British Columbia[J]. Canadian Journal of Earth Sciences, 1978, 15(12): 1893-1903.

Clark T. Petrology of the Turnagain ultramafic complex, northwestern British Columbia[J].

Canadian Journal of Earth Sciences, 1980, 17: 744-757.

Colás V, González-Jiménez JM, Griffin WL, et al. Fingerprints of metamorphism in chromite: New insights from minor and trace elements[J]. Chemical Geology, 2014, 389: 137-152.

Collinet M, Charlier B, Namur O, et al. Crystallization history of enriched shergottites from Fe and Mg isotope fractionation in olivine megacrysts[J]. Geochimica et Cosmochimica Acta, 2017, 207: 277-297.

Coogan LA, Jenkin GR, Wilson RN. Constraining the cooling rate of the lower oceanic crust: A new approach applied to the Oman ophiolite[J]. Earth and Planetary Science Letters, 2002, 199(1-2): 127-146.

Cooper RWL. 1997. Magmatic unconformities and stratigraphic relations in the Peridotite zone, Stillwater Complex, Montana[J]. Canadian Journal of Earth Sciences, 1997, 34(4): 407-425.

Cui MM, Su BX, Wang J, et al. Alaskan-type nature and PGE mineralization of the Wuxing mafic-ultramafic complex in eastern part of the Central Asian Orogenic Belt[J]. Ore Geology Reviews, 2020, 123: 1-24.

Dauphas N, Roskosz M, Alp EE, et al. Magma redox and structural controls on iron isotope variations in Earth's mantle and crust[J]. Earth and Planetary Science Letters, 2014, 398: 127-140.

Dauphas N, Teng FZ, Arndt NT. Magnesium and iron isotopes in 2.7 Ga Alexo komatiites: Mantle signatures, no evidence for Soret diffusion, and identification of diffusive transport in zoned olivine[J]. Geochimica et Cosmochimica Acta, 2010, 74(11): 3274-3291.

Deer WA, Howie RA, Zussman J. An introduction to the rock-forming minerals 2nd edition[M]. England: Longman, 1992.

DePaolo DJ, Wasserburg GJ. Sm-Nd age of the Stillwater Complex and the mantle evolution curve for neodymium[J]. Geochimica et Cosmochimica Acta, 1979, 43: 999-1008.

Dick HJB, Bullen T. Chrornian spinal as a petrogenetic indicator in abyssal and alpine-type peridotites and spatiallyassociated lavas[J]. Contributions to Mineralogy and Petrology, 1984, 86: 54-76.

Dickey JS, Yoder HS. Partitioning of chromium and aluminium between clinopyroxene and spinel[J]. Carnegie Inst. Washington Yearbook, 1972, 71: 384-392.

Dixon JE, Dixon TH, Bell DR, et al. Lateral variation in upper mantle viscosity: role of water[J]. Earth and Planetary Science Letters, 2004, 222(2): 451-467.

Dixon JE, Stolper EM, Holloway JR. An experimental study of water and carbon dioxide solubilities in mid-ocean ridge basaltic liquids. Part I: calibration and solubility models[J]. Journal of Petrology, 1995, 36: 1607-1631.

Dodson MH. Closure profiles in cooling systems[J]. Materials Science Forum, 1986, 7: 145-154.

Dodson MH. Closure temperature in cooling geochronological and petrological systems[J]. Contributions to Mineralogy and Petrology, 1973, 40(3): 259-274.

Dohmen R, Becker HW, Chakraborty S. Fe-Mg diffusion in olivine I: Experimental determination between 700 and 1200°C as a function of composition, crystal orientation and oxygen fugacity[J]. Physics and Chemistry of Minerals, 2007, 34: 389-407.

Dohmen R, Chakraborty S. Fe-Mg diffusion in olivine II: Point defect chemistry, change of diffusion mechanisms and a model for calculation of diffusion coefficients in natural olivine[J]. Biomed Research International, 2007, 34: 409-430.

Donaldson CH. Forsterite dissolution in superheated basaltic, andesitic and rhyolitic melts[J]. Mineralogical Magazine, 1990, 54: 67-74.

Donaldson CH. Ultrabasic breccias in layered intrusions-the Rhum complex[J]. The Journal of Geology, 1975, 83: 33-45.

Drake MJ, Newsom HE, Capobianco CJ. V, Cr, and Mn in the Earth, Moon, EPB, and SPB and the origin of the Moon: Experimental studies[J]. Geochimica et Cosmochimica Acta, 1989, 53(8): 2101-2111.

Eales HV, Botha WJ, Hattingh PJ, et al. The mafic rocks of the Bushveld Complex: A review of emplacement and crystallization history, and mineralization, in light of recent data[J]. Journal of African Earth Sciences, 1993, 16: 121-142.

Eales HV, Cawthorn RG. The Bushveld Complex[J]. Developments in Petrology, 1996, 15: 181-229.

Eales HV, Costin G. Crustally contaminated komatiite: primary source of the chromitites and Marginal, Lower, and Critical Zone magmas in a staging chamber beneath the Bushveld Complex[J]. Economic Geology, 2012, 107: 645-665.

Eales HV. Upper Critical Zone chromitite layers at RPM Union section mine, western Bushveld Complex[J]. Evolution of chromium ore fields, 1987, 144-168.

Edmonds M, Brett A, Herd RA, et al. Magnetite-bubble aggregates at mixing interfaces in andesite magma bodies[J]. Geological Society London Special Publications, 2015, 410(1): 95-121.

Edwards SJ, Pearce JA, Freeman J. New insights concerning the influence of water during the formation of podiform chromite[J]. Geological Society of America, 2000, 349: 139-147.

EI Goresy A, Prinz M, Ramdohr P. Zoning in spinels as an indicator of the crystallization histories of mare basalts[J]. Proceedings of the 7th Lunar Science Conference, 1976, 7: 1261-1279.

EI Rahman YA, Helmy HM, Shibata T, et al. Mineral chemistry of the Neoproterozoic Alaskan-type Akarem intrusion with special emphasis on amphibole: Implications for the pluton origin and evolution of subduction-related magma[J]. Lithos, 2012, 155: 410-425.

Emeleus CH, Cheadl, MJ, Hunter RH, et al. The Rum Layered Suite[J]. Developments in Petrology, 1996, 15(96): 403-439.

Evans BW, Frost BR. Chrome-spinel in progressive metamorphism-a preliminary analysis[J]. Geochimica et Cosmochimica Acta, 1975, 39: 959-972.

Evans BW, Moore JG. Mineralogy as a function of depth in the prehistoric Makaopuhi tholeiitic lava lake, Hawaii[J]. Contributions to Mineralogy and Petrology, 1968, 17(2): 85-115.

Farkaš J, Chrastný V, Novák M, et al. Chromium isotope variations ($\delta^{53/52}$Cr) in mantle-derived sources and their weathering products: Implications for environmental studies and the evolution of $\delta^{53/52}$Cr in the Earth's mantle over geologic time[J]. Geochimica et Cosmochimica Acta, 2013, 123: 74-92.

Farver JR, Giletti BJ. Oxygen and strontium diffusion kinetics in apatite and potential applications to thermal history determinations[J]. Geochimica et Cosmochimica Acta, 1989, 53(7): 1621-1631.

Farver JR, Yund RA. Silicon diffusion in forsterite aggregates: Implications for diffusion accommodated creep[J]. Geophysical Research Letters, 2000, 27: 2337-2340.

Faure M, Trap P, Lin W, et al. Polyorogenic evolution of the Paleoproterozoic Trans-North China Belt, new insights from the Lüliangshan-Hengshan-Wutaishan and Fuping massifs[J]. Episodes 2007, 30: 95-106.

Feig ST, Koepke J, Snow JE. Effect of oxygen fugacity and water on phase equilibria of a hydrous tholeiitic basalt[J]. Contributions to Mineralogy and Petrology, 2010, 160(4): 551-568.

Ferreira Filho CF, Naldrett AJ, Asif M. Distribution of platinum-group elements in the Niquelandia layered mafic-ultramafic intrusion, Brazil: implications with respect to exploration[J]. Canadian Mineralogist, 1995, 33(1): 165-184.

Fiege A, Holtz F, Cichy SB. Bubble formation during decompression of andesitic melts[J]. American Mineralogist, 2014, 99(5-6): 1052-1062.

Findlay D. Origin of the Tulameen ultramafic-gabbro complex, southern British Columbia[J]. Canadian Journal of Earth Sciences, 1969, 6(3): 399-425.

Fisk MR, Bence AE. Experimental crystallization of chrome spinel in FAMOUS basalt 527-1-1[J]. Earth and Planetary Science Letters, 1980, 48(1):111-123.

Foley SF, Andronikov AV, Jacob DE, et al. Evidence from Antarctic mantle peridotite xenoliths for changes in mineralogy, geochemistry and geothermal gradients beneath a developing rift[J]. Geochimica et Cosmochimica Acta, 2006, 70(12): 3096-3120.

Foley SF, Jacob DE, O'Neill SC. Trace element variations in olivine phenocrysts from Ugandan potassic rocks as clues to the chemical characteristics of parental magmas[J]. Contributions to Mineralogy and Petrology, 2011, 162(1): 1-20.

Foley SF, Prelevi'c D, Rehfeldt T, et al. Minor and trace elements in olivines as probes into early igneous and mantle melting processes[J]. Earth and Planetary Science Letters, 2013, 363(2): 181-191.

Ford CE, Biggar GM, Humphries DJ, et al. Role of water in the evolution of the lunar crust: An indication of lunar calc-alkaline volcanism[J]. Geochimica et Cosmochimica Acta, 1972, 3: 207-229.

Forsythe LM, Fisk MR. Comparison of experimentally crystallized and natural spinels from Leg 135[J]//Hawkins J, Parson L, Allan J. Proceedings of the Ocean Drilling Program: Scientific Results, State of Texas: Ocean Drilling Program, 1994, 135: 585-594.

Freer R. Diffusion in silicate minerals and glasses: A data digest and guide to the literature[J]. Contributions to Mineralogy and Petrology, 1981, 76(4): 440-454.

Gaetani GA, Grove TL. The influence of water on melting of mantle peridotite[J]. Contributions to

Mineralogy and Petrology, 1998, 131: 323-346.

Ganguly J, Ito M, Zhang X. Cr diffusion in orthopyroxene: Experimental determination, ^{53}Mn-^{53}Cr thermochronology, and planetary applications[J]. Geochimica et Cosmochimica Acta, 2007, 71: 3915-3925.

Ganguly J, Tirone M, Hervig RL. Diffusion kinetics of samarium and neodymium in garnet, and a method for determining cooling rates of rocks[J]. Science, 1998, 281(5378): 805-807.

Ganguly J, Tirone M. Diffusion closure temperature and age of a mineral with arbitrary extent of diffusion: theoretical formulation and applications[J]. Earth and Planetary Science Letters, 1999, 170: 131-140.

Ganguly J, Tirone M. Relationship between cooling rate and cooling age of a mineral: Theory and applications to meteorites[J]. Meteoritics and Planetary ence, 2001, 36(1): 167-175.

Ganguly J. Diffusion kinetics in minerals: principles and applications to tectono-metamorphic processes[J]. European Mineralogical Union Notes in Mineralogy, 2002, 4(10): 271-309.

Gao S, Rudnick RL, Xu WL, et al. Recycling deep cratonic lithosphere and generation of intraplate magmatism in the North China Craton[J]. Earth and Planetary Science Letters, 2008, 270: 41-53.

Gargiulo MF, Bjerg EA, Mogessie A. Spinel group minerals in metamorphosed ultramafic rocks from Río de Las Tunas belt, Central Andes, Argentina[J]. Geologica Acta, 2013, 11(2): 133-148.

Garuti G, Proenza JA, Zaccarini F. Distribution and mineralogy of platinum-group elements in altered chromitites of the Campo Formoso layered intrusion (Bahia State, Brazil): Control by magmatic and hydrothermal processes[J]. Mineralogy and Petrology, 2007, 89(3-4): 159-188.

Garuti G, Proenza JA, Zaccarini F. Platinum-group element distribution and mineralogy in altered chromitite of the Campo Formoso layered intrusion (Bahia state, Brazil)[J]. Geology and Petrography, 2005, 82-85.

Gervilla F, Padrón-Navarta JA, Kerestedjian T, et al. Formation of ferrian chromite in podiform chromitites from the Golyamo Kamenyane serpentinite, Eastern Rhodopes, SE Bulgaria: A two-stage process[J]. Contributions to Mineralogy and Petrology, 2012, 164: 643-657.

Ghiorso MS, Sack RO. Chemical mass transfer in magmatic processes IV. A revised and internally consistent thermodynamic model for the interpolation and extrapolation of liquid-solid equilibria

in magmatic systems at elevated temperatures and pressures[J]. Contributions to Mineralogy and Petrology, 1995, 119(2): 197-212.

Giachetti T, Gonnermann HM, Gardner JE, et al. Bubble Coalescence and Percolation Threshold in Expanding Rhyolitic Magma[J]. Geochemistry Geophysics Geosystems, 2019, 20: 1054-1074.

Giletti BJ. Diffusion effects on oxygen isotope temperatures of slowly cooled igneous and metamorphic rocks[J]. Earth and Planetary Science Letters, 1986, 77: 218-228.

Girardi VAV, Ferrario A, Correia CT, et al. A comparison of selected Precambrian Brazilian chromitites: Chromite, PGE-PGM, and Re/Os as parental source indicators[J]. Journal of South American Earth Sciences, 2006, 20(4): 303-313.

Giret A, Bonin B, Léger JM. Amphibole compositional trend in over-saturated and undersaturated alkaline plutonic ring complexes[J]. The Canadian Mineralogist, 1980, 18: 481-495.

Gnyloskurenko SV, Byakova AV, Raychenko OI, et al. Influence of wetting conditions on bubble formation at orifice in an inviscid liquid. Transformation of bubble shape and size[J]. Colloids and Surfaces A, 2003, 218(1): 73-87.

Godel B, Barnes SJ, Gurer D, et al. Chromite in komatiites: 3D morphologies with implications for crystallization mechanisms[J]. Contributions to Mineralogy and Petrology, 2013, 165: 173-189.

Goel G, Zhang L, Lacks DJ, et al. Isotope fractionation by diffusion in silicate melts: Insights from molecular dynamics simulations[J]. Geochimica et Cosmochimica Acta, 2012, 93: 205-213.

González-Jiménez JM, Reich M, Camprubí A, et al. Thermal metamorphism of mantle chromites and the stability of noble-metal nanoparticles[J]. Contributions to Mineralogy and Petrology, 2015, 170(2): 15.

Grant KJ, Ingrin J, Lorland JP, et al. Water partition between mantle minerals from peridotite xenoliths[J]. Contributions to Mineralogy and Petrology, 2007, 154: 15-34.

Green DH, Ringwood AE, Ware NG, et al. Experimental petrology and petrogenesis of Apollo 14 basalt[J]. Geochimica et Cosmochimica Acta, 1972, 3: 197.

Greenbaum D. The chromitiferous rocks of the Troodos ophiolite, Cyprus[J]. Economic Geology. 1977, 72: 1175-1194.

Gross J, Filiberto J, Herd CDK, et al. Petrography, mineral chemistry, and crystallization history of olivine-phyric shergottite NWA 6234: A new melt composition[J]. Meteoritics and Planetary

Sciences, 2013, 48(5): 854-871.

Grove TL, Baker MB, Kinzler RJ. Coupled CaAl-NaSi diffusion in plagioclase feldspar: Experiments and applications to cooling rate speedometry[J]. Geochimica et Cosmochimica Acta, 1984, 48(10): 2113-2121.

Gualda GA, Ghiorso MS. Magnetite scavenging and the buoyancy of bubbles in magmas. Part II: Energetics of crystal-bubble attachment in magmas[J]. Contributions to Mineralogy and Petrology, 2007, 154(4): 479-490.

Guild PW, Balsley JR. Chromite deposits of Red Bluff Bay and Vicinity, Baranof Island, Alaska[M]. Washington: US Government Printing Office, 1942.

Guillou-Frottier L, Burov E, Auge T, et al. Rheological conditions for emplacement of Ural-Alaskan-type ultramafic complexes[J]. Tectonophysics, 2014, 631: 130-145.

Guo JH, O'Brien PJ, Zhai MG. High-pressure granulites in the Sangan area, North China Craton: Metamorphic evolution, P-T paths and geotectonic significance[J]. Journal of Metamorphic Geology, 2010, 20(8): 741-756.

Guo JH, Sun M, Zhai MG. Sm-Nd and SHRIMP U-Pb zircon geochronology of high-pressure granulites in the Sanggan area, North China Craton: Timing of Paleoproterozoic continental collision[J]. Journal of Asian Earth Sciences. 2005, 24: 629-642.

Guo JH, Zhai MG. Sm-Nd age dating of high-pressure granulites and amphibolites from Sanggan area, North China Craton[J]. Chinese Science Bulletin, 2001, 46(2): 106-111.

Guotana JMR, Payot BD, Dimalanta CB, et al. Petrological and geochemical characteristics of the Samar Ophiolite ultramafic section: Implications on the origins of the ophiolites in Samar and Leyte islands, Philippines[J]. International Geology Review, 2018, 60: 401-417.

Habtoor A, Ahmed AH, Harbi H. Petrogenesis of the Alaskan-type mafic-ultramafic complex in the Makkah quadrangle, western Arabian Shield, Saudi Arabia[J]. Lithos, 2016, 263: 33-51.

Hamlyn PR, Keays RR. Sulfur saturation and second-stage Melts: Application to the Bushveld platinum metal deposits[J]. Economic Geology, 1986, 81: 1431-1445.

Hamlyn PR, Keays RR. Origin of chromite compositional variation in the Panton Sill, Western Australia[J]. Contributions to Mineralogy and Petrology, 1979, 69(1): 75-82.

Han R, Qin L, Brown ST, et al. Differential isotopic fractionation during Cr (VI) reduction by an

aquifer-derived bacterium under aerobic versus denitrifying conditions[J]. Applied and Environmental Microbiology, 2012, 78(7): 2462-2464.

Hao Y, Xia Q, Li Q, et al. Partial melting control of water contents in the Cenozoic lithospheric mantle of the Cathaysia block of South China[J]. Chemical Geology, 2014, 380: 7-19.

Hart SR, Davis KE. Nickel partitioning between olivine and silicate melt[J]. Earth and Planetary Science Letters, 1978, 40: 203-219.

Haskin LA, Salpas PA. Genesis of compositional characteristics of Stillwater AN-I and AN-II thick anorthosite units[J]. Geochimica et Cosmochimica Acta, 1992, 56(3): 1187-1212.

Hatton CJ, Von Gruenewaldt G. Early Precambrian layered intrusions[M]. New York: Early Precambrian Basic Magmatism, 1990.

Hatton CJ, Von Gruenewaldt G. Chromite from the Swartkop chrome mine-an estimate of the effects of subsolidus re-equilibration[J]. Economic Geology, 1985, 80(4): 911-924.

He L, Chen L, Dorji HZ, et al. 2018. Mapping chromite deposits with audio magnetotellurics in the Luobusa ophiolite of southern Tibet[J]. Geophysics, 2018, 83: 47-57.

He LF, Hu XM, Zha YB, et al. Distribution and origin of high magnetic anomalies at Luobusa Ophiolite in Southern Tibet[J]. Chinese Science Bulletin, 2014, 59(23): 2898-2908.

He YS, Ke S, Teng FZ, et al. High precision iron isotope analysis of geological standards by resolution MC-ICPMS[J]. Geostandards and Geoanalytical Research, 2015, 39: 341-356.

Helmy HM, EI Mahallawi MM. Gabbro Akarem mafic-ultramafic complex, Eastern Desert, Egypt: A Late Precambrian analogue of Alaskan-type complexes[J]. Mineralogy and Petrology, 2003, 77(1): 85-108.

Helmy HM, EI Rahman YMA, Yoshikawa M, et al. Petrology and Sm-Nd dating of the Genina Gharbia Alaskan-type complex (Egypt): Iinsights into deep levels of Neoproterozoic island arcs[J]. Lithos, 2014, 198-199: 263-280.

Helmy HM, Mogessie A. Gabbro Akarem, eastern Desert, Egypt: Cu-Ni-PGE mineralization in a concentrically zoned mafic-ultramafic complex[J]. Mineralium Deposita, 2001, 36(1): 58-71.

Helmy HM, Yoshikawa M, Shibata T, et al. Sm-Nd and Rb-Sr isotope geochemistry and petrology of Abu Hamamid intrusion, eastern Desert, Egypt: An Alaskan-type complex in a backarc setting[J]. Precambrian Research, 2015, 258: 234-246.

Helz RT. Experimental constraints on the origin of the Ultramafic series of the Stillwater Complex, Montana[J]. Geological Society of America, 1992: A85-A86.

Helz RT. Phase relations of basalts in their melting range at P_{H_2O} = 5 kb as a function of oxygen fugacity: Part I. Mafic phases[J]. Journal of Petrology, 1973, 14: 249-302.

Helz RT. The Stillwater Complex, Montana: A subvolcanic magma chamber?[J]. American Mineralogist, 1995, 80: 1343-1346.

Henderson P, Suddaby P. The nature and origin of the chrome-spinel of the Rhum layered intrusion[J]. Contributions to Mineralogy and Petrology, 1971, 33: 21-31.

Henderson P, Wood RJ. Reaction relationships of chrome-spinels in igneous rocks-further evidence from the layered intrusion of Rhum and Mull, Inner Hebrides, Scotland[J]. Contributions to Mineralogy and Petrology, 1981, 78: 225-229.

Henderson P. Reaction trends shown by chrome-spinels of the Rhum layered intrusion[J]. Geochimica et Cosmochimica Acta, 1975, 39: 1035-1044.

Herzberg C, O'hara MJ. Plume-associated ultramafic magmas of Phanerozoic age[J]. Journal of Petrology, 2002, 43: 1857-1883.

Herzberg CT, Chapman NA. Clinopyroxene geothermometry of spinel-lherzolites[J]. American Mineralogist, 1976, 61: 7-8.

Hess GB. Heat and mass transport during crystallization of the Stillwater igneous complex[J]. Geological Society of America Bulletin, 1972, 132: 503-520.

Hess HH, Smith JR. Stillwater igneous complex, Montana, a quantitative mineralogical study[J]. Geological Society of America, 1960, 80: 230.

Higgins SJ, Snyder GA, Mitchell JN, et al. Petrology of the early Proterozoic Burakovsky layered intrusion, southern Karelia, Russia; mineral and whole-rock major-element chemistry[J]. Canadian Journal of Earth Sciences, 1997, 34(4): 390-406.

Hill R, Roeder P. The crystallization of spinel from basaltic liquid as a function of oxygen fugacity[J]. The Journal of Geology, 1974, 82: 709-729.

Hillier S, Roe MJ, Geelhoed JS, et al. Role of quantitative mineralogical analysis in the investigation of sites contaminated by chromite ore processing residue[J]. Science of the Total Environment, 2003, 308: 195-210.

Himmelberg GR, Loney RA. Characteristics and petrogenesis of Alaskan-type ultramafic-mafic intrusions, southeastern Alaska[R]. United States Geological Survey Professional Paper, 1995, 1564: 1-47.

Himmerberg GR, Loney RA. Petrology of ultramafic and gabbroic rocks of the Canyon mountain ophiolite, Oregon[J]. American Journal of Science, 1980, 280: 232-268.

Holloway JR, Burnham CW. Melting relations of basalt with equilibrium water pressure less than total pressure[J]. Journal of Petrology, 1972, 13(1): 1-29.

Horan MF, Morgan JW, Walker RJ, et al. Re-Os isotopic constraints on magma mixing in the peridotite zone of the Stillwater Complex, Montana, USA[J]. Contributions to Mineralogy and Petrology, 2001, 141: 446-457.

Hu SL, Luo D, Chen LH. Genesis of sieve-textured rim of spinel in mantle xenoliths[J]. Acta Petrologica Sinica, 2017, 33: 69-80.

Hu Y, Teng FZ, Ionov DA. Magnesium isotopic composition of metasomatized upper sub-arc mantle and its implications to Mg cycling in subduction zones[J]. Geochimica et Cosmochimica Acta, 2020, 278: 219-234.

Hu Y, Teng FZ, Zhang HF, et al. Metasomatism-induced mantle magnesium isotopic heterogeneity: Evidence from pyroxenites[J]. Geochimica et Cosmochimica Acta, 2016, 185: 88-111.

Huang F, Chakraborty P, Lundstrom CC, et al. Isotope fractionation in silicate melts by thermal diffusion[J]. Nature, 2010, 464: 396.

Huang F, Chen LJ, Wu ZQ, et al. First-principles calculations of equilibrium Mg isotope fractionations between garnet, clinopyroxene, orthopyroxene, and olivine: Implications for Mg isotope thermometry[J]. Earth and Planetary Science Letters, 2013, 367: 61-70.

Huang F, Zhang ZF, Lundstrom CC, et al. Iron and magnesium isotopic compositions of peridotite xenoliths from Eastern China[J]. Geochimica et Cosmochimica Acta, 2011, 75: 3318-3334.

Hugh R. Using geochemical data: Evaluation, presentation, interpretation[M]. New York: Longman Scientific and Technical, 1993.

Hurwitz S, Navon O. Bubble nucleation in rhyolitic melts: Experiments at high pressure, temperature, and water content[J]. Earth and Planetary Science Letters, 1994, 122: 267-280.

Irvine TN, Keith, DW, Todd, SG. The J-M platinum palladium reef of the Stillwater Complex,

Montana: II. Origin by double-diffusive convective magma mixing and implications for the Bushveld Complex[J]. Economic Geology, 1983, 78: 1287-1334.

Irvine TN. Heat transfer during solidification of layered intrusions. I. Sheets and sills[J]. Canadian Journal of Earth Sciences, 1970, 7(4): 1031-1061.

Irvine TN. The ultramafic complex and related rocks of Duke Island, southeastern Alaska[D]. Los Angeles: California Institute of Technology, Pasadena, 1959.

Irvine TN. Origin of the ultramafic complex at Duke Island, southeastern Alaska[J]. Mineralogical Society of America Special Paper, 1963, 1: 36-45.

Irvine TN. Chromian spinel as a petrogenetic indicator. Part 1. Theory[J]. The Canadian Journal of Earth Science, 1965, 2(6): 648-672.

Irvine TN. Chromian spinel as a petrogenetic indicator: Part 2. Petrologic applications[J]. Canadian Journal of Earth Sciences, 1967, 4(1): 71-103.

Irvine TN. Bridget Cove volcanics, Juneau area, Alaska: Possible parental magma of Alaskan-type ultramafic complexes[J]. Carnegie Inst Washington Yearb, 1973, 72: 478-491.

Irvine TN. Petrology of the Duke Island ultramafic complex Southern Alaska[J]. Geological Society of American Memoir, 1974, 138: 240-241.

Irvine TN. Crystallization sequences in the Muskox intrusion and other layered intrusions; Part II, Origin of chromitite layers and similar deposits of other magmatic ores[J]. Geochimica et Cosmochimica Acta, 1975, 39: 991-1020.

Ito M, Ganguly J. Diffusion kinetics of Cr in olivine and ^{53}Mn-^{53}Cr thermochronology of early solar system objects[J]. Geochimica et Cosmochimica Acta, 2006, 70: 799-809.

Jackson ED. Primary textures and mineral associations in the ultramafic zone of the Stillwater complex, Montana[J]. Mathematical Bioences, 1961, 31(1-2):175-190.

Jackson ED. The chromite deposits of the Stillwater Complex, Montana[J]//Ridge JD. Ore deposits of the United States, 1933-1967 (Graton-Sales volume). New York: The American Institute of Mining, Metallurgical, and Petroleum Engineers, Incorporation, 1968, 2: 1495-1510.

Jackson ED. Chemical variation in coexisting chromite and olivine in chromitite zones of the Stillwater Complex[J]. Economic Geology Monographs Pages, 1969: 41-71.

Jambon A, Lussiez P, Clocchiatti R, et al. Olivine growth rates in a tholeiitic basalt: An experimental

study of melt inclusions in plagioclase[J]. Chemical Geology, 1992, 96: 277-287.

Jan MQ, Windley BF. Chromian spinel-silicate chemistry in ultramafic rocks of the Jijal complex, Northwest Pakistan[J]. Journal of Petrology, 1990, 31(3): 667-715.

Jaques AL. Petrology and petrogenesis of cumulate peridotites and gabbros from the Marum ophiolite complex, northern Papua New Guinea[J]. Journal of Petrology, 1981, 22: 1-40.

Jenkins MC, Mungall JE. Genesis of the Peridotite Zone, Stillwater Complex, Montana, USA[J]. Journal of Petrology, 2018, 59: 2157-2189.

Jing JJ, Su BX, Xiao Y, et al. Cryptic metasomatism revealed by Li isotopes of mantle xenoliths beneath the Thrace Basin, NW Turkey[J]. Journal of Asian Earth Sciences, 2018, 166: 270-278.

Johan Z. Alaskan-type complexes and their platinum-group element mineralization[J]//Cabri LJ. Geology, geochemistry, mineralogy and mineral beneficiation of Platinum-Group elements. Quebec: Canadian Institute of Mining, Metallurgy and Petroleum, 2002.

Johan Z. Platinum-group minerals from placers related to the Nizhni Tagil (Middle Urals, Russia) Uralian-Alaskan-type ultramafic complex: Ore-mineralogy and study of silicate inclusions in (Pt, Fe) alloys[J]. Mineralogy and Petrology, 2006, 87(1): 1-30.

Johan Z, Martin RF, Ettler V. Fluids are bound to be involved in the formation of ophiolitic chromite deposits[J]. European Journal of Mineralogy, 2017, 29: 543-555.

Jollands MC, O'Neill HSC, Van Orman J, et al. Substitution and diffusion of Cr^{2+} and Cr^{3+} in synthetic forsterite and natural olivine at 1200-1500° C and 1 bar[J]. Geochimica et Cosmochimica Acta, 2017, 220: 407-428.

Jones WR, Peoples JW, Howland AL. Igneous and tectonic structures of the Stillwater Complex, Montana[J]. United States of Geological Survey Bulletin, 1960, 1071: 281-340.

Kahl M, Chakraborty S, Costa F, et al. Dynamic plumbing system beneath volcanoes revealed by kinetic modeling, and the connection to monitoring data: An example from Mt. Etna[J]. Earth and Planetary Science Letters, 2011, 308: 11-22.

Kamenetsky VS, Crawford AJ, Meffre S. Factors controlling chemistry of magmatic spinel: An empirical study of associated olivine, Cr-spinel and melt inclusions from primitive rocks[J]. Journal of Petrology, 2001, 42: 655-671.

Kaufmann FED, Vukmanovic Z, Holness MB, et al. Orthopyroxene oikocrysts in the MG1

chromitite layer of the Bushveld Complex: implications for cumulate formation and recrystallization[J]. Contributions to Mineralogy and Petrology, 2018, 173: 1-17.

Kawamoto T. Experimental constraints on differentiation and H_2O abundance of calc-alkaline magmas[J]. Earth and Planetary Science Letters, 1996, 144: 577-589.

Kelemen PB, Whitehead JA, Aharonov E, et al. Experiments on flow focusing in soluble porous media, with applications to melt extraction from the mantle[J]. Journal of Geophysical Research, 1995, 100: 475-496.

Kennedy AK, Lofgren GE, Wasserburg GJ. An experimental study of trace element partitioning between olivine, orthopyroxene and melt in chondrules: Equilibrium values and kinetic effects[J]. Earth and Planetary Science Letters, 1993, 115: 177-195.

Klemme S, O'Neill HSC. The near-solidus transition from garnet lherzolite to spinel lherzolite[J]. Contributions to Mineralogy and Petrology, 2000, 138: 237-248.

Kloeck W, Palme H. Partitioning of siderophile and chalcophile elements between sulfide, olivine, and glass in a naturally reduced basalt from Disko Island, Greenland[J]. Lunar and Planetary Science conference Proceedings, 1988, 18: 471-483.

Knipping JL, Bilenker LD, Simon AC, et al. Giant Kiruna-type deposits form by efficient flotation of magmatic magnetite suspensions[J]. Geology, 2015, 43: 591-594.

Knipping JL, Webster JD, Simon AC, et al. Accumulation of magnetite by flotation on bubbles during decompression of silicate magma[J]. Scientific Reports, 2019, 9: 3852.

Krause J, Brügmann GE, Pushkarev EV. Accessory and rock forming minerals monitoring the evolution of zoned mafic-ultramafic complexes in the Central Ural mountains[J]. Lithos, 2007, 95(1): 19-42.

Kröner A, Wilde SA, Li JH, et al. Age and evolution of a late Archaean to early Palaeozoic upper to lower crustal section in the Wutaishan-Hengshan-Fuping terrain of northern China[J]. Journal of Asian Earth Sciences, 2005, 24: 577-595.

Labotka TC, Kath RL. Petrogenesis of the contactmetamorphic rocks beneath the Stillwater Complex, Montana[J]. Geological Society of America Bulletin, 2001, 113: 1312-1323.

Labotka TC. Petrogenesis of metamorphic rocks beneath the Stillwater Complex: Assemblages and conditions of metamorphism[J]//Czamanske GK, Zientek ML. The Stillwater Complex,

Montana: Geology and guide. Butte: Montana Bureau of Mines and Geology, 1985.

Lambert DD, Simmons EC. Magma evolution in the Stillwater Complex, Montana: I. Rare earth element evidence for the formation of the Ultramafic series[J]. American Journal of Science, 1987, 287: 1-32.

Lambert DD, Walker RJ, Morgan JW, et al. Re-Os and Sm-Nd isotope geochemistry of the Stillwater Complex, Montana: Implications for the petrogenesis of the J-M Reef[J]. Journal of Petrology, 1994, 35: 1717-1753.

Lanphere MA, Eberlein GD. Potassium-argon ages of magnetite-bearing ultramafic complexes in southeastern Alaska[J]. Geological Society of America Special Paper, 1966, 87: 94.

Lanphere MA. Sr-Rb-K and Sr isotopic relationships in ultramafic rocks, southeastern Alaska[J]. Earth and Planetary Science Letters, 1968, 4(3): 185-190.

Latypov R, Costin G, Chistyakova S, et al. Platinum-bearing chromite layers are caused by pressure reduction during magma ascent[J]. Nature Communications, 2018, 9: 462.

Leake BE, Woolley AR, Arps CES, et al. Nomenclature of amphiboles: Report of the subcommittee on amphiboles of the international mineralogical association, commission on new minerals and mineral names[J]. The Canadian Mineralogist, 1997, 35: 219-246.

Leblanc M, Nicolas A. Ophiolitic chromitites[J]. International Geological Review, 1992, 34(7): 653-686.

Leblanc M. Chromite growth, dissolution and deformation from a morphological view point: SEM investigations[J]. Mineral Deposita, 1980, 15: 201-210.

Lee CA. A Review of Mineralization in the Bushveld Complex and some other Layered Intrusions[J]. Developments in Petrology, 1996, 15(96):103-145.

Lehmann J. Diffusion between olivine and spinel: application to geothermometry[J]. Earth and Planetary Science Letters, 1983, 64: 123-138.

Lemarchand F, Benoit V, Calais G. Trace element distribution coefficients in alkaline series[J]. Geochimica et Cosmochimica Acta, 1987, 51(5): 1071-1081.

Lenaz D, Velicogna M, Halenius U, et al. Structural parameters of Cr-bearing spinels and pleonaste from the Cuillin Igneous Complex (Isle of Skye, Scotland): Implications for metamorphic and cooling history[J]. Mineralogical Magazine, 2016, 80: 749-764.

Leroy LW. Troctolite-anorthosite zone I and the J-M reef: Frog Pond Adit to Graham Creek area[J]//Czamanske GK, Zientek ML. The Stillwater Complex, Montana: Geology and guide. Butte: Montana Bureau of Mines and Geology, 1985.

Lesher CE, Walker D. Solution properties of silicate liquids from thermal diffusion experiments[J]. Geochimica et Cosmochimica Acta, 1986, 50: 1397-1411.

Li C, Naldrett AJ, Ripley EM. Controls on the Fo and Ni contents of olivine in sulfide-bearing mafic-ultramafic intrusions: Principles, modeling, and examples from Voisey's Bay[J]. Earth Science Frontiers, 2007, 14: 177-185.

Li C, Naldrett AJ. Geology and petrology of the Voisey's Bay intrusion: Reaction of olivine with sulfide and silicate liquids[J]. Lithos, 1999, 47: 1-31.

Li C, Ripley EM, Sarkar A, et al. Origin of phlogopite-orthopyroxene inclusions in chromites from the Merensky Reef of the Bushveld Complex, South Africa[J]. Contributions to Mineralogy and Petrology, 2005, 150: 119-130.

Li C, Ripley EM, Thakurta J, et al. Variations of olivine Fo-Ni contents and highly chalcophile element abundances in arc ultramafic cumulates, southern Alaska[J]. Chemical Geology, 2013, 351: 15-28.

Li C, Ripley EM. The relative effects of composition and temperature on olivine-liquid Ni partitioning: Statistical deconvolution and implications for petrologic modeling[J]. Chemical Geology, 2010, 275: 99-104.

Li C, Xu Z, Waal SAD, et al. Compositional variations of olivine from the Jinchuan Ni-Cu sulfide deposit, Western China: Implications for ore genesis[J]. Mineralium Deposita, 2004, 39: 159-172.

Li CS, Thakurta J, Ripley EM. Low-Ca contents and kink-banded textures are not unique to mantle olivine: Evidence from the Duke Island complex, Alaska[J]. Mineralogy and Petrology, 2012, 104(3): 147-153.

Li JL, Wang KY, Wang QC, et al. Early Proterozoic collision orogenic belt in Wutaishan area China[J]. Chinese Journal of Geology, 1990, 25(1): 1-11.

Li P, Scott JM, Liu J, et al. Lateral H_2O variation in the Zealandia lithospheric mantle controls orogen width[J]. Earth and Planetary Science Letters, 2018, 502: 200-209.

Liang Z, Xiao Y, Thakurta J, et al. Exsolution lamellae in olivine grains of dunite units from different types of mafic-ultramafic complexes[J]. Acta Geologica Sinica-English Edition, 2018, 92(2): 586-599.

Libowitzky E, Rossman GR. An IR absorption calibration for water in minerals[J]. American Mineralogist, 1997, 82: 1111-1115.

Libowitzky E, Rossman GR. Principles of quantitative absorbance measurements in anisotropic crystals[J]. Physics and Chemistry of Minerals, 1996, 23: 319-327.

Liermann HP, GangulyJ. Diffusion kinetics of Fe^{2+} and Mg in aluminous spinel: Experimental determination and applications[J]. Geochimica et Cosmochimica Acta, 2002, 66: 2903-2913.

Lipin BR. Pressure increases, the formation of chromite seams, and the development of the ultramafic series in the Stillwater Complex, Montana[J]. Journal of Petrology, 1993, 34(5): 955-976.

Liu P, Teng F, Dic, HJ, et al. Magnesium isotopic composition of the oceanic mantle and oceanic Mg cycling[J]. Geochimica et Cosmochimica Acta, 2017, 206: 151-165.

Liu PP, Zhou MF, Luais B, et al. Disequilibrium iron isotopic fractionation during the high-temperature magmatic differentiation of the Baima Fe-Ti oxide-bearing mafic intrusion, SW China[J]. Earth and Planetary Science Letters, 2014, 399: 21-29.

Liu SA, Teng FZ, He YS, et al. Investigation of magnesium isotope fractionation during granite differentiation: Implication for Mg isotopic composition of the continental crust[J]. Earth and Planetary Science Letters, 2010, 297: 646-654.

Liu SA, Teng FZ, Yang W, et al. High-temperature inter-mineral magnesium isotope fractionation in mantle xenoliths from the North China craton[J]. Earth and Planetary Science Letters, 2011, 308: 131-140.

Liu X, Su BX, Xiao Y, et al. Initial subduction of Neo-Tethyan ocean: Geochemical records in chromite and mineral inclusions in the Pozantı-Karsantı ophiolite, southern Turkey[J]. Ore Geology Reviews, 2019, 110: 102926.

Liu Y, Zhang Y. Bubble growth in rhyolitic melt[J]. Earth and Planetary Science Letters, 2000, 181: 251-264.

Loney RA, Brew DA, Muffler LJP. Reconnaissance geology of Chichagof, Baranof, and Kruzof

islands, southeastern Alaska[R]. United States Geological Survey Professional Papers, 1975, 792: 1-111.

Loney RA, Himmelberg GR, Shew N. Salt Chuck palladium-bearing ultramafic body, Prince of Wales Island[J]//Hamilton TD, Galloway JP. Geologic studies in Alaska by the US geological survey during 1986. Alaska: United States Geological Survey Circular, 1987.

Loney RA, Himmelberg GR. Petrogenesis of the Pd-rich intrusion at Salt Chuck, Prince of Wales Island; an Early Paleozoic Alaskan-type ultramafic body[J]. The Canadian Mineralogist, 1992, 30(4): 1005-1022.

Longhi J, Fram MS, Auwera JV, et al. Pressure effects, kinetics, and rheology of anorthositic and related magmas[J]. American Mineralogist, 1993, 78: 1016-1030.

Longhi J, Wooden JL, Coppinger KD. The petrology of high-Mg dikes from the Beartooth Mountains, Montana: a search for the parent magma of the Stillwater Complex[J]. Journal of Geophysical Research, 1983, 88: 53-69.

Longhi J. Experimental petrology and petrogenesis of mare volcanics[J]. Geochimica et Cosmochimica Acta, 1992, 56: 2235-2251.

Longpre MA, Klugel A, Diehl A, et al. Mixing in mantle magma reservoirs prior to and during the 2011-2012 eruption at El Hierro, Canary Islands[J]. Geology, 2014, 42: 315-318.

Lorand JP, Ceuleneer G. Silicate and base-metal sulfide inclusions in chromites from the Maqsad area (Oman ophiolite, Gulf of Oman): A model for entrapment[J]. Lithos, 1989, 22: 173-190.

Lord RA, Prichard HM, Sá JHS, et al. Chromite geochemistry and PGE fractionation in the Campo Formoso complex and Ipueria-Medrado sill, Bahia State, Brazil[J]. Economic Geology, 2004, 99: 339-363.

Loucks RR. Discrimination of ophiolitic from nonophiolitic ultramafic-mafic allochthons in orogenic belts by the Al/Ti ratio in clinopyroxene[J]. Geology, 1990, 18(4): 346-349.

Lugmair GW, Shukolyukov A. Early solar system timescales according to ^{53}Mn-^{53}Cr systematics[J]. Geochimica et Cosmochimica Acta, 1998, 62: 2863-2886.

Luth WC. Studies in the system $KAlSiO_4$-Mg_2SiO_4-SiO_2-H_2O, Inferred phase relations and petrologic implications[J]. Journal of Petrology, 1967, 8: 372-416.

Macris CA, Manning CE, Young ED. Crystal chemical constraints on inter-mineral Fe isotope

fractionation and implications for Fe isotope disequilibrium in San Carlos mantle xenoliths[J]. Geochimica et Cosmochimica Acta, 2015, 154: 168-185.

Maier WD, Barnes SJ, Chinyepi G, et al. The composition of magmatic Ni-Cu-(PGE) sulfide deposits in the Tati and Selebi-Phikwe belts of eastern Botswana[J]. Mineralium Deposita, 2008, 43(1): 37-60.

Maier WD, Barnes SJ, Groves DI. The Bushveld Complex, South Africa: Formation of platinum-palladium, chrome- and vanadium-rich layers via hydrodynamic sorting of a mobilized cumulate slurry in a large, relatively slowly cooling, subsiding magma chamber[J]. Mineralium Deposita, 2012, 48: 1-56.

Maier WD, Peltonen P, Halkoaho T, et al. Geochemistry of komatiites from the Tipasjärvi, Kuhmo, Suomussalmi, Ilomantsi and Tulppio greenstone belts, Finland: Implications for tectonic setting and Ni sulphide prospectivity[J]. Precambrian Research, 2013, 228: 63-84.

Malitch KN, Auge T, Badanina IY, et al. Os-rich nuggets from Au-PGE placers of the Maimecha-Kotui Province, Russia: A multi-disciplinary study[J]. Mineralogy and Petrology, 2002, 76(1): 121-148.

Malitch KN, Thalhammer OAR. Pt-Fe nuggets from clinopyroxene-dunite massifs, Russia: A structural, compositional and osmium-isotope study[J]. The Canadian Mineralogist, 2002, 40: 395-417.

Mallmann G, O'Neill HSC. The crystal/melt partitioning of V during mantle melting as a function of oxygen fugacity compared with some other elements (Al, P, Ca, Sc, Ti, Cr, Fe, Ga, Y, Zr and Nb)[J]. Journal of Petrology. 2009, 50: 1765-1794.

Manoochehri S, Schmidt MW. Settling and compaction of chromite cumulates employing a centrifuging piston cylinder and application to layered mafic intrusions[J]. Contributions to Mineralogy and Petrology, 2014, 168: 1091.

Manor MJ, Scoates JS, Nixon GT, et al. The giant mascot Ni-Cu-PGE deposit, British Columbia: Mineralized conduits in a convergent margin tectonic setting[J]. Economic Geology, 2016, 111: 57-87.

Marques JC, Ferreira-Filho CF. The chromite deposit of the Ipueira-Medrado Sill, São Francisco Craton, Bahia State, Brazil[J]. Economic Geology, 2003, 98: 87-108.

Mathez EA, Hunter RH, Kinzler R. 1997. Petrologic evolution of partially molten cumulate: The Atok section of the Bushveld Complex[J]. Contributions to Mineralogy and Petrology, 1997, 129: 20-34.

Mattsson T. The Roots of a Magma Chamber, the Central Intrusion, Rum, NW-Scotland[R]. United States Geological Survey Professional Papers, 2014.

Matveev S, Ballhaus C. Role of water in the origin of podiform chromitite deposits[J]. Earth and Planetary Science Letters, 2002, 203: 235-243.

Mavrogenes JA, O'Neill HTC. The relative effects of pressure, temperature and oxygen fugacity on the solubility of sulfide in mafic magmas[J]. Geochimica et Cosmochimica Acta, 1999, 63: 1173-1180.

McBirney AR, Noyes RM. Crystallization and layering of the Skaergaard intrusion[J]. Journal of Petrology, 1979, 20(3): 487-554.

McCallum IS, Domeneghetti MC, Schwartz JM, et al. Cooling history of lunar Mg-suite gabbronorite 76255, troctolite 76535 and Stillwater pyroxenite SC-936: The record in exsolution and ordering in pyroxenes[J]. Geochimica et Cosmochimica Acta, 2006, 70: 6068-6078.

McCallum IS, O'Brien HE. Stratigraphy of the lunar highland crust: Depths of burial of lunar samples from cooling-rate studies[J]. American Mineralogist, 1996, 81: 1166-1175.

McCallum IS, Raedeke LD, Mathez EA. Investigations in the Stillwater Complex: Part I. Stratigraphy and structure of the Banded zone[J]. American Journal of Science, 1980, 280: 59-87.

McCallum IS, Thurber DW, O'Brien HE, et al. Lead isotopes in sulfides from the Stillwater Complex, Montana: Evidence for subsolidus remobilization[J]. Contributions to Mineralogy and Petrology, 1999, 137: 206-219.

McCallum IS. The Stillwater complex[J]. Petroleum Exploration and Development, 1996, 15: 441-483.

McCallum IS. The Stillwater complex: A review of the geology[C]//Stillwater Complex Geology and Guide. Billings, Montana: 9th International Platinum Symposium, 2002, 21: 25.

McDonald JA. Liquid immiscibility as one factor in chromitite seam formation in the Bushveld Igneous Complex[J]. Economic Geology, 1965, 60: 1674-1685.

McKenzie D, O'Nions RK. Partial melt distributions from inversion of rare Earth element concentrations[J]. Journal of Petrology, 1991, 32: 1021-1091.

McNeil AM, Edgar AD. Sodium-rich metasomatism in the upper mantle: implications of experiments on the pyrolite-Na_2O-rich fluid system at 950°C, 20 kbar[J]. Geochimica et Cosmochimica Acta, 1987, 51: 2285-2294.

Medaris JrLG. Coexisting spinel and silicates in alpine peridotites of the granulite facies[J]. Geochimica et Cosmochimica Acta, 1976, 39: 947-958.

Meen JK, Ross DK, Elthon D. Gross isotopic heterogeneity in layered ultramafic cumulates[J]. Transactions of the American Geophysical Union, 1991, 72: 521.

Melche F, Grum W, Simon G, et al. Petrogenesis of the ophiolitic giant chromite deposits of Kempirsai, Kazakhstan: A study of solid and fluid inclusions in chromite[J]. Journal of Petrology, 1997, 38: 1419-1458.

Melnik O, Sparks RSJ. Controls on conduit magma flow dynamics during lava dome building eruptions[J]. Journal of Geophysical Research Atmospheres, 2005, 110: 161-162.

Merlini A, Grieco G, Diella V. Ferritchromite and chromian-chlorite formation in mélange-hosted Kalkan chromitite (Southern Urals, Russia)[J]. American Mineralogist, 2009, 94: 1459-1467.

Mertie JB. The Goodnews platinum deposits, Alaska[M]. Bulletin: United States Government Printing Office, 1940.

Meurer WP, Boudreau AE. The petrology and mineral compositions of the Middle Banded series of the Stillwater Complex, Montana[J]. Journal of Petrology, 1996, 37: 583-607.

Milman-Barris MS, Beckett JR, Baker MB, et al. Zoning of phosphorus in igneous olivine[J]. Contributions to Mineralogy and Petrology, 2008, 155: 739-765.

Mitchell RH, Keays RR. Abundance and distribution of gold, palladium and iridium in some spinel and garnet lherzolites: Implications for the nature and origin of precious metal-rich intergranular components in the upper mantle[J]. Geochimica et Cosmochimica Acta, 1981, 45(12): 2425-2442.

Mogk DW, Mueller PA. Evidence for Archean accretionary tectonics in the northern Wyoming Province, SW Montana[J]. Geological Society of America Abstracts with Programs, 1990, 22(262): 2-15.

Mondal SK, Mathez EA. Origin of the UG2 chromitite layer, Bushveld Complex[J]. Journal of Petrology, 2007, 48(3): 495-510.

Morse SA. Reaction constants for En-Fo-Sil equilibria: an adjustment and some applications[J]. American Journal of Science, 1979, 279: 1060-1069.

Moynier F, Yin QZ, Schauble E. Isotopic evidence of Cr partitioning into Earth's core[J]. Science, 2011, 331: 1417-1420.

Mukherjee R, Mondal SK, Rosing MT, et al. Compositional variations in the Mesoarchean chromites of the Nuggihalli schist belt, western Dharwar Craton (India): Potential parental melts and implications for tectonic setting[J]. Contributions to Mineralogy and Petrology, 2010, 160: 865-885.

Mungall JE, Brenan JM, Godel B, et al. Transport of metals and sulphur in magmas by flotation of sulphide melt on vapour bubbles[J]. Nature Geoscience, 2016, 8: 216-219.

Mungall JE, Hanley JJ, Arndt NT, et al. Evidence from meimechites and other low-degree mantle melts for redox controls on mantle-crust fractionation of platinum-group elements[J]. Proceedings of the National Academy of Sciences, 2006, 103(34): 12695-12700.

Mungall JE, Kamo SL, McQuade S. U-Pb geochronology documents out-of-sequence emplacement of ultramafic layers in the Bushveld Igneous Complex of South Africa[J]. Nature Communications, 2016, 7: 1-13.

Murray C. Zoned ultramafic complexes of the Alaskan type: Feeder pipes of andesitic volcanoes[J]. Geological Society of America Bulletin, 1972, 132: 313-335.

Mussallam K, Jung D, Burgath K. Textural features and chemical characteristics of chromites in ultramafic rocks, Chalkidiki complex (Northeastern Greece)[J]. Tschermaks Mineralogische und Petrographische Mitteilungen, 1981, 29: 75-101.

Mysen BO, Richet P. Silicate Glasses and Melts: Properties and structure[J]. Developments in Geochemistry, 2005, 10: 111-112.

Naldrett A, Kinnaird J, Wilson A, et al. The origin of chromitites and related PGE mineralization in the Bushveld Complex: New mineralogical and petrological constraints[J]. Mineralium Deposita, 2012, 47: 209-232.

Naldrett AJ. Key factors in the genesis of Noril'sk, Sudbury, Jinchuan, Voisey's Bay and other

world-class Cu-Ni-PGE deposits: Implication for exploration[J]. Australian Journal of Earth Sciences, 1997, 44: 283-315.

Naldrett AJ. Magmatic sulfide deposits; Geology, geochemistry and exploration[M]. Berlin: Springer-Verlag, 2004.

Naldrett AJ. Fundamentals of Magmatic Sulfide Deposits[J]//Li C, Ripley EM. Magmatic Ni-Cu and PGE deposits: Geology, geochemistry, and genesis. Society of Economic Geologists, 2011: 1-50.

Nandedkar RH, Ulmer P, Müntener O. Fractional crystallization of primitive, hydrous arc magmas: An experimental study at 0.7 GPa[J]. Contributions to Mineralogy and Petrology, 2014, 167: 1015.

Naslund HR, McBirney AR. Mechanisms of Formation of Igneous Layering[J]. Developments in Petrology, 1996:1-43.

Naumov VB, Kovalenko VI, Dorofeeva VA, et al. Average compositions of igneous melts from main geodynamic settings according to the investigation of melt inclusions in minerals and quenched glasses of rocks[J]. Geochemistry International, 2010, 48, 1185-1207.

Nazimova YV, Zaitsev VP, Petrov SV. The Galmoenan massif, Kamchatka, Russia: Geology, PGE minerlization, applied mineralogy, and beneficiation[J]. The Canadian Mineralogist, 2011, 49: 1433-1453.

Neave DA, Shorttle O, Oeser M, et al. Mantle-derived trace element variability in olivines and their melt inclusions[J]. Earth and Planetary Science Letters, 2018, 483: 90-104.

Nicholson DM, Mathez EA. Petrogenesis of the Merensky Reef in the Rustenburg section of the Bushveld Complex[J]. Contributions to Mineralogy and Petrology, 1991, 107: 293-309.

Nielsen RL, Forsythe LM, Gallaghan WE, et al. Major and trace element magnetite/melt partitioning[J]. Chemical Geology, 1994, 117: 167-191.

Nixon GT, Cabri LJ, Laflamme JHG. Platinum-group-element mineralization in lode and placer deposits associated with the Tulameen Alaskan-type complex, British Columbia[J]. The Canadian Mineralogist, 1990, 28(3): 503-535.

Nixon GT, Hammack JL, Ash CH, et al. Geology and platinum-group-element mineralization of Alaskan-type ultramafic-mafic complexes in British Columbia[M]. Columbia: British Columbia

Ministry of Employment and Investment, 1997.

Nixon GT. Ni-sulphide mineralization in the Turnagain Alaskan-type complex: A unique magmatic environment[J]. Geological Survey of British Columbia, 1998, 18: 1-12.

Noble JA, Taylor HP. Correlation of the ultramaficcomplexes of southeastern Alaska with those of North Americaand the World[R]. 21st International Geological Congress in Copenhagen, 1960, 13: 188-197.

Novella D, Frost DJ, Hauri EH, et al. The distribution of H_2O between silicate melt and nominally anhydrous peridotite and the onset of hydrous melting in the deep upper mantle[J]. Earth and Planetary Science Letters, 2014, 400: 1-13.

Nunes PD, Tilton GR. Uranium-lead ages of minerals from the Stillwater Igneous Complex and associated rocks, Montana[J]. Geological Society of America Bulletin, 1971, 82: 2231-2250.

Nunes PD. The age of the Stillwater Complex; a comparison of U-Pb zircon and Sm-Nd isochron systematics[J]. Geochimica et Cosmochimica Acta, 1981, 45: 1961-1963.

O'Driscoll B, Day JMD, Daly JS, et al. Rhenium-osmium isotopes and platinum-group elements in the Rum Layered Suite, Scotland: Implications for Cr-spinel seam formation and the composition of the Iceland mantle anomaly[J]. Earth and Planetary Science Letters, 2009, 286: 41-51.

O'Driscoll B, Donaldson CH, Daly JS, et al. The roles of melt infiltration and cumulate assimilation in the formation of anorthosite and a Cr-spinel seam in the Rum Eastern Layered Intrusion, NW Scotland[J]. Lithos, 2009, 111: 6-20.

O'Hanley DS, Chernosky JV, Wicks FJ. The stability of lizardite and chrysotile[J]. Canadian Mineralogist, 1989, 27: 483-493.

O'Neill HSC, Jenner FE. Causes of the compositional variability among ocean floor basalts[J]. Journal of Petrology. 2016, 57: 2163-2194.

O'Neill HSC, Pownceby MI. Thermodynamic data from redox reactions at high temperatures. I. An experimental and theoretical assessment of the electrochemical method using stabilized zirconia electrolytes, with revised values for the Fe-"FeO", Co-CoO, Ni-NiO and Cu-Cu2O oxygen buffers, and new data for the W-WO_2 buffer[J]. Contributions to Mineralogy and Petrology, 1993, 114: 296-314.

Oeser M, Dohmen R, Horn I, et al. Processes and time scales of magmatic evolution as revealed by Fe–Mg chemical and isotopic zoning in natural olivines[J]. Geochimica et Cosmochimica Acta, 2015, 154: 130-150.

Ohnenstetter C, Wakinson DH, Jones PC, et al. Cryptic compositional variation in laurite and enclosing chromite from the Bird River Sill, Manitoba[J]. Economic Geology, 1986, 81: 1159-1168.

Ohtani E, Kawabe I, Moriyama J, et al. Partitioning of elements between majorite garnet and melt and implications for petrogenesis of komatiite[J]. Contributions to Mineralogy and Petrology, 1989, 103: 263-269.

Ono A. Fe-Mg partitioning between spinel and olivine[J]. The Journal of the Japanese Association of Mineralogists, Petrologists and Economic Geologists, 1983, 78: 115-122.

O'Reilly SY, Chen D, Griffin WL, et al. Minor elements in olivine from spinel lherzolite xenoliths: Implications for thermobarometry[J]. Mineralogical Magazine, 1997, 61(405):257-269.

Ozawa K. Evaluation of olivine-spinel geothermometry as an indicator of thermal history for peridotites[J]. Contributions to Mineralogy and Petrology, 1983, 82: 52-65.

Ozawa K. Olivine-spinel geospeedometry: Analysis of diffusion-controlled Mg-Fe2+ exchange[J]. Geochimica et Cosmochimica Acta, 1984, 48: 2597-2611.

Page NJ, Moring BC. Petrology of the noritic and gabbronoritic rocks below the J-M reef in the Mountain View area, Stillwater Complex, Montana[R]. United States Geological Survey Bulletin, 1987, 1674-C: 1-47.

Page NJ, Nokleberg WJ. Geologic map of the Stillwater Complex, Montana[R]. United States Geological Survey Miscellaneous Investigations Series I-797, 1974.

Page NJ. Stillwater Complex, Montana: Rock succession, metamorphism and structure of the Complex and adjacent rocks[R]. United States Geological Survey Professional Paper, 1977.

Page NJ. 1979. Stillwater Complex, Montana: Structure, mineralogy, and petrology of the Basal Zone with emphasis on the occurrence of sulfides[R]. United States Geological Survey Professional Papers, 1979.

Pagé P, Barnes SJ. Using trace elements in chromites to constrain the origin of podiform chromitites in the Thetford Mines ophiolite, Québec, Canada[J]. Economic Geology. 2009, 104, 997-1018.

Papike JJ, Karner JM, Shearer CK. Comparative planetary mineralogy: Valence state partitioning of Cr, Fe, Ti, and V among crystallographic sites in olivine, pyroxene, and spinel from planetary basalts[J]. American Mineralogist. 2005, 90: 277-290.

Papike JJ, Spilde MN, Fowler GW, et al. SIMS studies of planetary cumulates: Orthopyroxene from the Stillwater Complex, Montana[J]. American Mineralogist, 1995, 80(11-12): 1208-1221.

Park JW, Kamenetsky V, Campbell I, et al. Empirical constraints on partitioning of platinum group elements between Cr-spinel and primitive terrestrial magmas[J]. Geochimica et Cosmochimica Acta, 2017, 216: 393-416.

Parsons I. Origins of igneous layering[M]. Holland: Reidel Publishing Company, 1987.

Paster TP, Schauwecker DS, Haskin LA. The behavior of some trace elements during solidification of the Skaergaard layered series[J]. Geochimica et Cosmochimica Acta, 1974, 38(10): 1549-1577.

Pearce JA, Harris NB, Tindle AG. Trace element discrimination diagrams for the tectonic interpretation of granitic rocks[J]. Journal of Petrology, 1984, 25(4): 956-983.

Peltonen P. Crystallization and re-equilibration of zoned chromite in ultramafic cumulates, Vammala Ni-Belt, Southwestern Finland[J]. The Canadian Mineralogist. 1995, 33(3), 521-535.

Peng P, Zhai MG, Zhang HF, et al. Geochronological constraints on the Paleoproterozoic evolution of the North China craton: SHRIMP zircon ages of different types of mafic dikes. International Geology Review, 2005, 47: 492-508.

Peslier AH, Hnatyshin D, Herd CDK, et al. Crystallization, melt inclusion, and redox history of a Martian meteorite: Olivine-phyric shergottite Larkman Nunatak 06319[J]. Geochimica et Cosmochimica Acta, 2010, 74: 4543-4576.

Peslier AH, Woodland AB, Wolff JA. Fast kimberlite ascent rates estimated from hydrogen diffusion profiles in xenolithic mantle olivines from southern Africa[J]. Geochimica et Cosmochimica Acta, 2008, 72: 2711-2722.

Pettigrew NT, Hattori KH. The Quetico intrusions of Western Superior Province: Neo-archean examples of Alaskan/Ural-type mafic-ultramafic intrusions[J]. Precambrian Research, 2006, 149(1-2): 21-42.

Plank T, Kelley KA, Zimmer MM, et al. Why do mafic arc magmas contain 4 wt.% water on

average?[J]. Earth and Planetary Science Letters, 2013, 364: 168-179.

Pleše P, Higgins MD, Baker DR, et al. Production and detachment of oxide crystal shells on bubble walls during experimental vesiculation of andesitic magmas[J]. Contributions to Mineralogy and Petrology, 2019, 174: 1-21.

Pogge von Strandmann PAE, Elliot T, Marschall HR, et al. Variations of Li and Mg isotope ratios in bulk chondrite and mantle xenoliths[J]. Geochimica et Cosmochimica Acta, 2011, 75: 5247-5268.

Pogge von Strandmann PAE, Stüeken Eva E, et al. Selenium isotope evidence for progressive oxidation of the Neoproterozoic biosphere[J]. Nature Communications, 2015, 6: 10157.

Poitrasson F, Delpech G, Grégoire M. On the iron isotope heterogeneity of lithospheric mantle xenoliths: Implications for mantle metasomatism, the origin of basalts and the iron isotope composition of the Earth[J]. Contributions to Mineralogy and Petrology, 2013, 165: 1243-1258.

Polat A, Kusky TM, Li JH, et al. Geochemistry of Neoarchean (ca. 2.55–2.50 Ga) volcanic and ophiolitic rocks in the Wutaishan greenstone belt, central orogenic belt, North China Craton: Implications for geodynamic setting and continental growth[J]. Geological Society of America Bulletin, 2005, 117: 1387-1399.

Polyakov VB, Clayton RN, Horita J, et al. Equilibrium iron isotope fractionation factors of minerals: reevaluation from the data of nuclear inelastic resonant X-ray scattering and Mössbauer spectroscopy[J]. Geochimica et Cosmochimica Acta, 2007, 71: 3833-3846.

Polyakov VB, Mineev SD. The use of Mössbauer spectroscopy in stable isotope geochemistry[J]. Geochimica et Cosmochimica Acta, 2000, 64: 849-865.

Popov V, Belyatsky B. Sm-Nd age of dunite-clinopyroxenite-tylaite association of the Kytlym massif, the platinum belt of the Urals[J]. Doklady Earth Sciences, 2006, 409(1): 795-800.

Posner ES, Ganguly J, Hervig R. Diffusion kinetics of Cr in spinel: Experimental studies and implications for 53Mn-53Cr cosmochronology[J]. Geochimica et Cosmochimica Acta, 2016, 175: 20-35.

Power MR, Pirrie D, Andersen JCØ, et al. Testing the validity of chrome spinel chemistry as a provenance and petrogenetic indicator[J]. Geology, 2000, 28(11): 1027-1030.

Prelević D, Foley SF. Accretion of arc-oceanic lithospheric mantle in the Mediterranean: Evidence

from extremely high-Mg olivines and Cr-rich spinel inclusions in lamproites[J]. Earth and Planetary Science Letters, 2007, 256: 120-135.

Prelević D, Jacob DE, Foley SF. Recycling plus: A new recipe for the formation of Alpine-Himalayan orogenic mantle lithosphere[J]. Earth and Planetary Science Letters, 2013, 362: 187-197.

Premo WR, Helz RT, Zientek ML, et al. U-Pb and Sm-Nd ages for the Stillwater Complex and its associated dikes and sills, Beartooth Mountains, Montana: Identification of a parent magma[J]. Geology, 1990, 18: 1065-1068.

Prichard HM, Barnes SJ, Godel B, et al. The structure of and origin of nodular chromite from the Troodos ophiolite, Cyprus, revealed using high-resolution X-ray computed tomography and electron backscatter diffraction[J]. Lithos, 2015, 218: 87-98.

Qin L, Alexander CMD, Carlson RW, et al. Contributors to chromium isotope variation of meteorites[J]. Geochimica et Cosmochimica Acta, 2010, 74: 1122-1145.

Qin L, Wang X. Chromium isotope geochemistry. Reviews in Mineralogy and Geochemistry[J]. 2017, 82: 379-414.

Raedeke LD. Petrogenesis of the Stillwater Complex[D]. Seattle: University of Washington, 1982.

Raedeke LD, McCallum IS. Investigations in the Stillwater complex: Part II. Petrology and petrogenesis of the ultramafic series[J]. Journal of Petrology, 1984, 25: 395-420.

Richter FM, Davis AM, Depaolo DJ, et al. Isotope fractionation by chemical diffusion between molten basalt and rhyolite[J]. Geochimica et Cosmochimica Acta, 2003, 67: 3905-3923.

Richter FM, Liang Y, Davis AM. Isotope fractionation by diffusion in molten oxides[J]. Geochimica et Cosmochimica Acta, 1999, 63: 2853-2861.

Richter FM, Watson EB, Mendybaev RA, et al. Isotopic fractionation of the major elements of molten basalt by chemical and thermal diffusion[J]. Geochimica et Cosmochimica Acta, 2009, 73: 4250-4263.

Richter FM, Watson EB, Mendybaev RA, et al. Magnesium isotope fractionation in silicate melts by chemical and thermal diffusion[J]. Geochimica et Cosmochimica Acta, 2008, 72: 206-220.

Roeder P, Gofton E, Thornber C. Cotectic proportions of olivine and spinel in olivine-tholeiitic basalt and evaluation of pre-eruptive processes[J]. Journal of Petrology, 2005, 47: 883-900.

Roeder PL, Campbell IH, Jamieson HE. A re-evaluation of the olivine-spinel geothermometer[J]. Contributions to Mineralogy and Petrology, 1979, 68: 325-334.

Roeder PL, Emslie RF. Olivine-liquid equilibrium[J]. Contributions to Mineralogy and Petrology, 1970, 29: 275-289.

Roeder PL, Poustovetov A, Oskarsson N. Growth forms and composition of chromian spinel in MORB magma: Diffusion-controlled crystallization of chromian spinel[J]. The Canadian Mineralogist, 2001, 39(2): 397-416.

Roeder PL, Reynolds I. Crystallization of chromite and chromium stability in basaltic melts[J]. Journal of Petrology, 1991, 32: 909-934.

Rollinson H, Mameri L, Barry T. Polymineralic inclusions in mantle chromitites from the Oman ophiolite indicate a highly magnesian parental melt[J]. Lithos, 2018, 310: 381-391.

Rubin CM, Saleeby JB. Tectonic history of the eastern edge of the Alexander terrane, southeast Alaska[J]. Canadian Journal of Earth Sciences, 1992, 11(3): 586-602.

Ruckmick JC, Noble JA. Origin of the ultramafic complex at Union Bay, southeastern Alaska[J]. Geological Society of America Bulletin, 1959, 70(8): 981-1018.

Sack RO, Ghiorso MS. Chromite as a petrogenetic indicator[J]. Reviews in Mineralogy and Geochemistry, 1991, 25: 323-353.

Saleeby JB. Age and tectonic setting of the Duke Island ultramafic intrusion, southeast Alaska[J]. Canadian Journal of Earth Sciences, 1992, 29(3): 506-522.

Salpas PA, Haskin LA, McCallum IS. 1983. Stillwater anorthosites: A lunar analog?[C] Proceedings of the 14th Lunar and Planetary Science Conference, 88: B27-B39.

Sato K, Miyamoto T, Kawasaki T. Fe^{2+}-Mg partitioning experiments between orthopyroxene and spinel using ultrahigh-temperature granulite from the Napier Complex, East Antarctica[J]. Geological Society Special Publication, 2008, 308: 431-447.

Sattari P, Brenan JM, Horn I, et al. Experimental constraints on the sulfide- and chromite-silicate melt partitioning behavior of rhenium and platinum-group elements[J]. Economic Geology, 2002, 97: 385-398.

Schauble EA. First-principles estimates of equilibrium magnesium isotope fractionation in silicate, oxide, carbonate and hexaaquamagnesium (2+) crystals[J]. Geochimica et Cosmochimica Acta,

2011, 75: 844-869.

Scheel JE, Scoates JS, Nixon GT. Chromian spinel in the Turnagain Alaskan-type ultramafic intrusion, northern British Columbia, Canada[J]. The Canadian Mineralogist, 2009, 47(1): 63-80.

Schiller M, Van Kooten E, Holst JC, et al. Precise measurement of chromium isotopes by MC-ICPMS[J]. Journal of Analytical Atomic Spectrometry, 2014, 29(8): 1406-1416.

Schoenberg R, Merdian A, Holmden C, et al. The stable Cr isotopic compositions of chondrites and silicate planetary reservoirs[J]. Geochimica et Cosmochimica Acta, 2016, 183: 14-30.

Schoenberg R, Zink S, Staubwasser M, et al. The stable Cr isotope inventory of solid Earth reservoirs determined by double spike MC-ICP-MS[J]. Chemical Geology, 2008, 249(3-4): 294-306.

Scoon RN, Costin G. Chemistry, morphology and origin of magmatic-reaction chromite stringers associated with anorthosite in the Upper Critical Zone at Winnaarshoek, Eastern Limb of the Bushveld Complex[J]. Journal of Petrology, 2018, 59: 1551-1578.

Scott SR, Sims KW, Frost BR, et al. On the hydration of olivine in ultramafic rocks: implications from Fe isotopes in serpentinites[J]. Geochimica et Cosmochimica Acta, 2017, 215: 105-121.

Scowen PAH, Roeder PL, Helz RT. Reequilibration of chromite within Kilauea Iki lava lake, Hawaii[J]. Contributions to Mineralogy and Petrology, 1991, 107: 8-20.

Sekerka RF. Role of instabilities in determination of the shapes of growing crystals[J]. Journal of Crystal Growth, 1993, 128(1-4): 1-12.

Selkin PA, Gee JS, Meurer WP, et al. Paleointensity record from the 2.7 Ga Stillwater complex, Montana[J]. Geochemistry Geophysics Geosystems, 2008, 9(12): 1-23.

Sharkov EV, Bogatikov OA, Grokhovskaya TL, et al. Petrology and Ni-Cu-Cr-PGE mineralization of the largest mafic pluton in Europe: The Early Proterozoic Burakovsky layered intrusion, Karelia, Russia[J]. International Geology Review, 1995, 37(6): 509-525.

Shen J, Liu J, Qin L, et al. Chromium isotope signature during continental crust subduction recorded in metamorphic rocks[J]. Geochemistry Geophysics Geosystems, 2015, 16: 3840-3854.

Shen J, Qin L, Fang Z, et al. High-temperature inter-mineral Cr isotope fractionation: A comparison of ionic model predictions and experimental investigations of mantle xenoliths from the North

China Craton[J]. Earth and Planetary Science Letters, 2018, 499: 278-290.

Sidorov EG, Kutyrev AV, Zhitova ES, et al. Origin of platinum-group mineral assemblages from placers in Rivers Draining from the Ural-Alaskan type Itchayvayamsky ultramafics, Far East Russia[J]. The Canadian Mineralogist, 2019, 57(1): 91-104.

Sigurdsson H, Schilling JG. Spinels in Mid-Atlantic Ridge basalts: chemistry and occurrence[J]. Earth and Planetary Science Letters, 1976, 29: 7-20.

Sigurdsson H. Spinels in Leg 37 basalts and peridotites: Phase chemistry and zoning[J]//Aumento F, Melson WG, Hall JM. Initial Reports of the Deep Sea Drilling Project, Texas, 1977, 37: 883-891.

Sinton JM. Equilibration history of the basal alpine-type peridotite, Red Mountain, New Zealand[J]. Journal of Petrology, 1977, 18(2), 216-246.

Sio CK, Dauphas N, Teng FZ, et al. Discerning crystal growth from diffusion profiles in zoned olivine by in situ Mg-Fe isotopic analyses[J]. Geochimica et Cosmochimica Acta, 2013, 123: 302-321.

Sio CK, Roskosz M, Dauphas N, et al. The isotope effect for Mg-Fe interdiffusion in olivine and its dependence on crystal orientation, composition and temperature[J]. Geochimica et Cosmochimica Acta, 2018, 239: 463-480.

Sisson TW, Grove TL. Experimental investigations of the role of H_2O in calc-alkaline differentiation and subduction zone magmatism[J]. Contributions to Mineralogy and Petrology, 1993, 113: 143-166.

Smith D, Ehrenberg SN. Zoned minerals in garnet peridotite nodules from the Colorado Plateau: Implications for mantle metasomatism and kinetics[J]. Contributions to Mineralogy and Petrology, 1984, 86: 274-285.

Snoke AW, Quick JE, Bowman HR. Bear mountain igneous complex, Klamath mountains, California: An ultrabasic to silicic cale-alkaline suite[J]. Journal of Petrology, 1981, 22(4): 501-552.

Sobolev AV, Chaussidon M. H_2O concentrations in primary melts from supra-subduction zones and mid-ocean ridges: Implications for H_2O storage and recycling in the mantle[J]. Earth and Planetary Science Letters, 1996, 137: 45-55.

Sobolev AV, Hofmann AW, Kuzmin DV, et al. The amount of recycled crust in sources of mantle derived melts[J]. Science, 2007, 316: 412-417.

Sobolev AV, Hofmann AW, Sobolev SV, et al. An olivine-free mantle source of Hawaiian shield basalts[J]. Nature, 2005, 434: 590-597.

Sossi PA, Foden JD, Halverson GP. Redox-controlled iron isotope fractionation during magmatic differentiation: An example from the Red Hill intrusion, S. Tasmania[J]. Contributions to Mineralogy and Petrology, 2012, 164: 757-772.

Spandler CJ, Mavrogenes JA, Arculus R. Origin of chromitites in layered intrusions: Evidence from chromite-hosted melt inclusions from the Stillwater Complex[J]. Geology, 2005, 33(11): 893-896.

Sparks RSJ, Barclay J, Jaupart CPMA, et al. Physical aspects of magma degassing; 1, Experimental and theoretical constraints on vesiculation[J]. Reviews in Mineralogy and Geochemistry, 1994, 30: 413-445.

Spear FS. Metamorphic phase equilibria and pressure-temperature-time paths[J]. Mineralogical Society of America, 1995, 1: 172-174.

Stowe CW. Compositions and tectonic settings of chromite deposits through time[J]. Economic Geology, 1994, 89: 528-546.

Su BX, Hu Y, Teng FZ, et al. Chromite-induced magnesium isotope fractionation during mafic magma differentiation[J]. Science Bulletin, 2017, 62(22): 1538-1546.

Su BX, Qin KZ, Sakyi PA, et al. Occurrence of an Alaskan-type complex in the middle Tianshan massif, Central Asian Orogenic Belt: Inferences from petrological and mineralogical studies[J]. International Geology Review, 2012, 54(3): 249-269.

Su BX, Qin KZ, Zhou MF, et al. Petrological, geochemical and geochronological constraints on the origin of the Xiadong Ural-Alaskan type complex in NW China and tectonic implication for the evolution of southern Central Asian Orogenic Belt[J]. Lithos, 2014, 200-201: 226-240.

Su BX, Robinson PT, Chen C, et al. The occurrence, origin, and fate of water in chromitites in ophiolites[J]. American Mineralogist, 2020, 105: 894-903.

Su BX, Zhang HF, Sakyi PA, et al. The origin of spongy texture in minerals of mantle xenoliths from the Western Qinling, central China[J]. Contributions to Mineralogy and Petrology, 2011,

161: 465-482.

Sutton SR, Jones KW, Gordon B, et al. Reduced chromium in olivine grains from lunar basalt 15555: X-ray absorption near edge structure (XANES)[J]. Geochimica et Cosmochimica Acta, 1993, 57: 461-468.

Suzuki AM, Yasuda A, Ozawa K. Cr and Al diffusion in chromite spinel: experimental determination and its implication for diffusion creep[J]. Physics and Chemistry of Minerals, 2008, 35(8): 433-445.

Talkington RW, Lipin BR. Platinum-group minerals in chromite seams of the Stillwater Complex, Montana[J]. Economic Geology, 1986, 8: 1179-1186.

Tamura A, Arai S. Unmixed spinel in chromitite from the Iwanai-Dake peridotite complex, Hokkaido, Japan: A reaction between peridotite and highly oxidized magma in the mantle wedge[J]. American Mineralogist, 2005, 90: 473-480.

Taylor HP. The zoned ultramafic complexes of southeastern Alaska[J]//Wyllie PJ. Ultramafic related rocks. New York: John Wiley and Sons Incorporated, 1967.

Teng FZ, Dauphas N, Helz RT, et al. Diffusion-driven magnesium and iron isotope fractionation in Hawaiian olivine[J]. Earth and Planetary Science Letters, 2011, 308: 317-324.

Teng FZ, Dauphas N, Helz RT. Iron isotope fractionation during magmatic differentiation in Kilauea Iki lava lake[J]. Science, 2008, 320: 1620-1622.

Teng FZ, Li WY, Ke S, et al. Magnesium isotopic composition of the Earth and chondrites[J]. Geochimica et Cosmochimica Acta, 2010, 74: 4150-4166.

Teng FZ, Li WY, Ke S, et al. Magnesium isotopic compositions of international geological reference materials[J]. Geostandards and Geoanalytical Research, 2015, 39: 329-339.

Teng FZ, Wadhwa M, Helz RT. Investigation of magnesium isotope fractionation during basalt differentiation: Implications for a chondritic composition of the terrestrial mantle[J]. Earth and Planetary Science Letters, 2007, 261: 84-92.

Teng, FZ, Hu Y, Chauvel C. Magnesium isotope geochemistry in arc volcanism[J]. Proceedings of the National Academy of Sciences, 2016, 113: 7082-7087.

Tepley FJ, Davidson JP. Mineral-scale Sr-isotope constraints on magma evolution and chamber dynamics in the Rum layered intrusion, Scotland[J]. Contributions to Mineralogy and Petrology,

2003, 145(5): 628-641.

Tepper JH, Kuehner SM. Complex zoning in apatite from the Idaho batholith: A record of magma mixing and intracrystalline trace element diffusion[J]. American Mineralogist, 1999, 84(4): 581-595.

Tessalina SG, Malitch KN, Augé T, et al. Origin of the Nizhny Tagil clinopyroxenite-dunite massif, Uralian platinum belt, Russia: Insights from PGE and Os isotope systematics[J]. Journal of Petrology, 2016, 56(12): 2297-2318.

Thakurta J, Ripley EM, Li C. Geochemical constraints on the origin of sulfide mineralization in the Duke Island Complex, southeastern Alaska[J]. Geochemistry Geophysics Geosystems, 2008, 9(7): 3562-3585.

Thakurta J, Ripley EM, Li C. Platinum group element geochemistry of sulfide-rich horizons in the Ural-Alaskan-Type ultramafic complex of Duke island, southeastern Alaska[J]. Economic Geology, 2014, 109: 643-659.

Theyer P. Petrography, chemistry and distribution of platinum and palladium in ultramafic rocks of the Bird River Sill, SE Manitoba, Canada[J]. Mineralium Deposita, 1991, 26: 165-174.

Thompson RN, Gibson SA. Transient high temperatures in mantle plume heads inferred from magnesian olivines in Phanerozoic picrites[J]. Nature, 2000, 407: 502-505.

Thy P. Spinel minerals in transitional and alkali basaltic glasses from Iceland[J]. Contributions to Mineralogy and Petrology, 1983, 83: 141-149.

Tian HC, Zhang C, Teng FZ, et al. Diffusion-driven extreme Mg and Fe isotope fractionation in Panzhihua ilmenite: Implications for the origin of mafic intrusion[J]. Geochimica et Cosmochimica Acta, 2020, 278: 361-375.

Tistl M. Geochemistry of platinum-group elements of the zoned ultramafic Alto Condoto Complex, northwest Colombia[J]. Economic Geology, 1994, 89(1): 158-167.

Todd SG, Keith DW, LeRoy LW, et al. The J-M Pt-Pd reef of the Stillwater Complex, Montana: I. Stratigraphy and petrology[J]. Economic Geology, 1982, 77: 1454-1480.

Tolstykh ND, SidorovE, Laajoki K, et al. The association of platinum-group minerals in placers of the Pustaya River, Kamchatka, Russia[J]. The Canadian Mineralogist, 2000, 38(5): 1251-1264.

Tomkins AG, Rebryna KC, Weinberg RF, et al. Magmatic sulfide formation by reduction of oxidized

arc basalt[J]. Journal of Petrology, 2012, 53: 1537-1567.

Turnbull RE, Size WB, Tulloch AJ, et al. The ultramafic-intermediate Riwaka complex, New Zealand: Summary of the petrology, geochemistry and related Ni-Cu-PGE mineralisation[J]. New Zealand Journal of Geology and Geophysics, 2017, 60(3): 270-295.

Turner AR, Wolfgram D, Barnes SJ. Geology of the Stillwater County sector of the J-M reef, including the Minneapolis adit[J]//Czamanske GK, Zientek ML. Stillwater Complex. Montana Bureau of Mines and Geology, Special Publication, 1985, 92: 210-230.

Ulmer GC. Experimental investigations of chromite spinels[J]. Magmatic Ore Deposits, 1969, 4: 114-131.

Ulmer P. Partial melting in the mantle wedge-the role of H_2O in the genesis of mantle-derived 'arc-related' magmas[J]. Physics of the Earth and Planetary Interiors, 2001, 127: 215-232.

Van Orman JA, Crispin KL. Diffusion in Oxides[J]. Reviews in Mineralogy and Geochemistry, 2010, 72(1): 757-825.

Vogt K, Dohmen R, Chakraborty S. Fe-Mg diffusion in spinel: New experimental data and a point defect model. American Mineralogist, 2015, 100: 2112-2122.

Wager LR, Brown GM. Layered Igneous Rocks[M]. Edinburgh and London: Oliver and Boyd, 1968.

Wall CJ, Scoates JS, Weis D, et al. The Stillwater Complex: Integrating Zircon Geochronological and Geochemical Constraints on the Age, Emplacement History and Crystallization of a Large, Open-System Layered Intrusion[J]. Journal of Petrology, 2018, 59: 153-190.

Wang ZH, Wilde SA, Wan JL. Tectonic setting and significance of the 2.1-2.3Ga events in the Trans-North China Orogen: New constraints from the Yanmenguan mafic-ultramafic intrusion in the Hengshan-Wutai-Fuping area[J]. Precambrian Research, 2010, 178(1): 27-42.

Watson EB, Baker DR. Chemical diffusion in magmas: An overview of experimental results and geochemical applications[J]//Perchuk LL, Kushiro I. Physical Chemistry of Magmas. Berlin: Springer, 1991: 120-151.

Watson EB, Liang Y. A simple model for sector zoning in slowly grown crystals: implications for growth rate and lattice diffusion, with emphasis on accessory minerals in crustal rocks[J]. American Mineralogist, 1995, 80: 1179-1187.

Watson EB, Muller T. Non-equilibrium isotopic and elemental fractionation during diffusion-

controlled crystal growth under static and dynamic conditions[J]. Chemical Geology, 2009, 267: 111-124.

Weidendorfer D, Mattsson HB, Ulmer P. Dynamics of magma mixing in partially crystallized magma chambers: textural and petrological constraints from the basal complex of the Austurhorn intrusion (SE Iceland)[J]. Journal of Petrology, 2014, 55(9): 1865-1903.

Weis FA, Lazor P, Skogby H. Hydrogen analysis in nominally anhydrous minerals by transmission Raman spectroscopy[J]. Physics and Chemistry of Minerals, 2018, 45: 597-607.

Wendt AS, Altenberger U, D'Arco P. Radiating cracks around chromite inclusions in olivine: Constraints on P-T histories based on the thermoelastic properties of minerals[J]. Swiss Journal of Geosciences Supplement, 1998, 78(3):365-374.

Weyer S, Anbar AD, Brey GP, et al. Iron isotope fractionation during planetary differentiation[J]. Earth and Planetary Science Letters, 2005, 240: 251-265.

Weyer S, Ionov D. Partial melting and melt percolation in the mantle: The message from Fe isotopes[J]. Earth and Planetary Science Letters, 2007, 259: 119-133.

Wijbrans CH, Klemme S, Berndt J, et al. Experimental determination of trace element partition coefficients between spinel and silicate melt: The influence of chemical composition and oxygen fugacity[J]. Contributions to Mineralogy and Petrology, 2015, 169: 1-33.

Williams HM, Peslier AH, McCammon CA, et al. Systematic iron isotope variations in mantle rocks and minerals: The effects of partial melting and oxygen fugacity[J]. Earth and Planetary Science Letters, 2005, 235: 435-452.

Wilson AH. The Great Dyke of Zimbabwe[J]. Developments in Petrology, 1996, 15: 365-402.

Wilson AH. The geology of the Great "Dyke", Zimbabwe: The ultramafic rocks[J]. Journal of Petrology, 1982, 23: 240-292.

Witham F, Blundy J, Kohn SC, et al. SolEx: A model for mixed COHSCl-volatile solubilities and exsolved gas compositions in basalt[J]. Computers and Geoences, 2012, 45: 87-97.

Wooden JL, Czamanske GK, Zientek ML. A lead isotopic study of the Stillwater Complex, Montana: constraints on crustal contamination and source regions[J]. Contributions to Mineralogy and Petrology, 1991, 107(1): 80-93.

Wooden JL, Mueller PA. Pb, Sr, and Nd isotopic compositions of a suite of late Archean igneous

rocks, eastern Beartooth Mountains: implications for crust-mantle evolution[J]. Earth and Planetary Science Letters, 1988, 87: 59-72.

Wu S, Karius V, Schmidt BC, et al. Comparison of Ultrafine Powder Pellet and Flux-free Fusion Glass for Bulk Analysis of Granitoids by Laser Ablation-Inductively Coupled Plasma-Mass Spectrometry[J]. Geostandards and Geoanalytical Research, 2018, 42: 575-591.

Wyllie PJ. Ultramafic and related rocks[J]. Journal of Geology, 1967, 76: 724-725.

Xia J, Qin L, Shen J, et al. Chromium isotope heterogeneity in the mantle[J]. Earth and Planetary Science Letters, 2017, 464: 103-115.

Xiao Y, Teng FZ, Su BX, et al. Iron and magnesium isotopic constraints on the origin of chemical heterogeneity in podiform chromitite from the Luobusa ophiolite, Tibet[J]. Geochemistry Geophysics Geosystems, 2016, 17: 940-953.

Xiao Y, Teng FZ, Zhang HF, et al. Large magnesium isotope fractionation in peridotite xenoliths from eastern North China craton: product of melt-rock interaction[J]. Geochimica et Cosmochimica Acta, 2013, 115: 241-261.

Xiong F, Yang J, Dilek Y, et al. Nanoscale diopside and spinel exsolution in olivine from dunite of the Tethyan ophiolites, southwestern Turkey: Implications for the multi-stage process[J]. Journal of Nanoscience and Nanotechnology, 2017, 17(7): 6587-6596.

Xiong FH, Yang JS, Robinson PT, et al. Origin of podiform chromitite, a new model based on the Luobusa ophiolite, Tibet[J]. Gondwana Research, 2015, 27: 525-542.

Xu YG, Luo ZY, Huang XL, et al. Zircon U–Pb and Hf isotope constraints on crustal melting associated with the Emeishan mantle plume[J]. Geochimica Et Cosmochimica Acta, 2008, 72(13): 3084-3104.

Yang K, Seccombe PK. Chemical variation of chromite in the ultramafic cumulates of the Great Serpentinite Belt, Upper Bingara to Doonba, New South Wales, Australia[J]. Canadian Mineralogist, 1993, 31: 75-87.

Yokoyama K. Nikubuchi peridotite body in the Sanbagawa metamorphic belt; thermal history of the “Al-pyroxene-rich suite” peridotite body in high pressure metamorphic terrain[J]. Contributions to Mineralogy and Petrology, 1980, 73: 1-13.

Young ED, Manning CE, Schauble EA, et al. High-temperature equilibrium isotope fractionation of

non-traditional stable isotopes: Experiments, theory, and applications[J]. Chemical Geology, 2015, 395: 176-195.

Young ED, Tonui E, Manning CE, et al. Spinel-olivine magnesium isotope thermometry in the mantle and implications for the Mg isotopic composition of Earth[J]. Earth and Planetary Science Letters, 2009, 288: 524-533.

Yu JH, Wang DZ, Wang XY. Ages of the Luliang Group and its main metamorphism in the Luliang Mountains, Shank evidence from single-grain zircon U-Pb ages[J]. Geological Review, 1997, 43, 403-408.

Zaccarini F, Garuti G, Pushkarev EV. Unusually PGE-rich chromitite in the Butyrin vein of the Kytlym Uralian-Alaskan complex, northern Urals, Russia[J]. The Canadian Mineralogist, 2011, 49(6): 1413-1431.

Zellmer GF, Sakamoto N, Matsuda N, et al. On progress and rate of the peritectic reaction Fo + SiO2 = En in natural andesitic arc magmas[J]. Geochimica et Cosmochimica Acta, 2016, 185: 383-393.

Zhai MG, Guo JH, Yan YH. Discovery and preliminary study of the Archean high-pressure granulites in the North China. Science China, 1992, 12B: 1325-1330.

Zhang J, Wang F, Wang Z, et al. 2014. Water Content and Deformation Microstructure of Layered Panzhihua Gabbro: Implications for the Origin of Rhythmic Layering[C]. American Geophysical Union Fall Meeting, 2014, T31A-4572.

Zhang JS, Dirks HGM, Passchier CW. Extensional collapse and uplift in a polymetamorphic granulite terrain in the Archaean and Palaeoproterozoic of north China[J]. Precambrian Research, 1994, 67(1-2): 37-57.

Zhao GC, Wilde SA, Cawood PA, et al. Archean blocks and their boundaries in the North China Craton: Lithological, geochemical, structural and P-T path constraints and tectonic evolution[J]. Precambrian Research, 2001, 107: 45-73.

Zhao GC, Wilde SA, Cawood PA, et al. SHRIMP U-Pb zircon ages of the Fuping Complex: Implications for Late Archean to Paleoproterozoic accretion and assembly of the North China Craton[J]. American Journal of Science, 2002, 302(3):191-226.

Zhao GC, Sun M, Wilde SA, et al. A Paleo-Mesoproterozoic supercontinent: Assembly, growth and

breakup[J]. Earth ence Reviews, 2004, 67(1-2): 91-123.

Zhao GC, Liu SW, Sun M, et al. What happened in the Trans-North China Orogen in the period 2560-1850 Ma? Acta Geologica Sinica, 2006, 80(6): 790-806.

Zhao XM, Cao HH, Mi X, et al. Combined iron and magnesium isotope geochemistry of pyroxenite xenoliths from Hannuoba, North China Craton: implications for mantle metasomatism[J]. Contributions to Mineralogy and Petrology, 2017, 172: 40.

Zhao XM, Zhang HF, Zhu XK, et al. Iron isotope variations in spinel peridotite xenoliths from North China Craton: implications for mantle metasomatism[J]. Contributions to Mineralogy and Petrology, 2010, 160: 1-14.

Zhao XM, Zhang HF, Zhu XK, et al. Effects of melt percolation on iron isotopic variation in peridotites from Yangyuan, North China Craton[J]. Chemical Geology, 2015, 401: 96-110.

Zhou MF, Robinson PT, Malpas J, et al. Podiform chromitites in the Luobusa Ophiolite (southern Tibet): Implications for melt -rock interaction and chromite segregation in the upper mantle[J]. Journal of Petrology, 1996, 37(1): 3-21.

Zientek ML. Retrogenesis of the Basal Zone of the Stillwater Complex, Montana[D]. California: Stanford University, 1984.

9. Appendix for the Chapter 3

Part I: Supplementary figures and tables for the optical images and compositions

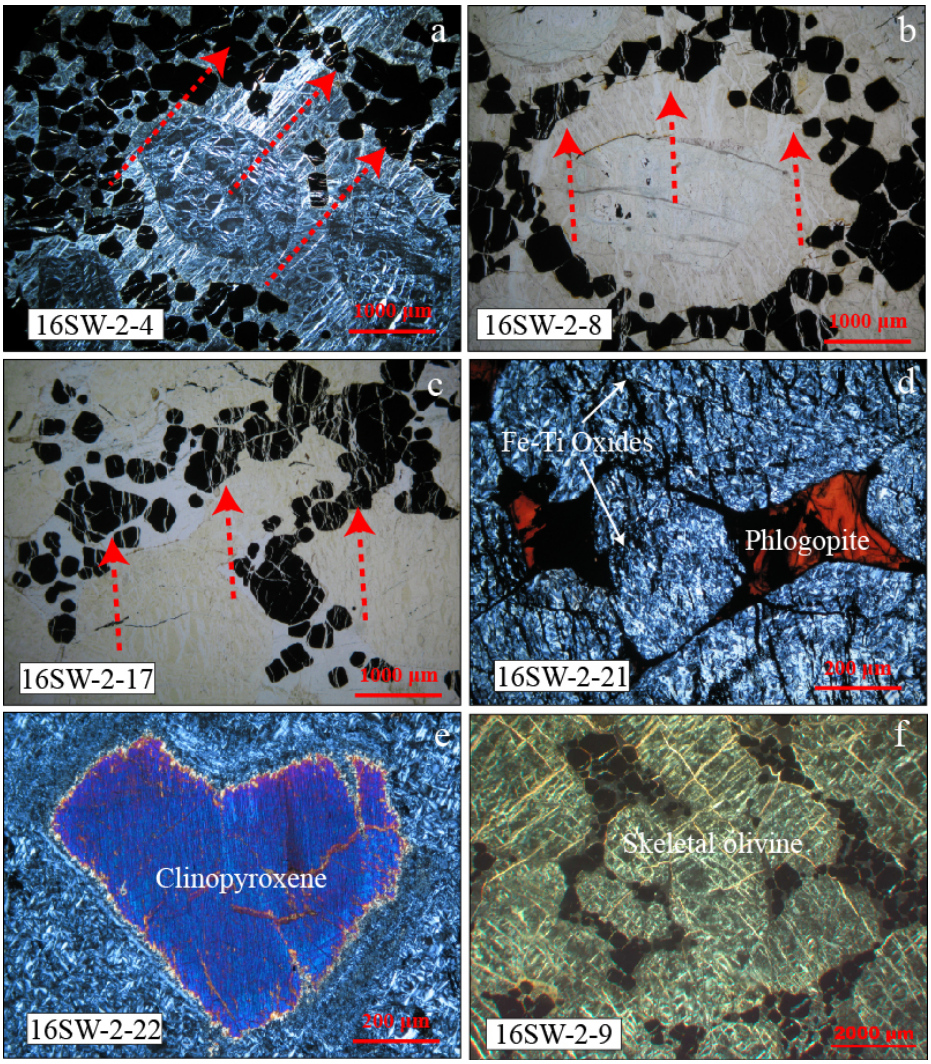

Figure S9.1

Figure caption S9.1: Plane- and cross-polarized optical images of chromitite and silicates samples in B chromitite. Olivine and orthopyroxene in the B chromitite are locally altered to serpentine and exhibit intra-crystalline fracture networks and distinct grain boundaries, with feathery micro-symplectic intergrowths of Fe-Ti oxides within skeletal pseudomorphs.

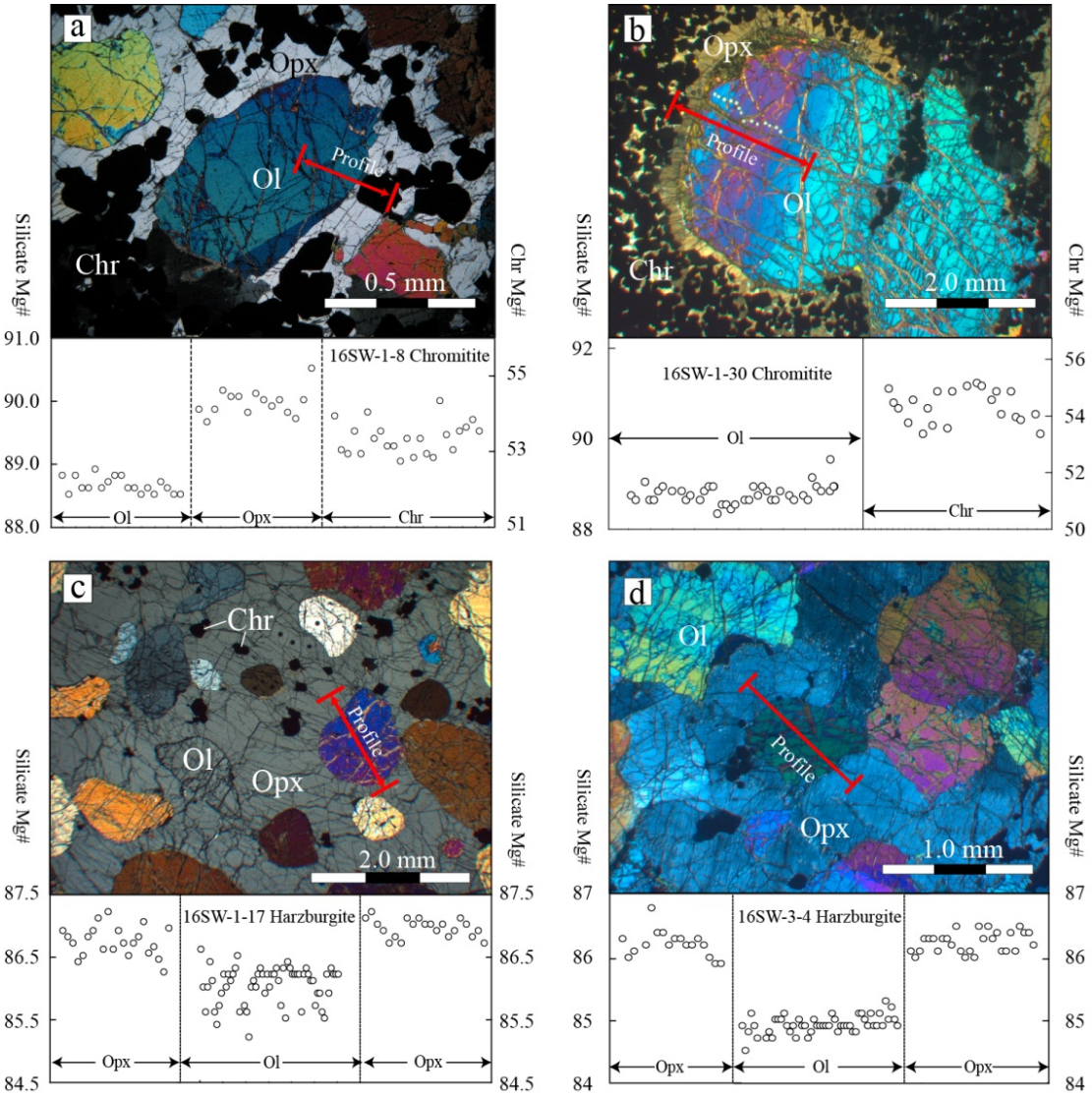

Figure S9.2

Figure captions S9.2 The profiles of Fo or Mg# values traverse olivine, orthopyroxene and chromite in (a) sample 16SW-1-8 (anti-nodular chromitite), (b) sample 16SW-1-30 (anti-nodular chromitite), (c) sample 16SW-1-17 (harzburgite), and (d) sample 16SW-3-4 (dunite).

Table S9.1: Major elemental compositions of olivine, orthopyroxene and chromite in our samples.

Sample	16SW-1-8	16SW-1-8	16SW-1-8	16SW-1-8	16SW-1-8	16SW-1-9	16SW-1-9	16SW-1-9	16SW-1-10	16SW-1-10	16SW-1-11
Mineral	Ol	Ol	Ol	Ol	Ol	Ol	Ol	Ol	Ol	Ol	Ol
SiO_2	39.9	39.9	40.4	40.5	40.8	40.9	40.8	40.9	40.9	39.5	39.8
TiO_2	0.03	0.02	0.00	0.01	0.00	0.01	0.01	0.00	0.00	0.00	0.00
Al_2O_3	0.00	0.00	0.00	0.00	0.00	0.00	0.00	0.00	0.00	0.06	0.00
Cr_2O_3	0.01	0.01	0.02	0.01	0.02	0.01	0.01	0.00	0.01	0.32	0.00
FeO	11.2	10.8	11.5	11.4	10.0	11.5	12.1	12.6	13.3	13.0	13.7
MnO	0.18	0.19	0.19	0.15	0.15	0.19	0.15	0.18	0.19	0.19	0.19
MgO	48.4	48.3	47.8	47.8	48.9	46.6	46.1	46.2	45.9	45.4	46.1
CaO	0.03	0.06	0.03	0.03	0.05	0.02	0.04	0.02	0.03	0.15	0.02
NiO	0.37	0.30	0.35	0.33	0.32	0.29	0.26	0.27	0.31	0.28	0.25
Fo	90.1	90.2	88.5	88.4	89.7	87.8	87.1	86.7	86.0	86.2	86.4

Sample	16SW-1-11	16SW-1-12	16SW-1-13	16SW-1-13	16SW-1-13	16SW-1-14	16SW-1-14	16SW-1-14	16SW-1-15	16SW-1-15	16SW-1-15
Mineral	Ol	Ol	Ol	Ol	Ol	Ol	Ol	Ol	Ol	Ol	Ol
SiO_2	40.5	41.0	40.9	41.3	40.9	40.8	40.5	40.9	40.2	40.6	40.5
TiO_2	0.01	0.00	0.00	0.00	0.01	0.03	0.00	0.03	0.01	0.01	0.00
Al_2O_3	0.00	0.00	0.00	0.00	0.00	0.00	0.00	0.00	0.00	0.00	0.01
Cr_2O_3	0.00	0.01	0.00	0.02	0.00	0.00	0.00	0.01	0.00	0.01	0.01
FeO	14.1	11.3	12.0	11.7	11.9	11.5	11.5	11.8	13.3	13.4	13.5
MnO	0.22	0.14	0.16	0.17	0.17	0.20	0.17	0.13	0.19	0.20	0.18
MgO	45.4	47.9	48.0	47.7	47.1	47.6	48.1	47.4	45.2	46.0	46.1
CaO	0.05	0.05	0.03	0.03	0.04	0.01	0.04	0.06	0.02	0.02	0.05
NiO	0.26	0.30	0.29	0.34	0.29	0.33	0.29	0.27	0.28	0.28	0.26
Fo	85.2	88.3	87.7	87.9	87.6	88.1	88.6	87.8	85.8	86.0	85.9

Sample	16SW-1-16	16SW-1-16	16SW-1-17	16SW-1-17	16SW-1-17	16SW-1-19	16SW-1-19	16SW-1-24	16SW-1-24	16SW-1-24	16SW-1-25
Mineral	Ol	Ol	Ol	Ol	Ol	Ol	Ol	Ol	Ol	Ol	Ol
SiO_2	40.9	41.3	40.5	40.8	40.2	40.5	40.5	41.5	40.7	40.8	40.4
TiO_2	0.00	0.00	0.00	0.01	0.02	0.01	0.00	0.02	0.03	0.02	0.00
Al_2O_3	0.00	0.00	0.00	0.01	0.00	0.00	0.00	0.00	0.00	0.00	0.00
Cr_2O_3	0.01	0.00	0.01	0.01	0.02	0.00	0.02	0.00	0.01	0.00	0.01
FeO	10.5	10.5	14.2	14.0	14.3	14.0	14.0	9.9	9.8	10.4	16.4
MnO	0.16	0.16	0.24	0.23	0.22	0.21	0.18	0.14	0.14	0.15	0.19
MgO	48.2	48.5	45.6	44.7	45.9	45.7	45.6	49.1	48.8	48.2	43.4
CaO	0.05	0.07	0.04	0.01	0.04	0.03	0.02	0.05	0.04	0.04	0.04
NiO	0.35	0.35	0.32	0.32	0.29	0.22	0.23	0.38	0.36	0.35	0.22
Fo	89.1	89.2	85.1	85.0	85.5	85.4	85.4	89.9	89.9	89.2	82.5

Sample	16SW-1-25	16SW-1-25	16SW-1-26	16SW-1-26	16SW-1-26	16SW-1-27	16SW-1-27	16SW-1-28	16SW-1-28	16SW-1-28	16SW-1-30
Mineral	Ol	Ol	Ol	Ol	Ol	Ol	Ol	Ol	Ol	Ol	Ol
SiO_2	41.0	40.4	41.0	41.2	41.2	40.6	40.5	40.4	40.5	40.6	41.0
TiO_2	0.00	0.00	0.00	0.00	0.03	0.01	0.02	0.01	0.03	0.00	0.02
Al_2O_3	0.00	0.01	0.00	0.00	0.00	0.00	0.00	0.00	0.00	0.00	0.00
Cr_2O_3	0.02	0.34	0.00	0.01	0.00	0.00	0.00	0.00	0.03	0.01	0.01
FeO	15.0	14.9	9.74	9.78	9.92	12.5	12.3	13.9	13.7	13.1	11.9
MnO	0.19	0.18	0.14	0.14	0.16	0.17	0.18	0.20	0.19	0.22	0.17
MgO	44.9	45.8	47.8	48.7	48.7	46.7	47.1	45.8	46.0	46.4	47.5
CaO	0.02	0.07	0.03	0.05	0.04	0.03	0.03	0.02	0.02	0.03	0.00
NiO	0.26	0.27	0.33	0.31	0.35	0.28	0.30	0.25	0.27	0.26	0.32
Fo	84.2	84.9	89.7	89.9	89.7	86.9	87.3	85.5	85.6	86.4	87.7

Sample	16SW-1-30	16SW-1-30	16SW-1-30	16SW-1-30	16SW-1-30	16SW-1-31	16SW-1-31	16SW-1-31	16SW-1-31	16SW-1-31	16SW-1-31
Mineral	Ol	Ol	Ol	Ol	Ol	Ol	Ol	Ol	Ol	Ol	Ol
SiO_2	41.5	41.3	41.0	41.5	41.4	40.7	40.4	40.8	40.5	40.6	40.8
TiO_2	0.00	0.00	0.03	0.00	0.01	0.02	0.00	0.00	0.00	0.00	0.00
Al_2O_3	0.00	0.00	0.00	0.00	0.00	0.01	0.01	0.00	0.00	0.00	0.01
Cr_2O_3	0.01	0.04	0.00	0.00	0.00	0.01	0.00	0.02	0.03	0.01	0.03
FeO	11.9	11.9	10.9	10.9	10.9	13.6	13.5	13.6	13.8	13.8	13.9
MnO	0.15	0.17	0.18	0.14	0.15	0.20	0.16	0.19	0.19	0.23	0.19
MgO	47.4	47.4	47.9	48.4	48.6	45.9	45.8	46.2	46.1	45.2	45.8
CaO	0.04	0.05	0.03	0.07	0.03	0.04	0.01	0.03	0.03	0.02	0.03
NiO	0.31	0.28	0.34	0.33	0.33	0.30	0.24	0.27	0.28	0.23	0.33
Fo	87.6	87.7	88.7	88.8	88.8	85.8	85.8	85.8	85.6	85.4	85.5

Sample	16SW-1-32	16SW-1-32	16SW-1-34	16SW-1-34	16SW-1-35	16SW-1-35	16SW-1-35	16SW-1-35	16SW-3-2	16SW-3-2	16SW-3-2
Mineral	Ol	Ol	Ol	Ol	Ol	Ol	Ol	Ol	Ol	Ol	Ol
SiO_2	39.9	41.3	40.8	40.8	40.7	40.8	41.3	41.4	40.3	39.8	40.2
TiO_2	0.02	0.00	0.00	0.03	0.00	0.00	0.00	0.02	0.00	0.00	0.01
Al_2O_3	0.00	0.00	0.00	0.00	0.00	0.00	0.00	0.00	0.00	0.00	0.00
Cr_2O_3	0.01	0.00	0.01	0.02	0.01	0.03	0.01	0.02	0.01	0.00	0.00
FeO	11.5	10.6	11.5	11.9	11.4	10.5	11.2	11.3	14.8	14.8	14.5
MnO	0.16	0.14	0.17	0.19	0.19	0.14	0.17	0.18	0.19	0.22	0.20
MgO	46.7	48.5	48.4	46.4	48.3	48.0	47.8	47.9	45.6	45.6	45.7
CaO	0.02	0.03	0.02	0.06	0.02	0.03	0.01	0.05	0.02	0.02	0.05
NiO	0.30	0.34	0.32	0.30	0.32	0.34	0.30	0.29	0.27	0.27	0.28
Fo	87.8	89.1	88.6	87.4	88.7	89.1	88.4	88.3	84.7	85.5	85.1

Sample	16SW-3-3	16SW-3-3	16SW-3-3	16SW-3-4	16SW-3-4	16SW-3-5	16SW-3-5	16SW-3-9	16SW-3-9	16SW-3-11	16SW-3-11
Mineral	Ol	Ol	Ol	Ol	Ol	Ol	Ol	Ol	Ol	Ol	Ol
SiO_2	40.2	40.3	40.6	40.6	39.7	40.5	40.6	39.2	40.1	40.1	40.3
TiO_2	0.00	0.00	0.00	0.02	0.00	0.03	0.03	0.00	0.00	0.00	0.02
Al_2O_3	0.00	0.00	0.00	0.00	0.01	0.00	0.00	0.00	0.00	0.00	0.00
Cr_2O_3	0.00	0.01	0.02	0.00	0.03	0.00	0.00	0.01	0.00	0.03	0.00
FeO	14.5	14.5	14.5	14.6	14.4	14.4	14.1	14.7	14.7	16.4	16.3
MnO	0.21	0.19	0.22	0.21	0.21	0.18	0.19	0.22	0.23	0.24	0.26
MgO	45.8	45.6	45.6	45.3	45.6	45.7	45.7	45.5	45.2	44.3	44.1
CaO	0.04	0.01	0.02	0.04	0.03	0.06	0.02	0.05	0.07	0.05	0.04
NiO	0.30	0.29	0.24	0.24	0.23	0.23	0.29	0.28	0.26	0.29	0.28
Fo	85.1	84.9	84.9	84.7	85.6	85.0	85.3	86.2	84.5	82.9	82.9

Sample	16SW-1-8	16SW-1-8	16SW-1-8	16SW-1-8	16SW-1-8	16SW-1-8	16SW-1-8	16SW-1-9	16SW-1-10	16SW-1-10	16SW-1-12
Mineral	Opx	Opx	Opx	Opx	Opx	Opx	Opx	Opx	Opx	Opx	Opx
SiO_2	55.1	54.8	54.8	56.7	56.3	57.8	57.1	56.8	56.5	55.4	56.2
TiO_2	0.07	0.10	0.10	0.07	0.10	0.10	0.07	0.07	0.11	0.08	0.10
Al_2O_3	1.51	1.53	1.52	1.33	1.31	1.10	1.36	1.41	1.49	1.58	1.77
Cr_2O_3	0.51	0.56	0.57	0.60	0.48	0.41	0.42	0.41	0.39	0.70	0.63
FeO	7.28	7.26	7.33	7.43	7.35	6.82	7.48	7.94	8.60	8.51	7.42
MnO	0.18	0.19	0.16	0.19	0.15	0.17	0.16	0.19	0.17	0.20	0.18
MgO	32.6	31.7	32.0	33.5	33.1	34.1	33.8	31.7	31.6	30.8	31.2
CaO	1.16	2.26	1.88	0.71	0.65	0.49	0.51	0.95	0.90	1.12	2.50
NiO	0.08	0.09	0.05	0.14	0.06	0.10	0.08	0.08	0.04	0.07	0.07
Fo	88.8	88.6	88.6	88.9	88.9	89.9	88.9	87.7	86.7	86.6	88.2

Sample	16SW-1-13	16SW-1-13	16SW-1-14	16SW-1-14	16SW-1-14	16SW-1-15	16SW-1-15	16SW-1-16	16SW-1-17	16SW-1-17	16SW-1-17
Mineral	Opx	Opx	Opx	Opx	Opx	Opx	Opx	Opx	Opx	Opx	Opx
SiO_2	56.8	57.2	56.6	56.1	56.4	55.8	55.9	56.8	56.5	55.5	56.3
TiO_2	0.12	0.09	0.06	0.06	0.06	0.10	0.05	0.08	0.10	0.11	0.12
Al_2O_3	1.68	1.40	1.51	1.65	1.66	1.69	1.65	1.66	1.67	1.94	1.70
Cr_2O_3	0.59	0.48	0.54	0.59	0.68	0.61	0.63	0.52	0.57	0.70	0.66
FeO	7.92	7.67	7.54	7.82	7.68	8.82	8.58	7.38	9.08	8.57	9.04
MnO	0.19	0.21	0.17	0.20	0.17	0.22	0.24	0.19	0.21	0.22	0.21
MgO	32.1	32.4	31.4	32.2	31.1	31.0	31.4	32.4	30.7	29.4	30.2
CaO	1.06	1.02	2.20	1.66	2.91	1.18	1.39	1.26	2.08	3.80	1.99
NiO	0.10	0.06	0.06	0.10	0.06	0.06	0.02	0.05	0.10	0.08	0.06
Fo	87.8	88.3	88.1	88.0	87.8	86.2	86.7	88.7	85.8	86.0	85.6

Sample	16SW-1-17	16SW-1-18	16SW-1-18	16SW-1-23	16SW-1-23	16SW-1-23	16SW-1-24	16SW-1-24	16SW-1-24	16SW-1-25	16SW-1-25
Mineral	Opx	Opx	Opx	Opx	Opx	Opx	Opx	Opx	Opx	Opx	Opx
SiO_2	56.5	56.5	56.0	57.7	58.1	56.8	56.4	56.4	55.5	56.6	55.9
TiO_2	0.17	0.19	0.13	0.13	0.08	0.07	0.06	0.10	0.08	0.14	0.12
Al_2O_3	1.73	1.22	1.59	1.12	0.98	1.08	1.45	1.28	1.28	1.15	1.37
Cr_2O_3	0.53	0.55	0.48	0.44	0.44	0.47	0.45	0.43	0.45	0.38	0.41
FeO	9.35	9.66	10.10	5.81	5.52	5.47	7.23	6.89	7.24	8.85	9.51
MnO	0.21	0.21	0.23	0.14	0.14	0.14	0.18	0.20	0.18	0.18	0.20
MgO	31.3	30.6	31.3	34.7	34.8	35.0	33.0	32.7	33.2	32.0	31.1
CaO	1.00	1.55	0.89	0.79	0.73	0.65	0.82	1.01	0.95	0.69	1.16
NiO	0.02	0.06	0.10	0.06	0.09	0.10	0.11	0.10	0.09	0.10	0.09
Fo	85.7	85.0	84.7	91.4	91.8	91.9	89.0	89.4	89.1	86.6	85.3

Sample	16SW-1-25	16SW-1-26	16SW-1-26	16SW-1-26	16SW-1-27	16SW-1-27	16SW-1-30	16SW-1-30	16SW-1-30	16SW-1-30	16SW-1-30
Mineral	Opx	Opx	Opx	Opx	Opx	Opx	Opx	Opx	Opx	Opx	Opx
SiO_2	55.6	56.9	57.1	57.0	56.8	55.5	57.1	56.5	56.4	57.0	57.0
TiO_2	0.15	0.08	0.10	0.05	0.06	0.10	0.06	0.03	0.10	0.07	0.07
Al_2O_3	1.54	1.30	1.33	1.18	1.25	1.39	1.34	1.19	1.73	1.32	1.25
Cr_2O_3	0.54	0.44	0.37	0.37	0.51	0.70	0.41	0.34	0.66	0.40	0.42
FeO	10.03	6.75	6.65	6.90	7.71	8.03	7.06	6.97	7.66	7.14	7.05
MnO	0.23	0.18	0.19	0.16	0.18	0.20	0.16	0.16	0.20	0.17	0.17
MgO	29.7	33.2	33.2	33.2	33.0	32.6	32.9	32.4	31.6	32.6	33.4
CaO	1.46	0.65	0.90	0.66	0.57	0.68	0.90	2.05	2.21	1.32	0.88
NiO	0.08	0.05	0.04	0.07	0.05	0.05	0.06	0.05	0.09	0.07	0.04
Fo	84.1	89.8	89.9	89.6	88.4	87.9	89.2	89.2	88.0	89.0	89.4

Sample	16SW-1-31	16SW-1-31	16SW-1-31	16SW-1-31	16SW-1-31	16SW-1-32	16SW-1-32	16SW-1-32	16SW-1-34	16SW-1-34	16SW-1-35
Mineral	Opx	Opx	Opx	Opx	Opx	Opx	Opx	Opx	Opx	Opx	Opx
SiO_2	56.4	56.3	56.8	56.4	56.2	55.4	56.7	57.5	56.8	56.5	57.1
TiO_2	0.24	0.26	0.08	0.10	0.07	0.08	0.06	0.08	0.07	0.08	0.03
Al_2O_3	1.26	1.38	1.64	1.66	1.72	1.22	1.53	1.13	1.62	1.71	1.58
Cr_2O_3	0.32	0.40	0.56	0.54	0.67	0.34	0.46	0.43	0.65	0.59	0.61
FeO	8.97	8.92	8.81	8.69	8.87	7.76	7.79	6.39	7.75	7.57	7.79
MnO	0.22	0.23	0.22	0.21	0.20	0.19	0.18	0.15	0.20	0.19	0.16
MgO	31.7	31.8	31.4	30.8	30.9	32.3	32.8	34.6	32.3	32.0	32.1
CaO	0.72	0.98	1.82	2.24	1.71	0.71	0.97	0.68	1.13	1.97	1.59
NiO	0.04	0.08	0.06	0.10	0.02	0.10	0.06	0.05	0.08	0.04	0.06
Fo	86.3	86.4	86.4	86.3	86.1	88.1	88.2	90.6	88.1	88.3	88.0

Sample	16SW-1-35	16SW-1-35	16SW-1-35	16SW-1-35	16SW-1-35	16SW-1-35	16SW-3-2	16SW-3-2	16SW-3-2	16SW-3-3	16SW-3-3
Mineral	Opx	Opx	Opx	Opx	Opx	Opx	Opx	Opx	Opx	Opx	Opx
SiO_2	56.3	56.6	56.6	56.5	57.4	57.5	56.0	56.4	55.8	56.5	56.4
TiO_2	0.06	0.03	0.06	0.07	0.02	0.09	0.12	0.11	0.12	0.10	0.09
Al_2O_3	1.84	1.65	1.69	1.57	1.31	1.14	1.48	1.18	1.45	1.71	1.26
Cr_2O_3	0.64	0.70	0.62	0.61	0.36	0.47	0.46	0.32	0.47	0.65	0.41
FeO	8.27	7.38	7.87	7.52	7.51	6.54	9.26	9.24	9.23	8.96	9.23
MnO	0.21	0.19	0.23	0.20	0.20	0.15	0.21	0.22	0.25	0.20	0.24
MgO	30.9	30.9	32.1	31.6	33.0	33.7	32.0	32.3	31.7	31.3	32.0
CaO	2.37	3.19	1.68	2.02	0.89	0.78	0.63	0.64	0.86	1.70	0.77
NiO	0.09	0.07	0.05	0.09	0.09	0.07	0.04	0.05	0.04	0.05	0.05
Fo	87.0	88.2	87.9	88.2	88.7	90.2	86.0	86.2	86.0	86.2	86.1

Sample	16SW-3-4	16SW-3-4	16SW-3-5	16SW-3-5	16SW-3-5	16SW-3-6	16SW-3-6	16SW-3-6	16SW-3-9	16SW-3-9	16SW-3-9
Mineral	Opx	Opx	Opx	Opx	Opx	Opx	Opx	Opx	Opx	Opx	Opx
SiO_2	56.7	55.6	56.7	57.0	57.1	56.3	55.4	56.9	56.5	55.3	57.0
TiO_2	0.05	0.09	0.09	0.13	0.06	0.13	0.13	0.09	0.10	0.13	0.10
Al_2O_3	1.48	1.60	1.48	1.39	1.37	1.32	1.22	1.24	1.65	1.39	1.33
Cr_2O_3	0.60	0.64	0.50	0.42	0.44	0.57	0.54	0.57	0.57	0.51	0.36
FeO	8.98	9.20	8.85	8.97	9.10	8.59	9.36	9.31	8.93	9.11	9.20
MnO	0.21	0.21	0.21	0.23	0.23	0.18	0.21	0.21	0.20	0.23	0.21
MgO	31.3	31.8	31.7	31.8	32.2	29.7	31.4	31.4	30.9	32.0	31.6
CaO	1.57	0.75	1.00	0.57	0.59	3.39	1.71	1.48	1.76	0.87	1.60
NiO	0.05	0.05	0.06	0.05	0.06	0.10	0.07	0.06	0.03	0.10	0.09
Fo	86.1	86.0	86.4	86.3	86.3	86.0	85.7	85.7	86.1	86.2	86.0

Sample	16SW-1-8	16SW-1-8	16SW-1-8	16SW-1-8	16SW-1-8	16SW-1-8	16SW-1-8	16SW-1-8	16SW-1-8	16SW-1-8	16SW-1-8
Mineral	Chr	Chr	Chr	Chr	Chr	Chr	Chr	Chr	Chr	Chr	Chr
SiO_2	0.02	0.02	0.03	0.03	0.03	0.07	0.02	0.00	0.06	0.02	0.01
TiO_2	0.49	0.51	0.48	0.46	0.47	0.45	0.48	0.46	0.46	0.46	0.50
Al_2O_3	19.8	19.6	19.8	19.4	19.5	19.4	19.3	19.6	19.5	19.2	18.9
Cr_2O_3	44.9	45.4	45.0	45.0	44.9	44.7	44.9	45.1	44.7	44.3	44.6
FeO	23.8	24.1	24.0	23.6	24.3	24.1	24.3	24.4	24.6	24.1	24.1
MnO	0.16	0.23	0.21	0.23	0.24	0.22	0.24	0.23	0.23	0.26	0.19
MgO	11.2	11.1	11.1	10.8	11.0	11.1	10.8	11.2	10.8	10.5	10.4
CaO	0.02	0.00	0.03	0.00	0.01	0.02	0.00	0.03	0.02	0.00	0.01
NiO	0.11	0.13	0.08	0.12	0.12	0.13	0.06	0.17	0.11	0.09	0.15
Mg#	51.8	51.5	51.6	50.8	51.3	52.0	50.6	52.2	50.3	49.8	49.5

Sample	16SW-1-8	16SW-1-9	16SW-1-9	16SW-1-9	16SW-1-9	16SW-1-9	16SW-1-10	16SW-1-10	16SW-1-10	16SW-1-10	16SW-1-10
Mineral	Chr	Chr	Chr	Chr	Chr	Chr	Chr	Chr	Chr	Chr	Chr
SiO_2	0.02	0.02	0.01	0.04	0.05	0.00	0.02	0.00	0.02	0.04	0.03
TiO_2	0.47	0.46	0.49	0.49	0.41	0.49	0.75	0.81	0.31	0.71	0.46
Al_2O_3	19.3	20.8	20.7	20.6	22.1	20.8	20.1	19.4	16.5	20.6	19.6
Cr_2O_3	44.8	42.9	42.2	42.4	42.3	42.4	41.5	40.4	44.0	41.2	43.5
FeO	24.8	26.3	28.3	28.7	24.2	26.1	28.4	29.0	30.7	28.1	26.9
MnO	0.23	0.40	0.39	0.42	0.34	0.37	0.36	0.39	0.38	0.33	0.32
MgO	10.6	9.16	8.22	7.70	10.7	9.20	8.25	7.95	6.07	8.98	9.59
CaO	0.00	0.01	0.00	0.00	0.00	0.01	0.01	0.00	0.00	0.01	0.01
NiO	0.11	0.11	0.12	0.05	0.14	0.10	0.11	0.11	0.06	0.10	0.13
Mg#	49.6	43.4	39.0	36.6	49.6	43.6	39.3	38.4	30.4	42.2	45.1

Sample	16SW-1-10	16SW-1-11	16SW-1-11	16SW-1-11	16SW-1-12	16SW-1-12	16SW-1-12	16SW-1-13	16SW-1-13	16SW-1-13	16SW-1-14
Mineral	Chr	Chr	Chr	Chr	Chr	Chr	Chr	Chr	Chr	Chr	Chr
SiO_2	0.01	0.04	0.02	0.02	0.01	0.00	0.03	0.03	0.00	0.03	0.03
TiO_2	0.78	1.54	1.18	1.66	0.56	0.56	0.44	0.54	0.38	0.52	0.47
Al_2O_3	20.8	18.5	19.9	18.7	20.0	20.5	20.9	20.1	20.3	19.8	20.2
Cr_2O_3	41.4	38.9	38.3	38.6	44.5	44.3	42.8	44.2	45.0	44.2	44.6
FeO	28.3	33.1	32.0	33.1	25.3	24.3	26.7	25.9	24.9	28.7	26.4
MnO	0.33	0.38	0.39	0.37	0.33	0.29	0.37	0.35	0.34	0.38	0.40
MgO	9.38	7.80	7.81	7.98	10.1	10.6	9.41	9.42	10.3	7.75	8.95
CaO	0.01	0.00	0.01	0.00	0.00	0.00	0.01	0.01	0.00	0.00	0.01
NiO	0.09	0.13	0.13	0.14	0.10	0.13	0.09	0.07	0.11	0.08	0.09
Mg#	43.5	36.4	36.9	37.1	47.1	49.1	44.1	44.1	47.8	36.6	42.1

Sample	16SW-1-14	16SW-1-14	16SW-1-15	16SW-1-15	16SW-1-16	16SW-1-16	16SW-1-17	16SW-1-17	16SW-1-17	16SW-1-17	16SW-1-18
Mineral	Chr	Chr	Chr	Chr	Chr	Chr	Chr	Chr	Chr	Chr	Chr
SiO_2	0.01	0.02	0.03	0.00	0.00	0.00	0.03	0.03	0.10	0.01	0.23
TiO_2	0.40	0.39	0.70	0.81	0.43	0.47	1.03	0.92	0.99	0.68	0.37
Al_2O_3	19.4	19.2	20.8	19.5	21.0	19.8	18.3	19.6	19.5	20.9	7.5
Cr_2O_3	45.5	46.0	39.6	38.3	44.3	45.4	38.2	39.9	39.3	38.5	50.4
FeO	24.4	24.4	29.9	30.4	25.1	22.7	31.2	31.3	31.5	31.8	38.6
MnO	0.35	0.35	0.37	0.41	0.32	0.34	0.37	0.38	0.37	0.38	1.49
MgO	10.1	10.7	7.72	7.51	10.1	11.0	8.52	8.34	7.83	7.74	1.26
CaO	0.00	0.00	0.02	0.02	0.01	0.02	0.03	0.01	0.04	0.02	0.09
NiO	0.12	0.06	0.09	0.07	0.11	0.15	0.16	0.14	0.15	0.09	0.04
Mg#	47.9	50.0	36.9	36.8	47.0	51.8	41.1	39.3	37.2	36.7	6.9

Sample	16SW-1-19	16SW-1-20	16SW-1-20	16SW-1-20	16SW-1-20	16SW-1-20	16SW-1-21	16SW-1-21	16SW-1-21	16SW-1-21	16SW-1-22
Mineral	Chr	Chr	Chr	Chr	Chr	Chr	Chr	Chr	Chr	Chr	Chr
SiO_2	0.02	0.00	0.01	0.01	0.00	0.05	0.08	0.01	0.05	0.14	0.00
TiO_2	1.36	1.13	1.14	1.10	1.00	2.11	1.05	1.06	1.07	1.12	0.50
Al_2O_3	20.4	19.6	18.9	19.5	19.8	17.6	18.8	18.0	17.7	18.5	19.3
Cr_2O_3	38.8	38.7	39.0	39.3	39.2	36.7	38.0	38.8	38.4	40.0	46.2
FeO	30.3	30.9	31.6	31.1	31.2	38.0	35.1	34.2	34.5	31.3	21.6
MnO	0.38	0.31	0.33	0.31	0.32	0.43	0.39	0.44	0.41	0.40	0.31
MgO	8.60	8.30	8.48	8.17	8.14	4.16	6.06	6.42	6.05	7.84	12.1
CaO	0.02	0.02	0.00	0.00	0.00	0.00	0.05	0.00	0.01	0.01	0.01
NiO	0.19	0.14	0.10	0.16	0.14	0.11	0.09	0.14	0.10	0.08	0.11
Mg#	40.0	39.3	39.9	38.5	38.4	19.9	29.1	31.1	29.5	37.2	56.4

Sample	16SW-1-22	16SW-1-23	16SW-1-23	16SW-1-23	16SW-1-23	16SW-1-23	16SW-1-23	16SW-1-23	16SW-1-24	16SW-1-24	16SW-1-24
Mineral	Chr	Chr	Chr	Chr	Chr	Chr	Chr	Chr	Chr	Chr	Chr
SiO_2	0.01	0.00	0.00	0.00	0.00	0.00	0.02	0.01	0.00	0.00	0.01
TiO_2	0.43	0.39	0.41	0.47	0.43	0.45	0.44	0.47	0.42	0.40	0.45
Al_2O_3	19.5	17.7	17.2	17.4	17.3	17.3	17.4	16.4	20.8	19.6	20.3
Cr_2O_3	46.1	49.3	49.6	49.5	49.4	49.1	49.1	48.4	44.7	45.2	44.4
FeO	21.7	21.0	21.4	21.5	21.5	21.3	21.3	21.1	24.2	23.1	25.9
MnO	0.28	0.34	0.30	0.32	0.31	0.30	0.34	0.27	0.33	0.34	0.37
MgO	12.0	11.9	12.1	11.9	11.9	12.0	12.0	12.2	10.4	11.2	9.43
CaO	0.00	0.02	0.01	0.01	0.00	0.02	0.02	0.03	0.01	0.01	0.02
NiO	0.12	0.10	0.12	0.13	0.09	0.15	0.12	0.12	0.12	0.07	0.08
Mg#	55.7	55.8	56.3	55.4	55.6	56.2	56.0	57.8	48.5	52.7	44.2

Sample	16SW-1-25	16SW-1-25	16SW-1-25	16SW-1-26	16SW-1-26	16SW-1-26	16SW-1-27	16SW-1-27	16SW-1-27	16SW-1-27	16SW-1-28
Mineral	Chr	Chr	Chr	Chr	Chr	Chr	Chr	Chr	Chr	Chr	Chr
SiO_2	0.02	0.03	0.02	0.04	0.05	0.01	0.02	0.00	0.04	0.02	0.01
TiO_2	1.08	1.13	1.25	0.40	0.43	0.40	0.75	0.65	0.71	0.52	1.14
Al_2O_3	17.9	18.2	15.4	20.3	20.7	19.4	19.9	18.3	19.6	20.7	19.7
Cr_2O_3	42.1	41.5	41.9	44.8	44.8	45.7	42.2	43.5	42.6	43.4	39.7
FeO	29.5	29.3	35.2	22.4	22.6	22.6	28.1	29.2	28.6	24.9	32.3
MnO	0.35	0.31	0.40	0.29	0.29	0.34	0.37	0.40	0.40	0.34	0.36
MgO	8.89	9.13	5.50	11.5	11.5	11.3	8.17	7.68	7.88	10.26	7.53
CaO	0.01	0.02	0.00	0.00	0.02	0.00	0.02	0.03	0.01	0.01	0.02
NiO	0.16	0.13	0.12	0.17	0.13	0.15	0.07	0.07	0.10	0.12	0.10
Mg#	42.0	43.0	26.8	53.6	53.3	53.4	38.8	37.0	37.6	48.1	35.3

Sample	16SW-1-29	16SW-1-29	16SW-1-30	16SW-1-30	16SW-1-30	16SW-1-30	16SW-1-30	16SW-1-30	16SW-1-30	16SW-1-30	16SW-1-31
Mineral	Chr	Chr	Chr	Chr	Chr	Chr	Chr	Chr	Chr	Chr	Chr
SiO_2	0.01	0.03	0.06	0.00	0.01	0.00	0.00	0.02	0.00	0.02	0.05
TiO_2	1.00	0.96	0.44	0.40	0.47	0.41	0.41	0.38	0.39	0.45	1.40
Al_2O_3	17.2	17.2	20.0	19.8	18.5	20.0	18.8	19.4	19.7	18.9	18.9
Cr_2O_3	42.9	42.8	44.6	45.1	45.5	44.8	44.3	45.4	43.8	46.7	40.7
FeO	30.7	32.1	24.4	25.0	23.2	23.7	25.7	24.2	23.5	23.3	31.3
MnO	0.27	0.33	0.28	0.28	0.31	0.32	0.35	0.31	0.31	0.28	0.41
MgO	8.61	7.38	10.8	10.6	11.5	11.2	10.1	11.0	10.9	11.4	7.83
CaO	0.00	0.02	0.02	0.00	0.01	0.03	0.00	0.00	0.01	0.01	0.02
NiO	0.12	0.10	0.15	0.17	0.11	0.18	0.16	0.11	0.15	0.10	0.10
Mg#	40.6	35.0	50.4	49.2	54.3	52.3	48.2	51.1	51.6	52.9	36.5

Sample	16SW-1-31	16SW-1-31	16SW-1-31	16SW-1-31	16SW-1-31	16SW-1-31	16SW-1-32	16SW-1-32	16SW-1-32	16SW-1-33	16SW-1-33
Mineral	Chr	Chr	Chr	Chr	Chr	Chr	Chr	Chr	Chr	Chr	Chr
SiO_2	0.00	0.07	0.11	0.05	0.04	0.02	0.03	0.03	0.04	0.02	0.01
TiO_2	1.47	1.76	1.66	0.68	0.68	0.68	0.65	0.44	0.39	0.56	0.89
Al_2O_3	18.2	18.2	18.6	22.6	22.6	20.6	19.9	19.1	18.5	16.6	20.3
Cr_2O_3	40.5	40.4	39.4	39.4	39.3	41.1	43.0	45.0	46.6	41.5	35.8
FeO	32.1	32.1	32.3	29.2	29.1	29.3	26.4	26.1	23.4	33.7	36.0
MnO	0.37	0.37	0.37	0.38	0.34	0.33	0.35	0.34	0.30	0.33	0.38
MgO	7.41	7.71	7.53	8.54	8.53	8.67	9.54	9.82	11.7	8.07	7.09
CaO	0.01	0.02	0.05	0.04	0.00	0.01	0.01	0.00	0.02	0.00	0.00
NiO	0.11	0.15	0.14	0.15	0.13	0.15	0.17	0.12	0.11	0.16	0.17
Mg#	34.9	35.8	35.2	39.7	39.8	40.6	44.9	46.1	54.5	38.6	33.6

Sample	16SW-1-34	16SW-1-34	16SW-1-34	16SW-1-34	16SW-1-34	16SW-1-35	16SW-1-35	16SW-1-35	16SW-1-35	16SW-1-36	16SW-1-36
Mineral	Chr	Chr	Chr	Chr	Chr	Chr	Chr	Chr	Chr	Chr	Chr
SiO_2	0.03	0.02	0.01	0.00	0.02	0.03	0.03	0.00	0.01	0.04	0.02
TiO_2	0.37	0.38	0.44	0.54	0.43	0.39	0.41	0.19	0.44	1.17	1.22
Al_2O_3	19.6	18.4	19.3	20.1	19.2	19.2	20.1	21.4	21.1	17.8	17.2
Cr_2O_3	46.0	46.5	45.4	44.3	43.8	46.8	44.2	43.5	44.6	41.7	41.8
FeO	23.6	24.0	23.5	26.3	26.0	23.7	27.3	25.9	23.1	30.9	32.1
MnO	0.34	0.32	0.33	0.33	0.39	0.33	0.37	0.34	0.32	0.33	0.38
MgO	10.9	10.9	11.3	9.42	9.84	10.7	8.55	9.70	11.3	8.38	7.18
CaO	0.03	0.03	0.01	0.01	0.03	0.00	0.00	0.00	0.02	0.03	0.00
NiO	0.15	0.11	0.12	0.10	0.06	0.11	0.09	0.10	0.13	0.14	0.15
Mg#	50.9	51.3	53.0	44.2	46.7	50.0	40.4	45.4	52.4	39.4	34.3

Sample	16SW-1-36	16SW-1-36	16SW-2-4	16SW-2-4	16SW-2-4	16SW-2-4	16SW-2-4	16SW-2-4	16SW-2-4	16SW-2-4	16SW-2-4
Mineral	Chr	Chr	Chr	Chr	Chr	Chr	Chr	Chr	Chr	Chr	Chr
SiO_2	0.05	0.02	0.04	0.05	0.12	0.05	0.04	0.02	0.03	0.05	0.09
TiO_2	1.27	1.25	0.73	0.73	0.78	0.76	0.87	0.80	0.36	0.76	0.70
Al_2O_3	17.2	17.4	18.3	17.7	16.7	18.7	17.9	19.0	18.0	21.5	19.3
Cr_2O_3	42.0	41.7	39.3	39.4	39.5	39.3	40.5	40.0	46.1	41.5	42.2
FeO	32.2	31.5	33.8	35.4	35.8	32.0	33.5	31.8	25.9	26.7	27.3
MnO	0.39	0.39	0.38	0.43	0.39	0.37	0.37	0.34	0.35	0.36	0.37
MgO	7.22	8.04	7.70	6.47	6.03	8.45	7.00	8.43	9.25	9.77	8.41
CaO	0.00	0.00	0.03	0.03	0.00	0.03	0.01	0.01	0.00	0.00	0.00
NiO	0.16	0.15	0.16	0.08	0.07	0.16	0.15	0.15	0.15	0.16	0.08
Mg#	34.3	38.0	36.7	31.2	29.5	40.3	33.6	39.7	44.2	45.2	40.4

Sample	16SW-2-5	16SW-2-5	16SW-2-5	16SW-2-6	16SW-2-6	16SW-2-7	16SW-2-7	16SW-2-7	16SW-2-7	16SW-2-8	16SW-2-8
Mineral	Chr	Chr	Chr	Chr	Chr	Chr	Chr	Chr	Chr	Chr	Chr
SiO_2	0.01	0.00	0.00	0.00	0.02	0.26	0.05	0.04	0.04	0.04	0.03
TiO_2	0.43	0.46	0.39	0.46	0.53	0.78	1.16	1.18	1.27	0.39	0.38
Al_2O_3	19.9	20.5	18.7	20.2	20.4	17.8	19.5	18.7	16.7	19.4	18.9
Cr_2O_3	46.4	46.5	45.6	42.4	42.5	39.6	38.6	38.7	39.9	46.0	46.5
FeO	21.2	20.8	21.1	25.5	25.5	36.6	32.5	32.5	33.4	24.2	24.1
MnO	0.29	0.33	0.34	0.31	0.31	0.36	0.35	0.41	0.40	0.32	0.33
MgO	12.4	12.6	12.7	11.6	11.4	5.03	7.85	7.65	6.78	10.6	10.5
CaO	0.00	0.00	0.00	0.00	0.02	0.01	0.00	0.00	0.02	0.00	0.01
NiO	0.11	0.11	0.06	0.14	0.14	0.13	0.11	0.12	0.12	0.12	0.12
Mg#	57.2	57.6	59.8	53.6	52.5	24.3	36.9	36.4	32.8	49.5	49.3

Sample	16SW-2-8	16SW-2-9	16SW-2-10	16SW-2-10	16SW-2-11	16SW-2-11	16SW-2-12	16SW-2-12	16SW-2-13	16SW-2-13	16SW-2-13
Mineral	Chr	Chr	Chr	Chr	Chr	Chr	Chr	Chr	Chr	Chr	Chr
SiO_2	0.04	0.02	0.19	0.04	0.03	0.02	0.05	0.11	0.01	0.00	0.00
TiO_2	0.37	2.43	1.14	1.12	2.02	1.79	0.34	1.12	0.87	0.78	0.74
Al_2O_3	18.6	18.3	19.0	18.6	17.6	17.6	17.4	20.0	20.2	20.3	20.0
Cr_2O_3	45.8	35.7	38.9	39.1	37.3	37.3	45.7	38.2	42.8	43.1	42.5
FeO	23.4	34.9	32.3	32.7	34.4	34.3	27.2	31.5	25.1	24.7	25.5
MnO	0.35	0.35	0.37	0.36	0.41	0.38	0.35	0.39	0.28	0.32	0.31
MgO	10.1	8.87	8.68	8.39	8.22	8.32	9.51	8.65	11.2	11.2	11.5
CaO	0.01	0.01	0.01	0.00	0.02	0.01	0.02	0.00	0.03	0.01	0.00
NiO	0.16	0.21	0.11	0.14	0.16	0.15	0.14	0.11	0.10	0.09	0.13
Mg#	48.6	40.2	40.3	39.3	38.1	38.9	45.3	40.3	51.8	51.6	53.0

Sample	16SW-2-13	16SW-2-14	16SW-2-14	16SW-2-14	16SW-2-14	16SW-2-14	16SW-2-14	16SW-2-15	16SW-2-16	16SW-2-16	16SW-2-16
Mineral	Chr	Chr	Chr	Chr	Chr	Chr	Chr	Chr	Chr	Chr	Chr
SiO_2	0.01	0.02	0.02	0.03	0.02	0.04	0.03	0.02	0.01	0.02	0.03
TiO_2	0.81	0.36	0.33	0.35	0.38	0.38	0.35	0.43	0.43	0.44	0.44
Al_2O_3	18.2	17.4	18.5	18.8	19.1	19.1	16.5	17.5	18.3	15.9	17.3
Cr_2O_3	41.9	48.7	46.9	47.1	47.2	47.1	47.7	47.8	47.5	46.8	46.7
FeO	25.0	23.1	22.1	22.8	21.9	21.7	22.6	22.1	21.7	21.1	21.7
MnO	0.29	0.32	0.34	0.32	0.30	0.32	0.36	0.29	0.31	0.31	0.33
MgO	9.94	10.8	10.9	11.0	11.6	11.7	9.94	12.2	12.4	10.5	12.4
CaO	0.00	0.00	0.01	0.00	0.02	0.01	0.00	0.01	0.00	0.01	0.02
NiO	0.11	0.13	0.13	0.09	0.13	0.15	0.10	0.16	0.14	0.12	0.12
Mg#	48.3	51.1	52.1	51.8	54.1	54.6	48.7	57.1	57.6	52.2	58.8

Sample	16SW-2-17	16SW-2-17	16SW-2-17	16SW-2-18	16SW-2-18	16SW-2-19	16SW-2-19	16SW-2-19	16SW-2-19	16SW-2-19	16SW-2-20
Mineral	Chr	Chr	Chr	Chr	Chr	Chr	Chr	Chr	Chr	Chr	Chr
SiO_2	0.00	0.02	0.00	0.02	0.01	0.02	0.04	0.04	0.01	0.02	0.08
TiO_2	0.69	0.68	0.70	0.56	0.55	0.40	0.42	0.37	0.38	0.55	0.37
Al_2O_3	20.5	20.3	18.6	21.0	20.3	21.1	20.1	19.6	20.0	19.6	17.2
Cr_2O_3	43.9	43.3	43.5	44.1	44.7	43.7	44.0	45.0	43.4	44.0	47.1
FeO	24.8	25.4	26.7	21.3	21.3	24.2	24.6	24.0	24.7	24.0	23.4
MnO	0.33	0.34	0.39	0.29	0.28	0.35	0.34	0.33	0.37	0.31	0.34
MgO	10.5	10.5	8.37	12.9	12.1	10.8	10.1	10.9	9.61	10.2	11.8
CaO	0.01	0.01	0.00	0.01	0.00	0.00	0.00	0.00	0.00	0.01	0.04
NiO	0.11	0.11	0.10	0.12	0.12	0.12	0.09	0.10	0.14	0.12	0.14
Mg#	48.6	48.5	40.6	58.9	56.2	50.4	47.8	50.9	46.2	48.6	55.6

Sample	16SW-2-20	16SW-2-21	16SW-2-21	16SW-2-21	16SW-2-21	16SW-2-22	16SW-2-22	16SW-2-22	16SW-2-23	16SW-2-23	16SW-3-2
Mineral	Chr	Chr	Chr	Chr	Chr	Chr	Chr	Chr	Chr	Chr	Chr
SiO_2	0.03	0.06	0.01	0.06	0.09	0.02	0.07	0.02	0.05	0.03	0.03
TiO_2	0.34	2.19	1.99	2.31	2.45	1.40	2.96	3.15	0.40	0.32	0.59
Al_2O_3	16.2	14.3	14.5	13.6	14.5	18.0	14.9	14.3	17.1	17.0	21.9
Cr_2O_3	48.6	37.1	36.8	36.4	35.4	39.4	37.5	37.4	40.9	41.1	46.4
FeO	22.1	40.7	40.0	41.2	41.8	33.0	36.1	37.1	35.7	37.0	22.0
MnO	0.31	0.55	0.52	0.47	0.62	0.41	0.40	0.44	0.55	0.64	0.37
MgO	11.5	4.93	5.66	5.74	4.15	8.14	8.14	7.67	5.35	4.21	9.90
CaO	0.00	0.03	0.00	0.01	0.00	0.00	0.03	0.02	0.00	0.01	0.00
NiO	0.13	0.18	0.17	0.17	0.19	0.12	0.18	0.20	0.12	0.08	0.10
Mg#	54.9	23.7	27.2	27.3	20.0	38.3	37.3	35.3	26.4	21.0	45.8

Sample	16SW-3-2	16SW-3-2	16SW-3-2	16SW-3-3	16SW-3-3	16SW-3-4	16SW-3-4	16SW-3-4	16SW-3-5	16SW-3-5	16SW-3-5
Mineral	Chr	Chr	Chr	Chr	Chr	Chr	Chr	Chr	Chr	Chr	Chr
SiO_2	0.00	0.29	1.64	0.06	0.04	0.04	0.05	0.00	0.01	0.03	0.06
TiO_2	0.60	0.55	0.63	0.71	0.55	0.78	0.77	0.74	0.49	0.46	0.43
Al_2O_3	22.9	22.0	20.4	21.8	21.5	22.3	21.6	22.2	22.1	22.2	22.6
Cr_2O_3	45.1	45.3	45.2	45.4	45.7	44.3	45.3	44.9	45.1	45.3	43.8
FeO	22.7	22.2	22.7	24.3	22.2	24.2	24.6	24.9	24.1	22.7	25.4
MnO	0.35	0.31	0.35	0.37	0.36	0.39	0.41	0.37	0.38	0.35	0.42
MgO	9.73	9.77	9.55	8.45	10.20	8.23	8.54	8.04	8.50	9.12	7.20
CaO	0.01	0.05	0.39	0.01	0.01	0.01	0.02	0.00	0.00	0.00	0.00
NiO	0.11	0.10	0.07	0.10	0.07	0.07	0.07	0.08	0.07	0.08	0.06
Mg#	44.8	45.1	43.0	39.3	47.4	38.5	39.6	37.5	39.9	42.9	34.3

Sample	16SW-3-5	16SW-3-9	16SW-3-9	16SW-3-9	16SW-3-9	16SW-3-9	16SW-3-11	16SW-3-11	16SW-3-11	16SW-3-11	16SW-3-11
Mineral	Chr	Chr	Chr	Chr	Chr	Chr	Chr	Chr	Chr	Chr	Chr
SiO_2	0.02	0.02	0.07	0.01	0.02	0.02	0.04	0.02	0.04	0.04	0.02
TiO_2	0.60	0.49	0.65	0.65	0.61	0.67	0.81	0.38	0.68	1.12	0.95
Al_2O_3	22.8	23.0	21.6	20.9	22.1	22.3	20.5	17.8	19.0	17.7	19.0
Cr_2O_3	44.5	44.2	45.1	45.8	44.5	44.4	42.0	45.3	44.2	42.8	41.6
FeO	22.8	23.2	22.1	22.8	25.8	25.0	30.0	28.1	27.9	29.0	28.7
MnO	0.34	0.35	0.35	0.34	0.35	0.39	0.42	0.38	0.42	0.41	0.39
MgO	9.34	9.41	9.11	8.70	7.80	8.15	6.97	8.06	8.47	8.03	8.18
CaO	0.01	0.00	0.01	0.00	0.02	0.00	0.03	0.00	0.02	0.01	0.00
NiO	0.10	0.07	0.10	0.10	0.03	0.05	0.08	0.11	0.06	0.09	0.12
Mg#	43.4	43.6	43.1	41.4	36.5	38.0	33.0	38.9	40.0	38.4	39.2

Part II: Supplementary formulas and calculated process for the closure temperature (T_c) and the selected physical-chemistry parameters for model.

The concept of closure temperature (T_c) is defined as the temperature at which diffusion of the daughter product has effectively ceased during cooling (Dodson, 1973). Ozawa (1984) have demonstrated that the diffusion closure temperature (T_c) of Fe-Mg between olivine and spinel is a function of initial temperature (T_0), grain size. The closure temperature in this study was immediately calculated by the applications given by Ganguly and Tirone (1999), and the cooling rate can be calculated according to the formulation of Ganguly and Tirone (1999):

$$\frac{E}{RT_c} = \ln\left(-\frac{A'RT_c^2 D_0}{E\left(dT/dt\right)_{@T_c} a^2}\right)$$

Take olivine as the example, the $(dT/dt)_{\mathrm{Tc}}$ is the cooling rate at T_c, a is the radius of olivine grains in our samples, set to 1, 1.5, and 2 mm. The function A' can be expressed as $A' = A\exp(g)$, where A is a geometric factor that is given by $A = e^{G}$ (Dodson, 1973), and G = 4.0066 for sphere, 3.29506 for cylinder, and 2.15821 for plane sheet. The term (g), which is referred to as a "memory function", is a function of a dimensionless parameter, M. The formulation of M given by Dodson (1973) is expressed in the following form:

$$M = \frac{RD(T_0)}{E\eta a^2}$$

The values of g for specific M are presented in the tabular form given by Ganguly and Tirone (1999, 2001). In the above equation, $D(T_0)$ is the diffusion coefficient at the peak temperature, which makes the T_c dependent on the T_0. η is a cooling time constant (with a dimension of $K^{-1}t^{-1}$). The cooling was assumed to have followed an asymptotic law that is given by:

$$\frac{1}{T} = \frac{1}{T_0} + \eta t$$

The initial temperature (T_0) was assumed to be 1200, 1100 and 900 ºC. We can use a cooling rate at any temperature, T', instead of that at T_c. Therefore, we can get the curves for T_c vs. cooling rate for specific values of T_0 and a, using the D data (the calculated formula were presented in our new manuscripts).

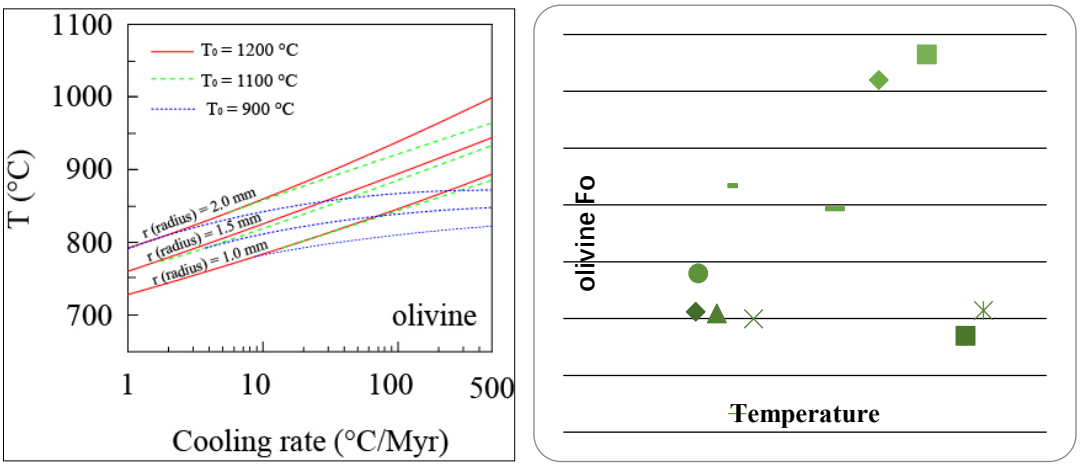

Figure caption: Closure temperature (T_c) of Fe-Mg diffusion in olivine and as a function of the initial temperature (T_0), cooling rate, and grain size. The cooling rate was set to 1 ºC/Myr. And the olivine-spinel Fe-Mg re-equilibrated thermometer of paired cumulus minerals after Balluhaus (1993), see the Part III in this text.

According to the melting experiments performed on the samples from the Stillwater Complex showed that olivine was the first phase in the crystallization sequence, with a liquidus temperature of 1200 ºC (Helz, 1995), this result was also supposed to thethermodynamic model by Hess (1972) and Talkington and Lipin (1986) for the rocks in the Stillwater Complex. Previous studies described olivine grain sizes to be 1.0–2.0 mm in silicate cumulates and 1.5–3.0 mm in chromite-bearing cyclic units (Jackson, 1961; Raedeke and McCallum, 1984). Based on those and our observations (Figure S1; Bai et al., 2019), we set the average length of diffusion profiles to be r = 1.5 mm, and the calculative closure temperature (T_c) could be closed to 750 ºC.

Melting experiments on the potential parental magma of the Stillwater Complex have shown that olivine was the first phase to crystallize at a liquidus temperature of 1200 °C

at P = 1.5–3 kbar (Helz, 1995). We assumed this temperature as the initial temperature in our model, as supported by the presence of RuS_2 in chromite of the Peridotite Zone, which is only stable at or below ~1200 °C (Talkington and Lipin, 1986). Hornfels mineral assemblages exposed at the base of the complex further constrain the pressure of the lowest contact zone to 2–3 kbar (McCallum, 1996). The oxygen fugacity of the system is restricted by the maximum stability of olivine at the aforementioned temperature and pressure conditions (Elliott et al., 1982; Boudreau, 1988), and was set to $\log(fO_2) = -8.41$, corresponding to the quartz-fayalite-magnetite buffer (O'Neill and Pownceby, 1993). The closure temperature defined here is the temperature at which diffusion of the daughter product has effectively ceased during cooling (at a cooling rate lower than 1 °C/Myr), which can be calculated from Dodson (1973) and Ganguly and Tirone (1999, 2001).

References list:

Boudreau, A.E., 1988. Investigations of the Stillwater Complex: 4. The role of volatiles in the petrogenesis of the JM Reef, Minneapolis adit section. The Canadian Mineralogist, 26, 193–208.

Dodson, M.H., 1973. Closure temperature in cooling geochronological and petrological systems. Contributions to Mineralogy and Petrology, 40, 259–274.

Elliott, W.C., Grandstaff, D.E., Ulmer, G.C., Buntin, T. Gold, D.P., 1982. An intrinsic oxygen fugacity study of the platinum-carbon associations in layered intrusions. Economic Geology, 77, 1493–1510.

Ganguly, J., Tirone, M., 1999. Diffusion closure temperature and age of a mineral with arbitrary extent of diffusion: theoretical formulation and applications. Earth and Planetary Science Letters, 170, 131–140.

Ganguly, J., Tirone, M., 2001. Relationship between cooling rate and cooling age of a mineral: theory and applications to meteorites. Meteoritics and Planetary Sciences, 36, 167–175.

O'Neill, H.S.C., Pownceby, M.I., 1993. Thermodynamic data from redox reactions at high temperatures. I. An experimental and theoretical assessment of the electrochemical method using stabilized zirconia electrolytes, with revised values for the Fe-"FeO", Co-CoO, Ni-NiO and Cu-Cu_2O oxygen buffers, and new data for the W-WO_2 buffer. Contributions to Mineralogy and Petrology, 114, 296-314.

Talkington, R.W., Lipin, B.R., 1986. Platinum-group minerals in chromite seams of the Stillwater Complex, Montana. Economic Geology, 8, 1179–1186.

Part III: Supplementary Table for the olivine-spinel geospeedomstry

	16SW-3-9	16SW-3-2	16SW-3-3	16SW-3-4	16SW-3-5	16SW-1-15	16SW-3-11	16SW-1-9	16SW-1-27	16SW-1-8	16SW-1-26
temp (C)	704.89	816.48	713.53	728.87	823.91	705.93	722.03	718.20	762.49	780.65	800.41
press(Gpa)	0.10	0.10	0.10	0.10	0.10	0.10	0.10	0.10	0.10	0.10	0.10
XFe-olv	0.15	0.15	0.15	0.15	0.15	0.14	0.17	0.13	0.13	0.11	0.10
XMg-olv	0.85	0.85	0.85	0.85	0.85	0.86	0.83	0.87	0.87	0.89	0.90
XFe^{2}-spin	0.58	0.51	0.59	0.58	0.51	0.63	0.64	0.57	0.56	0.50	0.47
XMg-spin	0.42	0.49	0.41	0.42	0.49	0.37	0.36	0.43	0.44	0.50	0.53
XAl-spin	0.44	0.44	0.42	0.43	0.42	0.38	0.38	0.39	0.36	0.35	0.36
XFe^{3}-spin	0.02	0.02	0.03	0.03	0.03	0.09	0.08	0.06	0.07	0.07	0.07
XCr-spin	0.54	0.54	0.55	0.54	0.55	0.53	0.54	0.55	0.57	0.58	0.57
XTi-spin	0.01	0.01	0.02	0.02	0.01	0.02	0.02	0.01	0.01	0.01	0.01
KD	7.82	5.77	8.08	7.69	6.01	10.21	8.96	9.09	8.44	8.28	7.54
lnKD	2.06	1.75	2.09	2.04	1.79	2.32	2.19	2.21	2.13	2.11	2.02
	0.27	0.27	0.27	0.27	0.27	0.27	0.27	0.27	0.27	0.27	0.27
	2.56	2.30	2.54	2.50	2.28	2.56	2.52	2.53	2.42	2.38	2.33
	-0.04	-0.04	-0.04	-0.04	-0.04	-0.04	-0.04	-0.04	-0.04	-0.04	-0.04
Thermo- calculation	4.96	4.89	4.96	4.94	4.97	5.09	4.67	5.38	5.30	5.80	5.91
	-2.37	-2.11	-2.35	-2.31	-2.11	-2.41	-2.23	-2.46	-2.34	-2.42	-2.40
	-0.48	-0.58	-0.46	-0.48	-0.58	-0.40	-0.38	-0.49	-0.50	-0.60	-0.66
	-6.63	-6.50	-6.25	-6.25	-6.19	-4.11	-4.49	-4.77	-4.56	-4.66	-4.73
	0.53	0.47	0.48	0.48	0.42	0.39	0.39	0.39	0.33	0.31	0.32
QFM	-1.20	-1.30	-0.86	-0.89	-0.98	1.34	0.70	0.81	0.89	1.04	1.01
log fo2	-18.1	-15.6	-17.5	-17.2	-15.1	-15.5	-15.8	-15.8	-14.6	-14.0	-13.6
T (C)	704.9	816.5	713.5	728.9	823.9	705.9	722.0	718.2	762.5	780.6	800.4

10. Appendix for the Chapter 4

Table S10.1 Major element compositions (wt%)

Comment	16SW-1-17	16SW-1-11	16SW-1-15	16SW-1-19	16SW-1-31	16SW-1-28	16SW-1-10	16SW-1-9	16SW-1-27	16SW-1-12	16SW-1-34	16SW-1-13
Mineral	olivine	olivine	olivine	olivine	olivine	olivine	olivine	olivine	olivine	olivine	olivine	olivine
SiO_2	40.8	39.7	40.2	40.5	40.6	40.3	40.9	40.8	40.6	40.9	40.7	40.9
FeO	14.0	13.7	13.3	14.0	13.8	13.9	13.3	11.5	12.5	11.3	11.9	11.9
MnO	0.23	0.19	0.19	0.21	0.23	0.20	0.19	0.19	0.17	0.14	0.19	0.17
MgO	44.7	46.0	45.1	45.6	45.2	45.8	45.9	46.6	46.7	47.8	46.3	47.0
CaO	0.01	0.02	0.02	0.03	0.02	0.02	0.03	0.02	0.03	0.05	0.06	0.04
NiO	0.32	0.25	0.28	0.22	0.23	0.25	0.31	0.29	0.28	0.30	0.30	0.29
Mg#	85.0	86.4	85.8	85.3	85.4	85.4	86.0	87.8	86.9	88.2	87.3	87.5

Comment	16SW-1-17	16SW-1-11	16SW-1-15	16SW-1-19	16SW-1-31	16SW-1-28	16SW-1-10	16SW-1-9	16SW-1-27	16SW-1-12	16SW-1-34	16SW-1-13
Mineral	olivine	olivine	olivine	olivine	olivine	olivine	olivine	olivine	olivine	olivine	olivine	olivine
SiO_2	40.8	39.8	40.2	40.5	40.6	40.4	40.9	40.9	40.6	41.0	40.8	40.9
FeO	14.0	13.7	13.3	14.0	13.8	13.9	13.3	11.5	12.5	11.3	11.9	11.9
MnO	0.23	0.19	0.19	0.21	0.23	0.20	0.19	0.19	0.17	0.14	0.19	0.17
MgO	44.7	46.1	45.2	45.7	45.2	45.8	45.9	46.6	46.7	47.9	46.4	47.1
CaO	0.01	0.02	0.02	0.03	0.02	0.02	0.03	0.02	0.03	0.05	0.06	0.04
NiO	0.32	0.25	0.28	0.22	0.23	0.25	0.31	0.29	0.28	0.30	0.30	0.29
Mg#	85.0	86.4	85.8	85.4	85.4	85.5	86.0	87.8	86.9	88.3	87.4	87.6

Comment	16SW-1-25	16SW-1-14	16SW-1-24	16SW-1-8	16SW-1-16	16SW-1-35	16SW-1-26	16SW-1-32	16SW-1-30A	16SW-1-30B	16SW-3-1	16SW-3-4
Mineral	olivine	olivine	olivine	olivine	olivine	olivine	olivine	olivine	olivine	olivine	olivine	olivine
SiO_2	41.0	40.8	41.5	39.9	40.9	40.8	41.0	39.9	41.0	41.0	39.5	39.7
FeO	15.0	11.5	9.85	10.8	10.5	10.5	9.74	11.5	11.9	10.9	14.4	14.4
MnO	0.19	0.20	0.14	0.19	0.16	0.14	0.14	0.16	0.17	0.18	0.20	0.21
MgO	44.9	47.6	49.1	48.3	48.2	48.0	47.8	46.7	47.5	47.9	45.6	45.6
CaO	0.02	0.01	0.05	0.06	0.05	0.03	0.03	0.02	0.00	0.03	0.04	0.03
NiO	0.26	0.33	0.38	0.30	0.35	0.34	0.33	0.30	0.32	0.34	0.29	0.23
Mg#	84.2	88.1	89.9	90.2	89.1	89.1	89.7	87.8	87.7	88.7	86.1	85.6

Comment	16SW-3-5	16SW-3-2	16SW-3-3	16SW-3-8	16SW-3-9	16SW-3-11	16SW-2-4
Mineral	olivine	olivine	olivine	olivine	olivine	olivine	olivine
SiO_2	40.6	39.8	39.9	40.0	39.2	40.3	40.5
FeO	14.1	14.8	14.6	14.7	14.7	16.3	13.2
MnO	0.19	0.22	0.24	0.18	0.22	0.26	0.15
MgO	45.7	45.6	44.8	45.5	45.5	44.1	45.8
CaO	0.02	0.02	0.06	0.01	0.05	0.04	0.04
NiO	0.29	0.27	0.25	0.25	0.28	0.28	0.29
Mg#	85.3	85.5	84.5	85.1	86.2	82.9	86.1

Comment	16SW-1-17	16SW-1-15	16SW-1-31	16SW-1-10	16SW-1-9	16SW-1-27	16SW-1-12	16SW-1-34	16SW-1-13	16SW-1-25
Mineral	orthopyroxene	orthopyroxene	orthopyroxene	orthopyroxene	orthopyroxene	orthopyroxene	orthopyroxene	orthopyroxene	orthopyroxene	orthopyroxene
SiO_2	56.3	55.8	56.4	56.5	56.8	56.8	56.2	56.8	57.2	56.6
TiO_2	0.12	0.10	0.24	0.11	0.07	0.06	0.10	0.07	0.09	0.14
Al_2O_3	1.70	1.69	1.26	1.49	1.41	1.25	1.77	1.62	1.40	1.15
Cr_2O_3	0.66	0.61	0.32	0.39	0.41	0.51	0.63	0.65	0.48	0.38
FeO	9.04	8.82	8.97	8.60	7.94	7.71	7.42	7.75	7.67	8.85
MnO	0.21	0.22	0.22	0.17	0.19	0.18	0.18	0.20	0.21	0.18
MgO	30.2	31.0	31.7	31.6	31.7	33.0	31.2	32.3	32.4	32.0
CaO	1.99	1.18	0.72	0.90	0.95	0.57	2.50	1.13	1.02	0.69
NiO	0.06	0.06	0.04	0.04	0.08	0.05	0.07	0.08	0.06	0.10
Cr#	20.6	19.4	14.5	14.9	16.1	21.4	19.4	21.3	18.7	18.1
Mg#	85.6	86.2	86.3	86.7	87.7	88.4	88.2	88.1	88.3	86.6

Comment	16SW-1-24	16SW-1-8	16SW-1-16	16SW-1-35	16SW-1-26	16SW-1-32	16SW-1-30A	16SW-1-30B	16SW-3-6	16SW-3-1
Mineral	orthopyroxene	orthopyroxene	orthopyroxene	orthopyroxene	orthopyroxene	orthopyroxene	orthopyroxene	orthopyroxene	orthopyroxene	orthopyroxene
SiO_2	56.4	56.3	56.8	56.3	56.9	56.7	57.1	57.0	56.3	56.2
TiO_2	0.06	0.10	0.08	0.06	0.08	0.06	0.06	0.07	0.13	0.06
Al_2O_3	1.45	1.31	1.66	1.84	1.30	1.22	1.34	1.32	1.32	1.51
Cr_2O_3	0.45	0.48	0.52	0.64	0.44	0.46	0.41	0.40	0.57	0.60
FeO	7.23	7.35	7.38	8.27	6.75	7.79	7.06	7.14	8.59	8.99
MnO	0.18	0.15	0.19	0.21	0.18	0.18	0.16	0.17	0.18	0.19
MgO	33.0	33.1	32.4	30.9	33.2	32.8	32.9	32.6	29.7	31.6
CaO	0.82	0.65	1.26	2.37	0.65	0.97	0.90	1.32	3.39	1.05
NiO	0.11	0.06	0.05	0.09	0.05	0.06	0.06	0.07	0.10	0.07
Cr#	17.3	19.7	17.3	18.9	18.4	16.9	17.0	16.9	22.4	21.2
Mg#	89.0	88.9	88.7	87.0	89.8	88.2	89.2	89.0	86.0	86.2

Comment	16SW-3-5	16SW-3-2	16SW-3-3	16SW-3-8	16SW-3-9	16SW-3-11
Mineral	orthopyroxene	orthopyroxene	orthopyroxene	orthopyroxene	orthopyroxene	orthopyroxene
SiO_2	56.7	55.8	56.4	55.2	55.3	56.2
TiO_2	0.09	0.12	0.09	0.04	0.13	0.06
Al_2O_3	1.48	1.45	1.26	1.17	1.39	1.73
Cr_2O_3	0.50	0.47	0.41	0.36	0.51	0.67
FeO	8.85	9.23	9.23	9.26	9.11	9.78
MnO	0.21	0.25	0.24	0.23	0.23	0.18
MgO	31.7	31.7	32.0	32.1	32.0	30.2
CaO	1.00	0.86	0.77	0.58	0.87	2.35
NiO	0.06	0.04	0.05	0.04	0.10	0.06
Cr#	18.3	17.8	17.9	17.0	19.8	20.6
Mg#	86.4	86.0	86.1	86.1	86.2	84.6

Comment	16SW-1-17	16SW-1-11	16SW-1-15	16SW-1-19	16SW-1-31	16SW-1-28	16SW-1-10	16SW-1-9	16SW-1-27	16SW-1-12	16SW-1-34	16SW-1-13	16SW-1-25
Mineral	chromite	chromite	chromite	chromite	chromite	chromite	chromite	chromite	chromite	chromite	chromite	chromite	chromite
TiO_2	0.99	1.18	0.70	1.36	1.47	1.13	0.75	0.49	0.65	0.56	0.427	0.54	1.13
Al_2O_3	19.5	19.9	20.8	20.4	18.2	19.1	20.1	20.8	18.3	20.5	19.2	20.1	18.2
Cr_2O_3	39.3	38.3	39.6	38.8	40.5	40.2	41.5	42.4	43.5	44.3	43.8	44.2	41.5
FeO	31.5	32.0	29.9	30.3	32.1	31.9	28.4	26.1	29.2	24.3	26.0	25.9	29.3
MnO	0.37	0.39	0.37	0.38	0.37	0.41	0.36	0.37	0.40	0.29	0.39	0.35	0.31
MgO	7.83	7.81	7.72	8.60	7.41	7.48	8.25	9.20	7.68	10.57	9.84	9.42	9.13
CaO	0.04	0.01	0.02	0.02	0.01	0.00	0.01	0.01	0.03	0.00	0.03	0.01	0.02
NiO	0.15	0.13	0.09	0.19	0.11	0.15	0.11	0.10	0.07	0.13	0.06	0.07	0.13
Cr#	57.5	56.3	56.1	56.0	59.9	58.6	58.1	57.7	61.5	59.2	60.4	59.5	60.4
Mg#	37.2	36.9	36.9	40	34.9	35.4	39.3	43.6	37	49.1	46.7	44.1	43

Comment	16SW-1-14	16SW-1-24	16SW-1-8	16SW-1-16	16SW-1-35	16SW-1-26	16SW-1-32	16SW-1-30A	16SW-1-30B	16SW-3-6	16SW-3-1	16SW-3-4	16SW-3-5
Mineral	chromite	chromite	chromite	chromite	chromite	chromite	chromite	chromite	chromite	chromite	chromite	chromite	chromite
TiO_2	0.40	0.40	0.46	0.47	0.41	0.40	0.65	0.44	0.47	0.80	0.50	0.78	0.43
Al_2O_3	19.4	19.6	19.4	19.8	20.1	20.3	19.9	20.0	18.5	17.1	20.3	22.3	22.6
Cr_2O_3	45.5	45.2	45.0	45.4	44.2	44.8	43.0	44.6	45.5	49.6	46.8	44.3	43.8
FeO	24.4	23.1	23.6	22.7	27.3	22.4	26.4	24.4	23.2	26.1	22.1	24.2	25.4
MnO	0.35	0.34	0.23	0.34	0.37	0.29	0.35	0.28	0.31	0.39	0.31	0.39	0.42
MgO	10.14	11.23	10.83	11.03	8.55	11.51	9.54	10.79	11.53	6.39	9.87	8.23	7.20
CaO	0.00	0.01	0.00	0.02	0.00	0.00	0.01	0.02	0.01	0.01	0.02	0.01	0.00
NiO	0.12	0.07	0.12	0.15	0.09	0.17	0.17	0.15	0.11	0.05	0.11	0.07	0.06
Cr#	61.1	60.7	60.8	60.6	59.6	59.6	59.2	60.0	62.3	66.0	60.7	57.2	56.6
Mg#	47.9	52.7	50.8	51.8	40.4	53.6	44.9	50.4	54.3	30.9	46.5	38.5	34.3

Comment	16SW-3-2	16SW-3-3	16SW-3-8	16SW-3-9	16SW-3-11	16SW-2-4	16SW-2-9	16SW-2-10	16SW-2-11	16SW-2-23	16SW-2-22	16SW-2-7	16SW-2-12
Mineral	chromite	chromite	chromite	chromite	chromite	chromite	chromite	chromite	chromite	chromite	chromite	chromite	chromite
TiO_2	0.55	0.55	0.57	0.65	1.12	0.78	2.43	1.14	1.79	0.40	3.15	1.18	1.12
Al_2O_3	22.0	21.5	19.9	20.9	17.7	16.7	18.3	19.0	17.6	17.1	14.3	18.7	20.0
Cr_2O_3	45.3	45.7	45.8	45.8	42.8	39.5	35.7	38.9	37.3	40.9	37.4	38.7	38.2
FeO	22.2	22.2	24.8	22.8	29.0	35.8	34.9	32.3	34.3	35.7	37.1	32.5	31.5
MnO	0.31	0.36	0.33	0.34	0.41	0.39	0.35	0.37	0.38	0.55	0.44	0.41	0.39
MgO	9.77	10.20	9.12	8.70	8.03	6.03	8.87	8.68	8.32	5.35	7.67	7.65	8.65
CaO	0.05	0.01	0.01	0.00	0.01	0.00	0.01	0.01	0.01	0.00	0.02	0.00	0.00
NiO	0.10	0.07	0.08	0.10	0.09	0.07	0.21	0.11	0.15	0.12	0.20	0.12	0.11
Cr#	58.0	58.7	60.7	59.5	61.9	61.4	56.8	57.9	58.8	61.6	63.7	58.2	56.1
Mg#	45.1	47.4	42.9	41.4	38.4	29.5	40.2	40.3	38.9	26.4	35.3	36.4	40.3

Comment	16SW-2-21	16SW-2-17	16SW-2-8	16SW-2-19	16SW-2-14	16SW-2-14	16SW-2-20	16SW-2-13	16SW-2-6	16SW-2-15	16SW-2-16	16SW-2-5	16SW-2-18
Mineral	chromite	chromite	chromite	chromite	chromite	chromite	chromite	chromite	chromite	chromite	chromite	chromite	chromite
TiO_2	1.99	0.69	0.37	0.42	0.33	0.33	0.34	0.87	0.46	0.43	0.44	0.39	0.55
Al_2O_3	14.5	20.5	18.6	20.1	18.5	18.5	16.2	20.2	20.2	17.5	17.3	18.7	20.3
Cr_2O_3	36.8	43.9	45.8	44.0	46.9	46.9	48.6	42.8	42.4	47.8	46.7	45.6	44.7
FeO	40.0	24.8	23.4	24.6	22.1	22.1	22.1	25.1	25.5	22.1	21.7	21.1	21.3
MnO	0.52	0.33	0.35	0.34	0.34	0.34	0.31	0.28	0.31	0.29	0.33	0.34	0.28
MgO	5.7	10.5	10.1	10.1	10.9	10.9	11.5	11.2	11.6	12.2	12.4	12.7	12.1
CaO	0.00	0.01	0.01	0.00	0.01	0.01	0.00	0.03	0.00	0.01	0.02	0.00	0.00
NiO	0.17	0.11	0.16	0.09	0.13	0.13	0.13	0.10	0.14	0.16	0.12	0.06	0.12
Cr#	63.0	59.0	62.3	59.5	63.0	63.0	66.8	58.7	58.4	64.6	64.4	62.1	59.7
Mg#	27.2	48.6	48.6	47.8	52.1	52.1	54.9	51.8	53.6	57.1	58.8	59.8	56.2

Table S10.2 The Cr elemental concentration profiles (ppm) in olivine and orthopyroxene data, and the Cr_2O_3 (wt%) profiles in chromite.

Orthopyroxene																	
Profile 6	16SW-3-3	2935	3537	3572	3223	3414	2881	3640	3797	3551	4338	3325	3674	4967	4051	4215	3147	3325
		2723	2696															
Profile 7	16SW-3-5	2443	3099	3640	3462	3045	3264	2812	3756	4618	3394	3756	4064	3667	4317	4098	3873	4051
		3927	3996	3770	3743	3517	2956											

Olivine														
Profile 1	16SW-1-9	58	46	45	38	28	25	22	29	31	-	-	-	
Profile 2	16SW-1-27	65	56	-	38	40	46	39	25	-	17	-	33	34
Profile 3	16SW-1-26	50	50	47	38	40	33							
Profile 4	16SW-3-4	35	41	35	35	31	29							
Profile 5	16SW-3-5	-	42	22	36	22	21	19	18					

Chromite																			
Profile 8	16SW-1-8	43.9	43.9	44.6	43.8	43.8	43.8	44.1	43.9	44.0	44.1	44.2	44	44.4	44.0	44.0	43.7	43.5	43.5

Table S10.3 Parameters used to calculate temperature and oxygen fugacity for each sample.

Samples	olivine		chromite						T(°C)	f_{O2} (QFM)
	Fe#	Mg#	Fe#	Mg#	Al^{3+}/R^{3+}	Fe^{3+}/R^{3+}	Cr^{3+}/R^{3+}	Ti		
16SW-3-9	0.15	0.85	0.58	0.42	0.44	0.02	0.54	0.013	710	-1.32
16SW-3-2	0.15	0.85	0.51	0.49	0.44	0.02	0.54	0.011	822	-1.41
16SW-3-3	0.15	0.85	0.59	0.41	0.42	0.03	0.55	0.017	718	-0.98
16SW-3-4	0.15	0.85	0.58	0.42	0.43	0.03	0.54	0.018	734	-1.01
16SW-3-5	0.15	0.85	0.51	0.49	0.42	0.03	0.55	0.015	829	-1.09
16SW-1-15	0.14	0.86	0.63	0.37	0.38	0.09	0.53	0.022	710	1.22
16SW-3-11	0.17	0.83	0.64	0.36	0.38	0.08	0.54	0.016	727	0.58
16SW-1-9	0.13	0.87	0.57	0.43	0.39	0.06	0.55	0.011	723	0.69
16SW-1-27	0.13	0.87	0.56	0.44	0.36	0.07	0.57	0.013	767	0.77
16SW-1-8	0.11	0.89	0.5	0.5	0.35	0.07	0.58	0.012	786	0.92
16SW-1-26	0.1	0.9	0.47	0.53	0.36	0.07	0.57	0.009	806	0.90

The temperatures and oxygen fugacity were calculated according to Bai et al. (2018) and references therein. Referenced samples and those temperatures were taken from Shen et al. (2018), Xia et al. (2017), and Chen et al. (2019).

Table S10.4 Mass balance calculation of chromite, orthopyroxene, and olivine proportions in each sample.

Sample	SiO_2	TiO_2	Al_2O_3	Cr_2O_3	FeO	MnO	MgO	CaO	Na_2O	K_2O	P_2O_5	SiO_2	TiO_2	Al_2O_3	Cr_2O_3	FeO	MnO	MgO	CaO	Na_2O	K_2O
	whole rocks											chromite									
16SW-3-2	42.6	0.08	2.15	2.21	13.1	0.19	35.2	1.31	0.00	0.02	0.01	0.00	0.60	22.9	45.1	22.7	0.35	9.73	0.01	0.00	0.00
16SW-3-3	42.7	0.08	1.92	1.96	13.4	0.20	34.6	1.39	0.00	0.01	0.01	0.04	0.55	21.5	45.7	22.2	0.36	10.2	0.01	0.00	0.00
16SW-3-4	40.4	0.07	1.35	1.80	13.5	0.18	35.9	1.51	0.00	0.01	0.00	0.04	0.78	22.3	44.3	24.2	0.39	8.23	0.01	0.00	0.00
16SW-3-9	42.6	0.08	2.34	3.21	13.9	0.19	35.4	1.18	0.00	0.01	0.01	0.07	0.65	21.6	45.1	22.1	0.35	9.11	0.01	0.00	0.00
16SW-3-5	44.9	0.08	1.69	1.78	12.9	0.20	35.5	1.34	0.00	0.01	0.01	0.01	0.49	22.1	45.1	24.1	0.38	8.50	0.00	0.00	0.01
16SW-3-11	38.4	0.14	6.07	3.02	14.3	0.18	27.5	3.54	0.32	0.04	0.01	0.05	1.02	18.0	42.6	29.2	0.39	7.65	0.01	0.01	0.00
16SW-1-15	41.6	0.06	2.24	0.76	12.0	0.18	35.3	1.41	0.00	0.01	0.01	0.03	0.70	20.8	39.6	29.9	0.37	7.72	0.02	0.02	0.01
16SW-1-8	26.0	0.25	9.67	21.4	16.9	0.17	24.4	1.79	0.04	0.01	0.01	0.02	0.51	19.6	45.4	24.1	0.23	11.1	0.00	0.01	0.00
16SW-1-9	38.3	0.06	2.10	2.36	13.5	0.18	37.8	2.07	0.00	0.01	0.01	0.01	0.49	20.7	42.2	28.3	0.39	8.22	0.00	0.00	0.00
16SW-1-27	34.8	0.10	3.58	4.83	15.0	0.18	38.5	0.56	0.04	0.02	0.02	0.02	0.75	19.9	42.2	28.1	0.37	8.17	0.02	0.01	0.00
16SW-1-26	16.7	0.29	13.5	28.6	18.4	0.18	19.7	1.20	0.20	0.02	0.02	0.01	0.40	19.4	45.7	22.6	0.34	11.3	0.00	0.03	0.00

Sample	SiO_2	TiO_2	Al_2O_3	Cr_2O_3	FeO	MnO	MgO	CaO	Na_2O	K_2O	SiO_2	TiO_2	Al_2O_3	Cr_2O_3	FeO	MnO	MgO	CaO	Na_2O	K_2O
	olivine										orthopyroxene									
16SW-3-2	39.8	0.00	0.00	0.00	14.8	0.22	45.6	0.02	0.00	0.00	56.0	0.12	1.48	0.46	9.26	0.21	32.0	0.63	0.02	0.01
16SW-3-3	39.9	0.01	0.00	0.03	14.6	0.24	44.8	0.06	0.01	0.00	56.4	0.09	1.26	0.41	9.23	0.24	32.0	0.77	0.00	0.00
16SW-3-4	39.7	0.00	0.01	0.03	14.4	0.21	45.6	0.03	0.00	0.00	56.7	0.05	1.48	0.60	8.98	0.21	31.3	1.57	0.02	0.00
16SW-3-9	39.2	0.00	0.00	0.01	14.7	0.22	45.5	0.05	0.00	0.01	55.3	0.13	1.39	0.51	9.11	0.23	32.0	0.87	0.01	0.00
16SW-3-5	40.6	0.03	0.00	0.00	14.1	0.19	45.7	0.02	0.00	0.01	57.0	0.13	1.39	0.42	8.97	0.23	31.8	0.57	0.00	0.00
16SW-3-11	40.3	0.02	0.00	0.00	16.3	0.26	44.1	0.04	0.00	0.01	56.8	0.10	1.13	0.29	10.3	0.22	31.6	0.65	0.00	0.00
16SW-1-15	40.2	0.01	0.00	0.00	13.3	0.19	45.2	0.02	0.00	0.01	56.4	0.06	1.66	0.68	7.68	0.17	31.1	2.91	0.07	0.00
16SW-1-8	39.9	0.02	0.00	0.01	10.8	0.19	48.3	0.06	0.00	0.00	55.1	0.07	1.51	0.51	7.28	0.18	32.6	1.16	0.02	0.00
16SW-1-9	40.8	0.01	0.00	0.01	12.1	0.15	46.1	0.04	0.00	0.00	56.8	0.07	1.41	0.41	7.94	0.19	31.7	0.95	0.03	0.00
16SW-1-27	40.6	0.01	0.00	0.00	12.5	0.17	46.7	0.03	0.00	0.00	56.8	0.06	1.25	0.51	7.71	0.18	33.0	0.57	0.01	0.00
16SW-1-26	41.2	0.03	0.00	0.00	9.92	0.16	48.7	0.04	0.02	0.00	57.0	0.05	1.18	0.37	6.90	0.16	33.2	0.66	0.03	0.02

11. Appendix for the Chapter 5

Table S11.1 GPS location of the studied samples from the Stillwater Complex.

Sample	Rock type	Mineral assemblage	Longitude	Latitude	Section location
16SW3-3	Dunite	ol+opx			Lowermost layer
16SW3-4	Dunite	ol+opx			Lowermost layer
16SW3-2	Harzburgite	ol+opx+cpx(pc)			Lowermost layer
16SW3-9	Harzburgite	ol+opx+cpx(pc)			Lowermost layer
16SW3-5	Harzburgite	ol+opx+cpx(pc)			Lowermost layer
16SW3-11	Basal Pl-harzburgite	ol+opx+cpx(pc)+pl(pc)			Lowermost layer
16SW3-6	Orthopyroxenite	opx+cpx(pc)			Lowermost layer
16SW1-15	Harzburgite	ol+opx(pc)+cpx(pc)			G chromitite
16SW1-8	Anti-nodular chromitite	ol+chr+opx(pc)+cpx(pc)			G chromitite
16SW1-9	Disseminated chromitite	ol+chr+opx(pc)+cpx(pc)			G chromitite
16SW1-26	Anti-nodular chromitite	ol+chr+opx(pc)+cpx(pc)			G chromitite
16SW1-27	Disseminated chromitite	ol+chr+opx(pc)+cpx(pc)			G chromitite
16SW1-34	Disseminated chromitite	ol+chr+opx(pc)+cpx(pc)			G chromitite

12. Appendix for the Chapter 6

Table S12.1 Number, brief descriptions, and locations of the studied samples from the Stillwater Complex.

Outcrop	Section location	Latitude	Longitude	Sample	Rock type	Mineral assemblage
Mountain View area	G chromitite	45.3817°N	109.8784°W	16SW1-7	Bronzitite	Pl+Opx+Cpx
Mountain View area	G chromitite	45.3818°N	109.8785°W	16SW1-18	Bronzitite	Pl+Opx+Cpx
Mountain View area	G chromitite	45.3818°N	109.8785°W	16SW1-10	Dunite	Ol+Pl+Opx+Cpx
Mountain View area	G chromitite	45.3818°N	109.8785°W	16SW1-11	Dunite	Ol+Pl+Opx+Cpx
Mountain View area	G chromitite	45.3818°N	109.8785°W	16SW1-19	Dunite	Ol+Pl+Opx+Cpx
Mountain View area	G chromitite	45.3818°N	109.8785°W	16SW1-15	Harzburgite	Ol+Opx+Cpx
Mountain View area	G chromitite	45.3818°N	109.8785°W	16SW1-28	Harzburgite	Ol+Opx+Cpx
Mountain View area	G chromitite	45.3818°N	109.8785°W	16SW1-17	Harzburgite	Ol+Opx+Cpx
Mountain View area	G chromitite	45.3818°N	109.8785°W	16SW1-31	Harzburgite	Ol+Opx+Cpx
Mountain View area	G chromitite	45.3818°N	109.8785°W	16SW1-8	Anti-nodular Chromitite	Ol+Chr+Opx+Cpx
Mountain View area	G chromitite	45.3818°N	109.8785°W	16SW1-12	Anti-nodular Chromitite	Ol+Chr+Opx+Cpx
Mountain View area	G chromitite	45.3818°N	109.8785°W	16SW1-13	Anti-nodular Chromitite	Ol+Chr+Opx+Cpx
Mountain View area	G chromitite	45.3818°N	109.8785°W	16SW1-16	Anti-nodular Chromitite	Ol+Chr+Opx+Cpx
Mountain View area	G chromitite	45.3819°N	109.8786°W	16SW1-35	Anti-nodular Chromitite	Ol+Chr+Opx+Cpx
Mountain View area	G chromitite	45.3818°N	109.8785°W	16SW1-24	Anti-nodular Chromitite	Ol+Chr+Opx+Cpx
Mountain View area	G chromitite	45.3818°N	109.8785°W	16SW1-34	Anti-nodular Chromitite	Ol+Chr+Opx+Cpx
Mountain View area	G chromitite	45.3818°N	109.8785°W	16SW1-9	Disseminated Chromitite	Ol+Chr+Opx+Cpx
Mountain View area	G chromitite	45.3818°N	109.8785°W	16SW1-14	Disseminated Chromitite	Ol+Chr+Opx+Cpx
Mountain View area	G chromitite	45.3818°N	109.8785°W	16SW1-25	Disseminated Chromitite	Ol+Chr+Opx+Cpx
Mountain View area	G chromitite	45.3818°N	109.8785°W	16SW1-26	Disseminated Chromitite	Ol+Chr+Opx+Cpx
Mountain View area	G chromitite	45.3818°N	109.8785°W	16SW1-27	Disseminated Chromitite	Ol+Chr+Opx+Cpx
Mountain View area	G chromitite	45.3818°N	109.8785°W	16SW1-22	Massive Chromitite	Chr+Opx+Cpx
Mountain View area	G chromitite	45.3818°N	109.8785°W	16SW1-23	Massive Chromitite	Chr+Opx+Cpx
Mountain View area	G chromitite	45.3818°N	109.8785°W	16SW1-29	Massive Chromitite	Chr+Opx+Cpx
Mountain View area	G chromitite	45.3818°N	109.8785°W	16SW1-30	Massive Chromitite	Ol+Chr+Opx+Cpx
Mountain View area	G chromitite	45.3818°N	109.8785°W	16SW1-32	Massive Chromitite	Chr+Opx+Cpx

Table S12.1 (continued)

Outcrop	Section location	Latitude	Longitude	Sample	Rock type	Mineral assemblage
Gish area	Lowermost layer	45.4784°N	110.2036°W	16SW3-7	Bronzitite	Opx+Cpx
Gish area	Lowermost layer	45.4784°N	110.2036°W	16SW3-5	Harzburgite	Ol+Opx+Cpx
Gish area	Lowermost layer	45.4784°N	110.2036°W	16SW3-2	Harzburgite	Ol+Opx+Cpx
Gish area	Lowermost layer	45.4784°N	110.2036°W	16SW3-4	Dunite	Ol+Opx
Gish area	Lowermost layer	45.4784°N	110.2036°W	16SW3-3	Dunite	Ol+Opx
Gish area	Lowermost layer	45.4784°N	110.2036°W	16SW3-9	Harzburgite	Ol+Opx+Cpx
Gish area	Lowermost layer	45.4784°N	110.2036°W	16SW3-11	Harzburgite	Ol+Opx+Cpx+Pl

Note: Ol, olivine; Opx, orthopyroxene; Cpx, clinopyroxene; Pl, plagioclase; Chr, chromite.

Table S12.2 Major element compositions of silicate minerals in two types of inclusions and interstitial matrix.

Sample	16SW-1-8	16SW-1-8	16SW-1-8	16SW-1-8	16SW-1-8	16SW-1-8	16SW-1-8	16SW-1-8	16SW-1-8	16SW-1-8
Rock type	An-chrt	An-chrt	An-chrt	An-chrt	An-chrt	An-chrt	An-chrt	An-chrt	An-chrt	An-chrt
Category	Interstitial	Interstitial	Interstitial	Interstitial	Interstitial	Interstitial	Interstitial	Single-phase	Single-phase	Polymineralic
Mineral	Opx	Opx	Opx	Opx	Opx	Opx	Opx	Opx	Opx	Opx
SiO_2	55.1	54.8	54.8	56.7	56.3	57.8	57.1	56.8	58.0	58.3
TiO_2	0.07	0.10	0.10	0.07	0.10	0.10	0.07	0.06	0.08	0.01
Al_2O_3	1.51	1.53	1.52	1.33	1.31	1.10	1.36	1.29	1.20	0.38
Cr_2O_3	0.51	0.56	0.57	0.60	0.48	0.41	0.42	0.95	0.38	0.62
FeOt	7.28	7.26	7.33	7.43	7.35	6.82	7.48	6.25	6.47	5.99
MnO	0.18	0.19	0.16	0.19	0.15	0.17	0.16	0.15	0.17	0.13
MgO	32.6	31.7	32.0	33.5	33.1	34.1	33.8	34.2	34.3	34.9
CaO	1.16	2.26	1.88	0.71	0.65	0.49	0.51	0.71	0.68	0.33
NiO	0.08	0.09	0.05	0.14	0.06	0.10	0.08	0.02	n.d.	0.07
Na_2O	0.02	0.05	0.05	0.02	n.d.	0.03	0.01	0.02	n.d.	0.03
K_2O	n.d.	n.d.	n.d.	0.01	n.d.	n.d.	n.d.	0.04	0.04	0.02

Sample	16SW-1-8	16SW-1-8	16SW-1-8	16SW-1-8	16SW-1-8	16SW-1-8	16SW-1-8	16SW-1-8	16SW-1-8
Rock type	An-chrt	An-chrt	An-chrt	An-chrt	An-chrt	An-chrt	An-chrt	An-chrt	An-chrt
Category	Polymineralic	Polymineralic	Polymineralic	Polymineralic	Polymineralic	Polymineralic	Polymineralic	Polymineralic	Polymineralic
Mineral	Hbl	Hbl	Hbl	Hbl	Hbl	Hbl	Hbl	Hbl	Hbl
SiO_2	48.0	41.9	42.1	45.5	43.9	38.3	47.9	38.5	40.6
TiO_2	1.62	2.07	2.41	1.57	0.74	2.34	2.24	3.75	2.50
Al_2O_3	8.80	10.7	10.5	8.07	10.5	12.7	9.3	14.4	14.3
Cr_2O_3	3.18	6.63	6.61	4.59	5.52	9.14	4.45	5.70	5.79
FeOt	3.44	3.56	4.32	3.76	4.60	6.37	3.54	3.60	2.89
MnO	0.06	0.05	0.04	0.10	0.06	0.11	0.07	0.04	0.03
MgO	19.4	22.0	22.5	19.4	20.5	17.2	20.6	23.8	25.4
CaO	9.23	4.42	5.85	10.8	9.16	9.80	9.88	0.54	0.18
NiO	n.d.	n.d.	n.d.	n.d.	n.d.	n.d.	n.d.	n.d.	n.d.
Na_2O	4.25	4.17	4.35	1.93	2.76	2.96	2.76	3.98	5.67
K_2O	0.08	0.24	0.22	0.09	0.06	0.22	0.16	0.41	0.40

Table S12.2 (continued)

Sample	16SW-1-8	16SW-1-8	16SW-1-8	16SW-1-8	16SW-1-8	16SW-1-8	16SW-1-9	16SW-1-9	16SW-1-9
Rock type	An-chrt	An-chrt	An-chrt	An-chrt	An-chrt	An-chrt	Diss-chrt	Diss-chrt	Diss-chrt
Category	Polymineralic	Polymineralic	Polymineralic	Polymineralic	Polymineralic	Polymineralic	Interstitial	Polymineralic	Polymineralic
Mineral	Hbl	Hbl	Hbl	Phl	Na-Pl	Na-Pl	Opx	Opx	Opx
SiO_2	38.4	39.2	37.7	40.0	70.4	66.4	56.8	56.1	56.1
TiO_2	3.31	3.66	3.71	3.30	n.d.	n.d.	0.07	0.10	0.35
Al_2O_3	14.6	15.7	15.2	14.2	18.7	19.0	1.41	1.12	1.68
Cr_2O_3	6.30	3.71	5.88	3.05	n.d.	n.d.	0.41	3.18	1.76
FeOt	3.49	2.10	3.55	1.99	0.35	1.27	7.94	5.89	7.32
MnO	0.04	0.01	0.05	n.d.	0.02	0.04	0.19	0.15	0.21
MgO	24.6	24.1	24.4	23.5	n.d.	n.d.	31.7	35.0	33.2
CaO	0.16	0.14	0.29	0.14	0.03	0.26	0.95	0.12	0.26
NiO	n.d.	n.d.	n.d.	0.19	n.d.	n.d.	0.08	0.05	0.06
Na_2O	5.66	4.86	4.91	1.45	10.5	10.3	0.03	0.12	0.46
K_2O	0.68	1.85	0.37	6.06	0.05	0.12	n.d.	0.02	0.03

Sample	16SW-1-10	16SW-1-10	16SW-1-10	16SW-1-10	16SW-1-10	16SW-1-11	16SW-1-11	16SW-1-11	16SW-1-11
Rock type	Du	Du	Du	Du	Du	Du	Du	Du	Du
Category	Single-phase	Polymineralic	Interstitial	Interstitial	Interstitial	Polymineralic	Interstitial	Interstitial	Interstitial
Mineral	Ol	Opx	Ca-Pl	Ca-Pl	Ca-Pl	Opx	Cpx	Cpx	Cpx
SiO_2	41.8	54.5	49.9	47.5	50.0	56.4	52.9	52.6	53.1
TiO_2	0.05	0.30	n.d.	n.d.	n.d.	0.35	0.35	0.38	0.35
Al_2O_3	0.08	1.95	31.8	32.4	31.9	2.15	2.93	2.96	2.80
Cr_2O_3	0.53	3.89	n.d.	n.d.	n.d.	2.39	1.13	1.18	1.13
FeOt	9.21	6.11	0.07	0.12	0.11	5.81	4.03	3.55	3.75
MnO	0.14	0.13	n.d.	n.d.	0.03	0.13	0.18	0.13	0.14
MgO	49.6	34.8	n.d.	n.d.	n.d.	33.7	16.5	16.2	17.0
CaO	0.03	0.37	15.2	15.5	15.6	0.57	21.9	22.7	21.6
NiO	0.28	0.05	n.d.	n.d.	n.d.	0.08	0.01	0.03	0.02
Na_2O	n.d.	0.30	2.93	2.56	2.78	0.34	0.51	0.51	0.45
K_2O	n.d.	0.02	0.09	0.12	0.07	0.06	n.d.	n.d.	n.d.

Table S12.2 (continued)

Sample	16SW-1-11	16SW-1-12	16SW-1-12	16SW-1-12	16SW-1-12	16SW-1-12	16SW-1-12	16SW-1-12	16SW-1-12
Rock type	Du	An-chrt	An-chrt	An-chrt	An-chrt	An-chrt	An-chrt	An-chrt	An-chrt
Category	Interstitial	Interstitial	Interstitial	Polymineralic	Polymineralic	Single-phase	Interstitial	Interstitial	Polymineralic
Mineral	Ca-Pl	Ol	Opx	Opx	Opx	Cpx	Cpx	Cpx	Hbl
SiO_2	48.5	39.5	56.2	56.9	57.6	54.2	52.9	53.6	40.8
TiO_2	n.d.	n.d.	0.10	0.25	0.32	0.44	0.37	0.15	3.73
Al_2O_3	33.2	0.06	1.77	1.54	1.58	2.51	2.76	1.50	12.2
Cr_2O_3	n.d.	0.32	0.63	1.03	1.10	0.98	1.09	0.95	6.31
FeOt	0.15	13.0	7.42	5.06	6.29	3.63	3.55	2.16	5.85
MnO	n.d.	0.19	0.18	0.17	0.17	0.12	0.10	0.08	0.09
MgO	n.d.	45.4	31.2	34.8	33.4	16.3	16.4	17.2	17.5
CaO	16.4	0.15	2.50	0.31	0.34	22.7	22.6	23.3	9.60
NiO	n.d.	0.28	0.07	0.10	0.08	0.03	0.02	0.01	n.d.
Na_2O	2.22	n.d.	0.06	0.33	0.34	0.42	0.47	0.49	3.49
K_2O	0.11	n.d.	n.d.	0.15	0.05	n.d.	n.d.	n.d.	0.24

Sample	16SW-1-13	16SW-1-13	16SW-1-13	16SW-1-13	16SW-1-13	16SW-1-14	16SW-1-14	16SW-1-14	16SW-1-14
Rock type	An-chrt	An-chrt	An-chrt	An-chrt	An-chrt	Diss-chrt	Diss-chrt	Diss-chrt	Diss-chrt
Category	Interstitial	Interstitial	Interstitial	Interstitial	Single-phase	Interstitial	Polymineralic	Polymineralic	Polymineralic
Mineral	Ol	Cpx	Cpx	Cpx	Cpx	Ol	Hbl	Hbl	Hbl
SiO_2	41.2	54.1	53.5	53.2	51.9	41.1	46.7	45.8	39.3
TiO_2	0.01	0.16	0.35	0.22	0.49	n.d.	2.21	2.19	3.66
Al_2O_3	n.d.	2.06	2.41	2.94	2.58	n.d.	9.36	9.06	15.1
Cr_2O_3	0.01	0.98	1.02	1.18	2.30	0.01	3.73	3.54	4.39
FeOt	12.7	2.98	3.25	3.41	4.47	13.2	3.82	4.05	3.05
MnO	0.20	0.14	0.09	0.10	0.11	0.20	0.08	0.11	0.04
MgO	47.1	16.8	16.9	16.6	16.1	46.8	19.2	19.0	25.1
CaO	0.03	22.9	22.7	22.4	22.0	0.03	10.1	9.60	0.10
NiO	0.27	0.04	0.08	0.02	n.d.	0.28	n.d.	n.d.	n.d.
Na_2O	n.d.	0.46	0.48	0.52	0.44	n.d.	3.48	3.33	5.05
K_2O	n.d.	n.d.	n.d.	n.d.	n.d.	n.d.	0.10	0.10	0.57

Table S12.2 (continued)

Sample	16SW-1-15	16SW-1-15	16SW-1-16	16SW-1-16	16SW-1-16	16SW-1-16	16SW-1-16	16SW-1-16	16SW-1-16
Rock type	Hz	Hz	An-chrt	An-chrt	An-chrt	An-chrt	An-chrt	An-chrt	An-chrt
Category	Interstitial	Single-phase	Interstitial	Polymineralic	Polymineralic	Polymineralic	Polymineralic	Polymineralic	Polymineralic
Mineral	Cpx	Cpx	Opx	Opx	Opx	Opx	Hbl	Hbl	Hbl
SiO_2	53.2	53.2	56.8	57.8	57.4	57.7	44.4	46.6	45.8
TiO_2	0.13	0.26	0.08	0.06	0.06	0.16	2.53	2.50	2.44
Al_2O_3	1.95	2.22	1.66	0.65	0.60	0.87	10.1	10.7	9.10
Cr_2O_3	0.96	1.79	0.52	1.41	1.41	1.23	3.20	2.68	4.34
FeOt	2.79	3.77	7.38	5.56	5.72	5.23	3.89	3.75	3.73
MnO	0.13	0.10	0.19	0.11	0.14	0.17	0.06	0.09	0.05
MgO	17.0	16.8	32.4	34.5	34.5	34.7	17.3	19.3	19.2
CaO	21.7	22.4	1.26	0.18	0.50	0.42	10.3	9.90	8.87
NiO	0.06	n.d.	0.05	0.05	0.05	0.09	n.d.	n.d.	n.d.
Na_2O	0.48	0.38	0.01	0.18	0.08	0.21	2.75	3.50	4.07
K_2O	n.d.	0.01	n.d.	n.d.	0.01	0.02	0.06	0.08	0.09

Sample	16SW-1-16	16SW-1-16	16SW-1-16	16SW-1-16	16SW-1-16	16SW-1-16	16SW-1-16	16SW-1-16	16SW-1-16
Rock type	An-chrt	An-chrt	An-chrt	An-chrt	An-chrt	An-chrt	An-chrt	An-chrt	An-chrt
Category	Polymineralic	Interstitial	Interstitial	Interstitial	Interstitial	Polymineralic	Polymineralic	Polymineralic	Polymineralic
Mineral	Hbl	Phl	Phl	Phl	Phl	Phl	Phl	Phl	Phl
SiO_2	46.3	39.1	39.2	38.8	37.9	37.6	38.2	40.8	39.9
TiO_2	2.53	1.36	3.73	3.72	3.86	3.72	3.77	0.88	2.21
Al_2O_3	10.2	16.2	15.1	15.6	15.7	14.3	14.5	13.7	13.4
Cr_2O_3	3.02	1.90	1.66	1.63	1.61	3.93	3.39	1.13	2.20
FeOt	3.20	3.78	3.10	3.11	2.92	2.52	1.83	1.75	2.33
MnO	0.06	0.02	0.02	0.03	0.02	0.06	n.d.	0.01	0.01
MgO	17.7	23.0	22.2	21.8	22.6	21.5	21.5	25.9	22.6
CaO	10.2	0.02	0.01	0.04	0.09	0.19	0.89	0.06	0.30
NiO	n.d.	0.15	0.17	0.22	0.19	0.23	0.27	0.19	0.21
Na_2O	4.52	1.07	0.54	0.53	0.59	1.11	0.81	1.88	2.57
K_2O	0.06	8.63	8.74	9.04	8.99	7.12	7.97	6.69	5.12

Table S12.2 (continued)

Sample	16SW-1-17	16SW-1-18	16SW-1-19	16SW1-22	16SW1-22	16SW1-22	16SW1-22	16SW1-22	16SW1-22
Rock type	Harzburgite	Bronzitite	Du	Ms-chrt	Ms-chrt	Ms-chrt	Ms-chrt	Ms-chrt	Ms-chrt
Category	Interstitial	Interstitial	Interstitial	Polymineralic	Polymineralic	Polymineralic	Polymineralic	Polymineralic	Polymineralic
Mineral	Ca-Pl	Ca-Pl	Ca-Pl	Opx	Opx	Opx	Opx	Opx	Opx
SiO_2	51.0	48.2	48.9	57.6	58.7	58.4	58.1	57.7	56.1
TiO_2	n.d.	n.d.	n.d.	0.05	0.30	0.04	0.06	0.17	0.07
Al_2O_3	31.8	31.6	33.0	0.35	1.27	0.32	0.38	2.37	0.75
Cr_2O_3	n.d.	n.d.	n.d.	0.97	1.15	0.97	0.88	2.01	1.90
FeOt	0.09	0.21	0.14	4.85	4.55	4.74	4.86	4.19	4.80
MnO	0.00	0.01	n.d.	0.14	0.10	0.10	0.17	0.09	0.11
MgO	n.d.	n.d.	n.d.	36.3	34.1	34.9	36.0	33.9	33.9
CaO	14.3	16.3	16.0	0.27	0.55	0.18	0.13	0.66	0.24
NiO	n.d.	n.d.	n.d.	0.05	0.07	0.03	0.05	0.04	0.08
Na_2O	3.53	2.47	2.44	0.02	0.37	0.06	0.12	1.13	0.12
K_2O	0.09	0.15	0.06	n.d.	n.d.	n.d.	0.01	0.03	n.d.

Sample	16SW1-22	16SW1-22	16SW-1-22	16SW-1-22	16SW-1-22	16SW-1-22	16SW-1-22	16SW-1-22	16SW1-22
Rock type	Ms-chrt	Ms-chrt	Ms-chrt	Ms-chrt	Ms-chrt	Ms-chrt	Ms-chrt	Ms-chrt	Ms-chrt
Category	Polymineralic	Polymineralic	Polymineralic	Polymineralic	Polymineralic	Polymineralic	Polymineralic	Polymineralic	Polymineralic
Mineral	Opx	Opx	Hbl	Hbl	Hbl	Hbl	Hbl	Hbl	Hbl
SiO_2	56.9	55.8	47.6	46.8	44.3	42.4	43.2	48.1	38.6
TiO_2	0.28	0.18	2.29	2.19	2.86	3.27	2.84	1.40	2.27
Al_2O_3	1.11	1.53	9.27	9.16	10.7	10.9	11.0	9.88	13.1
Cr_2O_3	0.76	2.16	3.47	3.87	3.23	3.80	4.63	4.22	6.74
FeOt	4.81	4.72	2.49	2.99	3.33	3.67	4.03	3.55	2.39
MnO	0.15	0.14	0.04	0.04	0.09	n.d.	0.08	0.06	n.d.
MgO	34.3	34.5	20.0	17.8	18.3	17.3	18.4	18.8	23.9
CaO	0.40	0.14	7.57	9.59	11.0	12.0	11.3	9.30	2.17
NiO	0.06	0.08	n.d.	n.d.	n.d.	n.d.	n.d.	n.d.	n.d.
Na_2O	0.25	0.48	4.87	4.47	3.14	2.67	3.05	3.67	5.86
K_2O	0.03	0.05	0.11	0.08	0.09	0.36	0.16	0.10	0.52

Table S12.2 (continued)

Sample	16SW1-22	16SW-1-22	16SW-1-22	16SW-1-22	16SW-1-22	16SW-1-22	16SW-1-22	16SW-1-22	16SW-1-22
Rock type	Ms-chrt	Ms-chrt	Ms-chrt	Ms-chrt	Ms-chrt	Ms-chrt	Ms-chrt	Ms-chrt	Ms-chrt
Category	Polymineralic	Interstitial	Interstitial	Polymineralic	Polymineralic	Polymineralic	Polymineralic	Polymineralic	Single-phase
Mineral	Hbl	Ca-Pl	Ca-Pl	Na-Pl	Na-Pl	Na-Pl	Na-Pl	Na-Pl	Ca-Pl
SiO_2	40.4	51.8	52.8	66.6	68.3	73.1	72.4	67.3	50.0
TiO_2	1.62	n.d.	n.d.	n.d.	n.d.	n.d.	n.d.	n.d.	n.d.
Al_2O_3	15.2	30.8	30.5	18.5	17.3	16.3	17.8	19.4	31.9
Cr_2O_3	4.83	n.d.	n.d.	n.d.	n.d.	n.d.	n.d.	n.d.	n.d.
FeOt	2.06	0.08	0.10	1.26	1.19	0.63	0.43	1.07	0.27
MnO	0.03	n.d.	n.d.	0.01	n.d.	n.d.	0.01	0.02	n.d.
MgO	25.1	n.d.	n.d.	n.d.	n.d.	n.d.	n.d.	n.d.	n.d.
CaO	0.04	13.2	13.0	0.06	0.06	0.17	0.09	0.07	14.4
NiO	n.d.	n.d.	n.d.	n.d.	n.d.	n.d.	n.d.	n.d.	n.d.
Na_2O	6.39	4.12	4.27	10.6	9.77	9.13	9.80	10.9	3.39
K_2O	0.36	0.02	0.05	0.01	n.d.	0.03	0.01	0.01	0.01

Sample	16SW-1-23	16SW-1-23	16SW1-23	16SW1-23	16SW1-23	16SW1-23	16SW1-23	16SW1-23	16SW-1-23
Rock type	Ms-chrt	Ms-chrt	Ms-chrt	Ms-chrt	Ms-chrt	Ms-chrt	Ms-chrt	Ms-chrt	Ms-chrt
Category	Interstitial	Interstitial	Polymineralic	Polymineralic	Interstitial	Interstitial	Interstitial	Single-phase	Polymineralic
Mineral	Opx	Opx	Opx	Opx	Cpx	Cpx	Cpx	Cpx	Hbl
SiO_2	56.8	57.7	58.9	57.9	54.4	53.7	53.2	54.2	48.5
TiO_2	0.07	0.13	0.03	0.06	0.14	0.15	0.15	0.15	1.68
Al_2O_3	1.08	1.12	0.20	0.43	1.83	1.88	1.87	1.69	8.44
Cr_2O_3	0.47	0.44	0.81	0.97	0.79	1.29	0.96	1.74	3.56
FeOt	5.47	5.81	4.35	4.61	3.22	2.68	3.02	2.68	2.70
MnO	0.14	0.14	0.08	0.10	0.06	0.09	0.08	0.09	0.03
MgO	35.0	34.7	36.6	36.3	17.2	17.1	17.2	17.2	19.2
CaO	0.65	0.79	0.15	0.29	22.8	23.1	21.6	23.0	9.28
NiO	0.10	0.06	0.07	0.08	0.04	0.02	0.04	0.04	n.d.
Na_2O	n.d.	0.02	0.03	0.02	0.36	0.47	0.49	0.55	4.58
K_2O	n.d.	0.02	0.01	n.d.	n.d.	n.d.	n.d.	0.02	0.02

Table S12.2 (continued)

Sample	16SW-1-23	16SW-1-23	16SW-1-23	16SW-1-23	16SW-1-23	16SW-1-24	16SW-1-24	16SW-1-24	16SW-1-24
Rock type	Ms-chrt	Ms-chrt	Ms-chrt	Ms-chrt	Ms-chrt	An-chrt	An-chrt	An-chrt	An-chrt
Category	Polymineralic	Polymineralic	Interstitial	Polymineralic	Polymineralic	Interstitial	Interstitial	Interstitial	Polymineralic
Mineral	Hbl	Phl	Ca-Pl	Na-Pl	Na-Pl	Opx	Opx	Opx	Opx
SiO_2	48.5	43.4	57.9	73.0	73.8	56.4	56.4	55.5	57.1
TiO_2	1.60	2.60	n.d.	n.d.	n.d.	0.06	0.10	0.08	0.13
Al_2O_3	7.74	13.1	27.2	19.4	19.6	1.45	1.28	1.28	1.68
Cr_2O_3	3.19	3.82	n.d.	n.d.	n.d.	0.45	0.43	0.45	0.76
FeOt	2.45	0.92	0.12	0.20	0.18	7.23	6.89	7.24	6.49
MnO	0.05	0.01	0.01	0.02	0.02	0.18	0.20	0.18	0.18
MgO	19.2	24.6	n.d.	n.d.	n.d.	33.0	32.7	33.2	33.4
CaO	9.40	0.33	8.92	0.04	0.02	0.82	1.01	0.95	0.34
NiO	n.d.	0.23	n.d.	n.d.	n.d.	0.11	0.10	0.09	0.06
Na_2O	4.70	3.22	6.77	8.91	7.13	0.03	0.01	0.02	0.23
K_2O	0.05	1.84	0.03	n.d.	n.d.	0.01	n.d.	n.d.	n.d.

Sample	16SW-1-24	16SW-1-24	16SW-1-24	16SW-1-24	16SW-1-24	16SW-1-24	16SW-1-24	16SW-1-24	16SW-1-24
Rock type	An-chrt	An-chrt	An-chrt	An-chrt	An-chrt	An-chrt	An-chrt	An-chrt	An-chrt
Category	Polymineralic	Polymineralic	Polymineralic	Polymineralic	Polymineralic	Polymineralic	Polymineralic	Polymineralic	Polymineralic
Mineral	Opx	Opx	Opx	Hbl	Hbl	Hbl	Hbl	Phl	Na-Pl
SiO_2	56.0	57.9	58.2	45.9	43.7	43.8	44.7	39.5	70.0
TiO_2	0.21	0.06	0.08	2.48	3.02	2.98	2.13	3.05	n.d.
Al_2O_3	1.84	0.60	0.89	10.7	11.1	11.9	10.4	14.6	19.6
Cr_2O_3	3.03	0.33	1.56	2.93	4.46	4.51	2.94	3.22	n.d.
FeOt	6.17	6.64	6.12	3.72	4.26	4.45	3.72	2.00	0.25
MnO	0.16	0.16	0.14	0.05	0.10	0.09	0.06	0.04	n.d.
MgO	34.3	34.1	34.3	17.9	18.1	18.3	18.4	24.3	n.d.
CaO	0.19	0.47	0.31	9.82	10.6	10.7	9.50	0.11	0.04
NiO	0.06	0.04	0.09	n.d.	n.d.	n.d.	n.d.	0.23	n.d.
Na_2O	0.41	0.07	0.13	4.46	3.14	2.95	4.13	0.15	10.6
K_2O	0.03	0.01	0.01	0.06	0.16	0.25	0.07	5.21	0.01

Table S12.2 (continued)

Sample	16SW-1-25	16SW-1-25	16SW-1-25	16SW-1-25	16SW-1-25	16SW-1-25	16SW-1-26	16SW-1-26	16SW-1-26
Rock type	Diss-chrt	Diss-chrt	Diss-chrt	Diss-chrt	Diss-chrt	Diss-chrt	Diss-chrt	Diss-chrt	Diss-chrt
Category	Interstitial	Interstitial	Interstitial	Interstitial	Interstitial	Single-phase	Polymineralic	Polymineralic	Polymineralic
Mineral	Ca-Pl	Ca-Pl	Cpx	Cpx	Cpx	Cpx	Hbl	Hbl	Hbl
SiO_2	53.0	51.4	52.1	54.1	53.6	53.7	45.2	39.3	37.3
TiO_2	n.d.	n.d.	0.12	0.09	0.18	0.24	2.44	4.21	2.85
Al_2O_3	29.6	30.6	1.93	1.56	2.12	2.18	10.9	15.9	12.6
Cr_2O_3	n.d.	n.d.	1.08	0.89	1.07	1.80	3.44	3.01	5.75
FeOt	0.14	0.14	3.06	2.62	2.73	5.02	3.71	2.10	4.02
MnO	0.02	0.00	0.06	0.10	0.09	0.12	0.06	0.03	0.08
MgO	n.d.	n.d.	16.7	16.8	16.9	17.7	18.3	23.7	25.5
CaO	12.5	13.9	22.1	23.9	23.2	21.2	11.3	0.28	0.33
NiO	n.d.	n.d.	0.05	0.04	0.02	0.03	n.d.	n.d.	n.d.
Na_2O	4.26	3.55	0.41	0.44	0.52	0.48	2.90	5.34	3.64
K_2O	0.33	0.17	n.d.	n.d.	n.d.	n.d.	0.13	1.15	0.91

Sample	16SW-1-26	16SW-1-26	16SW-1-26	16SW-1-26	16SW-1-26	16SW-1-26	16SW-1-26	16SW-1-26	16SW-1-26
Rock type	Diss-chrt	Diss-chrt	Diss-chrt	Diss-chrt	Diss-chrt	Diss-chrt	Diss-chrt	Diss-chrt	Diss-chrt
Category	Polymineralic	Interstitial	Interstitial	Interstitial	Single-phase	Single-phase	Single-phase	Polymineralic	Polymineralic
Mineral	Phl	Opx	Opx	Opx	Opx	Opx	Opx	Opx	Opx
SiO_2	40.9	56.9	57.1	57.0	57.2	58.1	57.5	55.9	55.1
TiO_2	3.47	0.08	0.10	0.05	0.06	0.10	0.08	0.10	0.38
Al_2O_3	15.4	1.30	1.33	1.18	1.38	1.15	1.44	1.92	1.48
Cr_2O_3	3.24	0.44	0.37	0.37	1.63	1.08	1.68	2.80	1.67
FeOt	1.60	6.75	6.65	6.90	5.75	5.38	5.74	5.96	7.25
MnO	n.d.	0.18	0.19	0.16	0.18	0.16	0.16	0.13	0.16
MgO	23.9	33.2	33.2	33.2	34.7	35.2	35.0	34.4	32.2
CaO	0.10	0.65	0.90	0.66	0.45	0.40	0.48	0.45	0.32
NiO	0.22	0.05	0.04	0.07	0.01	0.01	0.01	0.06	0.02
Na_2O	3.66	n.d.	0.00	0.03	0.01	n.d.	0.01	n.d.	0.42
K_2O	4.18	n.d.	0.00	0.02	0.06	0.02	0.10	0.01	0.02

Table S12.2 (continued)

Sample	16SW-1-27	16SW-1-27	16SW-1-28	16SW-1-29	16SW-1-29	16SW-1-29	16SW-1-29	16SW-1-29	16SW-1-29
Rock type	Diss-chrt	Diss-chrt	Harzburgite	Ms-chrt	Ms-chrt	Ms-chrt	Ms-chrt	Ms-chrt	Ms-chrt
Category	Polymineralic	Interstitial	Interstitial	Interstitial	Polymineralic	Interstitial	Interstitial	Interstitial	Interstitial
Mineral	Hbl	Ca-Pl	Ca-Pl	Phl	Phl	Cpx	Cpx	Cpx	Cpx
SiO_2	50.9	49.1	48.2	37.2	37.1	53.9	54.7	54.1	52.0
TiO_2	1.06	n.d.	n.d.	5.79	3.86	0.18	0.10	0.12	0.45
Al_2O_3	6.51	31.9	32.5	15.3	14.8	2.44	1.68	2.78	2.42
Cr_2O_3	3.25	n.d.	n.d.	1.47	4.61	1.13	0.92	1.23	2.48
FeOt	2.62	0.16	0.11	5.76	5.48	2.92	2.96	4.23	4.42
MnO	n.d.	n.d.	n.d.	0.01	0.01	0.13	0.12	0.15	0.12
MgO	25.4	n.d.	n.d.	19.5	22.9	16.7	16.9	18.5	16.7
CaO	0.16	14.8	15.6	0.02	0.08	22.9	23.0	19.5	22.2
NiO	n.d.	n.d.	n.d.	0.15	0.08	0.01	n.d.	0.07	0.07
Na_2O	2.63	2.96	2.70	0.71	0.54	0.62	0.65	0.42	0.37
K_2O	0.53	0.26	0.14	8.85	8.21	n.d.	n.d.	n.d.	n.d.

Sample	16SW-1-29	16SW-1-29	16SW-1-29	16SW-1-29	16SW-1-29	16SW-1-29	16SW-1-29	16SW-1-29	16SW-1-30
Rock type	Ms-chrt	Ms-chrt	Ms-chrt	Ms-chrt	Ms-chrt	Ms-chrt	Ms-chrt	Ms-chrt	Ms-chrt
Category	Interstitial	Interstitial	Interstitial	Interstitial	Single-phase	Single-phase	Single-phase	Polymineralic	Polymineralic
Mineral	Cpx	Cpx	Cpx	Cpx	Cpx	Cpx	Cpx	Opx	Hbl
SiO_2	51.9	53.2	54.2	53.3	53.3	52.1	51.9	54.2	45.0
TiO_2	0.49	0.26	0.15	0.25	0.25	0.26	0.22	0.13	2.29
Al_2O_3	2.58	2.22	1.69	2.09	2.09	2.35	2.05	1.20	11.0
Cr_2O_3	2.30	1.79	1.74	1.99	1.99	3.42	2.34	1.69	2.94
FeOt	4.47	3.77	2.68	5.03	5.03	5.71	4.91	8.16	3.58
MnO	0.11	0.10	0.09	0.13	0.13	0.10	0.08	0.17	0.06
MgO	16.1	16.8	17.2	17.0	17.0	17.0	16.8	32.9	18.5
CaO	22.0	22.4	23.0	21.8	21.8	21.0	21.5	0.63	11.1
NiO	n.d.	n.d.	0.04	0.02	0.02	0.05	0.05	0.04	n.d.
Na_2O	0.44	0.38	0.55	0.40	0.40	0.33	0.33	n.d.	3.08
K_2O	n.d.	n.d.	n.d.	n.d.	n.d.	0.01	0.01	0.02	0.11

Table S12.2 (continued)

Sample	16SW-1-30	16SW-1-30	16SW-1-30	16SW-1-30	16SW-1-30	16SW-1-30	16SW-1-30	16SW-1-30	16SW-1-30
Rock type	Ms-chrt	Ms-chrt	Ms-chrt	Ms-chrt	Ms-chrt	Ms-chrt	Ms-chrt	Ms-chrt	Ms-chrt
Category	Polymineralic	Polymineralic	Polymineralic	Polymineralic	Polymineralic	Polymineralic	Polymineralic	Single-phase	Single-phase
Mineral	Hbl	Hbl	Hbl	Hbl	Hbl	Hbl	Phl	Ca-Pl	Ca-Pl
SiO_2	44.6	43.7	44.9	46.6	37.9	41.6	38.6	53.7	53.7
TiO_2	2.36	2.09	1.91	2.10	3.75	1.95	3.25	n.d.	n.d.
Al_2O_3	10.6	11.3	10.8	9.78	15.6	14.4	15.3	28.0	28.0
Cr_2O_3	3.31	3.71	3.38	3.06	3.29	3.40	1.64	n.d.	n.d.
FeOt	3.81	4.14	3.99	3.15	2.03	1.29	2.24	0.81	0.95
MnO	0.10	0.09	0.09	0.07	0.02	n.d.	n.d.	n.d.	0.03
MgO	18.3	18.4	20.3	18.0	23.6	23.8	22.9	n.d.	n.d.
CaO	10.8	11.3	10.3	9.60	0.28	0.14	0.02	9.70	9.66
NiO	n.d.	n.d.	n.d.	n.d.	n.d.	n.d.	0.24	n.d.	n.d.
Na_2O	3.24	2.29	2.01	4.72	5.91	6.12	0.84	5.59	5.92
K_2O	0.14	0.21	0.15	0.05	0.81	0.32	8.74	0.10	0.02

Sample	16SW-1-30	16SW-1-30	16SW-1-30	16SW-1-30	16SW-1-30	16SW-1-30	16SW-1-30	16SW-1-30	16SW-1-30
Rock type	Ms-chrt	Ms-chrt	Ms-chrt	Ms-chrt	Ms-chrt	Ms-chrt	Ms-chrt	Ms-chrt	Ms-chrt
Category	Single-phase	Single-phase	Single-phase	Single-phase	Interstitial	Interstitial	Interstitial	Interstitial	Interstitial
Mineral	Ca-Pl	Ca-Pl	Ca-Pl	Ca-Pl	Ca-Pl	Ca-Pl	Ca-Pl	Ca-Pl	Ca-Pl
SiO_2	53.6	52.0	54.4	53.1	53.3	53.1	53.2	54.8	55.2
TiO_2	n.d.	n.d.	n.d.	n.d.	n.d.	n.d.	n.d.	n.d.	n.d.
Al_2O_3	28.2	29.3	28.3	28.2	30.4	30.2	30.4	29.1	29.0
Cr_2O_3	n.d.	n.d.	n.d.	n.d.	n.d.	n.d.	n.d.	n.d.	n.d.
FeOt	1.01	0.61	0.65	1.29	0.16	0.09	0.08	0.09	0.06
MnO	n.d.	n.d.	0.01	0.02	n.d.	n.d.	0.00	0.03	0.01
MgO	n.d.	n.d.	n.d.	n.d.	n.d.	n.d.	n.d.	n.d.	n.d.
CaO	10.2	11.2	10.5	9.89	12.7	12.8	13.1	11.1	10.7
NiO	n.d.	n.d.	n.d.	n.d.	n.d.	n.d.	n.d.	n.d.	n.d.
Na_2O	5.47	5.05	5.58	5.63	4.56	4.40	4.27	5.44	5.53
K_2O	0.01	n.d.	0.02	0.05	0.02	0.10	0.09	0.03	0.01

Table S12.2 (continued)

Sample	16SW-1-30	16SW-1-30	16SW-1-30	16SW-1-30	16SW-1-30	16SW-1-30	16SW-1-30	16SW-1-30	16SW-1-30
Rock type	Ms-chrt	Ms-chrt	Ms-chrt	Ms-chrt	Ms-chrt	Ms-chrt	Ms-chrt	Ms-chrt	Ms-chrt
Category	Interstitial	Polymineralic	Single-phase	Single-phase	Single-phase	Single-phase	Single-phase	Single-phase	Single-phase
Mineral	Ca-Pl	Na-Pl	Cpx	Cpx	Cpx	Cpx	Cpx	Cpx	Cpx
SiO_2	55.5	71.2	53.0	52.6	52.9	54.0	53.2	52.7	53.9
TiO_2	n.d.	n.d.	0.18	0.19	0.17	0.17	0.14	0.18	0.18
Al_2O_3	28.7	18.7	2.14	2.08	1.82	2.13	1.93	2.13	1.83
Cr_2O_3	n.d.	n.d.	3.05	2.01	1.68	1.86	1.91	2.76	1.24
FeOt	0.11	0.35	3.62	3.23	2.88	3.17	3.08	3.48	2.74
MnO	0.02	0.01	0.08	0.12	0.08	0.08	0.11	0.11	0.08
MgO	n.d.	n.d.	17.3	16.6	16.9	17.0	17.1	17.0	16.9
CaO	10.9	0.05	21.6	22.2	22.6	22.5	23.0	22.0	23.0
NiO	n.d.	n.d.	0.07	0.05	0.03	0.03	0.06	0.03	0.07
Na_2O	5.46	10.7	0.39	0.40	0.45	0.45	0.46	0.44	0.47
K_2O	0.01	n.d.	n.d.	0.01	0.01	n.d.	0.01	n.d.	n.d.

Sample	16SW-1-30	16SW-1-30	16SW-1-30	16SW-1-30	16SW-1-30	16SW-1-30	16SW-1-30	16SW-1-30	16SW-1-30
Rock type	Ms-chrt	Ms-chrt	Ms-chrt	Ms-chrt	Ms-chrt	Ms-chrt	Ms-chrt	Ms-chrt	Ms-chrt
Category	Single-phase	Single-phase	Single-phase	Single-phase	Single-phase	Single-phase	Single-phase	Single-phase	Single-phase
Mineral	Cpx	Cpx	Cpx	Cpx	Cpx	Cpx	Cpx	Cpx	Cpx
SiO_2	53.6	52.4	53.7	53.2	52.0	52.4	52.9	52.0	52.4
TiO_2	0.15	0.18	0.11	0.15	0.17	0.19	0.14	0.17	0.17
Al_2O_3	1.95	2.17	1.66	2.14	2.26	2.11	2.22	2.38	1.95
Cr_2O_3	1.48	2.52	1.16	1.67	3.23	1.81	2.34	2.95	1.99
FeOt	3.15	3.44	2.84	3.20	3.46	3.26	3.27	3.64	3.19
MnO	0.07	0.09	0.09	0.11	0.09	0.10	0.10	0.11	0.10
MgO	16.9	16.9	17.1	17.0	16.8	16.9	17.1	17.0	17.2
CaO	22.8	22.2	22.8	22.7	22.4	22.2	22.2	21.8	22.3
NiO	0.02	0.02	0.05	0.05	0.07	0.05	0.04	0.02	0.05
Na_2O	0.45	0.40	0.40	0.43	0.43	0.45	0.41	0.43	0.46
K_2O	n.d.	0.01	0.01	0.01	n.d.	0.01	n.d.	n.d.	n.d.

Table S12.2 (continued)

Sample	16SW-1-30	16SW-1-30	16SW-1-30	16SW-1-30	16SW-1-30	16SW-1-30	16SW-1-30	16SW-1-30	16SW-1-30
Rock type	Ms-chrt	Ms-chrt	Ms-chrt	Ms-chrt	Ms-chrt	Ms-chrt	Ms-chrt	Ms-chrt	Ms-chrt
Category	Single-phase	Single-phase	Single-phase	Interstitial	Interstitial	Interstitial	Interstitial	Interstitial	Interstitial
Mineral	Cpx	Cpx	Cpx	Cpx	Cpx	Cpx	Cpx	Cpx	Cpx
SiO_2	49.0	47.3	48.7	52.1	51.9	53.0	52.6	52.9	54.0
TiO_2	0.18	0.18	0.18	0.26	0.22	0.18	0.19	0.17	0.17
Al_2O_3	2.24	2.53	2.75	2.35	2.05	2.14	2.08	1.82	2.13
Cr_2O_3	3.09	4.97	5.57	3.42	2.34	3.05	2.01	1.68	1.86
FeOt	3.63	4.13	4.28	5.71	4.91	3.62	3.23	2.88	3.17
MnO	0.09	0.10	0.11	0.10	0.08	0.08	0.12	0.08	0.08
MgO	17.0	16.8	17.1	17.0	16.8	17.3	16.6	16.9	17.0
CaO	21.7	21.0	20.7	21.0	21.5	21.6	22.2	22.6	22.5
NiO	0.07	0.05	0.05	0.05	0.05	0.07	0.05	0.03	0.03
Na_2O	0.40	0.38	0.40	0.33	0.33	0.39	0.40	0.45	0.45
K_2O	n.d.	0.01	n.d.	n.d.	n.d.	n.d.	n.d.	n.d.	n.d.

Sample	16SW-1-30	16SW-1-30	16SW-1-30	16SW-1-30	16SW-1-30	16SW-1-30	16SW-1-30	16SW-1-30	16SW-1-30
Rock type	Ms-chrt	Ms-chrt	Ms-chrt	Ms-chrt	Ms-chrt	Ms-chrt	Ms-chrt	Ms-chrt	Ms-chrt
Category	Interstitial	Interstitial	Interstitial	Interstitial	Interstitial	Interstitial	Interstitial	Interstitial	Interstitial
Mineral	Cpx	Cpx	Cpx	Cpx	Cpx	Cpx	Cpx	Cpx	Cpx
SiO_2	52.7	53.9	53.9	53.6	52.4	53.7	53.2	52.0	52.4
TiO_2	0.18	0.18	0.17	0.15	0.18	0.11	0.15	0.17	0.19
Al_2O_3	2.13	1.83	1.66	1.95	2.17	1.66	2.14	2.26	2.11
Cr_2O_3	2.76	1.24	1.39	1.48	2.52	1.16	1.67	3.23	1.81
FeOt	3.48	2.74	2.49	3.15	3.44	2.84	3.20	3.46	3.26
MnO	0.11	0.08	0.08	0.07	0.09	0.09	0.11	0.09	0.10
MgO	17.0	16.9	17.2	16.9	16.9	17.1	17.0	16.8	16.9
CaO	22.0	23.0	23.3	22.8	22.2	22.8	22.7	22.4	22.2
NiO	0.03	0.07	0.06	0.02	0.02	0.05	0.05	0.07	0.05
Na_2O	0.44	0.47	0.45	0.45	0.40	0.40	0.43	0.43	0.45
K_2O	n.d.	n.d.	n.d.	n.d.	n.d.	n.d.	n.d.	n.d.	n.d.

Table S12.2 (continued)

Sample	16SW-1-30	16SW-1-30	16SW-1-30	16SW-1-30	16SW-1-30	16SW-1-30	16SW-1-30	16SW-1-30	16SW-1-30
Rock type	Ms-chrt	Ms-chrt	Ms-chrt	Ms-chrt	Ms-chrt	Ms-chrt	Ms-chrt	Ms-chrt	Ms-chrt
Category	Interstitial	Interstitial	Interstitial	Interstitial	Interstitial	Interstitial	Interstitial	Interstitial	Interstitial
Mineral	Cpx	Cpx	Cpx	Cpx	Opx	Opx	Opx	Opx	Opx
SiO_2	52.0	52.4	50.9	48.7	57.1	56.5	56.4	57.0	57.0
TiO_2	0.17	0.17	0.18	0.18	0.06	0.03	0.10	0.07	0.07
Al_2O_3	2.38	1.95	2.39	2.75	1.34	1.19	1.73	1.32	1.25
Cr_2O_3	2.95	1.99	3.46	5.57	0.41	0.34	0.66	0.40	0.42
FeOt	3.64	3.19	3.72	4.28	7.06	6.97	7.66	7.14	7.05
MnO	0.11	0.10	0.09	0.11	0.16	0.16	0.20	0.17	0.17
MgO	17.0	17.2	16.9	17.1	32.9	32.4	31.6	32.6	33.4
CaO	21.8	22.3	21.5	20.7	0.90	2.05	2.21	1.32	0.88
NiO	0.02	0.05	0.04	0.05	0.06	0.05	0.09	0.07	0.04
Na_2O	0.43	0.46	0.45	0.40	0.02	0.03	0.04	n.d.	0.01
K_2O	n.d.	n.d.	n.d.	n.d.	n.d.	0.02	n.d.	n.d.	n.d.

Sample	16SW-1-30	16SW-1-30	16SW-1-30	16SW-1-30	16SW-1-30	16SW-1-30	16SW-1-30	16SW-1-30	16SW-1-30
Rock type	Ms-chrt	Ms-chrt	Ms-chrt	Ms-chrt	Ms-chrt	Ms-chrt	Ms-chrt	Ms-chrt	Ms-chrt
Category	Polymineralic	Polymineralic	Polymineralic	Polymineralic	Polymineralic	Polymineralic	Polymineralic	Polymineralic	Polymineralic
Mineral	Opx	Opx	Opx	Opx	Opx	Opx	Opx	Opx	Opx
SiO_2	54.8	56.7	56.1	57.8	55.1	55.6	55.6	58.4	58.0
TiO_2	0.10	0.08	0.24	0.05	0.18	0.07	0.09	0.02	0.02
Al_2O_3	1.79	1.40	1.40	0.63	1.72	1.40	1.53	0.44	0.36
Cr_2O_3	2.96	1.76	1.07	0.64	1.25	1.68	1.64	0.45	0.60
FeOt	6.30	5.69	5.28	5.87	5.52	5.78	5.80	5.86	5.80
MnO	0.16	0.15	0.11	0.19	0.14	0.14	0.13	0.17	0.12
MgO	34.2	34.9	34.3	34.3	33.1	34.2	34.3	35.3	34.6
CaO	0.50	0.62	0.28	0.57	0.87	0.45	0.52	0.51	0.23
NiO	0.04	0.09	0.05	0.06	0.08	0.08	0.07	0.07	0.08
Na_2O	n.d.	0.01	0.11	0.03	0.12	0.02	n.d.	0.04	0.02
K_2O	0.01	n.d.	0.11	n.d.	n.d.	0.01	n.d.	n.d.	n.d.

Table S12.2 (continued)

Sample	16SW-1-30	16SW-1-30	16SW-1-30	16SW-1-30	16SW-1-30	16SW-1-30	16SW-1-30	16SW-1-30	16SW-1-30
Rock type	Ms-chrt	Ms-chrt	Ms-chrt	Ms-chrt	Ms-chrt	Ms-chrt	Ms-chrt	Ms-chrt	Ms-chrt
Category	Single-phase	Interstitial	Interstitial	Interstitial	Interstitial	Interstitial	Interstitial	Single-phase	Single-phase
Mineral	Opx	Ol	Ol	Ol	Ol	Ol	Ol	Ol	Ol
SiO_2	56.1	41.0	41.5	41.3	41.0	41.5	41.5	42.0	38.9
TiO_2	0.12	0.02	n.d.	n.d.	0.03	n.d.	n.d.	0.03	0.08
Al_2O_3	1.58	n.d.	0.00	n.d.	n.d.	n.d.	n.d.	0.16	2.05
Cr_2O_3	2.44	0.01	0.01	0.04	0.00	n.d.	n.d.	0.61	4.38
FeOt	6.05	11.9	11.9	11.9	10.9	10.9	10.9	7.80	9.57
MnO	0.13	0.17	0.15	0.17	0.18	0.14	0.15	0.10	0.11
MgO	34.5	47.5	47.4	47.4	47.9	48.4	48.6	50.8	45.6
CaO	0.60	0.00	0.04	0.05	0.03	0.07	0.03	0.02	0.06
NiO	n.d.	0.32	0.31	0.28	0.34	0.33	n.d.	0.32	0.32
Na_2O	n.d.	n.d.	n.d.	n.d.	n.d.	n.d.	n.d.	n.d.	n.d.
K_2O	0.06	n.d.	n.d.	n.d.	n.d.	n.d.	n.d.	n.d.	n.d.

Sample	16SW-1-30	16SW-1-30	16SW-1-31	16SW-1-31	16SW-1-31	16SW-1-31	16SW-1-30	16SW-1-31	16SW-1-31
Rock type	Ms-chrt	Ms-chrt	Hz	Hz	Hz	Hz	Ms-chrt	Hz	Hz
Category	Single-phase	Single-phase	Interstitial	Interstitial	Interstitial	Interstitial	Single-phase	Single-phase	Single-phase
Mineral	Ol	Ol	Ca-Pl	Ca-Pl	Ca-Pl	Ca-Pl	Ol	Ol	Ol
SiO_2	41.1	41.5	48.4	49.6	51.0	50.8	40.4	39.6	40.0
TiO_2	0.06	0.02	n.d.	n.d.	n.d.	n.d.	0.03	0.03	0.03
Al_2O_3	0.23	0.22	32.3	32.5	32.0	32.3	0.55	0.09	0.89
Cr_2O_3	1.43	1.32	n.d.	n.d.	n.d.	n.d.	1.36	0.64	2.05
FeOt	7.99	7.56	0.12	0.11	0.15	0.13	5.67	12.1	10.7
MnO	0.12	0.10	0.02	n.d.	0.03	0.02	0.06	0.18	0.10
MgO	49.9	50.6	n.d.	n.d.	n.d.	n.d.	51.0	46.6	47.5
CaO	0.03	0.01	15.2	15.8	14.5	14.8	0.04	0.01	0.03
NiO	0.27	0.31	n.d.	n.d.	n.d.	n.d.	0.41	0.25	0.29
Na_2O	n.d.	n.d.	2.97	2.73	3.40	3.19	n.d.	n.d.	n.d.
K_2O	n.d.	n.d.	0.14	0.12	0.13	0.12	n.d.	n.d.	n.d.

Table S12.2 (continued)

Sample	16SW-1-31	16SW-1-31	16SW-1-31	16SW-1-31	16SW-1-31	16SW-1-32	16SW-1-32	16SW-1-32	16SW-1-32
Rock type	Hz	Hz	Hz	Hz	Hz	Ms-chrt	Ms-chrt	Ms-chrt	Ms-chrt
Category	Interstitial	Interstitial	Interstitial	Interstitial	Interstitial	Single-phase	Single-phase	Interstitial	Polymineralic
Mineral	Ol	Ol	Ol	Ol	Ol	Ca-Pl	Ca-Pl	Phl	Phl
SiO_2	40.4	40.8	40.5	40.6	40.8	53.2	53.7	37.8	37.1
TiO_2	n.d.	n.d.	n.d.	n.d.	n.d.	n.d.	n.d.	6.27	3.24
Al_2O_3	0.01	n.d.	n.d.	n.d.	0.01	29.3	29.2	14.8	15.4
Cr_2O_3	n.d.	0.02	0.03	0.01	0.03	n.d.	n.d.	1.49	5.97
FeOt	13.6	13.6	13.8	13.8	13.9	0.39	0.48	6.83	3.39
MnO	0.16	0.19	0.19	0.23	0.19	0.01	0.03	0.03	0.02
MgO	45.8	46.2	46.2	45.2	45.8	n.d.	n.d.	19.2	23.2
CaO	0.01	0.03	0.03	0.02	0.03	11.8	11.3	0.02	0.24
NiO	0.24	0.27	0.28	0.23	0.33	n.d.	n.d.	0.13	0.25
Na_2O	n.d.	n.d.	n.d.	n.d.	n.d.	4.85	5.04	0.39	1.98
K_2O	n.d.	n.d.	n.d.	n.d.	n.d.	0.02	0.02	8.85	6.28

Sample	16SW-1-34	16SW-1-34	16SW-1-35	16SW-1-35	16SW-2-5	16SW-2-5	16SW-2-5	16SW-2-5	16SW-2-8
Rock type	An-chrt	An-chrt	An-chrt	An-chrt	Ms-chrt	Ms-chrt	Ms-chrt	Ms-chrt	Diss-chrt
Category	Interstitial	Interstitial	Interstitial	Single-phase	Interstitial	Interstitial	Polymineralic	Polymineralic	Polymineralic
Mineral	Opx	Opx	Cpx	Cpx	Phl	Phl	Phl	Phl	Hbl
SiO_2	56.8	56.5	54.4	54.4	38.1	38.6	39.8	40.5	51.2
TiO_2	0.07	0.08	0.17	0.17	6.15	4.73	2.43	1.84	1.66
Al_2O_3	1.62	1.71	1.70	1.70	15.0	15.6	13.0	14.6	7.02
Cr_2O_3	0.65	0.59	1.40	1.40	1.39	1.53	3.37	3.28	1.90
FeOt	7.75	7.57	2.72	2.72	5.79	5.21	1.56	1.20	3.18
MnO	0.20	0.19	0.11	0.11	0.01	0.02	n.d.	n.d.	0.07
MgO	32.3	32.0	17.5	17.5	19.4	20.3	26.2	26.0	20.3
CaO	1.13	1.97	22.8	22.8	0.02	0.03	1.00	0.10	9.74
NiO	0.08	0.04	0.05	0.05	0.19	0.14	0.24	0.25	n.d.
Na_2O	0.04	0.04	0.56	0.56	0.66	0.81	0.12	0.67	2.73
K_2O	n.d.	0.02	n.d.	n.d.	8.66	8.79	5.42	7.57	0.10

Table S12.2 (continued)

Sample	16SW2-8	16SW-2-8	16SW2-13	16SW2-13	16SW2-13	16SW-2-15	16SW-2-15	16SW-2-15	16SW-2-15
Rock type	Diss-chrt	Diss-chrt	Ms-chrt	Ms-chrt	Ms-chrt	Ms-chrt	Ms-chrt	Ms-chrt	Ms-chrt
Category	Single-phase	Polymineralic	Single-phase	Polymineralic	Polymineralic	Polymineralic	Polymineralic	Polymineralic	Polymineralic
Mineral	Opx	Opx	Opx	Opx	Opx	Hbl	Hbl	Na-Pl	Na-Pl
SiO_2	55.5	58.6	59.7	58.5	58.0	47.5	45.0	68.6	69.0
TiO_2	0.35	0.02	0.25	0.10	0.11	2.43	2.95	n.d.	n.d.
Al_2O_3	1.87	0.27	0.68	0.31	0.33	8.80	10.8	19.6	19.5
Cr_2O_3	3.12	1.01	1.06	0.77	0.76	3.13	2.66	n.d.	n.d.
FeOt	6.02	5.66	5.71	5.68	5.74	3.01	3.13	0.21	0.35
MnO	0.15	0.16	0.16	0.16	0.11	0.02	0.03	n.d.	0.02
MgO	32.0	35.9	34.3	35.8	35.8	18.6	18.1	n.d.	n.d.
CaO	0.51	0.14	0.18	0.20	0.19	9.97	12.2	0.03	0.08
NiO	0.73	0.07	0.16	0.04	0.05	n.d.	n.d.	n.d.	n.d.
Na_2O	0.12	0.05	0.02	0.04	0.01	4.36	2.93	11.5	11.2
K_2O	0.05	n.d.	0.04	n.d.	0.01	0.08	0.53	0.19	n.d.

Sample	16SW-2-15	16SW-2-15	16SW-2-15	16SW2-15	16SW-2-16	16SW-2-16	16SW-2-16	16SW-2-16	16SW-2-16
Rock type	Ms-chrt	Ms-chrt	Ms-chrt	Ms-chrt	Ms-chrt	Ms-chrt	Ms-chrt	Ms-chrt	Ms-chrt
Category	Polymineralic	Polymineralic	Polymineralic	Polymineralic	Polymineralic	Polymineralic	Polymineralic	Polymineralic	Polymineralic
Mineral	Na-Pl	Na-Pl	Na-Pl	Opx	Hbl	Hbl	Hbl	Hbl	Hbl
SiO_2	68.5	67.9	69.3	58.8	46.1	53.2	47.0	44.7	40.2
TiO_2	n.d.	n.d.	n.d.	0.05	2.73	0.74	3.94	2.78	3.17
Al_2O_3	19.9	18.6	19.0	0.21	10.1	3.49	7.71	9.77	14.9
Cr_2O_3	n.d.	n.d.	n.d.	0.62	3.58	1.66	2.65	3.39	3.27
FeOt	0.30	0.70	0.37	4.93	2.61	1.15	2.31	1.96	0.94
MnO	n.d.	n.d.	0.03	0.11	n.d.	0.03	0.08	0.03	n.d.
MgO	n.d.	n.d.	n.d.	36.2	20.0	28.3	20.9	22.3	24.1
CaO	0.07	0.07	0.08	0.19	8.49	3.08	10.2	7.10	0.07
NiO	n.d.	n.d.	n.d.	0.08	n.d.	n.d.	n.d.	n.d.	n.d.
Na_2O	11.4	10.3	10.7	0.03	3.91	1.92	1.65	3.99	5.97
K_2O	0.01	0.21	0.01	n.d.	0.28	0.06	0.66	0.29	0.64

Table S12.2 (continued)

Sample	16SW-2-16	16SW2-16	16SW2-16	16SW-2-17	16SW-2-17	16SW-2-17	16SW-2-19	16SW-2-19
Rock type	Ms-chrt	Ms-chrt	Ms-chrt	Diss-chrt	Diss-chrt	Diss-chrt	An-chrt	An-chrt
Category	Polymineralic	Polymineralic	Polymineralic	Polymineralic	Polymineralic	Polymineralic	Polymineralic	Polymineralic
Mineral	Hbl	Opx	Opx	Phl	Phl	Phl	Phl	Phl
SiO_2	41.2	54.7	59.2	34.8	37.9	36.6	34.5	36.8
TiO_2	2.27	0.42	0.07	3.00	5.04	4.56	5.57	3.82
Al_2O_3	14.8	1.60	0.50	11.9	14.7	15.2	15.5	15.9
Cr_2O_3	3.39	1.67	1.06	2.84	2.60	2.56	2.52	2.81
FeOt	1.00	4.16	3.13	5.75	3.06	3.55	3.47	2.62
MnO	n.d.	0.06	0.09	0.09	0.01	0.05	0.01	0.02
MgO	25.2	35.0	34.2	26.7	23.4	23.1	23.3	24.3
CaO	0.07	0.21	0.13	0.18	0.05	0.21	0.09	0.03
NiO	n.d.	0.06	0.09	0.16	0.18	0.17	0.17	0.20
Na_2O	5.99	0.56	0.13	0.35	2.53	0.36	3.85	0.36
K_2O	0.40	0.04	n.d.	4.43	3.67	7.21	3.49	6.64

Notes: An-chrt, anti-nodular chromitite; Diss-chrt, disseminated chromitite; Ms-chrt, massive chromitite; Du, dunite, Hz, harzburgite; n.d., not detected, under operating conditions.

Table S12.3 Major element concentrations of bulk inclusion and proposed parental magmas for the ultramafic series

Sample	SiO_2	TiO_2	Al_2O_3	Cr_2O_3	FeO^{total}	MnO	MgO	CaO	Na_2O	K_2O
Bulk inclusion composition[1]	57.0	0.80	11.5	1.66	2.68	0.06	15.4	2.32	5.56	0.09
Longhi et al. 1983[2]	51.3	0.65	9.56		10.3		17.6	8.39	1.60	0.58
Longhi et al. 1983[3]	55.2	2.83	13.8		12.6		3.50	7.01	3.31	1.72
Helz, 1985	48.6	1.51	14.3		15.3	0.24	6.99	11.1	1.58	0.23
Lipin, 1993[4]	51.9	0.73	13.1	0.12	13.7	0.18	10.5	8.38	1.11	0.27
Lipin, 1994[5]	52.3	0.77	13.8	0.13	13.7	0.19	8.81	1.17	0.29	0.10
Raedeke, 1979	50.5	0.14	16.2	0.14	6.49	0.13	14.7	10.3	1.33	0.05

[1] Also contain 2.6 wt% H_2O, may have few other liquid constitutes, such as the F and Cl.

[2] High-magnesium bronzite diabase dike that cuts the Stillwater complex in the lower banded series. Identified by Longhi et al. (1983) as a possible parental magma candidate for the ultramafic series.

[3] The chilled margin of high-magnesian bronzite diabase dike (WSD-14) (Wooden et al., 1982; Longhi et al., 1983).

[4] The model composition was used by Lipin (1993) in his calculations of magma volume, from a mixture of basal series sill and dike compositions.

[5] Liquid phase after crystallization of a small aliquot of olivine and orthopyroxene.

Analytical condition for back-scattered electron imaging

Polished thin sections of collected samples were investigated with a FEI Nova NanoSEM 450 and QEMSCAN 650F, equipped with energy dispersive X-ray spectrometry from Oxford Instruments at the Institute of Geology and Geophysics, Chinese Academy of Sciences (IGGCAS), Beijing, and at RWTH Aachen University, Germany. High-resolution back-scattered electron images of inclusions were obtained under working conditions of 20 kV accelerating voltage and 3.5 nA beam current, with a working distance of 4 mm from the polepiece to the sample surface. The acquisition time of the BSE images was about 2 min. Semi-quantitative spot analyses of minerals inclusions were obtained at an accelerating voltage of 20 kV and a beam current of 8.8 nA. The acquisition time of each spot was about 15 s, yielding spectra exceeding 2.5 × 106 counts.

Figure S12.1 Back-scattered electron images showing the distribution of polymineralic inclusions in chromite from the Stillwater Complex.

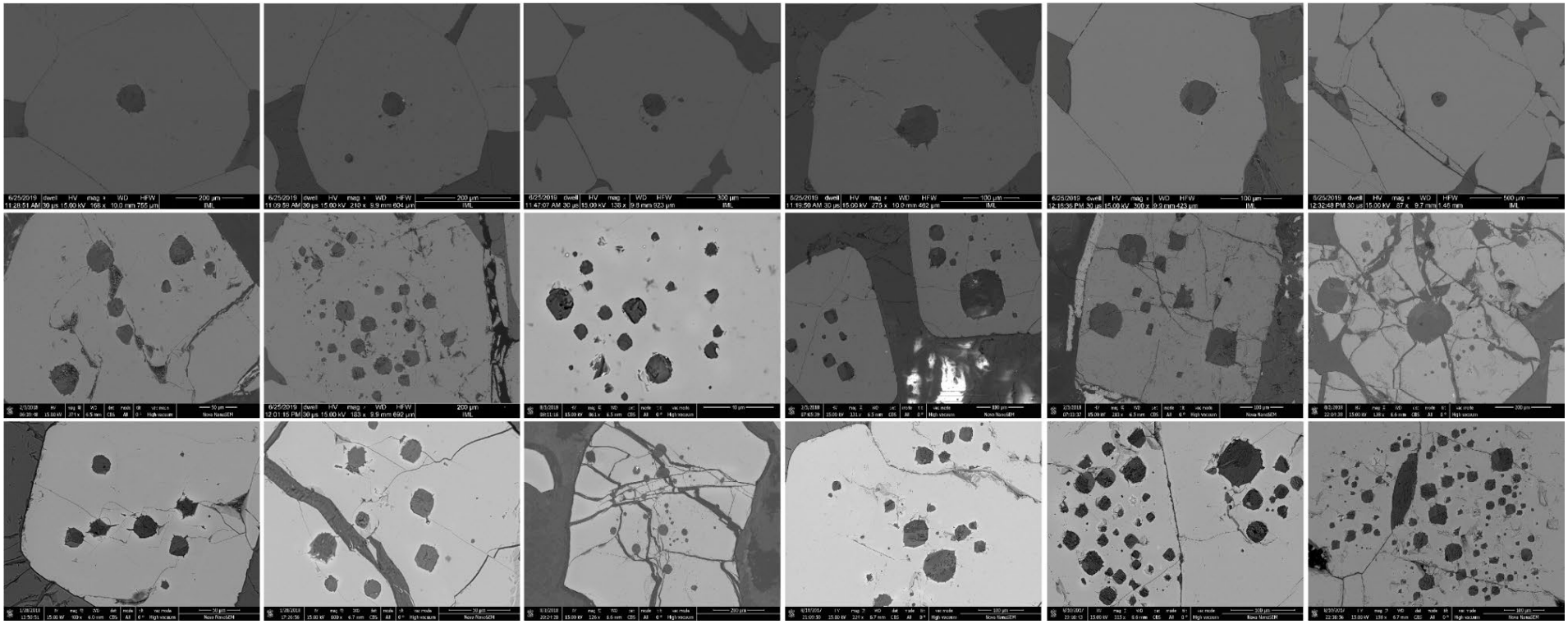

Figure S12.2 Details of back-scattered electron images showing morphology, texture, and mineral assemblage of polymineralic inclusions in chromite from the Stillwater Complex. Abbreviations: Na-Pl, plagioclase; Hbl, hornblende; Ap, apatite.

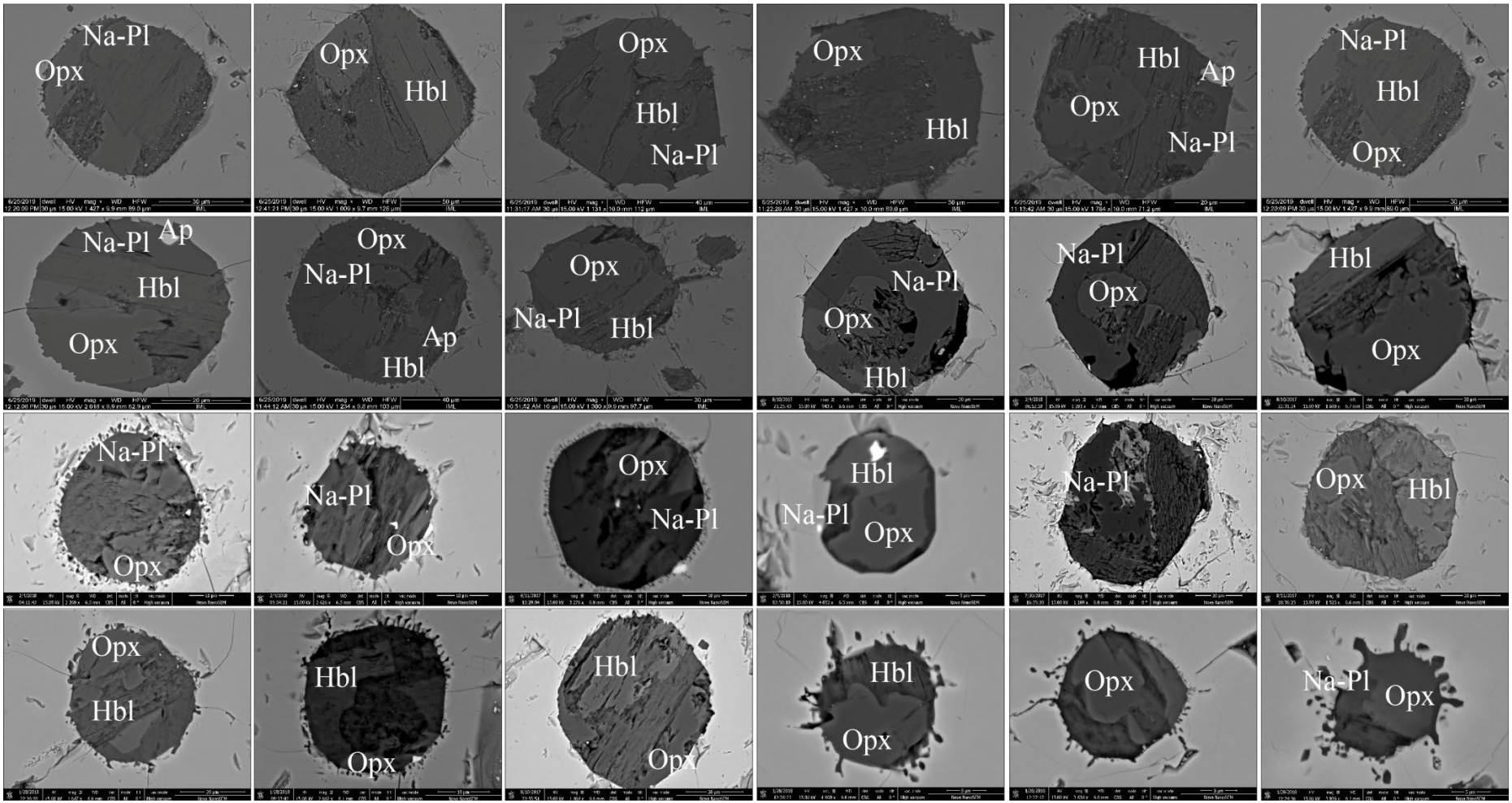

Figure S12.3 Details of back-scattered electron images of single-phase inclusions occurring in margins of chromite grains. The distributed orientations are usually consistent with the edge strikes of the chromite hosts (e.g., Figure S12.3A, B), and the inclusions commonly range in size from 0.05 to 0.2 mm, occasionally occupying the almost half area of the chromite hosts. Inclusion might appear alone, or occasionally, arranged with others along the rims of chromite hosts (Figure S12.3C). The silicates inclusions are dominated by olivine (Figure S12.3A, B) and orthopyroxene (Figure S12.3C, D) with subordinate clinopyroxene (Figure S12.3E-G) and plagioclase (Figure S12.3H). They normally have subhedral to irregular outlines with elongated shapes and fill the negative crystals of chromite hosts (e.g., Figure S12.3H). On the other hand, inclusions have sharp contacts with chromite hosts, and neither high-reflective aureoles nor porous alterations can be found in conjoining boundaries of chromite. As these figures showing, the types of single-phase silicate inclusions have distinct mineralogy, texture, and containing minerals with polymineralic inclusions. These inclusions are compositionally similar to the interstitial silicate minerals, and are even optically continuous with the adjacent silicate minerals (McDonald, 1965; Li et al., 2005). The only significant difference is that some grains in the inclusions have higher Mg numbers than would be expected if they formed by subsolidus diffusion (Spandler et al., 2007; Xiao et al., 2016). Thus, it is more likely that the inclusions represent material trapped during volatile fluxing (e.g., Boudreau, 2016, 2019). Once settled, chromite grains will recrystallize, coarsen and anneal at a later stage (maybe subsolidus conditions), forming the single-phase silicate inclusions in the rims of chromite or acting as the stylolite seam between two chromite grains.

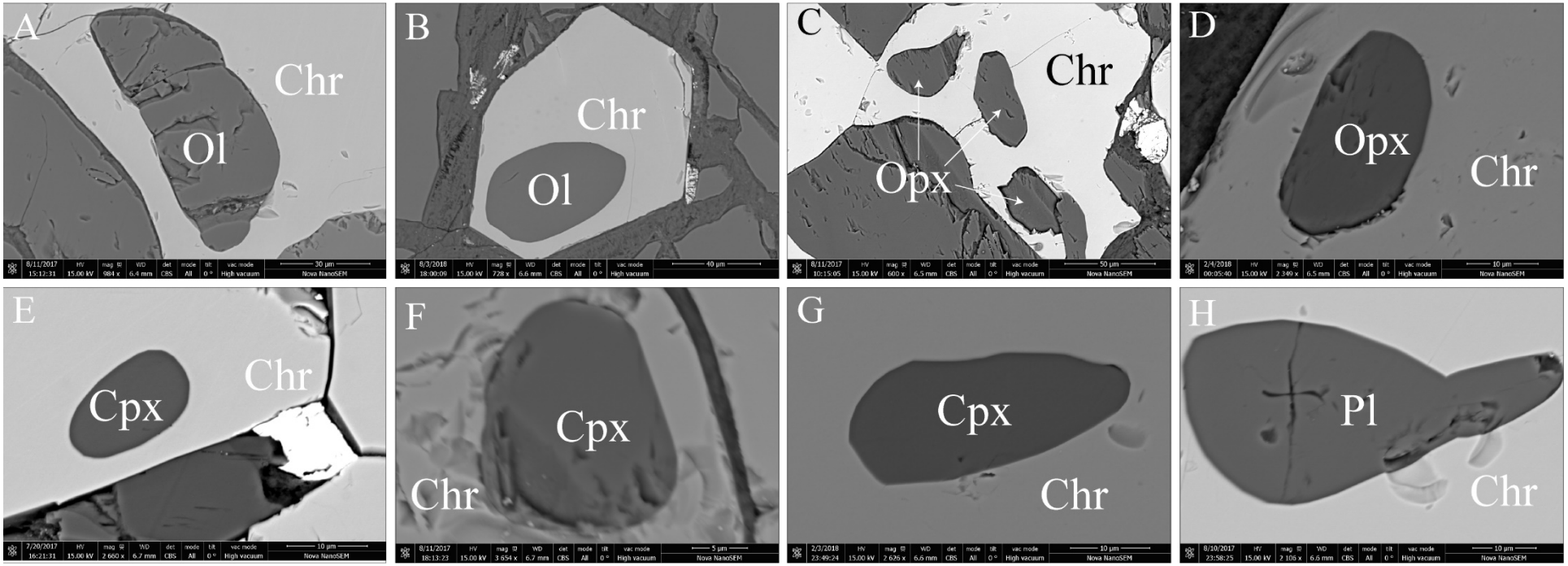

Figure S12.4 Cross-polarized photomicrographs for selected samples. All the microscopic photographs were taken by Olympus microscope BX53 with a lens combination of 2.5×10 magnification. After that, the ImageJ software was used to stitch these photographs together to obtain a larger field of view and observe the structure of the minerals.

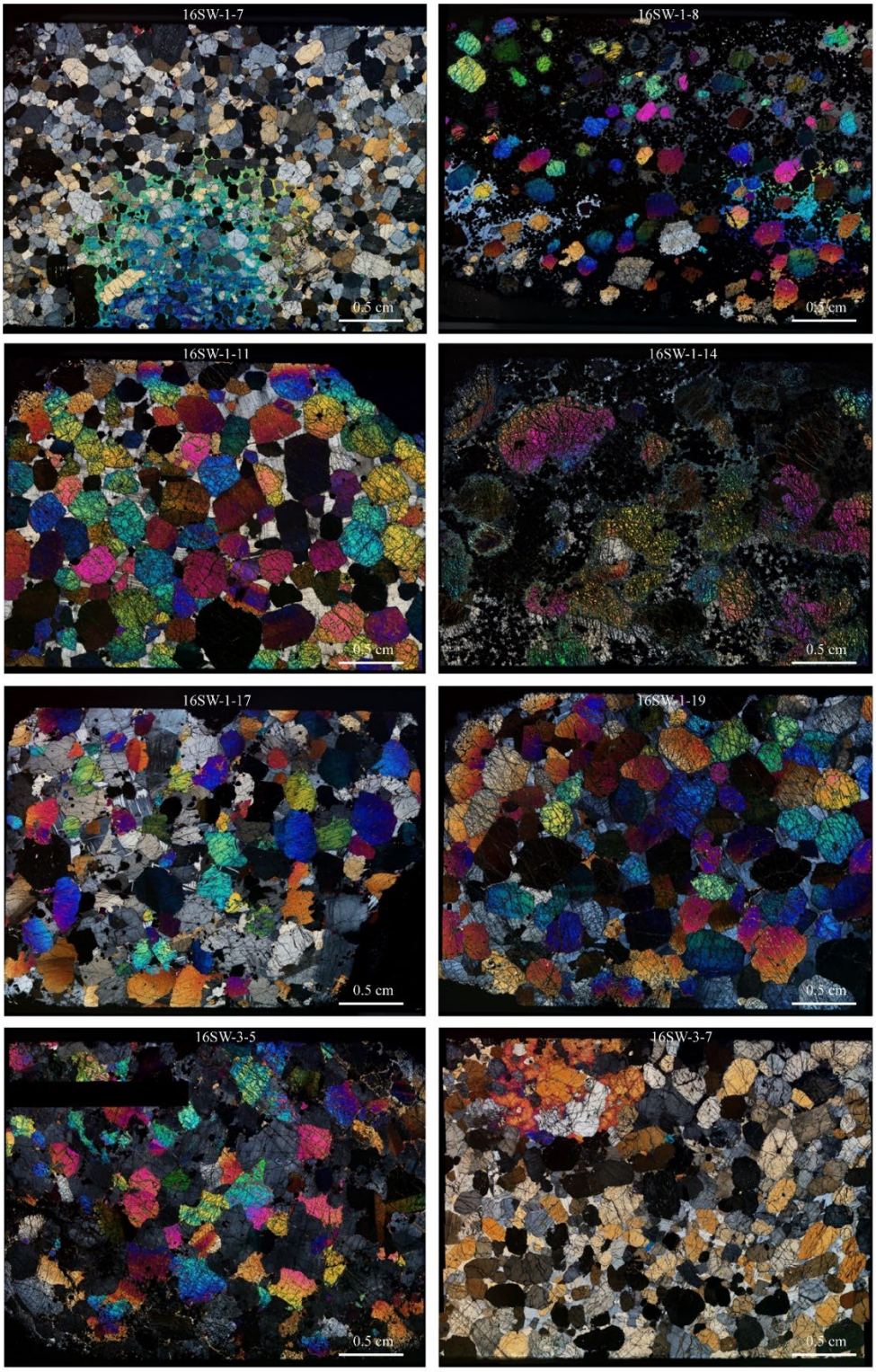

Figure S12.4 (continued)

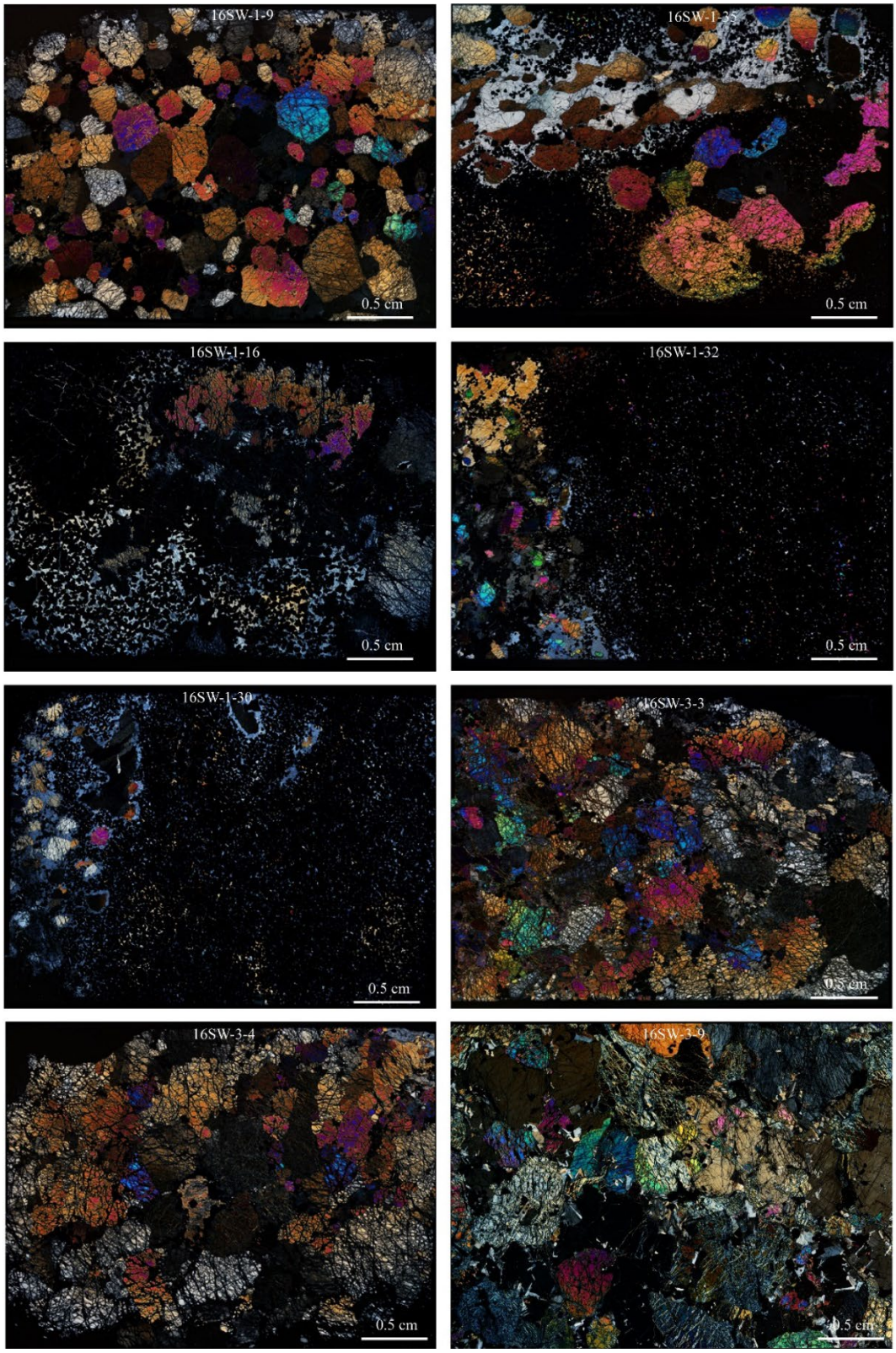

Figure S12.5 Obtained the unpolarized IR absorption spectra for olivine, orthopyroxene and clinopyroxene from the Stillwater Complex.

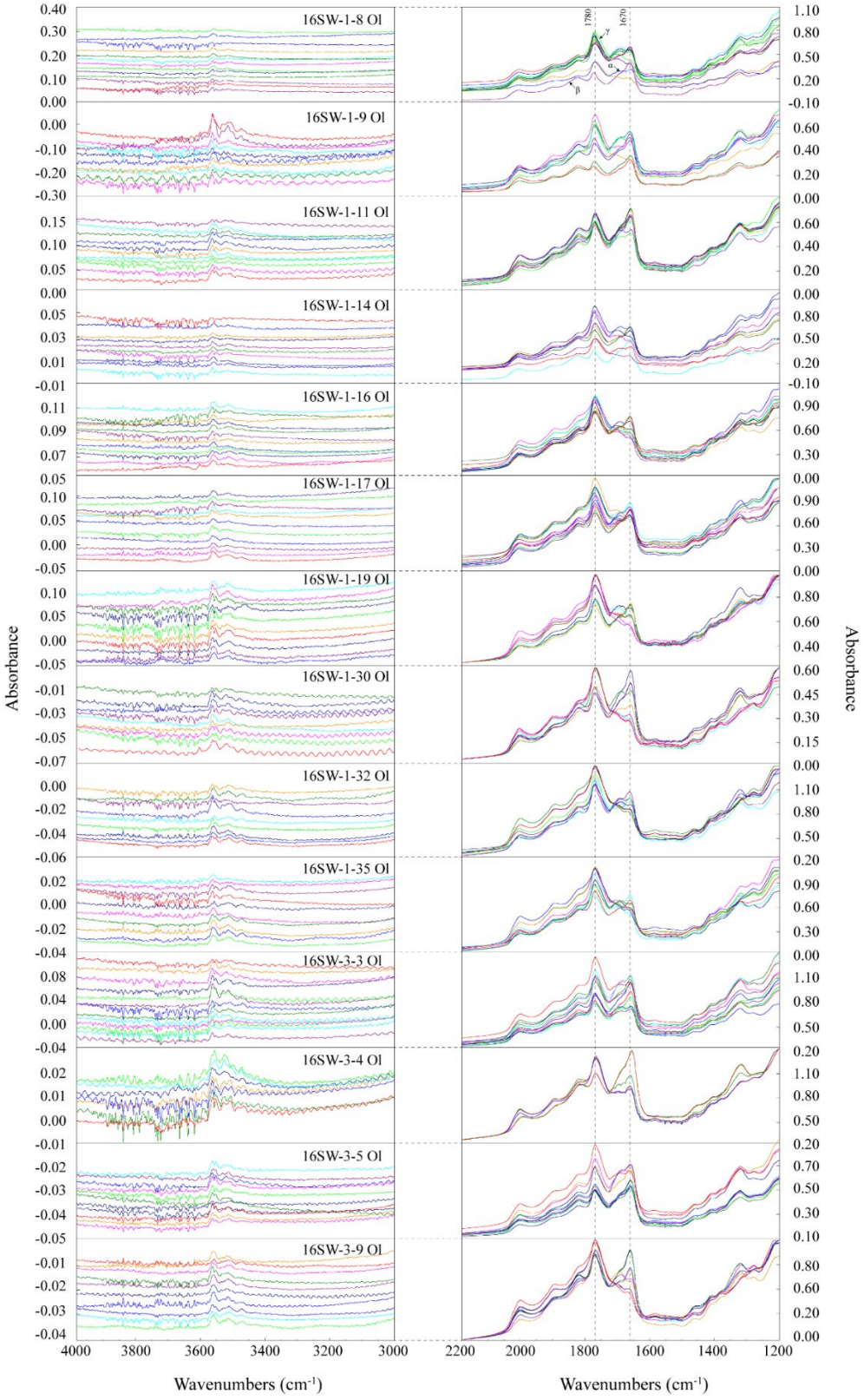

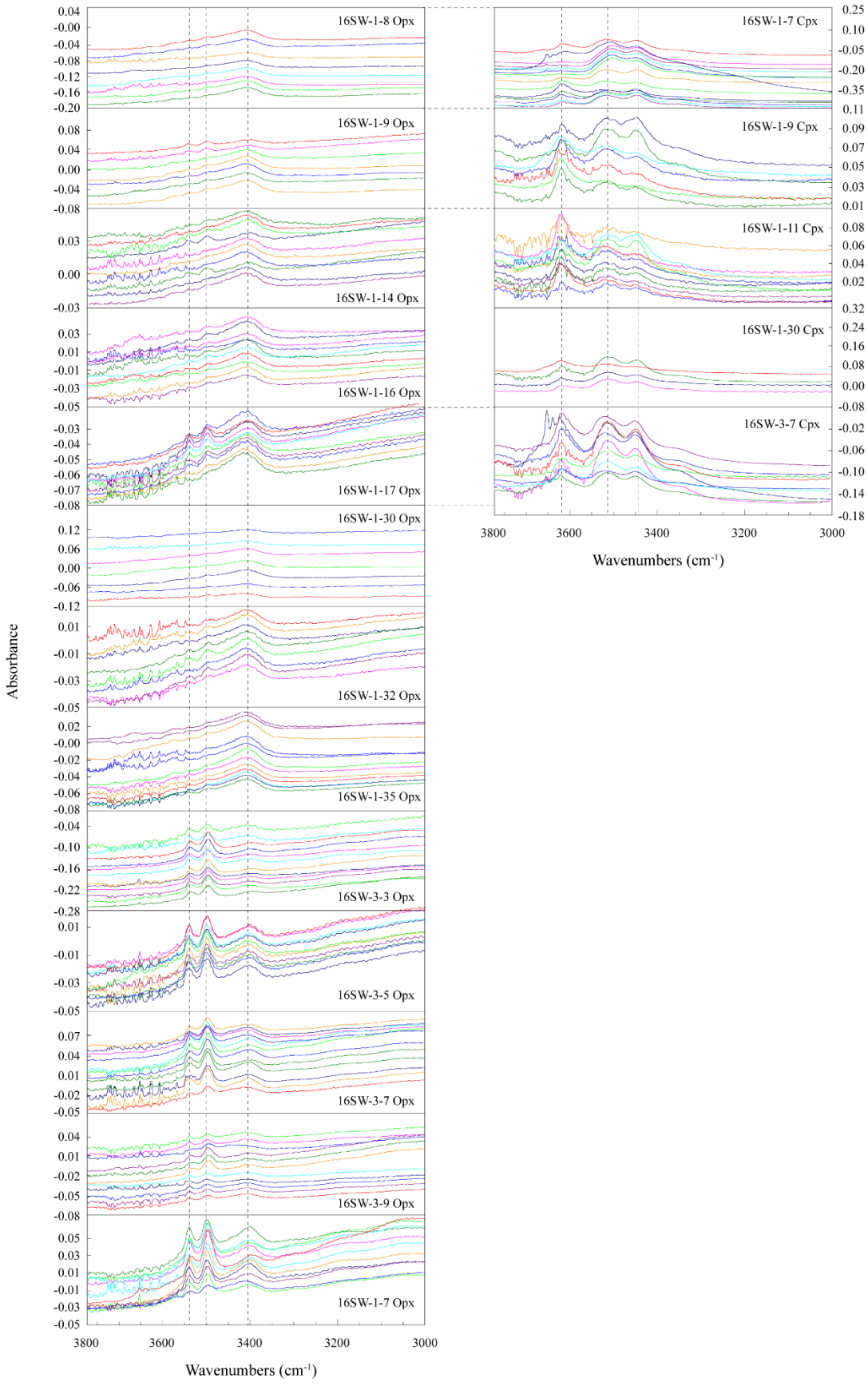
16SW-1-8 Opx
16SW-1-9 Opx
16SW-1-14 Opx
16SW-1-16 Opx
16SW-1-17 Opx
16SW-1-30 Opx
16SW-1-32 Opx
16SW-1-35 Opx
16SW-3-3 Opx
16SW-3-5 Opx
16SW-3-7 Opx
16SW-3-9 Opx
16SW-1-7 Opx
16SW-1-7 Cpx
16SW-1-9 Cpx
16SW-1-11 Cpx
16SW-1-30 Cpx
16SW-3-7 Cpx
Absorbance
Wavenumbers (cm-1)
Wavenumbers (cm-1)